Firing Statistics in Neurons as Non-Markovian First Passage Time Problem

DISSERTATION

zur Erlangung des akademischen Grades
doctor rerum naturalium
(Dr. rer. nat.)
im Fach Physik

eingereicht an der
Mathematisch-Naturwissenschaftlichen Fakultät I
Humboldt-Universität zu Berlin

von
Frau Dipl.-Phys. Tatiana Engel geb. Verechtchaguina
geboren am 31.08.1980 in Vologda

Präsident der Humboldt-Universität zu Berlin:
Prof. Dr. Christoph Markschies

Dekan der Mathematisch-Naturwissenschaftlichen Fakultät I:
Prof. Dr. Christian Limberg

Gutachter:

1. Prof. L. Schimansky-Geier
2. Prof. A.V.M. Herz
3. Prof. J. Garcia-Ojalvo

eingereicht am: 20. Dezember 2006
Tag der mündlichen Prüfung: 5. März 2007

Abstract

Recent experiments revealed the non-Markovian character of the escape dynamics in many physical, chemical and biological systems on time scales prior to relaxation. The escape rates in the non-Markovian case are time-dependent and the escape times are dictated by the initial conditions. Complex, multipeak distributions of the first passage time are characteristic for the non-Markovian case. The non-Markovian first passage time problem cannot be reduced to Kramers' rate description and requires a more detailed, time-dependent approach. In this thesis we investigate various aspects of the non-Markovian first passage time problem and in particular its application to the dynamics of neurons.

Analytical, numerical and experimental methods are jointly used in this work to provide a deeper insight into the many facets of the non-Markovian first passage time problem. On the one hand, the analytical treatment allows for a closer inspection and comprehension of the complex multipeak distributions. On the other hand, comparison of the analytical and numerical predictions with experimental data uncovers the mechanisms underlying the experimentally observed phenomena and stimulates the development of more complete neuron models.

We elaborate an analytical approach to the non-Markovian first passage time problem, which is based on the theory of level-crossings, and obtain several analytical approximations for the first passage time density of a random process with differentiable trajectories. Based on an exact expression for the first passage time density in form of an infinite series of integrals over the joint densities of level-crossings, the approximations are derived either by truncations (direct truncations and Padé approximants) or by correlations decoupling (Hertz and Stratonovich approximations). We compare the quality of these approximations and ascertain their regions of validity. Our approximations are applicable and provide accurate results for different types of dynamics, ranging from almost Markovian to strongly non-Markovian cases.

These analytical approximations in combination with numerical methods are applied to investigate the spike patterns observed in resonant and nonresonant neurons. In particular, we focus on spontaneous (driven by intrinsic noise) spike patterns obtained in stellate (resonant) and pyramidal (nonresonant) cells in the entorhinal cortex in rat. These two types of neurons exhibit striking different spike patterns attributed to the differences in their subthreshold dynamics. We use the phenomenological resonate-and-fire model, which can capture both types of subthreshold dynamics and is still analytically tractable. By applying the Stratonovich approximation, we show that the resonate-and-fire model with experimentally estimated parameter values can quantitatively reproduce the interspike interval distributions measured in resonant as well as in nonresonant cells. We also found negative interspike interval correlations in both types of neurons. To capture these negative correlations, we introduce a novel nonrenewal threshold mechanism in the resonate-and-fire model. The nonrenewal model can quantitatively reproduce both: the striking differences in the interspike interval distributions as well as similar correlations observed experimentally in stellate and in pyramidal cells.

Zusammenfassung

Der Charakter der Schwellwertdynamik (*engl.* escape dynamics) vieler physikalischer, chemischer und biologischer Systeme hat sich in neueren Experimenten als im wesentlichen nicht Markowsch herausgestellt. In diesem Fall sind die Übergangsraten (*engl.* escape rates) von der Zeit und den Anfangsbedingungen abhängig und es stellen sich komplexe Wahrscheinlichkeitsverteilungen für die erste Durchgangszeit (*engl.* first passage time) ein. Aufgrund der Zeitabhängigkeit lässt sich das nicht Markowsche Schwellwertproblem nicht mit Kramers Ratentheorie beschreiben und erfordert die Entwicklung eines Ansatzes mit expliziter Zeitabhängigkeit für die Übergangsraten. In dieser Arbeit werden verschiedene Aspekte nicht Markowscher Schwellwertprobleme und deren Anwendung bei der Beschreibung der Dynamik von Neuronen untersucht.

Durch die Anwendung analytischer, numerischer und experimenteller Methoden konnten wir einen detaillierten Einblick in den Bereich nicht Markowscher Schwellwertdynamik erhalten. Einerseits erlaubt uns der analytische Zugang eine nähere Untersuchung und ein besseres Verständnis der Wahrscheinlichkeitsverteilung der ersten Durchgangszeit. Andererseits hilft uns der Vergleich von analytischen als auch numerischen Vorhersagen mit experimentellen Daten, die grundlegenden Mechanismen der Neuronendynamik zu verstehen und die Entwicklung detaillierter Neuronmodelle besser zu motivieren.

In dieser Arbeit entwickeln wir einen analytischen Zugang zu nicht Markowschen Problemen, dem die Theorie der Schwellwertüberschreitung (*engl.* level crossings) zu Grunde liegt. Im Ergebnis erhalten wir mehrere analytische Näherungen für die Wahrscheinlichkeitsverteilung der ersten Durchgangszeit für Zufallsprozesse mit differenzierbaren Trajektorien. Ausgangspunkt für die Entwicklung dieser Näherungen ist eine unendliche Reihe von Integralen über die Verbundsdichten der Schwellwertüberschreitungen. Dieser mathematisch exakte Ausdruck für die Wahrscheinlichkeitsdichte der ersten Durchgangszeit wird durch den Abbruch der Reihe (endlicher Abbruch der Reihe oder Padénäherung) oder durch die Entkopplung der Korrelationen (Hertz- oder Stratonovichnäherung) genähert. Die Qualität und der Gültigkeitsbereich der Näherungen werden von uns sorgfältig untersucht. Die abgeleiteten Näherungen decken dabei den gesamten Bereich zwischen fast Markowschen und stark nicht Markowschen Problemen ab.

Diese analytischen Näherungen werden in Kombination mit numerischen Methoden genutzt, um Spikemuster in resonanten und nicht-resonanten Neuronen zu untersuchen. Im Besonderen haben wir uns dabei für die Entstehung spontaner, durch zellinternes Rauschen hervorgerufener, Spikemuster in stellaten (resonanten) und pyramidalen (nicht-resonanten) Zellen des entorhinalen Kortex in Ratten interessiert. Diese zwei Neuronentypen zeigten deutliche Unterschiede in den Spikemustern, die den jeweiligen Unterschieden in den unterschwelligen Dynamiken zuzuordnen sind. Es ist hervorzuheben, dass die Anwendung der Stratonovichnäherung für den Fall des Resonate-and-Fire Modells, die Interspikeintervalldichte resonanter und nicht-resonanter Neuronen wiederzugeben vermag. Des weiteren wurden negative Korrelationen in den Spikesequenzen für beide Neuronentypen gefunden. Um diese negativen Korrelationen angemessen zu beschreiben, haben wir einen nicht erneuerbaren (*engl.* nonrenewal) Schwellenmechanismus in das Resonate-and-Fire Modell integriert. Das so modifizierte Resonate-and-Fire Modell kann die starken Unterschiede in den Interspikeintervalldichten als auch ähnliche Korrelationen in resonanten und nicht-resonanten Neuronen beschreiben.

Contents

1

Introduction

Natural sciences have long been dominated by the study of systems in thermodynamic equilibrium. Equilibrium is a stationary state, in which fluxes of all macroscopic quantities vanish and the values of all state variables are uniquely determined by the condition of detailed balance. Classical thermodynamics is concerned with infinitely slow reversible transitions between equilibrium states. The time evolution of macroscopic systems is predetermined by the second law of thermodynamics, the fundamental principle expressing irreversibility. Any initially perturbed isolated system will tend to return to the equilibrium state due to intrinsic irreversible processes.

Most physical systems are not isolated and do not reside in the equilibrium state. In- and effluxes of energy, entropy and matter are invariably present in the majority of physical systems due to the exchange with their surroundings. These fluxes represent constraints driving the system to a state far from the thermodynamic equilibrium. Examples of nonequilibrium systems are many, but the most intriguing nonequilibrium state might be life itself. Every living organism and its parts (individual cells or biomolecules) maintain intrinsic irreversible processes, using the energy influx from their surroundings, and expel thereby produced entropy back to the surroundings. The exploration of general principles underlying phenomena in living systems became a branch of modern physics, which is concerned with the study of systems far from the thermodynamic equilibrium.

A striking difference exists in the behavior of linear and nonlinear systems when subjected to nonequilibrium constraints. The evolution of a linear system is governed by a set of linear equations for the state variables, whose solutions possess a mathematical simplicity related to the properties of superposition and scaling. The behavior of a linear system under nonequilibrium conditions is predictable and similar to its behavior near the equilibrium state. Favored by their simplicity, linear equations are frequently used to describe various phenomena. However, linearity as well as equilibrium states are rather exceptional in our world, and linear equations reveal their inherent limitations when confronted with the diversity of complex situations encountered in physics, biology and chemistry.

For nonlinear systems the property of superposition does not hold: a small change in the amplitude of a perturbation may evoke a dramatic change in the amplitude of the system's response. Far from thermodynamic equilibrium, nonlinearities give rise to symmetry breaking, multistability, and feedback loops. These mechanisms lead to diversification of dynamical behavior and emergence of complexity and lay the foundation for evolution and life (Ebeling and Feistel, 1994; Waldrop, 1992; Nicolis and Prigogine, 1989; Haken, 1983).

The presence of nonlinearities is especially vital for living organisms, where they are involved in mechanisms underlying cell communication and in particular cell signaling (Alberts et al., 2002; Keener and Sneyd, 1998). Many cell signals are carried by molecules (hormones or neurotransmitters) that are released by one cell and bind to the receptors of another cell. Typically the activation of a receptor triggers a chain of reactions altering the behavior of several interacting proteins. This so called signal transduction pathway may involve feedback loops, signal amplification, and interactions between multiple signals. Complex signal transduction pathways provide a nonlinear regulatory mechanism controlling the function of an individual cell and of the entire organism.

Certain cells, for example cardiac cells, neurons and muscles, can communicate by electrical signals using the potential difference across their membranes (Dayan and Abbott, 2001). The membrane potential is sustained at a nonzero level by the action of ion pumps, which move the ions in- and outward the cell against their concentration gradients. This active ion flux maintains the membrane in a far-from-equilibrium state, in which due to nonlinear feedback mechanisms many cells, including most neurons, exhibit *excitability*.

Formally, every excitable system possesses a resting, an excited and a refractory state. An unperturbed excitable system resides in its steady-state (resting state). Perturbations with a small amplitude lead to a small, almost linear response (subthreshold response), whereas sufficiently strong perturbations evoke large excursions of the state variables (excited state or suprathreshold response). After excitation the system returns back to its resting state. It takes a certain time, called refractory time, before the system recovers and can be excited again. The whole cycle including excited and refractory states is usually referred to as a *spike*. In response to input stimuli spikes can occur repeatedly in an excitable system giving rise to temporal and spatiotemporal spike patterns.

It is important to understand the spike patterns generated in an excitable system. For example, in epidemiology spikes correspond to outbreaks of diseases. The comprehension of the system dynamics leading to a particular spike pattern may help to develop more efficient vaccination strategies (Viboud et al., 2006). In the nervous system spikes can be reliably distinguished from the background noise and can travel almost without attenuation over long distances from one cell to another. By these two reasons spikes are thought to be the main information unit involved in the *neural computation* (Koch, 1999; Rieke et al., 1997). The term "neural computation" refers to the processing of incoming sensory signals and the control of the motor output performed by the nervous system. The current hypothesis in computational neuroscience is that neurons encode information by the spike frequency, spike timing and correlations between spike times on the levels of an individual neuron and assemblies of neurons. The neural code still remains far from being deciphered. Understanding of the spike patterns generated on neural membranes may provide new insights into this topical problem.

Two factors jointly shape spike patterns in neurons: the deterministic response properties of the membrane and noise. The deterministic properties are dictated by the composition of voltage dependent ion channels in the membrane, namely by the number of channels and their type. Noise in neurons originates from the random synaptic input, from the stochastic nature of synaptic transmission and from fluctuations of the membrane conductance. Due to the invariable action of noise the spike patterns generated by neurons have a strong stochastic component, and noise cannot be excluded from consideration when studying neuron dynamics. Rather than being a dispensable nuance, noise was shown to be essential for the function of the nervous system (Traynelis and Jaramillo, 1998; White et al., 2000). Noise can introduce coherence, improve the signal transmission and enhance the synchronization of coupled excitable units. The idea that noise can play a constructive role in nonlinear dynamical systems is now widely accepted and supported by a quantitative theory and measurements (Lindner et al., 2004; Gammaitoni et al., 1998).

This work contains novel results which, we hope, will prove to be useful in statistical physics as well as in neuroscience. We try to answer two questions:

I. *How do stochastic and deterministic properties of neuron dynamics jointly shape the spike patterns?* Stochastic and deterministic influences can hardly be separated in experiments. Therefore we choose to investigate the spike patterns in resonant and nonresonant neurons. Resonant neurons show a subthreshold resonance with maximal response amplitude achieved at a finite resonance frequency. The subthreshold response amplitudes in nonresonant neurons decay monotonically with the frequency. Based on the fact that the deterministic behavior of these neurons is known to be different, a similar stochastic input should therefore reveal the influence of the deterministic component alone. By studying the differences in random spike patterns, we ascertain the impact of the deterministic subthreshold dynamics on the spiking behavior.

By reducing the neuron output to a sequence of spikes, all details about the subthreshold dynamics are neglected. In Chapter 3 we examine whether the description in terms of spike sequences is sufficient in the case of resonant neurons, which exhibit a complex subthreshold dynamics. Using the FitzHugh-Nagumo model we demonstrate that the whole neuron output can be reconstructed from the statistics of spike times.

II. *What are the mechanisms responsible for the appearance of complex spike patterns in resonant neurons?* Excitable systems generate a spike whenever the state variables reach their threshold values. The statistics of spike times is therefore related to the statistics of the corresponding first passage times. We ascertain that the escape mechanism of the membrane potential over its excitation threshold is Markovian in nonresonant neurons and non-Markovian in resonant neurons, which explains the differences in spike patterns observed experimentally. Markovian escape dynamics is characterized by a constant escape rate independent of initial conditions and can be treated in terms of Kramers' rate theory. Chapter 4 reviews the Markovian approach to the first passage time problem and exposes its limitations.

In non-Markovian models the initial conditions dictate the escape times leading to time-dependent escape rates and complex spike patterns. Kramers' description is not applicable to the case of a non-Markovian dynamics. Therefore we devote Chapter 5 to elaborate appropriate analytical methods to treat the non-Markovian first passage time problem. As the main theoretical result, we obtain several analytical approximations for the first passage time probability density in non-Markovian models. Based on the theory of level-crossings, these approximations can be applied to random processes with differentiable trajectories. We compare the quality of different approximations and ascertain their regions of validity. The approximations are mutually complementary in the sense, that in different dynamical regimes different approximations turn out to be more accurate. The regions of validity of our approximations cover all types of escape dynamics ranging from almost Markovian to strongly non-Markovian cases. In Chapter 5 we apply these approximations to a harmonic oscillator with threshold and reset driven by white or colored Gaussian noise and to the FitzHugh-Nagumo model, in order to demonstrate the validity of our approximations in linear as well as in nonlinear systems of arbitrary dimension.

The analytical methods developed in Chapter 5 facilitate the analysis of random spike patterns in resonant and nonresonant neurons. In Chapters 6 and 7 our analytical approximations are applied to experimental data. In Chapter 6 we study the changes in spike patterns of resonant and nonresonant neurons in response to the variation of parameters of the input signal.

Chapter 7 is devoted to the investigation of spike patterns observed experimentally in stellate (resonant) and pyramidal (nonresonant) cells of the entorhinal cortex in rat. The neuron dynamics is mathematically described in terms of the resonate-and-fire model. This simple model can capture both – resonant and nonresonant – types of the subthreshold behavior and extracts the dynamical mechanism shaping the spike patterns. Using experimentally estimated values for the subthreshold model parameters, we theoretically predict the spike patterns in stellate and pyramidal cells, which are in excellent agreement with experimental data. To account for spike-induced correlations, experimentally found in both types of neurons, we introduce a novel nonrenewal spike generation mechanism in the resonate-and-fire model. This nonrenewal model captures both – the striking differences in the spike patterns as well as similar correlations in resonant and nonresonant neurons.

This work was inspired by the dynamics of neurons and we frequently appeal to these example throughout the text. However, the effects of noise in nonlinear systems are rather general and independent of the system's nature. Excitability and stochasticity are encountered in a vast variety of nonlinear physical systems far from equilibrium ranging from lasers and chemical reactions to climate dynamics and cardiac cells. Besides in resonant neurons, the non-Markovian escape mechanism is found in thermochemical systems (Nowakowski and Kawczyński, 2006) as well as in chemical reactions on the femtoseconds time scales (Diau et al., 1998). We hope that the theoretical results obtained in this work will find an application in a broader class of noise driven excitable systems of physical, chemical or biological nature.

2

Basic facts and concepts

To investigate the non-Markovian first passage time problem and its application to neuron dynamics, we take advantage of methods developed in the theory of random processes as well as of concepts developed in neurophysiology. In this chapter both are briefly reviewed. We do not intend to provide a detailed presentation, since the knowledge accumulated in both fields is enormously large and cannot be covered in one chapter. The aim is to introduce the main ideas and models which will be used throughout this work. For a more complete account the reader is referred to the literature cited in this text.

2.1 Deterministic aspects of neuron dynamics

Neurons are highly nonlinear excitable systems, which inherently include a stochastic component in their dynamics. Therefore neurons are a suitable physical system to study noise driven escape dynamics. Exhaustive accounts on physiological aspects and mathematical description of neural dynamics can be found in Dayan and Abbott (2001); Koch (1999); Keener and Sneyd (1998) and Tuckwell (1988).

2.1.1 Neurons

Neurons are particular cells specialized to perform computation: Neurons can receive, process and transmit information coded by electrical pulses. The membrane of a neural cell is a lipid bilayer, selectively permeable for ions. The voltage drop across the membrane is nonzero. The potential inside the cell membrane is usually about -70 mV relative to the potential outside the cell (which is conventionally defined to be 0 mV). This voltage drop is called the *membrane potential* and the cell is said to be polarized. A nonzero membrane potential is maintained by the action of ion pumps, moving ions across the membrane against their concentration gradients. The neuron membrane also contains a large number and diversity of *ion channels*, allowing ions to flow across the membrane down their electrochemical gradient. The stationary value of the membrane potential is called the *resting potential.* The co-acting in- and outward ion fluxes result in a complex dynamics of the voltage across the membrane. These changes in the membrane potential represent electrical signals in neurons.

Neurons differ histologically depending on their location within the brain and their function in information processing pathways. However, three important morphological specializations can be distinguished in most neurons: the dendrites, the soma and the axon.

Dendrites constitute a wide branching tree of links between neurons, which allow a neuron to receive signals from other cells. Signals are transmitted between cells through specialized junctions, called *synapses*, which may be of chemical or electrical nature. A signal arriving at a chemical synapse triggers the release of a neurotransmitter. The neurotransmitter molecules diffuse and bind to the receptors on the dendritic spine exciting a postsynaptic potential. The postsynaptic potential in electrical synapses is caused by the direct electrical coupling between neurons. Dendritic trees and synaptic connections allow neurons to form associated circuits and are crucial for the neural computation.

The *soma*, or the cell body, is the central part of a neuron, where signals arriving through dendrites are collected and processed. As a result, a response to incoming signals is generated in the soma and transmitted to other cells along the axon.

The *axon* is a long projection of a neuron, that conducts electrical signals away from the soma and is connected by synapses to dendrites of other neurons.

The response of a neuron to an input signal is determined by processes taking place in the soma. The evolution of the membrane potential is governed by the dynamics of ion channels, which open and close controlling the ion flow across the membrane. Typically the opening and closing of ion channels is voltage dependent and the resulting voltage dynamics is therefore highly nonlinear. Ion channels are selectively permeable for specific ions. The main channel types are the sodium (Na^+), potassium (K^+) and calcium (Ca^{2+}) channels. Moreover, ion channels differ in their dynamics, characterized by the activation time, maximum conductivity and reversal potential. Therefore the composition of ion channels in the membrane, namely the number of channels and their types, determines the net current across the membrane and the type of the voltage dynamics.

To the best of our knowledge, the majority of neurons are excitable. When a neuron is depolarized sufficiently, such that the voltage exceeds a threshold value, a positive feedback process is initiated leading to an *action potential*, also referred to as a *spike*. An action potential is a rapid swing in the polarity of the voltage from negative to positive and back. The entire cycle lasts a few milliseconds only, see Fig. 2.1. The peak amplitude of a spike typically reaches about 100 mV. In a particular neuron spikes have an almost uniform shape, which can slightly differ from cell to cell. After every spike, the voltage is reset to approximately the same value, which is typically below the resting potential. This effect is called *afterhyperpolarization*. Few milliseconds after every spike it is impossible to evoke another action potential even by a very strong stimulation, this period is called the *absolute refractory time*. During the next interval lasting for tens of milliseconds, called the *relative refractory time*, the initiation of an action potential requires stronger stimulation than otherwise. We refer to the voltage dynamics below the excitation threshold as the *subthreshold* voltage dynamics.

Spikes can be transmitted along an axon over long distances almost without attenuation, therefore a spike is thought to be the main information unit in the brain. Deciphering of

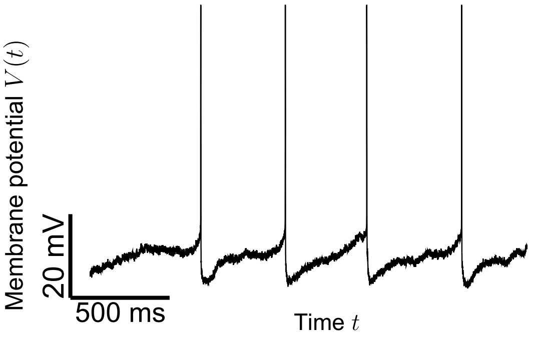

Figure 2.1: Typical time evolution of the voltage $V(t)$ across the neuron membrane. The data were recorded *in vitro* from a pyramidal cell in the entorhinal cortex in rat. The spikes have an almost uniform shape. After every spike the voltage is reset to approximately the same value below the resting potential (afterhyperpolarization).

the neuron code still remains an unsolved problem. Various concepts have been introduced to explain how information may be encoded in a spike train. The most habitual are the concepts of rate and temporal coding. The former assumes that information is contained in the instantaneous firing frequency of a neuron. The latter is based on the precise timing of every spike. The independent-spike, independent-neuron and correlation codes have been proposed as well. A recent trend is to suppose, that a neuron combines different coding strategies depending on the functional situation, e.g. the frequency range of stimulation or the activity of the surrounding network (Vaadia et al., 1995; Chacron et al., 2001). Many experiments provide evidence, that neurons can fire spikes with millisecond precision under specific conditions (Abeles, 2004). This implies importance of spike timing for the neural code and makes it important to understanding spike patterns generated by neurons.

Though information is believed to be contained in spike trains rather than in subthreshold voltage evolution, the properties of the subthreshold voltage dynamics strongly influence the spike generation process. Different types of neurons respond with different spike patterns to the same stimulation. It is therefore substantial to understand how the subthreshold properties of a neuron affect the firing patterns.

2.1.2 Subthreshold resonance

Subthreshold resonance is a subthreshold property of the voltage dynamics to respond selectively to incoming signals. The response amplitudes depend on the stimulation frequency and the maximum response amplitude is achieved at a nonzero *resonance frequency.* Subthreshold resonance is a widespread property found in many neuron types throughout the entire nervous system: in mesencephalic trigeminal neurons (Wu et al., 2001), dorsal root ganglion neurons (Amir et al., 1999), neocortical neurons (Hutcheon et al., 1996; Gutfreund et al., 1995), thalamic neurons (Puil et al., 1994) and in many others.

For small response amplitudes, the voltage dynamics can be treated as linear in good approximation. Under this assumption, the resonance properties of a cell can be characterized by a complex impedance function $Z(f)$, which relates the voltage response amplitude $V(f)$ to the harmonic input current $I(f)$ with the frequency f. Spectra of the input current $I(f)$ and of the voltage response $V(f)$ are connected by:

$$V(f) = Z(f)I(f). \tag{2.1}$$

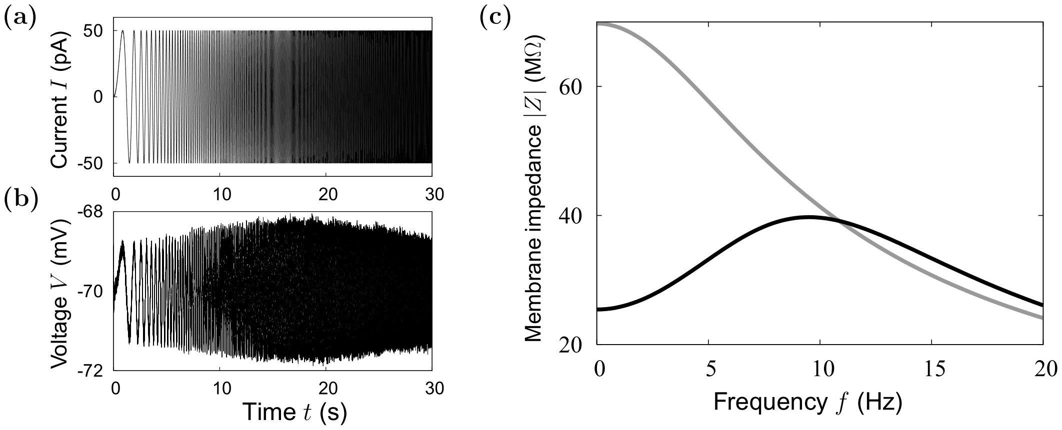

Figure 2.2: Measurement of the subthreshold resonance. (a) Input current $I(t)$ sweeping through many frequencies over time (ZAP input) is injected into the cell. (b) Typical record of a voltage response $V(t)$ to the ZAP current. (c) Amplitude of the impedance function $|Z|(f)$ for typical resonant (black) and nonresonant (gray) cells. $|Z|(f)$ decays monotonically with the frequency in the nonresonant cell, and has a pronounced maximum in the resonant cell.

In experiments it is impossible to inject consecutively many harmonic signals with different frequencies into the cell, in order to measure the impedance function. Therefore one usually applies a ZAP current to the cell, which sweeps through many frequencies over time (Lampl and Yarom, 1997):

$$I(t) = I_0 \sin\left(2\pi f \frac{t}{T} t\right). \tag{2.2}$$

Here T is the duration of the stimulus and f is its maximal frequency. If the stimulus frequency increases slowly with time, the impedance function can be well approximated by Eq. (2.1) as the Fourier transform of the measured voltage divided over the Fourier transform of the injected current.

Figs. 2.2(a) and 2.2(b) show a typical ZAP stimulus and a typical voltage response to this stimulus, respectively. The amplitude of the impedance function $|Z|(f)$ is illustrated in Fig. 2.2(c) for a resonant and a nonresonant cells. The impedance function decays monotonically with the frequency in nonresonant cells, whereas in resonant cells it exhibits a well pronounced maximum at a nonzero frequency, called the resonance frequency.

The subthreshold resonance is closely related to the *subthreshold oscillations* of the membrane potential (Erchova et al., 2004). In resonant cells, a small depolarization of the membrane evokes oscillations of the membrane potential with a frequency close to the resonance frequency. Rhythmic subthreshold activity is pronounced in a resonance peak in the voltage power spectrum and in the oscillating voltage autocorrelation function (Desmaisons et al., 1999). Since after every spike the membrane potential is reset to an almost constant value different from the resting potential (afterhyperpolarization), every spike is followed by a subthreshold oscillation with a fixed initial phase. This oscillation modulates the voltage distance to the excitation threshold and may affect the spike generation process.

Many experimental and theoretical studies reveal, that the subthreshold resonance influences the suprathreshold spiking response of neurons. The firing rate of a resonant neuron was found to depend on the stimulus frequency content in a resonant way (Schreiber et al., 2004). The spike timing in resonant neurons (Desmaisons et al., 1999; Haas and White, 2002; Verechtchaguina et al., 2004) and the firing rate modulation (Brunel et al., 2003; Richardson et al., 2003) were also related to the subthreshold resonance.

The long lasting interest in the oscillatory properties of individual neurons and associated resonance phenomena is explained by the fact, that the rhythmic activity on the single-cell level is likely to influence and support network oscillations. Synchronized rhythmic activity in the brain has been related to behavior, memory and perception, as well as to pathologies as diverse as epilepsy and insomnia (Hughes and Crunelli, 2005; Destexhe and Sejnowski, 2003; McCormick and Contreras, 2001; Steriade, 2000). Neural synchrony was also suggested to be essential for the neural coding (Singer, 1999).

2.1.3 Neuron models

Mathematical treatment of neuron dynamics requires the construction of appropriate neuron models. Usually models are designed to reproduce the main features of the voltage dynamics. If spatial variations of the membrane potential can be neglected, changes in the membrane potential can be described by a single voltage variable V. Here, we only consider this type of neuron models, called the *single-compartment models.*

The neuron membrane is charged: an excess negative charge is located on the inside surface of the cell membrane, balanced by a positive charge on its outside surface. The membrane has a capacitance C, and changes in the voltage drop V across the membrane are described by a standard equation:

$$C \frac{dV}{dt} = -I_{\mathrm{ion}} + I, \tag{2.3}$$

where I_{ion} is the net current produced by ions flowing across the membrane, and I is an input current injected into the cell. The membrane capacity is proportional to the surface area of the cell, and a specific membrane capacity (per unit area) is approximately the same for all neurons and is independent of the membrane potential. Note, that in neuron models like Eq. (2.3) the transmembrane current I_{ion} results from the ion fluxes, unlike electrical circuits, where charge is carried by electrons. Moreover, the ion channel conductance has a gating nature (a channel is either open or closed), with the consequence that noise in conducting membranes has different origins than the shot noise in electrical circuits.

The analogy with electrical circuit has proven to be useful in constructing neuron models. These models can be divided into phenomenological and biophysically substantiated models. The former include effective membrane parameters, which result from the averaging over many ion channel types. The latter incorporate separate dynamical equations for different types of ion channels and are therefore more complex.

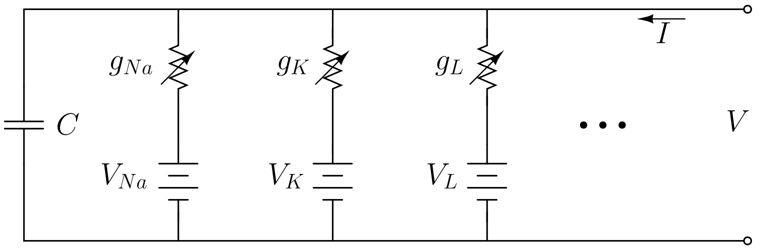

Figure 2.3: Electrical circuit diagram for the Hodgkin-Huxley model.

I. Hodgkin-Huxley type models. The most important class of models for the excitable dynamics of the membrane potential constitute the Hodgkin-Huxley type models. Originally Hodgkin and Huxley (1952) developed their equations to explain propagation of an electrical signal along a giant axon of squid. The Hodgkin-Huxley type models have been widely adopted to a broad variety of excitable cells. Here we present the classical form of the Hodgkin-Huxley equations.

In many neural cells the principle transmembrane current is carried by sodium (Na^+) and potassium (K^+) ions. The contribution of other ionic currents is rather small and can be summarized in a net leak current. If we denote the corresponding conductances by g_{Na}, g_{K} and g_{L}, respectively, the equation (2.3) for the voltage variable $V(t)$ takes the form:

$$C\,\frac{dV}{dt} = -g_{\mathrm{Na}}(V - V_{\mathrm{Na}}) - g_{\mathrm{K}}(V - V_{\mathrm{K}}) - g_{\mathrm{L}}(V - V_{\mathrm{L}}) + I. \tag{2.4}$$

Here V_{Na}, V_{K} and V_{L} are the reversal potentials for the sodium, potassium and leak currents, respectively. These are the equilibrium values of the membrane potential for specific ionic currents, hence the direction of current flow through the channel switches as the membrane potential passes through the reversal potential.

The Hodgkin-Huxley model can be represented by the electrical circuit diagram in Fig. 2.3. It can be extended by including additional conductances and batteries, which account for additional types of ion channels, into the circuit Fig. 2.3.

The sodium $g_{\mathrm{Na}}(V)$ and potassium $g_{\mathrm{K}}(V)$ conductances are voltage dependent, leading to a highly nonlinear dynamics in the Hodgkin-Huxley model Eq. (2.4). Full dynamical equations for the voltage dependent conductances and detailed explanation of the spike excitation mechanism in the Hodgkin-Huxley model can be found in Keener and Sneyd (1998). The Hodgkin-Huxley equations account for the main features of the spike generation process. For appropriate parameter values (Chik et al., 2001) the subthreshold resonance properties can be captured as well.

II. Phenomenological models. Although the biophysically substantiated models provide a more detailed and accurate description of the voltage dynamics, their complexity and extremely large number of involved variables and parameters hamper the mathematical treatment of the model and the appreciation of mechanisms underlying the observed phenomena. In contrast, simple phenomenological models, though being less precise, often allow for a comprehension of the basic dynamical mechanisms, which can be general for a broader class of models. Therefore we use extensively simple phenomenological models in the present work. These models are introduced in the following paragraphs in order of increasing complexity.

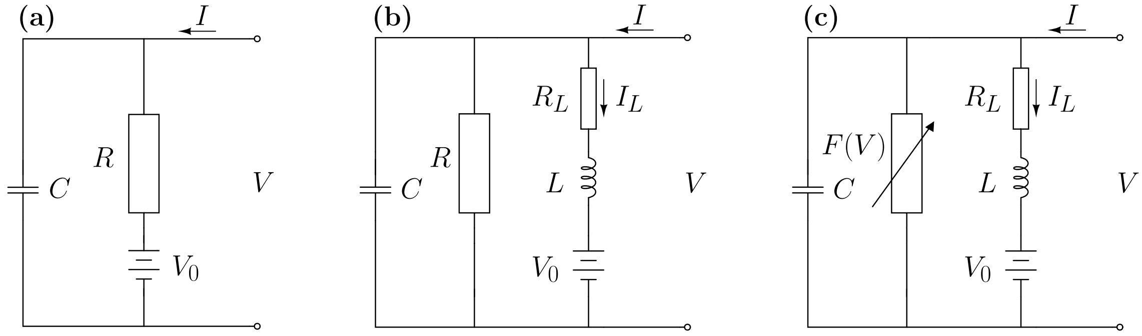

Figure 2.4: Electrical circuit diagrams for phenomenological neuron models: (a) integrate-and-fire model, (b) resonate-and-fire model, (c) FitzHugh-Nagumo model.

The ***integrate-and-fire model*** (IF) provides the simplest phenomenological description of the voltage dynamics. The subthreshold voltage evolution in the IF model is based on two simplifying assumptions. First, the IF model only accounts for an effective conductance g_{eff}, averaged over all types of ion channels. Second, the conductance g_{eff} is assumed to be constant through the entire subthreshold voltage range. Thus, the IF model is a reduction of the Hodgkin-Huxley model Eq. (2.4). If we introduce $g_{\text{eff}} = g_{\text{Na}} + g_{\text{K}} + g_{\text{L}}$ and $V_0 = (g_{\text{Na}}V_{\text{Na}} + g_{\text{K}}V_{\text{K}} + g_{\text{L}}V_{\text{L}})/g_{\text{eff}}$, then the IF model can be represented by the circuit diagram in Fig. 2.4(a). Here C is a constant membrane capacity, $R = 1/g_{\text{eff}}$ is an effective resistance, and the battery $V_0 < 0$ accounts for a nonzero resting potential due to the action of ion pumps.

Substitution of these averaged quantities into the Hodgkin-Huxley equation (2.4) yields an equation for the subthreshold voltage dynamics in the IF model:

$$C\,\frac{dV}{dt} \;=\; -\frac{1}{R}(V - V_0) \;+\; I. \tag{2.5}$$

Since the resistance R is assumed to be constant (voltage independent), the dynamics given by Eq. (2.5) is linear and does not exhibit excitable behavior. The excitability in the IF model is restored by introducing threshold and reset values for the voltage variable V. Whenever the voltage variable V reaches the threshold value V_b, a spike is generated and the voltage is reset to a prescribed reset value V_r after a time τ_r, which mimics the refractory time. We assume that $V_r < V_0 < V_b$. This simplified excitability mechanism is useful if the biophysical details of the spike initiation are not substantial for a particular problem.

In the absence of any input signal ($I = 0$), the voltage in the IF model relaxes to the resting potential $V_f = V_0$, which is the single fixed point (stable node) of the system Eq. (2.5). Any subthreshold perturbation decays exponentially to the fixed point with the characteristic time constant $\tau = RC$. Increase of the input current $I > 0$ shifts the fixed point towards the threshold $V_f = V_0 + IR$ and at $I = (V_b - V_0)/R$ the system bifurcates. For $I > (V_b - V_0)/R$ the system moves on a limit cycle and the IF neuron fires spikes periodically.

The integrate-and-fire model is sufficient to describe many experimental situations and is favored in theoretical studies due to its simplicity. However, its dynamical repertoire is rather restricted. In particular, the IF model does not account for the subthreshold resonance properties.

The ***resonate-and-fire model*** (RaF) is a simple generalization of the IF model, which is able to reproduce the subthreshold resonance properties of neurons. The RaF model can be derived by linearization of the Hodgkin-Huxley equations (Mauro et al., 1970; Villacorta and Panetsos, 2005). The resulting model can be represented by the circuit diagram in Fig. 2.4(b), which is formally obtained by the addition of a parallel inductive branch to the RC-circuit of the IF model, Fig. 2.4(a).

By virtue of Kirchhoff's laws, the dynamics of the voltage V and the current through the inductive branch I_L obey:

$$\begin{aligned} C\,\frac{dV}{dt} &= -\frac{1}{R}V - I_L + I, \\ L\,\frac{dI_L}{dt} &= -I_L R_L + V - V_0. \end{aligned} \tag{2.6}$$

Here all parameters of the RLC-circuit are assumed to be constant, thus the linear equations (2.6) only account for the subthreshold voltage dynamics. Excitability is again introduced into the model by stipulating a constant threshold value V_b and a reset value V_r for the voltage variable V. In this two-dimensional system, an additional reset condition for the second variable is required. It can be provided by resetting the voltage derivative to zero ($\dot{V} = 0$) after every spike.

Equations (2.6) can be rewritten as a single second order differential equation for the voltage variable $V(t)$:

$$C\,\frac{d^2V}{dt^2} + \left(\frac{1}{R} + \frac{CR_L}{L}\right)\frac{dV}{dt} + \frac{1}{L}\left(1 + \frac{R_L}{R}\right)V \;=\; \frac{1}{L}V_0 + \frac{R_L}{L}I + \frac{dI}{dt}. \tag{2.7}$$

The subthreshold dynamics in the autonomous system ($I = 0$) is equivalent to a damped harmonic oscillator with the eigenfrequency $\omega_0^2 = (1+R_L/R)/(LC)$ and a damping coefficient $\gamma = 1/(RC) + R_L/L$. Note, that nonlinearity enters the RaF model through the threshold and reset conditions.

In the absence of an input current $I = 0$, the RaF model has a single stable fixed point, corresponding to the resting potential $V_f = V_0/(1 + R_L/R)$. The fixed point can be either a focus (in the underdamped regime if $\gamma < 2\omega_0$) or a node (in the overdamped regime if $\gamma > 2\omega_0$). A subthreshold perturbation relaxes to the fixed point in oscillatory manner in the underdamped regime, whereas it decays monotonically in the overdamped regime. In the underdamped regime the amplitude of the impedance function has a maximum close to the frequency ω_0. Thus the underdamped RaF model accounts for the subthreshold resonance properties observed in resonant neurons.

Injection of a constant input current $I > 0$ shifts the fixed point towards the threshold $V_f = (V_0 + R_L I)/(1 + R_L/R)$. The situation in the overdamped regime is analogous to the situation in the IF model. For $I > \left(V_b - V_0 + V_b R_L/R\right)/R_L$ the system moves on a limit cycle and the RaF neuron generates spikes periodically. It can be shown, that in the underdamped regime a limit cycle exists if $V_f > [V_b - V_r \exp\left(-\gamma\pi/2\Omega\right)]$ with $\Omega = \sqrt{|\omega_0^2 - \gamma^2/4|}$.

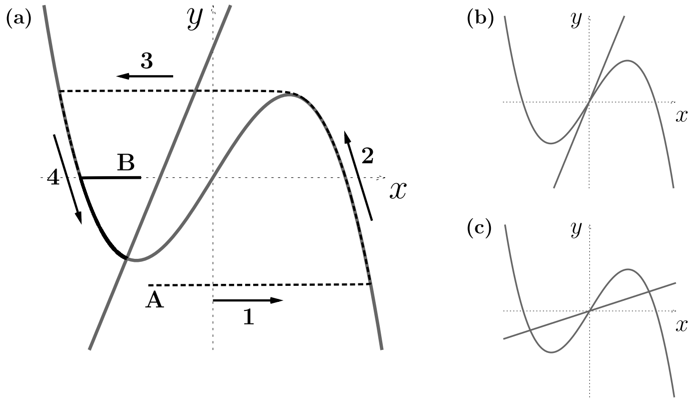

Figure 2.5: Nullclines for the FN model. (a) Excitable regime. Examples of trajectories in case of a *suprathreshold* (A) and a *subthreshold* (B) responses are shown with black lines. (b) Oscillatory regime. (c) Bistable regime.

The ***FitzHugh-Nagumo model*** (FN) is a two-dimensional model, which is able to reproduce excitable, bistable and oscillatory behaviors. The FN model is a reduction of the Hodgkin-Huxley model to a fast and a slow variables.

The FN model can be represented by the circuit diagram in Fig. 2.4(c), where $F(V)$ denotes the current through the nonlinear resistance. The equations for the dynamical variables V and I_L read:

$$\begin{aligned} C\,\frac{dV}{d\tau} &= -F(V) - I_L + I, \qquad (2.8)\\ L\,\frac{dI_L}{d\tau} &= -I_L R_L + V - V_0. \end{aligned}$$

The function $F(V)$ is assumed to be cubical.

If we transform to dimensionless time $t = \tau R_L/L$ and dimensionless variables $x = V/V_0$ and $y = (I_L - I)R/V_0$, where R is chosen to be the input resistance of the nonlinear element $R = 1/F'(0)$, then the equations (2.8) simplify to:

$$\begin{aligned} \epsilon\dot{x} &= f(x) - y, \qquad (2.9)\\ \dot{y} &= \gamma x - y + b. \end{aligned}$$

The new dimensionless parameters are

$$\epsilon = \frac{CRR_L}{L}, \qquad \gamma = \frac{R}{R_L}, \qquad b = \frac{R}{V_0}I - \frac{R}{R_L}. \qquad (2.10)$$

The function $f(x)$ is defined as $f(x) = -RF(V_0 x)/V_0$ and is also cubical. The physical meaning of the parameters of the electrical circuit in Fig. 2.4(c) implies, that the new parameters ϵ and γ are positive, while b can be either positive or negative depending on the input current I. Usually ϵ is assumed to be a small constant ($\epsilon \ll 1$, $\epsilon \ll 1/\gamma$), hence $|\dot{x}| \gg |\dot{y}|$. One therefore refers to x as the fast and to y as the slow variable.

Since the FN model is a two-dimensional system, it is very convenient to consider its dynamics in the phase plane. Nullclines $\dot{x} = 0$ and $\dot{y} = 0$ of the FN model are defined by the equations: $y = f(x)$ (cubic x-nullcline) and $y = \gamma x + b$ (linear y-nullcline). The cubic nullcline has two stable branches (left and right) and one unstable branch (middle), see Fig. 2.5. The intersection point of the nullclines is the fixed point of the FN system. The cubic shape of the x-nullcline yields three cases: (i) an excitable regime with one stable fixed point in the system, Fig. 2.5(a), (ii) an oscillatory regime with one unstable fixed point, Fig. 2.5b, and (iii) a bistable regime with one unstable and two stable fixed points, Fig. 2.5(c).

Let us consider how transitions between these regimes occur when the input current I is varied. Assume that all other parameters of the circuit in Fig. 2.4(c) are held constant. This is equivalent to changing the parameter b of the FN model Eq. (2.9) while keeping ϵ and γ constant.

For sufficiently large γ, such that $\gamma > \max_{(x_1,x_2)}[f'(x)]$ where x_1 and x_2 are the extremal points of $f(x)$, there exists a single fixed point in the system for arbitrary values of b. If the input current $I \ll 0$ and correspondingly $b \ll 0$ (see Eq. (2.10)), the fixed point is stable and is located on the right branch of the x-nullcline (excitable regime). As b increases, the fixed point moves towards the maximum of the x-nullcline. Near the maximum the fixed point looses its stability by the Hopf bifurcation, which can be sub- or supercritical depending on the shape of $f(x)$ and parameter values. Beyond the Hopf bifurcation the unstable fixed point coexists with a stable limit cycle. This is the oscillatory regime, (Fig. 2.5(b), when spikes are generated periodically. Further increase of b shifts the unstable fixed point towards the minimum of the x-nullcline. Near this minimum another Hopf bifurcation occurs (sub- or supercritical), beyond which the stable fixed point is located on the left branch of the x-nullcline (excitable regime, Fig. 2.5(a)).

For $\gamma < \max_{(x_1,x_2)}[f'(x)]$ there exists a range of b values, where the system possesses three fixed points. For $b \ll 0$, a single stable fixed point is located on the right branch of the cubic nullcline. At the critical value b_{c1}, the y-nullcline becomes tangent to the x-nullcline. This is the point of a saddle-node bifurcation, beyond which two stable and one unstable fixed points coexist (bistable regime, Fig. 2.5(c)). A further increase of b shifts the unstable fixed point towards the maximum of the x-nullcline, until at the critical value b_{c2} the y-nullcline becomes tangent to the x-nullcline. At b_{c2}, one stable and the unstable fixed point collide and disappear in a saddle-node bifurcation. For $b > b_{c2}$ the only stable fixed point of the system is located on the left branch of the cubic nullcline (excitable regime).

Changing the input current I forces the electrical circuit in Fig. 2.4(c) to operate either in an excitable, a bistable or an oscillatory regime. In this work, we apply the FN system to model the excitable dynamics of neurons, therefore the excitable regime is the most interesting regime for our purposes. Let us consider how the system responds to different initial perturbations in the excitable regime. The stable fixed point is the only attractive state in this regime, therefore any initial perturbation will relax to the fixed point. However, depending on the type of the perturbation, the relaxation can occur in two different ways.

Consider initial conditions below the cubic nullcline and apart from the fixed point, for example take the initial conditions A in Fig. 2.5(a). In this region of the phase plane $\dot{x} > 0$, so the x-variable increases rapidly until it approaches the right branch of the x-nullcline (where $\dot{x} = 0$), while the value of y remains almost unchanged. This part of the trajectory is marked as “1” in Fig. 2.5(a) and is called the upstroke. Thereafter the trajectory moves along the stable branch of the x-nullcline (excited state, indicated by 2 in Fig. 2.5(a)). The

x-nullcline becomes unstable near its maximum, and the trajectory enters the region above the x-nullcline, where $\dot{x} < 0$. Here y changes only slightly, while x rapidly approaches the left branch of the x-nullcline (refractory state, 3 in Fig. 2.5(a)). The system further relaxes to the fixed point along the left branch of the cubic nullcline (recovery state, 4 in Fig. 2.5(a)). Thus for specific initial conditions the system performs a large excursion in the phase plane before it is approaching the fixed point. Thereby x first rapidly rises to large values and then returns to the vicinity of the fixed point. This large excursion of the x-variable corresponds to a spike generated by the neuron. We refer to this kind of response as the *suprathreshold* response.

If initial conditions are chosen from another region in the phase plane, the perturbation will decay to the fixed point without approaching the right branch of the x-nullcline. An example is shown in Fig. 2.5(a) for the trajectory with initial conditions B. This kind of response is referred to as the *subthreshold* response. The separatrix between initial conditions leading to the sub- and suprathreshold response can be found numerically. Without going into details, we just mention that the separatrix passes close to the middle branch of the cubic nullcline. For an exhaustive discussion of this question we refer the reader to FitzHugh (1961) and Lindner (2002). Note, that the separatrix is a curve in the (x, y) plane rather than a vertical line at a fixed x value.

In summary, all initial perturbations can be divided into those leading to a subthreshold and those leading to a suprathreshold response. The FN model can account for the excitability in neuron dynamics. For appropriate parameter values the FN model can also capture subthreshold resonance properties. This will be discussed in Section 3.1.

2.2 Stochasticity in neurons

The idea that the spike timing can be indeed very precise is nowadays widely accepted. Recent studies reveal, that neurons can reproduce spike patterns with millisecond precision and provide evidence for the high reliability of the spike initiation process in various parts of the nervous system (Mainen and Sejnowski, 1995; Abeles, 2004; Shmiel et al., 2005).

On the other hand, noise is a fundamental ingredient to the dynamics of an individual neuron as well as in ensembles of neurons. In average, a single neuron is connected to as many as 10’000 other neurons, each firing at a rate of a few spikes per second. Therefore a small amount of noise in every input spike train produces a severalfold amplified noise in the target cell. Furthermore, signals are communicated from cell to cell through synapses, which are essentially noisy due to the random release and stochastic binding of a neurotransmitter. The dynamics of an individual cell is also intrinsically stochastic, since the opening and closing of ion channels is essentially random.

Thus noise cannot be excluded from consideration when studying the dynamics of a single or coupled neurons. In this section we briefly review some mathematical methods to model different noise sources in neural systems. We also discuss the constructive role, which noise can play in neural systems to understand how precise firing patterns can emerge in a noisy environment.

2.2.1 Mathematical description of random spike trains

Due to multiple noise sources in the brain, firing patterns of neurons are random and must be described using probabilistic measures. Current theories often assume that only the spike times are relevant for the neural code, while the parameters of an individual spike (such as spike duration, amplitude or shape) are irrelevant. The output signal of a neuron can therefore be reduced to a δ-pulse sequence:

$$\rho(t) = \sum_{i=1}^{N} \delta(t - t_i), \tag{2.11}$$

where t_i are the spike arrival times, and N is the number of spikes generated during the time interval $(0, \tau)$. The spike train in Eq. (2.11) constitutes a *point process*[1].

The spike-count rate r and the instantaneous firing rate $n_1(t)$ are the most basic statistical measures for a δ-spike train. The spike-count rate is the firing rate averaged over the duration of a single trial:

$$r = \frac{N}{\tau} = \frac{1}{\tau} \int_0^{\tau} \rho(t) dt. \tag{2.12}$$

The instantaneous firing rate is the average over an ensemble of trials

$$n_1(t) = \lim_{\Delta t \to 0} \frac{1}{\Delta t} \int_t^{t+\Delta t} \langle \rho(t') \rangle dt', \tag{2.13}$$

here the brackets denote the ensemble average. Definition (2.13) implies that $n_1(t)dt$ is the probability to obtain a spike within the interval $(t, t + dt)$. Evidently, for a stationary process with a time-independent firing rate $n_1(t) = n_0 = \text{const}$, the relation $n_0 = \lim_{\tau \to \infty} r$ holds.

The probability $\mathcal{P}_s$ to obtain a particular spike pattern, such that a spike occurs in each of p intervals $(t_1, t_1 + dt_1)$, ..., $(t_p, t_p + dt_p)$, is expressed through the joint density of spike times $n_p(t_1, \ldots, t_p)$ as $\mathcal{P}_s = n_p(t_1, \ldots, t_p) dt_1 \ldots dt_p$. Note, the functions $n_p(t_1, \ldots, t_p)$ are not normalized and are essentially joint firing rates rather than probability densities. A spike generation process is completely determined by the infinite sequence of all joint densities $n_p(t_1, \ldots, t_p)$ for $p = 1, 2, \ldots$. Unfortunately, the number of possible spike patterns in a typical experimental situation is so large, that it is impossible to estimate even roughly all joint densities $n_p(t_1, \ldots, t_p)$. At best only a few lower order densities are assessable experimentally. To predict the higher order densities one usually has to assume a statistical model underlying the spike generation process, which matches the lower order densities.

Such a statistical model can be a Poisson process, based on statistical independence of all spikes and stationarity of the spike train. By definition the joint densities of a Poisson process factorize $n_p(t_1, \ldots, t_p) = n_1(t_1) \ldots n_1(t_p)$, and due to stationarity we have $n_p(t_1, \ldots, t_p) = n_0^p$. Thus the measurement of the firing rate completely determines the spike generation process. Also an inhomogeneous Poisson process with a time-dependent rate $n_1(t)$ has proven to be useful. It is defined as a nonstationary point process with independent events.

Another statistical model can be a renewal process. The instantaneous firing rate $n_1(t)$ is assumed to depend on the time elapsed since the last occurred spike only. Hence, the

---

[1] The methods from the theory of point processes are reviewed in Section 2.3.

intervals between successive spikes are statistically independent and identically distributed. A description in terms of *interspike intervals* (ISI) is suitable for a renewal spike train, which is completely determined by the probability density function $\mathcal{F}(T)$ of the interspike intervals T. More generally, if the renewal assumption does not hold, a point process is determined by the infinite sequence of all joint ISI probability densities $\mathcal{F}(T_1, \ldots, T_p)$ for $p = 1, 2, \ldots$. This interval specification is equivalent to the description in terms of the densities $n_p(t_1, \ldots, t_p)$.

The important and experimentally assessable quantities are the mean $\langle T \rangle$ and the variance $\langle \Delta T^2 \rangle$ of the interspike interval T:

$$\langle T \rangle = \lim_{N \to \infty} \frac{1}{N-1} \sum_{i=2}^{N} (t_i - t_{i-1}), \qquad \langle \Delta T^2 \rangle = \lim_{N \to \infty} \frac{1}{N-1} \sum_{i=2}^{N} (t_i - t_{i-1})^2 - \langle T \rangle^2. \tag{2.14}$$

Both can be equivalently expressed in terms of the ISI probability density $\mathcal{F}(T)$:

$$\langle T \rangle = \int_0^\infty t \mathcal{F}(t) dt, \qquad \langle \Delta T^2 \rangle = \int_0^\infty t^2 \mathcal{F}(t) dt - \langle T \rangle^2. \tag{2.15}$$

The relation between the mean ISI and the instantaneous firing rate $n_1(t)$ can be obtained:

$$\langle T \rangle = \lim_{N \to \infty} \frac{\sum_{i=2}^{N} (t_i - t_{i-1})}{N-1} = \lim_{\tau \to \infty} \left(\frac{1}{\tau} \int_0^\tau \rho(t) dt \right)^{-1} = \lim_{\tau \to \infty} \left(\frac{1}{\tau} \int_0^\tau n_1(t) dt \right)^{-1}, \tag{2.16}$$

where both steps are legitimate in the limit $N, t \to \infty$. In the case of a stationary spike train, relation (2.16) reduces to $\langle T \rangle = 1/n_0$, i.e. the mean ISI equals the reciprocal firing rate.

2.2.2 Modeling noise in neurons

The neuron models discussed in Section 2.1.3 are inherently deterministic. To account for the stochasticity of neural dynamics we introduce a noise source into these models. In this section we briefly discuss how noise originating from the synaptic input and from the random action of ion channels can be modeled.

I. Modeling random synaptic input. Consider a neuron which receives incoming spikes from other cells at a large number of its synapses, which accumulate to the total synaptic input current I_s. Just as ionic currents could be expressed in terms of corresponding conductances in Section 2.1.3, the synaptic current can be expressed using the total synaptic conductance g_s. The voltage dynamics obeys:

$$C \frac{dV}{dt} = -I_{\text{ion}} + g_s (V - V_s), \tag{2.17}$$

where V_s is the *synaptic reversal potential.* The total ionic current I_{ion} can be described by any of the models introduced in Section 2.1.3 or by any other deterministic neuron model. Fluctuations in the synaptic conductance g_s enter Eq. (2.17) as a multiplicative noise term. However, due to the time scale separation between dynamics of voltage V and conductance g_s, the voltage dependence of the synaptic current can be neglected and the voltage V in front of g_s in Eq. (2.17) can be replaced by its stationary value (see Section 6.2 for details).

The total synaptic conductance is the sum over the conductances of all individual synapses:

$$g_s = \sum_k \bar{g}_k P_k(t), \tag{2.18}$$

with $\bar{g}_k$ denoting the maximal conductance of the k-th synapse. $P_k(t)$ is the open probability of the k-th synapse, which reflects that release and binding of a neurotransmitter are stochastic processes. Namely,

$$P_k(t) = \sum_j P^j_{\mathrm{rel}} P_{\mathrm{s}}(t - t_j), \tag{2.19}$$

where t_j are the spike arrival times at the k-th synapse. P^j_{rel} describes the release of a neurotransmitter in a presynaptic cell and is proportional to the number of released transmitter molecules. P^j_{rel} is a random variable and varies from spike to spike in every synapse. Due to the synaptic plasticity, P^j_{rel} can also depend systematically on time on time scales ranging from milliseconds to minutes and hours. However, here we neglect any effects of plasticity and consider synapses to be stationary.

Immediately after release of the transmitter its molecules bind to postsynaptic receptors, rapidly increasing the open probability $P_{\mathrm{s}}(t)$ of ion channels in the postsynaptic cell. Diffusion, degradation of the transmitter and presynaptic uptake mechanisms contribute to reduction of the transmitter concentration and cause a decrease of $P_{\mathrm{s}}(t)$. The time course of the open probability $P_{\mathrm{s}}(t)$ is described by a response function $s(t)$:

$$P_s(t) = \sum_j s(t - t_j)\Theta(t - t_j). \tag{2.20}$$

Here $\Theta(t)$ is the Heaviside step function. The response function $s(t)$ describes the unitary time course of $P_{\mathrm{s}}(t)$, and is assumed to be equal for all synapses.

Substitution of Eqs. (2.19) and (2.20) into Eq. (2.18) yields an equation for the evolution of the synaptic conductance:

$$g_s = \sum_i a_i s(t - t_i)\Theta(t - t_i), \tag{2.21}$$

where t_i are the spike arrival times at any of the cell synapses. $a_i = \bar{g}_k P^i_{\mathrm{rel}}$ are the random synaptic amplitudes summarizing the variation of the maximal synaptic conductances within the ensemble as well as the randomness of the neurotransmitter release.

Let us consider two particular response functions $s(t)$, which are usually used in the literature (Amemori and Ishii, 2001; Destexhe et al., 2001; Moreno-Bote and Parga, 2004). First, $s(t) = \exp(-t/\tau_s)$ corresponds to an immediate rise of the postsynaptic conductance, followed by an exponential decrease with a characteristic decay time τ_s, called the *synaptic time constant*. In this case, the random conductance Eq. (2.21) obeys the differential equation

$$\dot{g}_s = -\frac{1}{\tau_s} g_s + \xi(t), \tag{2.22}$$

where we introduced a stochastic term

$$\xi(t) = \sum_i a_i \delta(t - t_i). \tag{2.23}$$

Second, $s(t) = [\tau_1/(\tau_1 - \tau_2)]\,[\exp(-t/\tau_1) - \exp(-t/\tau_2)]$ describes an exponential rise in the conductance on the time scale τ_2 and a subsequent exponential decay on the time scale τ_1 ($\tau_1 > \tau_2$). The corresponding stochastic dynamics of the synaptic conductance is governed by

$$\begin{aligned} \dot{g}_s &= y, \\ \dot{y} &= -\Gamma\, y - \Omega_0^2\, g_s + \xi(t). \end{aligned} \tag{2.24}$$

with $\Gamma = (\tau_1^{-1} + \tau_2^{-1})$ and $\Omega_0^2 = (\tau_1 \tau_2)^{-1}$, and y being an auxiliary variable.

Equation (2.17) together with either of equations (2.22) or (2.24) describe the stochastic voltage dynamics of a neuron subjected to a random synaptic input. However, the statistical properties of the random force $\xi(t)$ still remain to be determined. Generally, these properties depend on the statistics in the input spike train t_i and on the distribution of synaptic amplitudes a_i. If both are specified, the correlation functions of $\xi(t)$ can be explicitely calculated using methods from the theory of point processes (Svirskis and Rinzel, 2000).

A simple case, called the *diffusion approximation*, is frequently used to model a random synaptic input (Gerstner and Kistler, 2000; Amemori and Ishii, 2001; Richardson, 2004). In this case, the input spike train is assumed to be an inhomogeneous Poisson process with a rate $n_1(t)$ and the distribution of random amplitudes a_i to be a Gaussian with mean A and variance σ_A^2. Then $\xi(t)$ is a δ-correlated (white) noise with mean $\langle \xi(t) \rangle = A n_1(t)$ and the correlation function $\langle \xi(t)\xi(t') \rangle - \langle \xi(t) \rangle \langle \xi(t') \rangle = \sqrt{2D(t)}\delta(t-t')$ where $2D(t) = (A^2 + \sigma_A^2) n_1(t)$ (Svirskis and Rinzel, 2000). If the higher order correlation functions are small compared to the first and second order correlation functions, one may consider $\xi(t)$ to obey a Gaussian probability distribution.

In case of a stationary Poisson input spike train ($n_1(t) = n_0$) and a balanced number of excitatory and inhibitory inputs ($A = 0$), the random force $\xi(t)$ is a white Gaussian noise with zero mean and intensity $2D = \sigma_A^2 n_0$. In this case the random process in Eq. (2.22) is an Ornstein-Uhlenbeck noise (Uhlenbeck and Ornstein, 1930), and the process in Eq. (2.24) is a harmonic noise (Schimansky-Geier and Zülicke, 1990).

The random synaptic input can be modeled as an additive colored noise term in Eq. (2.17) for the voltage dynamics. If spikes independently arrive at a large number of synapses, fluctuations of the total synaptic conductance can be described either by Ornstein-Uhlenbeck or by harmonic noise. The firing statistics for a resonate-and-fire neuron driven by colored noise is treated in Section 5.3.

II. Modeling channel noise. The conductance of ion channels is essentially stochastic. Every channel resides in one of many possible conformational states and transitions between these states occur randomly due to thermal fluctuations. Typically only one of all possible states is conducting, and the number of ion channels populating this state is proportional to the membrane conductance. The random opening and closing of ion channels leads to fluctuations of the membrane conductance.

The opening of a channel is associated with the activation of n subunit gates. In the conducting state all n subunit gates are activated, otherwise the channel is closed. We mark the different states of a channel by the number of activated subunit gates $0, 1, \ldots n$. Transitions between these states are governed by the kinetic scheme:

$$0 \quad \underset{\beta}{\overset{n\alpha}{\rightleftarrows}} \quad 1 \quad \underset{2\beta}{\overset{(n-1)\alpha}{\rightleftarrows}} \quad 2 \quad \ldots \quad \underset{n\beta}{\overset{\alpha}{\rightleftarrows}} \quad n.$$

The transition rates α and β are generally voltage dependent, and the factors $n, n-1, \ldots, 1$ in the transition rates correspond to the number of subunit gates available for the corresponding transition. The rate equations for this kinetic scheme read:

$$\begin{aligned} \dot{p}_0 &= -n\alpha p_0 + \beta p_1, \\ \dot{p}_i &= (n-i+1)\alpha p_{i-1} + (i+1)\beta p_{i+1} - (n-i)\alpha p_i - i\beta p_i, \qquad i = 1, \ldots, n-1, \\ \dot{p}_n &= -n\beta p_n + \alpha p_{n-1}. \end{aligned} \tag{2.25}$$

The population of N ion channels is characterized by the configuration $\mathbf{C} = (C_0, \ldots, C_n)$, where C_i denotes the number of channels in state i $(N = C_0 + \cdots + C_n)$. The instantaneous contribution of these channels to the membrane conductance equals $g = \bar{g}C_n$, with $\bar{g}$ being the conductance of a single channel. The resulting stochastic conductance enters the equation for the voltage dynamics, for example Eq. (2.4).

In numerical simulations the rate equations (2.25) can be used to track the states of individual channels. A more efficient and analytically tractable method is to use a Gaussian approximation of the channel noise (Fox and Lu, 1994). This approximation is based on the master equation for the probability distribution $P(\mathbf{C})$ of the configuration $\mathbf{C}$. For sufficiently large N this master equation can be reduced to the Langevin equation for the conductance dynamics. In Section 6.1 we derive the Langevin dynamics for a population of channels with only two possible states (open and closed). In Section 6.2 we obtain the resonate-and-fire model with an additive white noise term Eq. (6.11), which accounts for the intrinsic noise of ion channels. In rescaled variables the stochastic RaF model reads

$$\ddot{x} + \gamma\dot{x} + \omega_0^2 x = \sqrt{2D}\xi(t), \tag{2.26}$$

where $\xi(t)$ is a white Gaussian noise of unit intensity ($\langle\xi(t)\rangle = 0$, $\langle\xi(t)\xi(t')\rangle = \delta(t-t')$). This stochastic version of the RaF model will be used throughout Chapters 5 to 7.

2.2.3 Role of noise in signal processing

Noise is constantly present in neurons, originating from intrinsic conductance fluctuations and from random synaptic inputs. What influence may noise have on the function of the nervous system?

A straightforward implication of noise is, that it limits the reliability and the precision of spike firing in neurons. In the presence of noise, the spike times are not precise, but obey a probabilistic distribution. On the other hand, noise expands the repertoire of the dynamical behavior of some neurons. The deterministic neuron models introduced in Section 2.1.3 can only reproduce two dynamical behaviors: periodic oscillations when the system moves on a limit cycle, or a trivial silent state when the system rests in a stable fixed point[2]. The random action of noise perturbs deterministic trajectories and moves the system out of the vicinity of the fixed point. Occasionally the trajectory may reach a region in the phase space, where nonlinear deterministic mechanisms yield an excitation. These mechanisms can be a threshold in the IF and RaF models or a positive feedback in the Hodgkin-Huxley and FN models. After excitation the trajectory returns to the vicinity of the fixed point and may eventually escape over the excitation threshold again due to the action of noise. Hereby a random spike sequence is generated in an excitable system subjected to a stochastic force, similar to that in Fig. 2.1. Thus, the variability of a neuron output is enhanced by the action of noise.

Recently it has been realized, that noise can play a constructive role in signal processing. Notorious examples for the ordering role of noise are the effects of coherence and stochastic resonance (Pikovsky and Kurths, 1997; Gammaitoni et al., 1998; Lindner et al., 2004).

The phenomenon of *coherence resonance* is related to the occurrence of regular oscillations in a noise-driven excitable system. An excitable system driven by noise possesses a noise induced eigenfrequency and exhibits stochastic oscillations on the noise induced limit cycle. Coherence resonance corresponds to the existence of an optimal (finite) noise intensity, at which the noise induced oscillations are most regular. Coherence resonance was found experimentally in neural systems (Manjarrez et al., 2002; Gu et al., 2002), in laser diodes (Giacomelli et al., 2000), and in chemical reactions (Hou and Xin, 1999), as well as in theoretical models of excitable systems (for a review see Lindner et al., 2004). The occurrence of the opposite phenomenon, *anticoherence resonance*, was also reported (Lacasta et al., 2002; Lindner et al., 2002).

Noise can also affect the transmission of periodic and aperiodic signals by excitable systems. Adding noise can be beneficial for the transmission of weak signals by an excitable system, when the signal alone cannot excite a suprathreshold response. Maximal coherence between the input and output signal is achieved at a finite level of noise. This effect, referred to as *stochastic resonance*, was experimentally observed in neural systems (Levin and Miller, 1996; Collins et al., 1996; Jaramillo and Wiesenfeld, 1998), chemical reactions (Guderian et al., 1996) and in assemblies of ion channels (Bezrukov and Vodyanoy, 1995). Reviews of theoretical and experimental studies of stochastic resonance can be found in Gammaitoni et al. (1998) and Lindner et al. (2004).

New patterns of deterministic activity can arise in neurons due to the action of intrinsic channel noise (White et al., 2000). Channel noise was suggested to determine the reliability and the precision of spike timing (Schneidman et al., 1998) and to be essential for the existence of subthreshold oscillations of the membrane potential (Dorval and White, 2005).

---

[2] Chaotic behavior is observed in several neuron models, for example in the Hindmarsh-Rose model (Rose and Hindmarsh, 1989), which we do not consider in this work.

2.3 Brief theory of point processes

In the previous sections we have ascertained, that the evolution of the membrane potential in neurons is a stochastic process and that the times when a neuron fires are random. Therefore the set of firing times is a set of points placed in random on the time axes.

The set of points which have random positions in a given space is called a *point process* (Cox and Isham, 1980) or a *system of random points* (Stratonovich, 1967). The times, when nodes of a cluster fail, the centers of gravity of particles in statistical physics, the points of intersection of a random function with a given curve are all examples of point processes. Point processes have been intensively studied from several points of view (Cox and Lewis, 1966; Cox, 1967; Cox and Isham, 1980). In this section we briefly review some aspects relevant to the subsequent work. We restrict our presentation to the case of identical points randomly placed on the time axes.

A point process is completely characterized by the infinite sequence of *distribution functions* (Stratonovich, 1967; van Kampen, 1992):

$$n_1(t_1), \qquad n_2(t_2, t_1), \qquad n_3(t_3, t_2, t_1), \qquad \dots . \tag{2.27}$$

These functions determine the probability $n_p(t_p, \dots, t_1) dt_p \dots dt_1$, that at least one point falls in every of p non-overlapping intervals $(t_1, t_1 + dt_1), \dots, (t_p, t_p + dt_p)$.

Equivalently, the infinite sequence of *cumulant functions*

$$g_1(t_1), \qquad g_2(t_2, t_1), \qquad g_3(t_3, t_2, t_1), \qquad \dots . \tag{2.28}$$

completely determines a point process. Choose an arbitrary natural number r, and then fix r arbitrary numbers $z_1, \dots, z_r$ and r positive times $t_1, \dots, t_r$. The cumulant functions are defined by the relation:

$$1 + \sum_{p=1}^{\infty} \frac{1}{p!} \sum_{\alpha,\dots,\omega=1}^{r} n_p(t_\alpha, \dots, t_\omega) z_\alpha \dots z_\omega = \exp\left(\sum_{p=1}^{\infty} \frac{1}{p!} \sum_{\alpha,\dots,\omega=1}^{r} g_p(t_\alpha, \dots, t_\omega) z_\alpha \dots z_\omega \right). \tag{2.29}$$

Explicit relations between cumulant and distribution functions of a point process can be obtained by differentiating both sides of Eq. (2.29) over all z_i and then setting $z_i = 0, (i = 1, \dots, r)$, i.e. by applying the operator $\partial^r / (\partial z_1 \dots \partial z_r)\big|_{z_1 = \dots = z_r = 0}$. Doing so sequentially for $r = 1, 2, 3, \dots$ we obtain:

$$\begin{aligned} g_1(t_1) &= n_1(t_1), \\ g_2(t_2, t_1) &= n_2(t_2, t_1) - n_1(t_1) n_1(t_2), \\ g_3(t_3, t_2, t_1) &= n_3(t_3, t_2, t_1) - 3\{n_1(t_1) n_2(t_3, t_2)\}_s + 2 n_1(t_1) n_1(t_2) n_1(t_3), \ \dots . \end{aligned} \tag{2.30}$$

Here $\{\dots\}_s$ denotes the operation of symmetrization of the expression in the brackets with respect to all permutations of its arguments. The coefficients in these forms are the same as in the relations between the moments and the cumulants of a random variable.

A very useful tool in the theory of random points is the generating functional $L_T[v(t)]$, defined by (Stratonovich, 1967):

$$L_T[v(t)] = \left\langle \prod_{i=1}^{n} [1 + v(t_i)] \right\rangle \tag{2.31}$$

on the interval $0 \leqslant t \leqslant T$. Here n is the number of points falling in this interval and t_i are their positions. The class of functions $v(t)$ is rather restricted, but this will not be discussed here. Explicitely taking the average in Eq. (2.31) we obtain the relation between the generating functional $L_T[v(t)]$ and the distribution functions $n_p(t_p, \ldots, t_1)$:

$$L_T[v(t)] = 1 + \sum_{p=1}^{\infty} \frac{1}{p!} \int_0^T \ldots \int_0^T n_p(t_p, \ldots, t_1) v(t_p) \ldots v(t_1) dt_p \ldots dt_1. \tag{2.32}$$

To obtain an expression for $L_T[v(t)]$ in terms of the cumulant functions $g_p(t_p, \ldots, t_1)$, we take advantage of the fact that Eq. (2.29) does not change its form if we choose different times $t_1, \ldots, t_r$, different values $z_1, \ldots, z_r$ or change the number r. Thus extending r to infinity, allowing t to take all possible values between 0 and T, and choosing $z_i = v(t_i), (i = 1, \ldots, r)$, we get from Eqs. (2.29) and (2.32):

$$L_T[v(t)] = \exp \left(\sum_{p=1}^{\infty} \frac{1}{p!} \int_0^T \ldots \int_0^T g_p(t_p, \ldots, t_1) v(t_p) \ldots v(t_1) dt_p \ldots dt_1 \right). \tag{2.33}$$

To demonstrate the power of the generating functional approach, let us obtain the expression for the *waiting-time density* $\mathcal{F}(T)$ of a point process. Assume that the observation began at $t = 0$, then $\mathcal{F}(T)dT$ is the probability that the *first* event occurs at time $t \in (T, T + dT)$. The fact that the first event occurs at $t \in (T, T + dT)$ means, that no events occurred before $t = T$. The probability that no events occur at $t < T$ is called the *survival probability* $\Phi(T)$. The relation between $\Phi(T)$ and $\mathcal{F}(T)$ is evident (van Kampen, 1992; Risken, 1989):

$$\mathcal{F}(T) = -\frac{d}{dT}\Phi(T). \tag{2.34}$$

From Eq. (2.31) immediately follows $\Phi(T) = L_T[-1]$, hence

$$\Phi(T) = 1 + \sum_{p=1}^{\infty} \frac{(-1)^p}{p!} \int_0^T \ldots \int_0^T n_p(t_p, \ldots, t_1) dt_p \ldots dt_1. \tag{2.35}$$

In terms of the cumulant functions the survival probability $\Phi(T)$ reads

$$\Phi(T) = \exp \left(\sum_{p=1}^{\infty} \frac{(-1)^p}{p!} \int_0^T \ldots \int_0^T g_p(t_p, \ldots, t_1) dt_p \ldots dt_1 \right). \tag{2.36}$$

The relation between the waiting-time density $\mathcal{F}(T)$ and the distribution functions $n_p(t_p,\dots,t_1)$ is obtained by differentiation of Eq. (2.35) with respect to T:

$$\mathcal{F}(T)=\sum_{p=1}^{\infty}\frac{(-1)^p}{p!}\int_0^T\dots\int_0^T n_{p+1}(T,t_p,\dots,t_1)dt_p\dots dt_1. \tag{2.37}$$

These expressions for $\mathcal{F}(T)$ and $\Phi(T)$ will be used in Section 5.1 to obtain the first passage time densities for various random processes.

The most simple example of a point process is a set of *independent* random points. The distribution functions of independent points factorize $n_p(t_p,\dots,t_1)=n_1(t_p)\dots n_1(t_1)$. Hence, all cumulant functions vanish $g_p(t_p,\dots,t_1)=0,(p\geqslant 2)$, except for the first $g_1(t_1)=n_1(t_1)$. The set of independent points is completely characterized by $n_1(t)$. The probability that a point falls in the interval $(t,t+dt)$ is independent of positions of other points and equals $n_1(t)dt$. Thus $n_1(t)$ is the probability of an event occurrence per unit time and so is called the *rate*. The waiting-time density for a system of independent random points is obtained from Eq. (2.37):

$$\mathcal{F}(T)=n_1(T)\exp\left(-\int_0^T n_1(t)dt\right). \tag{2.38}$$

The system of random points is said to be stationary, if their distribution functions remain invariant under an arbitrary shift τ of all their arguments:

$$n_p(t_p,\dots,t_1)=n_p(t_p+\tau,\dots,t_1+\tau). \tag{2.39}$$

This implies, that $n_1(t)=n_0$ does not depend on time. The stationary system of independent random points has a constant rate n_0 and is called a *Poisson process.* The waiting-time density for the Poisson process is exponential:

$$\mathcal{F}_P(T)=n_0\exp(-n_0T). \tag{2.40}$$

Consider the random variable X_i, corresponding to the interval between the i-th and the $(i-1)$-th point. Evidently, for a stationary process the moments $\langle X_i\rangle$, $\langle X_i^2\rangle$ and $\langle X_iX_{i+j}\rangle$ do not depend on i; in particular $\langle X_i\rangle = 1/n_0$. We will omit the index i for stationary processes. For a Poisson process all intervals X are independent and identically distributed with the density Eq. (2.40). In this case the second moment and the variance of interval X read $\langle X^2\rangle = 2/n_0^2$ and $\langle\Delta X^2\rangle=\langle X^2\rangle-\langle X\rangle^2=1/n_0^2$.

The relative scattering of intervals for a stationary process is characterized by the coefficient of variation C_{var} (Cox, 1967; Cox and Lewis, 1966):

$$C_{\text{var}}=\frac{\sqrt{\langle\Delta X^2\rangle}}{\langle X\rangle}. \tag{2.41}$$

The Poisson process, for which $C_{\text{var}}=1$, usually serves as a basis for qualitative comparison, and C_{var} is a measure for the deviation of a stationary process from the Poisson case.

Correlations between intervals can by quantified by the serial correlation coefficients (SCC) ρ_k:

$$\rho_k = \frac{\langle X_i X_{i+k}\rangle - \langle X_i\rangle\langle X_{i+k}\rangle}{\sqrt{\langle \Delta X_i^2\rangle\langle \Delta X_{i+k}^2\rangle}}. \tag{2.42}$$

The Poisson process is a special case of a *renewal* process, defined as having independent intervals identically distributed with some (not necessary exponential) density. For all renewal processes, including the Poisson process, $\rho_k = 0$ for all $k > 0$.

We now introduce a random counting variable $N(t_1, t_2)$, which represents the number of points falling in the interval (t_1, t_2). We denote $N(0, T) \equiv N(T) \equiv N$. Let us express the first two moments of N in terms of the distribution functions. Consider the generating functional Eq. (2.31) with a constant function $v(t) = z$. Then $L_T[z] = \langle (1+z)^N\rangle$, and

$$\left.\frac{\partial L_T[z]}{\partial z}\right|_{z=0} = \langle N(1+z)^{N-1}\rangle\big|_{z=0} = \langle N\rangle, \qquad \left.\frac{\partial^2 L_T[z]}{\partial z^2}\right|_{z=0} = \langle N^2\rangle - \langle N\rangle. \tag{2.43}$$

Substituting $v(t) = z$ in Eq. (2.32) and then using the relations (2.43) we obtain for the first two moments of the random counting variable N:

$$\langle N\rangle = \int_0^T n_1(t)dt, \qquad \langle N^2\rangle = \langle N\rangle + \int_0^T\int_0^T n_2(t_2, t_1)dt_2dt_1. \tag{2.44}$$

It also has proven useful to introduce a measure similar to the coefficient of variation C_{var}, which describes the relative dispersion of the random counting variable N, the Fano factor $F(T)$ (Fano, 1947):

$$F(T) = \frac{\langle \Delta N^2\rangle}{\langle N\rangle}. \tag{2.45}$$

Here as usual $\langle \Delta N^2\rangle = \langle N^2\rangle - \langle N\rangle^2$. From the relations (2.44) it follows, that for the Poisson process $F(T) = 1$ on all time scales. The Poisson process again serves as a reference. One speaks about overdispersion if $F(T) > 1$ and about underdispersion if $F(T) < 1$ (Cox and Isham, 1980).

Whereas C_{var} is a number characterizing the variability of a point process on the time scale of the order of $\langle X_i\rangle$, the Fano factor is a function of T and gives the variability measure on all time scales. Consider M non-overlapping intervals on the time axes, each of length T. Let N_i be the number of random points falling in the i-th interval. Then the first two moments of the counting variable N read:

$$\langle N\rangle = \lim_{M\to\infty}\frac{1}{M}\sum_{i=1}^{M} N_i, \qquad \langle N^2\rangle = \lim_{M\to\infty}\frac{1}{M}\sum_{i=1}^{M} N_i^2. \tag{2.46}$$

For sufficiently small T, the probability that more than one point falls in an interval vanishes. In the limit $M \to \infty$, the number Mn_0T of intervals will contain one point, and the rest will not contain any. This implies, $\langle N\rangle = n_0T$, $\langle N^2\rangle = n_0T$, and $F(T) = 1 - n_0T$. Thus, $\lim_{T\to 0} F(T) = 1$ and the Fano factor linearly decreases on short time scales. For larger

T, the probability that more than one point fall into an interval becomes nonzero and the behavior of $F(T)$ becomes different from a linear decrease. The time T, when $F(T)$ starts to deviate from a linear decrease, gives the minimal interval between two successive points.

The asymptotic value F_∞ of the Fano factor is related to the serial correlation coefficients according to (Cox and Lewis, 1966):

$$F_\infty = \lim_{T\to\infty} F(T) = C_{\mathrm{var}}^2 \left(1 + 2\sum_{k=1}^{\infty} \rho_k\right). \tag{2.47}$$

Here we assumed that the series is convergent. For a renewal process $F_\infty = C_{\mathrm{var}}^2$.

A point process is completely characterized by its distribution or cumulant functions. However, in applications one deals with theoretical models, constructed to describe a given set of experimental data. The distribution and cumulant functions are not suitable for comparison of theoretical predictions with experiments, because they constitute an infinite set of functions which is hardly assessable experimentally. Therefore the coefficient of variation C_{var}, the Fano factor $F(T)$, the serial correlation coefficients ρ_k, which can be directly assessed in experiments, are of especial importance. Their values obtained experimentally can be compared with theoretical predictions or used as initial information to construct an appropriate model.

2.4 Multipeak first passage time densities

The times when a neuron fires spikes form a random point process. Suppose that information about the subthreshold dynamics of a neuron is available. How could it be used to predict the firing times or calculate the statistical characteristics of the resulting point process? To answer this question, the concept of the *first passage time* (FPT) is very helpful. Every spike engages a mechanism resetting the voltage to a given initial value x_0. The next spike will be generated when the membrane potential reaches the prescribed threshold value x_b for the first time. The interspike interval is thus given by the time of the first passage of the voltage variable $x(t)$ to the threshold x_b. Since the subthreshold voltage dynamics has an essential stochastic component, the corresponding first passage time T is a random variable whose probability density $\mathcal{F}(T)$ describes the distribution of interspike intervals. Besides being applicable to the neuron dynamics, a wide range of applications such as noise in vacuum tubes, chemical reactions, nucleation processes and risk management in finance can be described in terms of the first passage time problem (Tuckwell, 1988; Hänggi et al., 1990; Redner, 2001).

The present work is mainly motivated by the dynamics of resonant neurons. The voltage variable of such a neuron exhibits damped subthreshold oscillations around the attractive resting state, thereby the characteristic relaxation time is large compared to the mean ISI. After spiking the voltage variable $x(t)$ is reset to a fixed value far from the resting state and then $x(t)$ can reach the threshold *prior* to relaxation. The interspike interval densities obtained experimentally from the output of resonant neurons exhibit a sequence of decaying peaks separated by intervals whose length is of the order of the period of subthreshold oscillations.

Multimodal ISI probability densities can be reproduced by models with different mechanisms of subthreshold resonance. For example in the Hodgkin-Huxley model (Chik et al., 2001), the excitable FitzHugh-Nagumo model with the stable fixed point being a focus (Lacasta et al., 2002; Verechtchaguina et al., 2004) or in the region of a canard bifurcation (Volkov et al., 2003; Makarov et al., 2001). All these models have in common, that the multimodal ISI density is obtained for stochastic dynamical systems, which have at least two dynamical variables, exhibit weakly, moderately damped or self-amplifying oscillations and after a spike the system is reset to initial values which are not a fixed point. In the absence of noise these systems are referred to as resonate-and-fire neurons (Izhikevich, 2001).

The resonate-and-fire models belong to a broad class of non-Markovian models, which are notable for their sensitive dependence on initial conditions. The escape rate in non-Markovian models is time-dependent and the FPT densities have complex multimodal structures. In contrast, Markovian escape processes are characterized by a constant, time-independent escape rate. The FPT in Markovian models is independent of the initial state and is exponentially distributed. Hence, a Markovian escape process is described by a single characteristic time scale: the mean FPT equal to the inverse rate of escape. The non-Markovian models are much richer in the sense, that many different time scales are reflected in the complex multimodal structure of the FPT density. In the resonate-and-fire models these are the period and relaxation time of subthreshold oscillations.

Markovian models are discussed in great detail in Chapter 4. In this section, we discuss the mechanisms leading to multimodal FPT densities in non-Markovian models with subthreshold oscillations. We consider a simple non-Markovian dynamics, a harmonic oscillator driven by a white Gaussian noise:

$$\begin{aligned} \dot{x} &= v, \\ \dot{v} &= -\gamma v - \omega_0^2 x + \sqrt{2D}\xi(t), \end{aligned} \tag{2.48}$$

with the threshold at x_b and the reset at (x_0, v_0). The pair of equations (2.48) is equivalent to the resonate-and-fire model introduced in Section 2.1.3 with the refractory time set to zero. Here we fix $\omega_0 = 1$, $x_b = 1$, $v_0 = 0$ and qualitatively investigate changes in the structure of the FPT density in dependence on the friction γ, the noise intensity D and the initial position x_0.

The first passage time density can be found by solving the Fokker-Planck equation with absorbing boundary condition as discussed in Section 4.2. If the transition probability density $P_\Delta(x, v, t|x_0, v_0, 0)$ in the presence of absorbing boundary at x_b is known, the FPT density is given by the probability current at $x = x_b$ in the positive x-direction, see Eq. (4.24). The analytical solution for $P_\Delta(x, v, t|x_0, v_0, 0)$ is not available for the two-dimensional dynamics in Eq. (2.48). However, our aim is not to calculate the FPT densities, but to qualitatively understand their structure. Let us therefore consider the probability current $n_1(t)$ at $x = x_b$ disregarding the absorbing boundary:

$$n_1(t) = \int_0^\infty v P(x_b, v, t|x_0, v_0, 0) dv. \tag{2.49}$$

Here $P(x, v, t|x_0, v_0, 0)$ is the Gaussian transition probability density which obeys Eq. (5.12). For small t, before trajectories, which have already crossed x_b, can return and recross it, $n_1(t)$

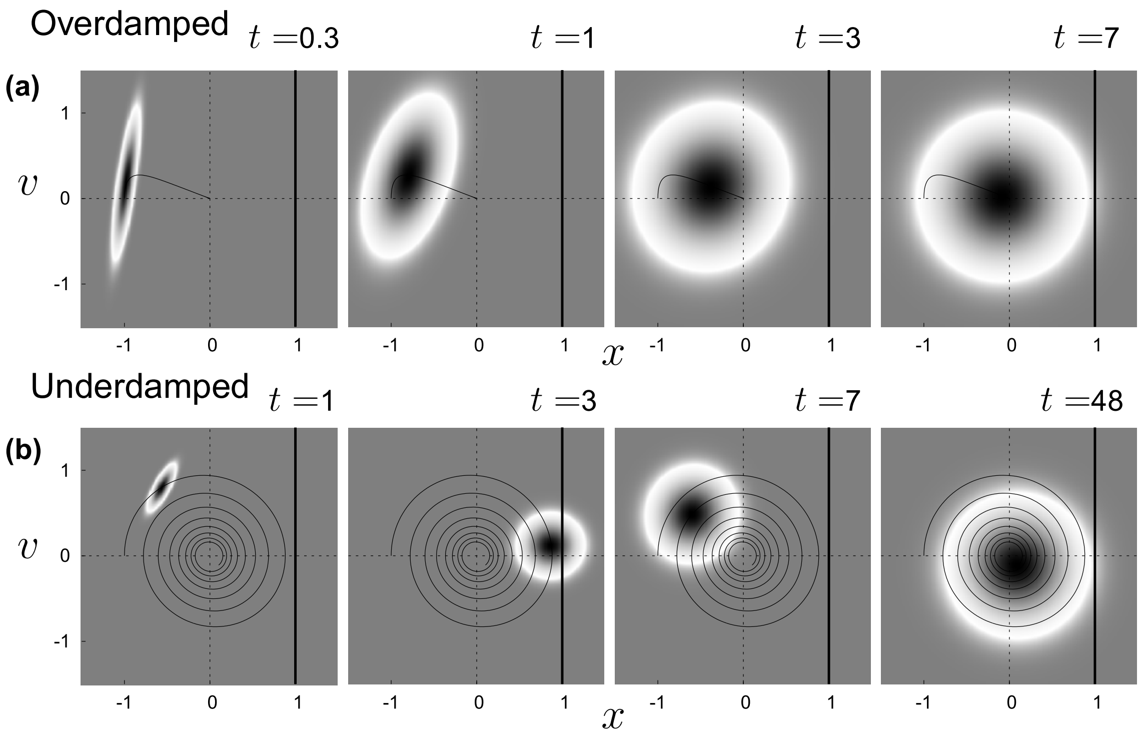

Figure 2.6: Time evolution of the joint probability density $P(x, v, t|x_0, v_0, 0)$ of coordinate x and velocity v of a harmonic oscillator driven by a white Gaussian noise. Grayscale colors change from white to black as the joint PDF is increasing; a light-gray background is used for the sake of clearness. Black vertical lines mark the position of the threshold $x_b = 1$ in the phase space. The center of the Gaussian probability density moves along the trajectory shown with a black solid line. (a) Overdamped regime ($\gamma = 3, D = 0.5$), escape occurs from the local quasiequilibrium state and is independent of initial conditions. (b) Underdamped regime ($\gamma = 0.08, D = 0.01$), escape occurs prior to relaxation and escape times depend crucially on initial conditions. Other parameters are $\omega_0 = 1, x_0 = -1, v_0 = 0$.

coincides with the FPT density. For intermediate values of t, $n_1(t)$ qualitatively reproduces the structure of the FPT density. For t exceeding the local relaxation time, $n_1(t)$ saturates to a constant value and the FPT density decays exponentially. For the harmonic oscillator Eq. (2.48) $n_1(t)$ can be calculated analytically, see Eq. (5.14).

Let us survey the evolution of $P(x, v, t|x_0, v_0, 0)$ in the phase space. At $t = 0$ the probability distribution is a two-dimensional δ-function $\delta(x - x_0)\delta(v - v_0)$, which then broadens out to the two-dimensional Gaussian distribution, whose center relaxes towards the potential minimum at $x = 0, v = 0$. The trajectory of the center of the Gaussian distribution is easily obtained by averaging Eqs. (2.48) over time and solving the resulting ordinary differential equations with given initial conditions (Wang and Uhlenbeck, 1945). In the underdamped regime ($\gamma < 2\omega_0$) the mean values of the coordinate x and velocity v obey for positive t:

$$\langle x\rangle = \frac{v_0}{\Omega}e^{-\frac{\gamma}{2}t}\sin(\Omega t) + \frac{x_0}{\Omega}e^{-\frac{\gamma}{2}t}\left(\Omega\cos(\Omega t) + \frac{\gamma}{2}\sin(\Omega t)\right), \tag{2.50a}$$

$$\langle v\rangle = \frac{v_0}{\Omega}e^{-\frac{\gamma}{2}t}\left(\Omega\cos(\Omega t) - \frac{\gamma}{2}\sin(\Omega t)\right) - \frac{x_0\omega_0^2}{\Omega}e^{-\frac{\gamma}{2}t}\sin(\Omega t), \tag{2.50b}$$

with $\Omega = \sqrt{|\omega_0^2 - \gamma^2/4|}$. In the overdamped regime ($\gamma > 2\omega_0$) the trigonometric functions must be replaced with their hyperbolic counterparts. Thus the center of the distribution follows the trajectory of a damped harmonic oscillator with given initial conditions.

In Figs. 2.6(a) and 2.6(b) the trajectories of the center of the distribution are depicted with black solid lines for the overdamped and underdamped regimes, respectively. In the overdamped regime ($\gamma = 3, D = 0.5$), $\langle x\rangle$ relaxes monotonically, the probability current $n_1(t)$ is vanishing for small times t and then monotonically increases till its stationary value is reached. Therefore, the FPT density in the overdamped regime has a single maximum and decays exponentially on times exceeding the local relaxation time. The FPT density for parameter values as in Fig. 2.6(a) is shown in Fig 2.9(a). It exhibits a monomodal structure characteristic for the overdamped regime. All FPT densities in Fig. 2.9 are obtained analytically using the Stratonovich approximation, discussed in Section 5.2.4.

In the underdamped regime (see Fig. 2.6(b) with $\gamma = 0.08, D = 0.01$) the center of the Gaussian distribution performs damped oscillations with frequency Ω. At the time $t = \pi/\Omega$, $\langle x\rangle$ passes its first maximum and the probability density at $x = x_b$ has increased values ($t = 3$ in Fig. 2.6(b)). Hence, the probability current $n_1(t)$ and the FPT density exhibit a peak at $t = \pi/\Omega$. After the next half period at $t = 2\pi/\Omega$, the center of the distribution is far from the threshold, the probability density at $x = x_b$ is low, therefore $n_1(t)$ and $\mathcal{F}(t)$ achieve a minimum. This process repeats periodically till the time of the order of the relaxation time. For t beyond the relaxation time, the oscillation amplitude of the distribution center becomes small compared to the variance of x and $n_1(t)$ saturates ($t = 48$ in Fig. 2.6(b)). Thus $\mathcal{F}(t)$ exhibits decaying peaks following with the period $2\pi/\Omega$ and separated by deep minima on short times. $\mathcal{F}(t)$ decays exponentially on times beyond the local relaxation time. The FPT density for parameter values as in Fig. 2.6(b) is depicted in Fig 2.9(b). Its multimodal structure is typical for the underdamped regime and initial conditions far from the rest state.

Thus in the underdamped regime, nonmonotonic relaxation of the distribution center modulates the probability current across the threshold x_b and causes multimodality of the FPT density. Interestingly, the probability current grows nonmonotonically also for initial conditions at the potential minimum ($x_0 = 0, v_0 = 0$), owing to an uneven increase of the variance of the coordinate $\sigma_{xx}^2(t)$ and velocity $\sigma_{vv}^2(t)$ and non-vanishing crosscorrelation $\sigma_{xv}^2(t)$ on short time scales. The dependence of the second moments on time ($t > 0$) for a harmonic oscillator reads (Wang and Uhlenbeck, 1945):

$$\sigma_{xx}^2(t) = \langle x^2\rangle - \langle x\rangle^2 = \frac{D}{\omega_0^2\gamma}\left[1 - \frac{1}{\Omega^2}e^{-\gamma t}\left(\Omega^2 + \frac{\gamma^2}{2}\sin^2(\Omega t) + \gamma\Omega\sin(\Omega t)\cos(\Omega t)\right)\right], \tag{2.51a}$$

$$\sigma_{vv}^2(t) = \langle v^2\rangle - \langle v\rangle^2 = \frac{D}{\gamma}\left[1 - \frac{1}{\Omega^2}e^{-\gamma t}\left(\Omega^2 + \frac{\gamma^2}{2}\sin^2(\Omega t) - \gamma\Omega\sin(\Omega t)\cos(\Omega t)\right)\right], \tag{2.51b}$$

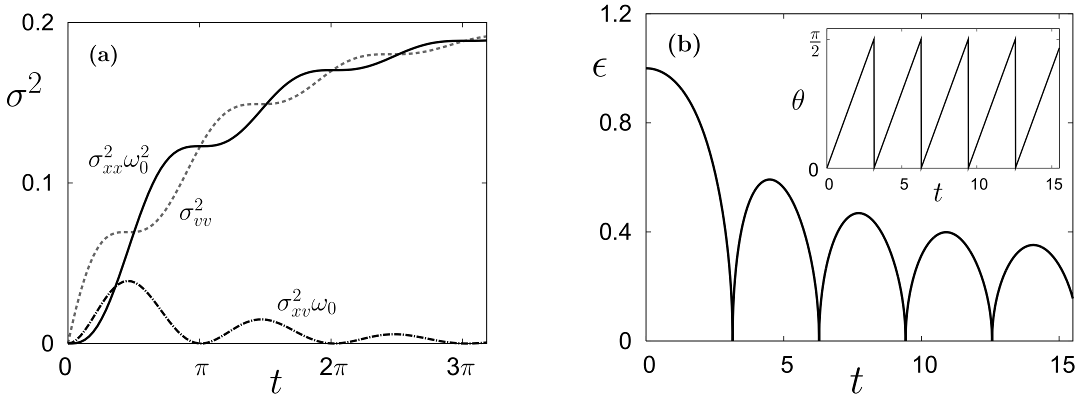

Figure 2.7: (a) Variance of coordinate $\omega_0^2\sigma^2_{xx}(t)$ (solid line) and of velocity $\sigma^2_{vv}(t)$ (dashed line), and the crosscorrelation $\omega_0\sigma^2_{xv}(t)$ (dash-dot line) for a harmonic oscillator driven by a white Gaussian noise and started at $t = 0$ with sharp initial conditions ($\omega_0 = 1, \gamma = 0.3, D = 0.06$). (b) Eccentricity ϵ of the distribution ellipse (main plot) and the angle θ between its major axis and the v-axis (inset) as functions of time, for a harmonic oscillator with a white Gaussian noise ($\omega = 1, \gamma = 0.01, D = 0.02$).

$$\sigma^2_{xv}(t) = \langle xv\rangle - \langle x\rangle\langle v\rangle = \frac{1}{\omega_0}\frac{D\omega_0}{\Omega^2}e^{-\gamma t}\sin^2(\Omega t). \tag{2.51c}$$

These functions are illustrated in Fig. 2.7(a) for $\gamma = 0.3$ and $D = 0.06$. Segments where the variance rapidly increases alternate with plateaus with the period π/Ω and the phase shift $\pi/2$ between $\sigma^2_{xx}(t)$ and $\sigma^2_{vv}(t)$. The crosscorrelation $\sigma^2_{xv}(t)$ vanishes periodically at times $k\pi/\Omega$ (k is a positive integer). At times exceeding the local relaxation time the functions saturate at their stationary values.

From the general form of the Gaussian distribution Eq. (5.12) it follows, that the probability density isolines in the phase plane (x, v) are determined by

$$\sigma^2_{vv}(t)x^2 - 2\sigma^2_{xv}(t)xv + \sigma^2_{xx}(t)v^2 = \text{const.} \tag{2.52}$$

The probability density has the shape of an ellipse. It is appropriate to consider the probability density in rescaled coordinates $(\omega_0 x, v)$. As Fig. 2.7(a) reveals, in the first half period $\sigma^2_{vv}(t) > \omega_0^2\sigma^2_{xx}(t)$ and the ellipse is elongated in the v-direction, in the second half period the relation of variances is inverse and the ellipse is elongated in the x-direction. At $t = k\pi/\Omega$ the crosscorrelation vanishes and the ellipse becomes a circle in rescaled coordinates.

The eccentricity ϵ of the ellipse and the angle θ between its major axis and the v-axis are obtained from Eqs. (2.52) and (2.51a)–(2.51c):

$$\tan(2\theta) = \frac{\omega_0}{\Omega}\tan(\Omega t), \tag{2.53a}$$

$$\epsilon^2 = \frac{\left(\sigma^2_{vv}(t) - \omega_0^2\sigma^2_{xx}(t)\right)\left(1 - \tan^2(\theta)\right) + 4\omega_0\sigma^2_{xv}(t)\tan(\theta)}{\sigma^2_{vv}(t) + 2\omega_0\sigma^2_{xv}(t)\tan(\theta) + \omega_0^2\sigma^2_{xx}(t)\tan^2(\theta)}. \tag{2.53b}$$

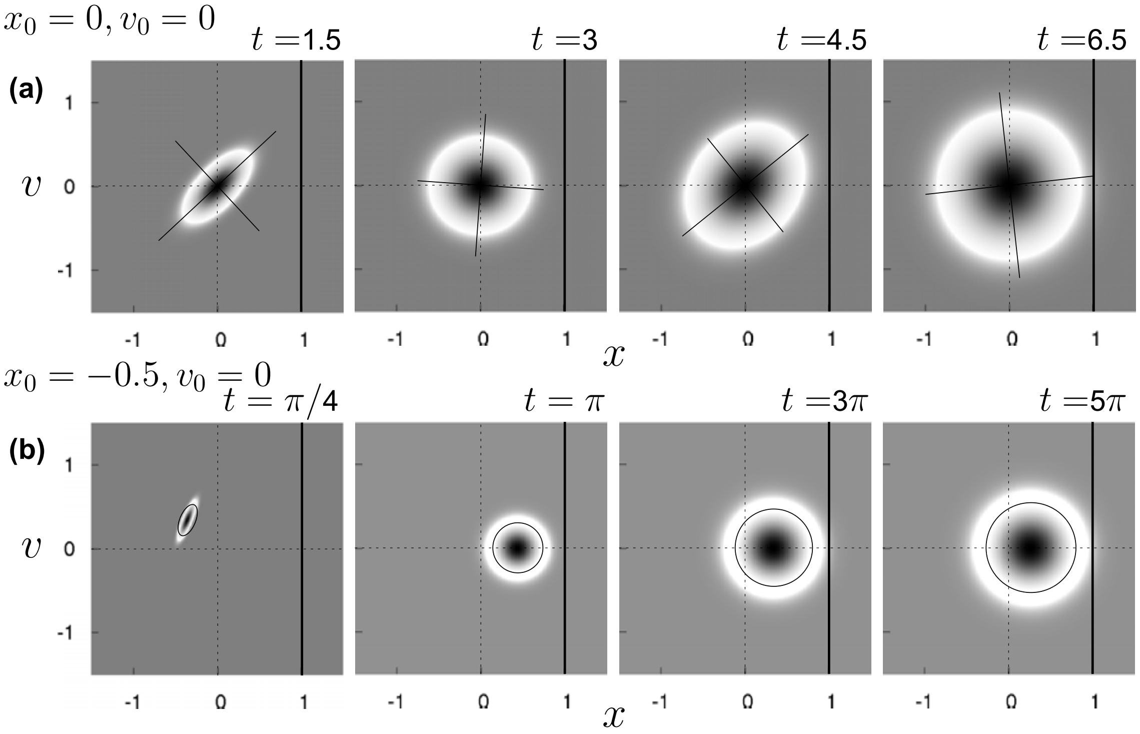

Figure 2.8: Same as in Fig. 2.6, however for different parameter values. (a) Underdamped regime ($\gamma = 0.01, D = 0.02$) with initial conditions at the bottom of the potential ($x_0 = 0, v_0 = 0$). The initial two-dimensional δ-function becomes an ellipse with the axis indicated by black solid lines. The distribution ellipse broadens out with time and its axis turn with the period π/Ω. (b) Interplay between growth of the variance and relaxation of the center of the distribution ($\gamma = 0.08, D = 0.008$). Initial conditions are $x_0 = -0.5, v_0 = 0$. Black solid line in each panel is the isoline enclosing 95.4% of the probability distribution. At $t = \pi$ the variance is not yet large enough and an escape is very improbable. The other parameters are as in Fig. 2.6.

These functions are presented in Fig. 2.7(b) for $\gamma = 0.01$, $D = 0.02$. The angle θ changes between 0 and $\pi/2$ with the period π/Ω. The eccentricity ϵ vanishes at times $k\pi/\Omega$ and has maxima at times $(1/2 + k)\pi/\Omega$, when the elongation of the distribution is maximal. This fact is illustrated in Fig. 2.8(a), where the evolution of the probability density is depicted for parameter values $\gamma = 0.01, D = 0.02, x_0 = 0, v_0 = 0$.

Let us now return to the probability current across the threshold $x = x_b$, see Eq. (2.49). The probability density at the threshold $P(x_b, v, t|x_0, v_0, 0)$ is Gaussian, with the maximum at the value $v_m = x_b\sigma^2_{xv}(t)/\sigma^2_{xx}(t)\omega_0$, where the line $x = x_b$ is tangent to one of the isolines Eq. (2.52). Using Eqs. (2.51b) and (2.51c) we infer, that v_m oscillates: v_m vanishes at times $t = k\pi/\Omega$ and has maxima at $t = (1/2 + k)\pi/\Omega$. The amplitude of this oscillation decays exponentially, and beyond the relaxation time v_m saturates to zero.

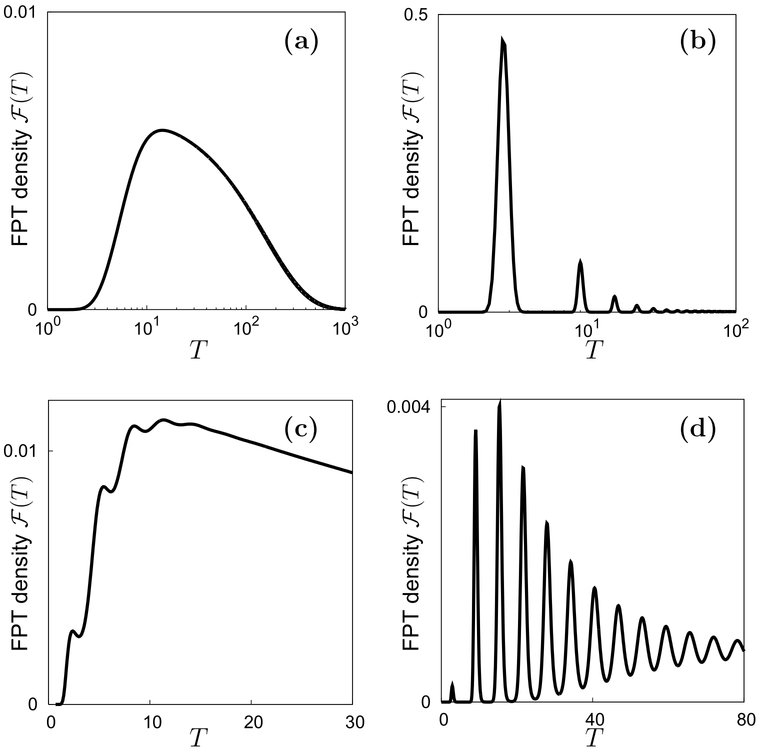

Figure 2.9: First passage time probability densities for a harmonic oscillator driven by a white Gaussian noise ($\omega_0 = 1, x_b = 1$). (a) Overdamped regime ($\gamma = 3, D = 0.5, x_0 = -1, v_0 = 0$), the FPT density is monomodal. (b) Underdamped regime ($\gamma = 0.08, D = 0.01$), sharp initial conditions at $x_0 = -1, v_0 = 0$, FPT density exhibits multiple decaying peaks. (c) Underdamped regime ($\gamma = 0.3, D = 0.06$), sharp initial conditions at the bottom of potential ($x_0 = 0, v_0 = 0$), FPT density growth in a stepwise manner on small times. (d) Underdamped regime ($\gamma = 0.08, \quad D = 0.01$), initial conditions at $x_0 = -0.5, v_0 = 0$, the third peak in the FPT density is higher than the first and the second ones. All FPT probability densities are obtained analytically in Stratonovich approximation.

The increase of the probability current $n_1(t)$ is slightly modulated by the oscillation of the center v_m of the Gaussian distribution $P(x_b, v, t|x_0, v_0, 0)$. The value of v_m is positive between two successive zeros, so that the probability density is shifted towards positive v-values. Around $t = k\pi/\Omega$, the current $n_1(t)$ exhibits a local minima, since the variance of x almost does not change at these times (plateaus in Fig. 2.7(a)). A small modulation due to the shift of the distribution center towards positive v-values becomes apparent: the probability current decreases immediately before $t = k\pi/\Omega$ and increases immediately after $t = k\pi/\Omega$. Hence, on short times the probability current $n_1(t)$ and the FPT density $\mathcal{F}(t)$ exhibit minima at $t = k\pi/\Omega$ preceded by small maxima. An example is presented in Fig. 2.9(c), where we plot the FPT density for a harmonic oscillator with parameters $\gamma = 0.3, D = 0.06$ and with initial conditions $x_0 = 0, v_0 = 0$. On short times a stepwise growth is observed in $\mathcal{F}(t)$, so that small maxima follow with the period π/Ω. This FPT structure is characteristic for the underdamped regime and initial conditions close to the potential minimum.

Let us see how the interplay between relaxation of the distribution center and growth of its variance may influence the structure of the FPT density. Consider a harmonic oscillator with parameters $\gamma = 0.08, D = 0.008$ and initial conditions at $x_0 = -0.5, v_0 = 0$. At the time $t = \pi/\Omega$ the center of the Gaussian distribution is close to the threshold $x_b = 1$, but the variance has not yet increased sufficiently and the probability density at the threshold is still low ($t = \pi$ in Fig. 2.8(b)). Hence the probability current $n_1(t)$ and the FPT density $\mathcal{F}(t)$ exhibit a small peak around $t = \pi/\Omega$. After one period at $t = 3\pi/\Omega$ the center of the distribution again approaches the threshold and the variance increased during elapsed time ($t = 3\pi$ in Fig. 2.8(b)). The probability current $n_1(t)$ at $t = 3\pi/\Omega$ appears to be larger than at $t = \pi/\Omega$, therefore the second peak in the FPT density is higher than the first one. This process repeats for several periods, until the height of the peaks begins to decrease. The isoline inclosing 95.4% of the probability distribution is shown with a black solid line in Fig. 2.8(b) and corresponds to the distribution ellipse with the major axis equal to $2\sigma_{xx}(t)$ and $2\sigma_{vv}(t)$. The FPT density for given parameter values is depicted in Fig. 2.9(d). It exhibits multiple peaks and the third peak is the highest one.

In summary, the first passage time in Markovian models is exponentially distributed. In contrast, non-Markovian models, which are characterized by a time-dependent escape rate, exhibit a big diversity of escape patterns. The latter are reflected in the multimodal structures of the FPT densities on times smaller than the local relaxation time. Thereby nonequilibrium (e.g. sharp) initial conditions are essential for the nonexponential FPT distribution. Characteristic time scales of the subthreshold dynamics are reflected in the FPT densities, for instance in positions and number of visible peaks. The structure of the FPT density depends on the system parameters and on initial conditions.

3

Characterization of firing patterns in resonant and nonresonant neurons

In Section 2.1.2 we have briefly mentioned the subthreshold frequency preference of a single neuron. A resonance peak appears at a well prescribed frequency in the impedance function of a resonant neuron. In contrast, the impedance function of a nonresonant neuron decays monotonically with the frequency (Wu et al., 2001; Hutcheon and Yarom, 2000). This subthreshold frequency preference gives rise to subthreshold oscillations of the membrane potential. In response to a small perturbation shifting the voltage from the resting potential, nonresonant neurons show a monotonic relaxation back to the resting potential, whereas in resonant neurons this relaxation is accompanied by subthreshold oscillations at a frequency close to the resonance frequency.

Subthreshold oscillations are observed experimentally in mesencephalic trigeminal neurons (Wu et al., 2001), dorsal root ganglion neurons (Amir et al., 1999), neocortical neurons (Hutcheon et al., 1996; Gutfreund et al., 1995) and thalamic neurons (Puil et al., 1994). To detect the subthreshold oscillations in experiments, a potential on the weakly depolarized neuron membrane is recorded in the subthreshold regime. A peak in the power spectrum of the recorded signal and its oscillating autocorrelation function serve as indicators for the subthreshold oscillations (Amir et al., 1999; Desmaisons et al., 1999; Steriade et al., 1991).

The subthreshold frequency preference in neurons may lead to a selective suprathreshold response to periodic or noisy stimuli. The subthreshold oscillations trigger sequences of spikes following with the preferred frequency (Reboreda et al., 2003; Haas and White, 2002; Llinas et al., 1991), referred to as the *spike clusters.* The relation between subthreshold oscillations and the firing-rate resonance was investigated theoretically in the generalized integrate-and-fire model (Izhikevich, 2000, 2001; Richardson et al., 2003; Brunel et al., 2003).

In experimental studies, the spectral analysis is commonly used for the quantitative characterization of the oscillatory activity under various experimental conditions (Reboreda et al., 2003; Lampl and Yarom, 1997; Steriade et al., 1991). Resonant and nonresonant neurons gen-

---

This chapter is adopted from Verechtchaguina et al. (2004).

erate spike trains looking rather similar if observed on short time scales. Observing at longer time scales and considering the power spectral densities of the spike trains unveil some differences. However, there is no striking difference in the *form* of the spectra of resonant and nonresonant neurons. The differences between spectra become noticeable in a different response to *changes of parameters* of the input signal. As we proceed to show, the assessment of dynamics based on such spectra is of limited value.

Therefore a reliable statistical instrument is required to characterize the differences in the firing patterns of resonant and nonresonant neurons and to account for such important features as the spike clustering in resonant neurons. In this chapter we show, that the interspike interval (ISI) probability density function provides a very sensitive instrument for the assessment of the type of the subthreshold dynamics. The differences between resonant and nonresonant spike patterns are clearly pronounced in the ISI density without additional data processing. Moreover, the ISI density contains practically all relevant information about the neuron output. The power spectral density of the neuron output can be restored from the ISI density and from the spectrum of a single spike.

In order to fulfill our task we need a theoretical model of a neuron which can readily reproduce both regimes (resonant and nonresonant) and is yet simple enough to allow for massive numerical simulations necessary for adequate statistical analysis. We have chosen the FitzHugh-Nagumo (FN) system and consider its response to a signal which is modeled by a white Gaussian noise. This form of noise allows for a mathematically sound formulation of the problem and the use of approved tools of stochastic modeling. From the physiological point of view, the noise models the intrinsic noise of ion channels. Another model we used was the Morris-Lecar model.

In both models the subthreshold oscillations result from a nonmonotonic relaxation to a fixed point, which possesses complex eigenvalues (focus). Note, that effects similar to those discussed in this chapter can also be obtained for systems with other types of the subthreshold oscillatory behavior. For example, in the FN model slightly beyond the supercritical Hopf bifurcation (in the “canard” region) the subthreshold oscillations occur on the stable limit cycle with a small amplitude (Makarov et al., 2001). In a one-dimensional bistable system, the excitable dynamics with subthreshold oscillations can be generated by a negative delay or feedback term (Lacasta et al., 2002).

In Section 3.1 we present a brief description of the subthreshold dynamics in the FN model in the resonant and nonresonant regimes and explain how subthreshold oscillations may influence the spike firing. Further, in Sections 3.2 and 3.3, power spectra and ISI densities of spike trains in the stochastic FN model are examined in both regimes and for varying input signal. Finally, in Section 3.4 we demonstrate that the power spectra can be obtained from the ISI densities, if the renewal assumption holds.

3.1 Subthreshold dynamics of the FitzHugh-Nagumo model

We have already introduced the deterministic FitzHugh-Nagumo model in Section 2.1.3. It is a formal model describing the neuron dynamics in terms of only two relevant variables: the voltage variable $x(t)$ and the recovery variable $y(t)$, the latter having the meaning of an effective membrane conductance:

$$\begin{aligned} \epsilon \dot{x} &= x - x^3 - y, \\ \dot{y} &= \gamma x - y + b. \end{aligned} \tag{3.1}$$

The parameter $\epsilon 0$ (the effective membrane capacity) is a small positive constant ($\epsilon \ll 1, \epsilon \ll 1/\gamma$), which ensures the time scale separation of the fast x and the slow y variable. The time evolution of $x(t)$ reproduces qualitative features of spike generation observed on neuron membranes. In the present version of the FN model Eq. (3.1), we transformed to dimensionless parameters and variables.

For different parameters γ and b the FN model can operate in different dynamical regimes, regarding the number and stability of fixed points in its phase space (see Section 2.1.3). Since our intention is to model the excitable dynamics of neurons, we exclusively concentrate on the excitable regime, where the system possesses a single stable fixed point. In this regime any initial perturbation relaxes to the fixed point, following one of two patterns in dependence on the amplitude of the initial perturbation. Large excursions in the phase space, such that the trajectory approaches the right branch of the cubic nullcline, are referred to as the suprathreshold response or spike. If the state point remains in the vicinity of the fixed point during the relaxation, one speaks about the subthreshold response. This is not a strict definition of what is called the subthreshold response, but it is sufficient for our purposes. In Lindner (2002) the reader can find a comprehensive discussion of where the boundary between sub- and suprathreshold responses should be drawn in the FN model.

The subthreshold dynamics of the FN model can be further differentiated into an excitable resonant and nonresonant regimes. The type of the fixed point and associated eigenvalues determine the character of the subthreshold relaxational behavior. The complex eigenvalues imply an oscillatory subthreshold relaxation, which corresponds to the resonant regime. The real eigenvalues imply a monotonic[1] subthreshold relaxation characteristic for the nonresonant regime.

To determine the parameter ranges corresponding to the resonant and nonresonant regimes, we fix $\gamma = 1.5$ and perform a stability analysis for the system Eq. (3.1). Linearization of the FN equations (3.1) around the fixed point (x_0, y_0) yields for the voltage dynamics:

$$\epsilon \ddot{x} + (\epsilon + 3x_0^2 - 1)\dot{x} + (\gamma + 3x_0^2 - 1)x = 0. \tag{3.2}$$

The eigenvalues $\lambda_{1,2}$ are found from the solution of the corresponding characteristic equation:

$$\epsilon \lambda^2 + (\epsilon + 3x_0^2 - 1)\lambda + (\gamma + 3x_0^2 - 1) = 0. \tag{3.3}$$

The results in parameter space (ϵ, b) are summarized in Fig. 3.1. In the excitable nonresonant regime the fixed point is a stable node with real negative eigenvalues ($\mathrm{Re}\lambda_{1,2} < 0, \mathrm{Im}\lambda_{1,2} = 0$) and the subthreshold relaxation is monotonic. For parameter values from the excitable

---

[1] By monotonic relaxations we mean those without oscillations. If a trajectory first approaches the left branch of the cubic nullcline and then relaxes to the fixed point, the voltage variable $x(t)$ passes through the minimum. However this is still classified as the monotonic relaxation if $x(t)$ does not have a subsequent maximum. As a criterion serve the real negative eigenvalues of the fixed point.

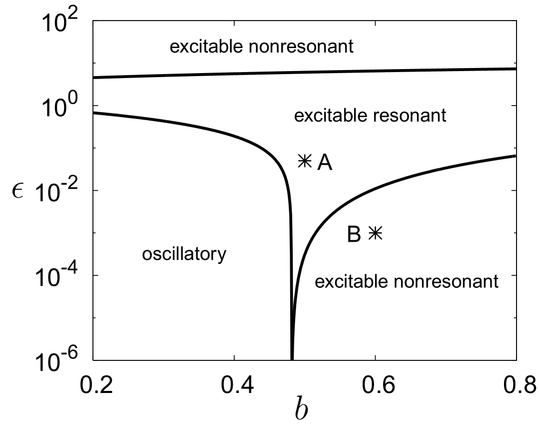

Figure 3.1: Stability diagram for the FN model in parameter space (ϵ, b) for a fixed value of $\gamma = 1.5$. Points A and B mark parameter sets used throughout this chapter to model resonant (point A, $\epsilon = 0.05, \gamma = 1.5, b = 0.5$) and nonresonant (point B, $\epsilon = 0.001, \gamma = 1.5, b = 0.6$) neurons. Note, that all quantities plotted in figures in this chapter are dimensionless.

resonant regime, the fixed point is a stable focus with two complex conjugated eigenvalues ($\mathrm{Re}\lambda_{1,2} < 0, \mathrm{Im}\lambda_1 = -\mathrm{Im}\lambda_2 \neq 0$) and the subthreshold relaxation is oscillatory. Note that the resonant regime is obtained only for finite values of ϵ, and the limit $\epsilon \to 0$ corresponds to the nonresonant case. Points A and B in Fig. 3.1 mark two particular parameter sets, which will be used throughout this chapter to model two types of subthreshold dynamics: point A ($\epsilon = 0.05, \gamma = 1.5, b = 0.5$) corresponds to the resonant and point B ($\epsilon = 0.001, \gamma = 1.5, b = 0.6$) to the nonresonant regime.

Relaxational dynamics in the FN model for these two parameter sets is illustrated in Figs. 3.2(a) and 3.2(b). Damped subthreshold oscillations in the resonant regime and monotonic subthreshold relaxation in the nonresonant regime are evident in the time evolution of the voltage variable. Whereas the subthreshold dynamics in the nonresonant regime is governed by a single relaxational time scale, there are two time scales, one relaxational and one oscillatory, in the resonant regime. Two intrinsic time scales, which characterize the dynamics of the system in the latter case, are indicated in Fig. 3.2(a). The first is the time T_1 between the beginning of a spike and the first maximum of the following subthreshold oscillation ($T_1 = 2\pi/\omega_1$, $T_1 \sim 2.5$, $\omega_1 \sim 2.4$), and the second is the period T_2 of subthreshold oscillations ($T_2 = 2\pi/\omega_2$, $T_2 \sim 1.12$, $\omega_2 \sim 5.6$).

One could expect that the intrinsic frequency of subthreshold oscillations might be reflected in the power spectrum. Therefore we plot the power spectral densities of a single pulse in the resonant and nonresonant regimes in Figs. 3.2(c) and 3.2(d), respectively. The spectral densities are calculated numerically and normalized on the total signal power. In the resonant regime, a tiny shoulder in the spectral density at a frequency close to ω_2 is caused by the subthreshold oscillation. However, there is no well pronounced peak at this frequency. The width of the suprathreshold spike contribution to the spectral density is proportional to the inverse spike duration ($\sim 2\pi/0.8 \sim 7.9$), and therefore overlaps with the peak arising from the subthreshold oscillation. Moreover, the total spike power significantly exceeds the total power in the successive subthreshold oscillation. In other words, the contribution of the subthreshold oscillations to the power spectrum cannot be distinguished from the contribution of the spike, since the spike duration is small compared to the period of subthreshold

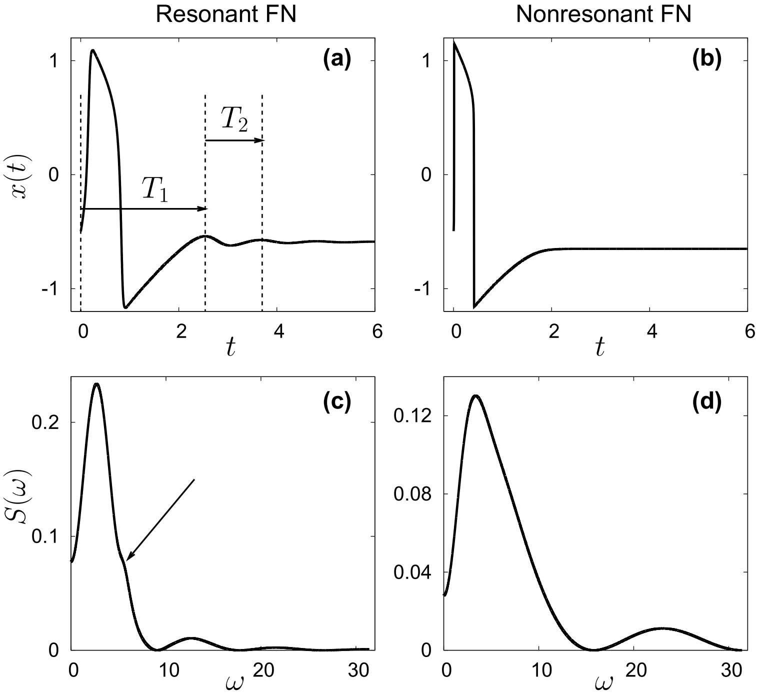

Figure 3.2: (a), (b): spike shape in the FN model: the voltage variable $x(t)$ as a function of time. (c), (d): power spectral density of a single spike in the deterministic FN model $D = 0$. The spectra are normalized so that the integral over the spectral density is unity. The arrow in panel (c) indicates a shoulder at the frequency close to that of subthreshold oscillations. (a), (c): resonant regime ($\epsilon = 0.05, \gamma = 1.5, b = 0.5$) with subthreshold oscillations. (b), (d): nonresonant regime ($\epsilon = 0.001, \gamma = 1.5, b = 0.6$).

oscillations. This difference in sub- and suprathreshold time scales is even more striking in resonant neurons. In stellate cells the spike duration lasts $\sim 2-5\,\mathrm{ms}$ and the period of the subthreshold oscillations is $\sim 100\,\mathrm{ms}$. The magnitude of the resulting shoulder in the spectral density at the frequency ω_2 is so small, that it cannot be distinguished from the background noise in stochastic spectra of neural responses to a noise-like input.

Having discussed the dynamical properties in the autonomous FN model, we can proceed to study its response to input signals. In particular we are interested in modeling the *in vitro* environment, when synaptic transmission is blocked and the intrinsic noise of ion channels plays a major role. This situation can be modeled by an additive noise term in the equation for the recovery variable $y(t)$:

$$\begin{aligned} \epsilon \dot{x} &= x - x^3 - y, \\ \dot{y} &= \gamma x - y + b + \sqrt{2D}\xi(t), \end{aligned} \tag{3.4}$$

where $\xi(t)$ is a white Gaussian noise of unit intensity ($\langle \xi(t) \rangle = 0$, $\langle \xi(t)\xi(t') \rangle = \delta(t - t')$). The Langevin approximation for the stochastic dynamics of a population of Markovian ion channels is derived in Section 6.1 for the resonate-and-fire model of a neuron. The derivation is analogous for the FN model and leads to the Langevin dynamics for $y(t)$ in the form of Eq. (3.4). Including an additive white noise term in the equation for the recovery variable is a common and mathematically consequent way to add a stochastic input to the FN model (Lindner et al., 2004; Ullner et al., 2003; Lacasta et al., 2002). The FN model with white or short correlated colored noise terms in the equations for the voltage variable and for both variables was studied previously (Collins et al., 1995b; Longtin, 1993; Izús et al., 1998; Kurrer and Schulten, 1991). It was observed, that the main features of the spiking statistics do not

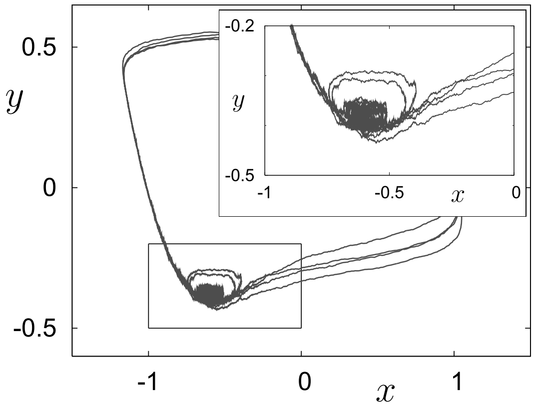

Figure 3.3: Simulations of the phase space trajectory in the FN model driven by a white Gaussian noise in the resonant regime. After every spike the trajectory returns to almost the same region in the vicinity of the fixed point. The inset shows magnification of the region around the fixed point marked by the rectangle in the main plot. $D = 0.0005$, other parameters are as specified in Fig. 3.1.

depend on the exact functional form of the noise term or the noise correlation time, as long as the latter remains small.

Input noise in the FN dynamics leads to fluctuations around the fixed point until an occasional escape provokes a spike. After every spike the trajectory returns to the vicinity of the fixed point and remains trapped until the next escape. As the spike dynamics is very fast and only slightly perturbed by noise, the trajectory returns to the fixed point passing through almost the same values of x and y on the left branch of the cubic nullcline, as Fig. 3.3 illustrates. In other words, a spike can be seen as a mechanism resetting variables x and y to almost fixed values, which fix the initial phase of the subthreshold oscillation following each spike.

The subthreshold oscillation modulates the distance to the excitation threshold, and hence the probability to generate the next spike. This probability is vanishing during the refractory period and depends on the time the trajectory has spent in the vicinity of the fixed point since the last reset. The escape probability reaches its maximum as the trajectory passes through the first maximum of the subthreshold oscillation, i.e. T_1 is the most probable interspike interval, see Fig. 3.2. If the second spike occurs during this time, the spikes follow with the frequency ω_1 and one speaks about a spike cluster. If no second spike was generated at T_1, there is a higher probability that it will be generated from the second maximum of the subthreshold oscillation, so that the ISI will be $T_3 = T_1 + T_2 \sim 3.6$ and the corresponding frequency is $\omega_3 = 2\pi/T_3 \sim 1.7$, and so on. On time scales beyond the relaxation time of the subthreshold oscillation, the initial phase becomes stationary and the escape rate saturates to a constant value. Hence the intrinsic characteristic times can be expected to be reflected in the suprathreshold responses of the resonant neurons to noisy input signals. Notice, that the dependence of the escape rate on the age of a state highlights the non-Markovian character of the escape dynamics in the resonant FN model.

Two typical examples of spike sequences generated in the FN model driven by noise are presented in Fig. 3.4, in the resonant (upper panel) and nonresonant regime (lower panel). It is difficult to distinguish between these two regimes by just observing signals during short time intervals. This makes it necessary to introduce reliable statistical instruments, which clearly distinguish between these two situations and characterize such features as a spike

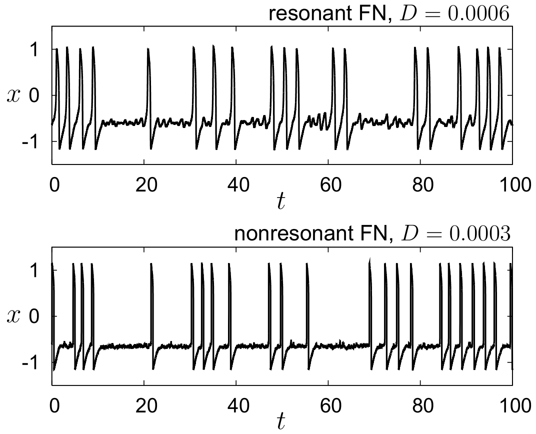

Figure 3.4: Typical pulse trains obtained in the FN model driven by white Gaussian noise. *Upper panel:* resonant regime, $D = 0.0006$, spike clustering and subthreshold oscillations can be observed. *Lower panel:* nonresonant regime, $D = 0.0003$. Other parameters as specified in Fig. 3.1. For chosen values of noise intensities the mean firing rates are similar in both cases.

clustering.

3.2 Power spectral density

It is customary to use power spectra to distinguish between resonant and nonresonant phenomena. The power spectral density $S_x(\omega)$ of the voltage variable $x(t)$ is defined as

$$S_x(\omega) = \langle x(\omega) x^*(\omega) \rangle, \tag{3.5}$$

with $x(\omega)$ being the Fourier-transform of the corresponding variable $x(t)$:

$$x(\omega) = \int_{-\infty}^{+\infty} x(t) e^{i\omega t} dt.$$

The spectrum of the stochastic FN model Eq. (3.4) was calculated analytically in the limit case $\epsilon \to 0$ (Lindner and Schimansky-Geier, 1999; Lindner, 2002). Collins et al. (1995b) use another analytical approximation, which also makes use of small values of ϵ and assumes a constant escape rate from the resting state. Hence only nonresonant neurons could be adequately described by these analytical approximations.

Let us first turn to the power spectral densities of the FN model obtained numerically. We used the output signal of the stochastic FN model sampled at 2^{15} points with the sampling interval 0.1, to compute the power spectral density by the Fast Fourier Transform (Press et al., 1999). The resulting spectra were averaged over 120 different realizations and normalized on the total signal power. Results are presented in Figs. 3.5(a) and 3.5(b) for the resonant and nonresonant regimes, respectively, and for different noise intensities.

The most prominent feature in all spectra is the existence of a well pronounced main peak at the mean firing frequency and of a lower peak at a higher frequency which disappears at high levels of noise. With increasing noise the main peak moves to higher frequencies due to the decrease of the mean interspike interval. However, this shift is much less pronounced in the resonant regime, where the frequency corresponding to this peak remains close to ω_1.

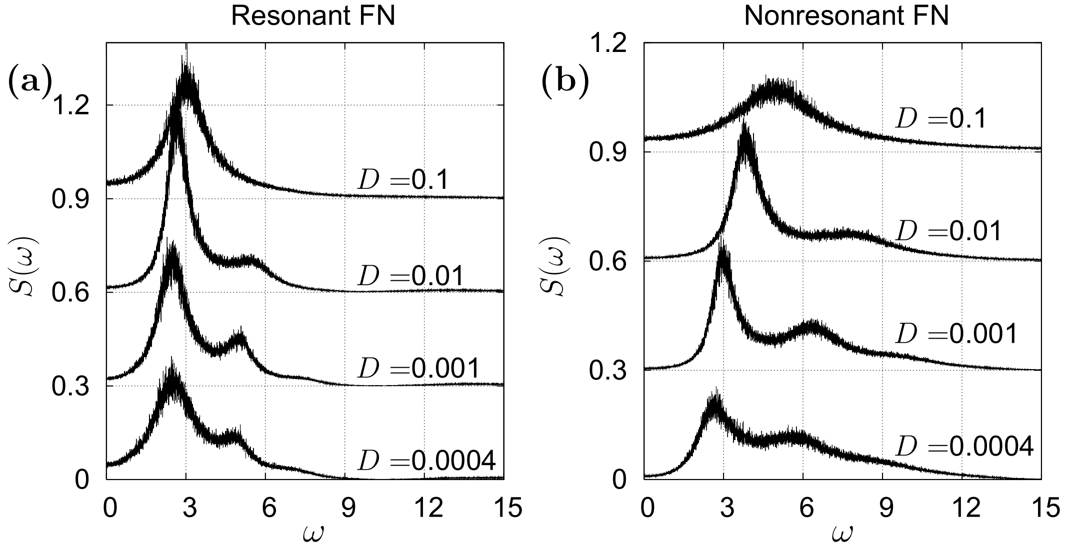

Figure 3.5: Power spectral density $S(\omega)$ for the FN model driven by white Gaussian noise in the resonant (a) and nonresonant (b) regimes for different noise intensities $D = 0.0004, D = 0.001, D = 0.01, D = 0.1$. Other parameters are as in Fig.3.1. The spectral densities are normalized on the total signal power. For clarity, the spectral densities for larger noise intensities are shifted vertically by 0.3.

Besides this fact and some quantitative differences, the resonant and nonresonant spectra are very similar. The second peak also moves to higher frequencies so that its frequency remains approximately the double frequency of the first peak, while the frequency of the subthreshold oscillations remains constant. This fact and the fact that the second peak is present in both resonant and nonresonant spectra witness in favor of its nature as the second harmonic.

3.3 Waiting-time density

Alternatively, the output of the FN model can be characterized by the probability density function (PDF) of interspike intervals. It is obtained from the FN output reduced to a δ-spike sequence, i.e. to a point process whose random points are identified with these δ-spikes, see Section 2.3. The interspike interval T is the time interval between two successive spike, and the ISI density $\mathcal{F}(T)$ is the waiting-time density for the corresponding point process. The whole dynamics between spikes is neglected, and the waiting-time density seems to be a very simplified function at first sight. Nevertheless, as we proceed to show, the waiting-time density contains almost all relevant information about the subthreshold dynamics. In particular, the spectra of the FN output can be reconstructed from the waiting-time density by the renewal theory and from the spectrum of a single spike.

We obtain the waiting-time density numerically from simulations of the stochastic FN

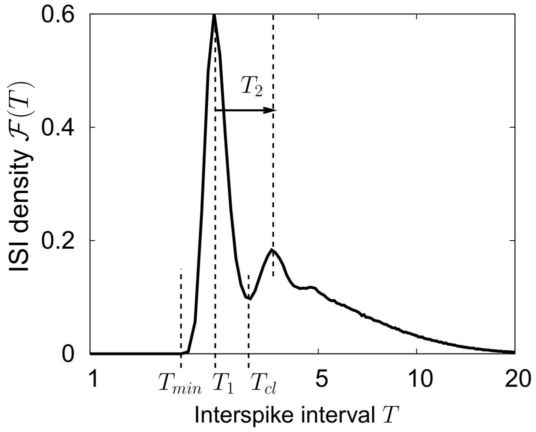

Figure 3.6: Interspike interval density $\mathcal{F}(T)$ obtained from simulations of the FN model driven by white Gaussian noise in the resonant regime for $D = 0.0006$. Other parameters as in Fig.3.1. Note the logarithmic scale.

equations Eq. (3.4) in the resonant ($\epsilon = 0.05, \gamma = 1.5, b = 0.5$) and nonresonant ($\epsilon = 0.001, \gamma = 1.5, b = 0.6$) regimes for different values of noise intensity D. Spikes have been defined as zero-level crossings from negative to positive values of the x-variable. We collected 10^6 interspike intervals T to obtain the waiting-time density (i.e. the interspike interval density) $\mathcal{F}(T)$.

The results are presented in Fig. 3.6 for the resonant FN model with $D = 0.0006$ and in Fig. 3.7 for the resonant and nonresonant FN model with $D = 0.0002$. The ISI probability density functions differ qualitatively for these two regimes: In the nonresonant regime $\mathcal{F}(T)$ possesses only one maximum, while the ISI density in the resonant regime shows an oscillatory behavior. The first sharp maximum in the latter case occurs near T_1 and corresponds to the ISI within a cluster. Further maxima follow in succession with the period of the subthreshold oscillations T_2 (the characteristic times T_1 and T_2 are the same in Figs. 3.6 and 3.2). The resonant ISI density has a long exponential tail, reflecting that spike clusters are separated by large, exponentially distributed intervals. A natural definition of a cluster is therefore that it is a sequence of spikes separated by intervals smaller than the time T_{cl} (see Fig. 3.6) up to the first *minimum* in the ISI density.

To understand how oscillatory behavior of the ISI density is consistent with the renewal property of a spike train, consider the following interpretation. Assume the spike generation process to be a renewal process. If a spike was generated at time $T = 0$, then $\mathcal{F}(T)dT$ is the time dependent probability that the next spike will be generated between T and $T + dT$ (and that there was no spike during the time T). This probability is modulated by the subthreshold oscillation in the resonant regime, as explained in the end of Section 3.1. In the nonresonant regime the waiting-time density lacks the oscillatory behavior: the spike train is more homogeneous in this case. After reset of variables performed by every spike, a quasistationary distribution quickly establishes around the fixed point prior to the next escape. Therefore the spikes are generated with a constant rate, and the ISI density is exponential.

Note, there is a certain minimal value T_{min}, such that for all $T < T_{min}$ the interspike interval density vanishes. The value T_{min} is marked in Fig. 3.6 and describes the relative

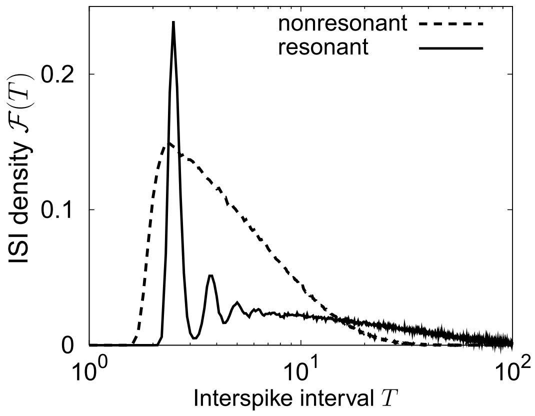

Figure 3.7: Interspike interval density $\mathcal{F}(T)$ obtained from simulations of the FN model driven by white Gaussian noise in resonant (solid line) and in nonresonant (dashed line) regimes, for the same noise intensity $D = 0.0002$ and the other parameters as specified in Fig.3.1. Note the logarithmic scale.

refractory time, which decreases with increasing noise intensity.

3.4 Power spectral density obtained from waiting-time density

In the previous section we have shown that the probability density of interspike intervals reflects the characteristic time scales of the subthreshold dynamics in the FN model. Let us now see how spectra of the FN model can be obtained from numerical data for the ISI density. Lacasta et al. (2002) have already proposed to use numerically obtained waiting-time densities in theoretical considerations. In our case, the combination of numerical and analytical methods allows to avoid many simplifying assumptions and to obtain the power spectral density even in the resonant case. The idea is the following:

(i) Instead of examining the complete dynamics of the stochastic FN model, our consideration is restricted only to "events" (spikes). The output $x(t)$ of the FN model is then replaced with a point process

$$\rho(t) = \sum \delta(t - t_i), \tag{3.6}$$

where t_i are successive spike times in the FN output $x(t)$.

(ii) Assuming this sequence of δ-spikes to be a *renewal point process*, we apply a formula derived by Stratonovich (1967), which connects the power spectral density of the renewal point process and its characteristic function $\mathcal{F}(\omega)$:

$$S_\rho(\omega) = \frac{1}{\langle T \rangle} \frac{1 - |\mathcal{F}(\omega)|^2}{|1 - \mathcal{F}(\omega)|^2} + \frac{2\pi}{\langle T \rangle^2} \delta(\omega). \tag{3.7}$$

Here $\langle T \rangle$ is the mean interspike interval given by

$$\langle T \rangle = \lim_{N \to \infty} \frac{1}{N} \sum_{i=1}^{N} T_i,$$

D	T_1	T_{min}	u_0	u_1	u_2	u_3	u_4
			resonant				
0.0006	2.1	2.1	0.582	0.564	4.44	0.199	4.517
0.002	2.1	1.9	0.479	0.457	5.383	0.579	1.488
0.02	2.1	1.54	0.222	0.298	2.736	0.758	0.835
0.09	2.0	1.07	0.237	0.435	2.061	0.632	0.847
			nonresonant				
0.0002	2.2	1.76	0.132	0.329	0.717	0.148	6.463
0.002	2.0	1.3	0.098	0.179	3.473	0.857	0.522
0.03	1.5	0.8	0.276	0.244	3.045	0.923	0.461
0.1	1.4	0.5	0.193	0.268	2.44	0.728	0.489

Table 3.1: The values of fit parameters.

and the characteristic function $\mathcal{F}(\omega)$ is the Fourier transform of the waiting-time density $\mathcal{F}(T)$:

$$\mathcal{F}(\omega) = \int_0^{\infty} \mathcal{F}(T) e^{i\omega T} dT. \tag{3.8}$$

Analogous calculations of the power spectrum based on the Stratonovich formula Eq. (3.7) were made for the leaky integrate-and-fire model (Lindner et al., 2002; Lindner, 2002) and for the nonresonant FitzHugh-Nagumo model (Lindner and Schimansky-Geier, 1999; Lindner, 2002). In contrast to these approaches, we obtain here the waiting-time density from simulations (Figs. 3.6 and 3.7) and fit it to an analytical function, which is then substituted into equations Eqs. (3.7) and (3.8).

To fit $\mathcal{F}(T)$ we used the following analytical function:

$$\mathcal{F}(T) = \Theta(T - T_{min}) \left[u_0 e^{-\frac{T-T_1}{u_1}} \sin[u_2(T - T_1)] + u_3 e^{-\frac{T-T_1}{u_4}} \right]. \tag{3.9}$$

Here $\Theta(T - T_{min})$ is the Heaviside step function, indicating that there are no interspike intervals smaller than T_{min}. The most probable interspike interval T_1 is the time between the beginning of a spike and the first maximum of the following subthreshold oscillation. These two parameters can be found immediately from simulation data. u_0, u_1, u_2, u_3, u_4 are fit parameters with the following meaning: u_1 is the relaxation time of the subthreshold oscillation, u_2 is its frequency, u_4 is the characteristic time of the Kramers escape mechanism (the inverse Kramers escape rate), and u_0 and u_3 are the weight parameters. The analytical

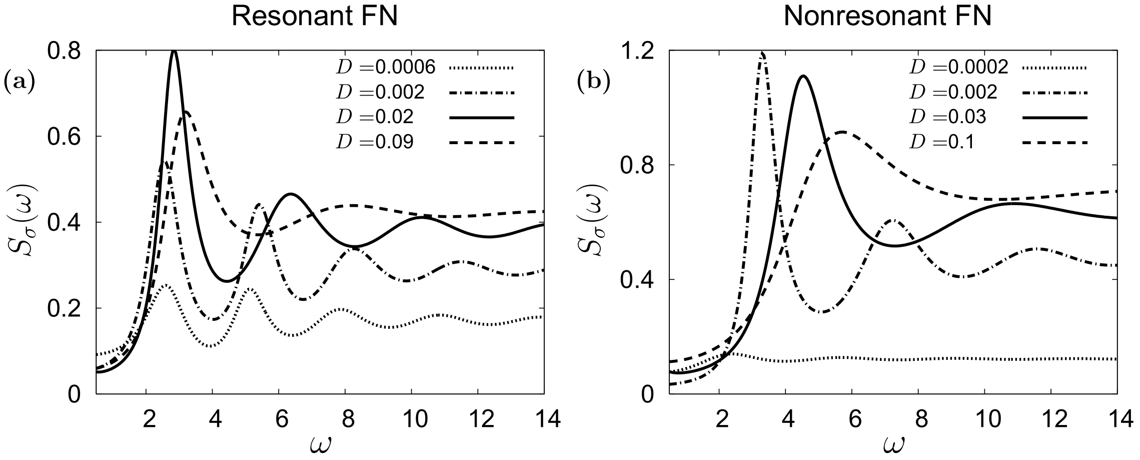

Figure 3.8: Power spectral density $S(\omega)$ calculated theoretically for the δ-spike output of the FN model driven by white Gaussian noise, for different noise intensities. (a) resonant regime, $D = 0.0006, 0.002, 0.02, 0.09$, (b) nonresonant regime, $D = 0.0002, 0.002, 0.03, 0.1$, and with other parameters as specified in Fig.3.1.

fit function Eq. (3.9) is interpretered as follows: on times smaller than the subthreshold relaxation time ($T < u_1$) the ISI density shows several peaks following with the frequency of the subthreshold oscillations (u_2). On times exceeding the subthreshold relaxation time ($T > u_1$), the escape is governed by a Kramers-like mechanism and proceeds with a constant rate (u_4^{-1}). Note, that u_0, u_1, u_2, u_3, u_4 are not independent due to the normalization condition $\int_0^\infty \mathcal{F}(T)dT = 1$.

The fit values of u_0, u_1, u_2, u_3, u_4 have to be determined for every noise intensity. To fit the function Eq. (3.9) to numerical data we used the Levenberg-Marquardt method (Press et al., 1999). The results are summarized in Table 3.1 for several values of the noise intensity. The Kolmogorov-Smirnov test (Press et al., 1999), which is the most sensible test for cumulative distribution functions, confirms a good fit quality with a confidence level better than 0.95. The Fourier transform of the function Eq. (3.9) can be derived exactly as a function of fit parameters.

The applicability of this semi-analytical approach is restricted by the amount of available data. For small data sets the form of the ISI density strongly depends on the bin size used to estimate this density, which makes a meaningful fit impossible. If only a limited amount of experimental data is available, this semi-analytical method still can be applied. In this case, the cumulative distribution function can be used for fitting, which is independent of the sampling interval. Subsequently, the ISI density and spectra can be derived analytically.

Semi-analytical results for the power spectral densities $S_\rho(\omega)$ of the δ-spike output in the FN model are plotted in Fig. 3.8 for noise intensities listed in Table 3.1. Let us consider the asymptotic behavior of these spectral densities in high and low frequency domains.

For high frequencies the spectral density $S_\rho(\omega)$ of the δ-spike sequence saturates at a certain level, the stationary mean firing rate r_0, see Eq. (3.7):

$$\lim_{\omega \to \infty} S_\rho(\omega) = r_0, \tag{3.10}$$

with $r_0 = \langle T \rangle^{-1}$. This is related to the fact, that a δ-spike train possesses an infinite variance: $\lim_{\tau \to 0} \langle \sigma(t)\sigma(t+\tau) \rangle = r_0 \delta(\tau)$ (Stratonovich, 1967) and the integral over the power spectral density diverges.

Using the expansion of the characteristic function $\mathcal{F}(\omega)$ and Eq. (3.7), it can be shown for low frequencies:

$$\lim_{\omega \to 0} S_\rho(\omega) = C_{\text{var}}^2 r_0, \tag{3.11}$$

where C_{var} is the coefficient of variation, $C_{\text{var}} = \sqrt{\langle \Delta T^2 \rangle} / \langle T \rangle$. If $C_{\text{var}} < 1$ then $S_\rho(\omega)$ is smaller in the low frequency limit than $S_\rho(\omega)$ in the high frequency limit. This low frequency dip is related to the refractory period (Franklin and Bair, 1995). For small noise intensities the mean excitation time is very large, therefore the refractory time becomes irrelevant and the spectral density approaches the flat Poisson limit ($C_{\text{var}} \to 1$) with a small dip. For intermediate noise levels, when the refractory and escape times are of the same order, refractoriness determines the firing rate and the neuron output becomes very regular. This effect is called coherence resonance (Pikovsky and Kurths, 1997). At the optimal noise intensity, the C_{var}-value is small and the low frequency dip in the power spectral density is maximal. Fig. 3.8 illustrates that the dip is smaller in the resonant case than in the nonresonant case, especially for weak noise. In the nonresonant regime the spike pattern is homogeneous, whereas in the resonant regime spike clusters separated by long intervals are typical. The existence of two time scales in the spike train results in higher values of C_{var}.

Visual inspection of the spectral densities in Fig. 3.8 reveals, that the frequency ω_{max} where the main peak appears, the height of the main peak and its shift to higher frequencies are analogous to those of the spectra estimated numerically (see Fig. 3.5). In the resonant regime and for increasing noise intensity, ω_{max} remains close to the frequency ω_1, which is in accord with numerical results, Fig. 3.5.

Nevertheless, the theoretical spectra differ from spectra obtained numerically. The theoretical spectra contain a considerable degree of higher harmonics and do not vanish in the high frequency limit. This can be explained by the fact that δ-spike sequences were used instead of the real spikes with finite duration and particular form. If we perform a convolution of a single spike with a δ-sequence indicating the positions of spikes (the forms of pulses are assumed to be identical), then we can also take the finite spike duration into account. In this case, the spectrum of the δ-spike sequence multiplied by the form-factor (which is the spectrum of a single spike) should coincide with the spectrum obtained numerically. Reasoning this way, we neglect all interspike dynamics, which contains subthreshold oscillations at the well prescribed frequency in the resonant case. The coincidence of spectra obtained theoretically and numerically is possible only if the frequency of subthreshold oscillations is not directly present in the power spectral densities.

We have numerically calculated the power spectral density of a single spike in the autonomous FN model in both regimes, see Figs. 3.2(c) and 3.2(d). The results of the multiplication of the theoretically calculated spectral densities with the form-factors are presented

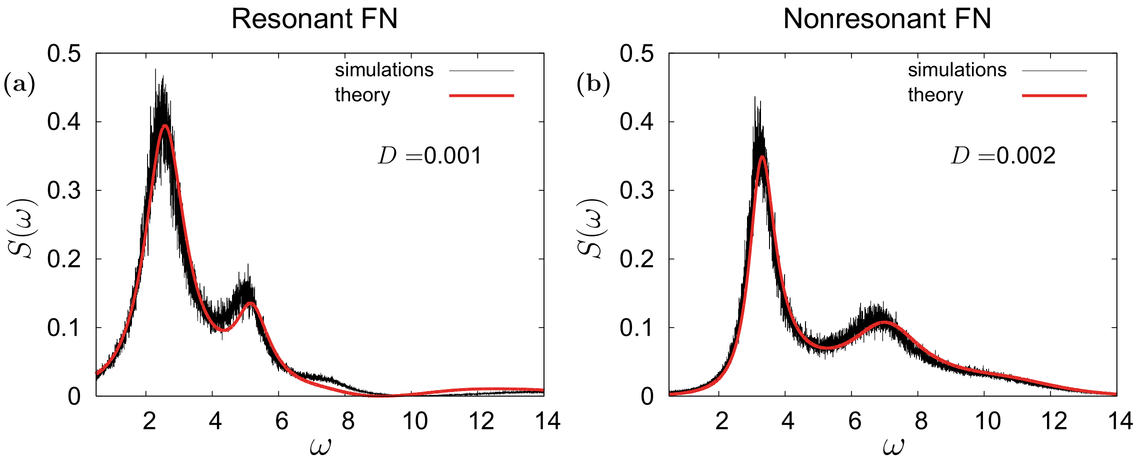

Figure 3.9: Power spectral densities $S(\omega)$ for the FN model driven by white Gaussian noise, comparison of spectra obtained numerically (black) and theoretical spectra multiplied by the form factor (red). (a) Resonant regime, $D = 0.001$, (b) nonresonant regime, $D = 0.002$. Other parameters are as in Fig.3.1. Spectral densities are normalized on the total signal power.

in Fig. 3.9 (red lines). The same plot shows numerically estimated spectral densities (black lines). A good agreement of numerical and theoretical results confirms our assumption that spike generation is a renewal process. The renewal assumption also holds in the case of the resonant FN model and therefore justifies the characterization of the firing patterns using the ISI density. Again we find, that the frequency of subthreshold oscillation is not directly reflected in the power spectral density.

The small difference between the numerical and the semi-analytical results may be due to the change of the spike form if external noise is applied, as this difference is larger for a strong noise ($D = 0.1$) and vanishing for small noise intensities. All higher harmonics present in the spectra calculated from the waiting-time density (Fig. 3.8) disappear after multiplication by the form-factor.

We repeated all simulations and calculations for the Morris-Lecar model (Koch, 1999):

$$\begin{aligned} C\frac{dV}{dt} &= -g_{Ca}m_\infty(V)(V-V_{Ca}) - g_K w(V-V_K) - g_L(V-V_L) + I, \\ \frac{dw}{dt} &= \phi\frac{w_\infty(V)-w}{\tau_w(V)}, \end{aligned} \tag{3.12}$$

where $m_\infty(V) = 0.5[1 + \tanh((V - V_1)/V_2)]$, $w_\infty(V) = 0.5[1 + \tanh((V - V_3)/V_4)]$, and $\tau_w(V) = 1/\cosh((V - V_3)/(2V_4))$. Parameter values used to simulate the resonant and nonresonant regimes are given in the legend to Fig. 3.10. In Fig. 3.10 the ISI density for a stochastic Morris-Lecar model is plotted in resonant and nonresonant regimes for $D = 5 \cdot 10^{-6}$. The results are analogous to those presented for the FN model, indicating the generality of our results.

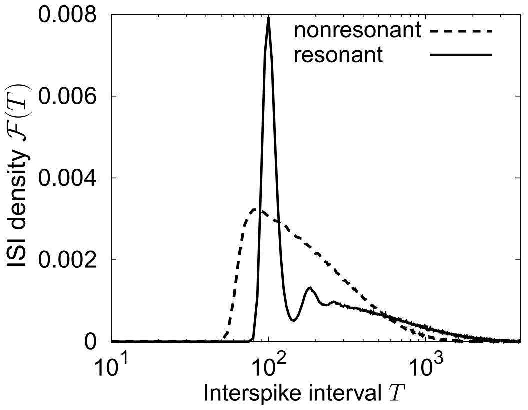

Figure 3.10: Interspike interval density $\mathcal{F}(T)$ obtained numerically in the Morris-Lecar model driven by white Gaussian noise, in resonant ($C = 20, I = 82$) and in nonresonant ($C = 2, I = 65$) regimes with same noise intensity $D = 5 \cdot 10^{-6}$. Other parameters are $V_1 = -1.2, V_2 = 18, V_3 = 2, V_4 = 30, \overline{g}_{Ca} = 4.4, \overline{g}_K = 8.0, \overline{g}_L = 2, V_K = -84, V_L = -60, V_{Ca} = 120, \phi = 0.04$. Note the logarithmic scale.

Summary

Firing patterns are known to be qualitatively different in resonant and nonresonant neurons. This difference is hard to quantify by just observing spike trains during short time intervals. Therefore, reliable statistical instruments are necessary to distinguish between resonant and nonresonant firing patterns and to characterize features like spike clustering.

In the present chapter, we discuss the spectral properties and the interspike interval densities in the FitzHugh-Nagumo model subjected to white Gaussian noise. We show that there is no pronounced qualitative difference between power spectral densities in resonant and nonresonant regimes. Small differences are found in the response of resonant and nonresonant neurons to a possible change of the parameters of external force. Spectral characteristics are very habitual and widely used, but they are indeed not so informative, as we have shown using simulations of a mathematical model of a neuron.

In contrast, the structure of the interspike interval probability density differs strongly for these two cases. The ISI density in the resonant regime shows oscillatory behavior reflecting subthreshold oscillations, whereas the ISI density in the nonresonant regime possesses only a single maximum. Moreover, the structure of the resonant ISI densities reflects the clustering effect observed in resonant neurons and provides an accurate definition of a spike cluster. An analytical fit function for the ISI density has been formulated for the FitzHugh-Nagumo model.

We reconstruct the power spectra of the output from the waiting-time densities, using the Stratonovich formula for the spectral density of a renewal point process and performing the convolution with the form-factor of a single spike. A good agreement of these spectra with the numerical estimates indicates, that the information contained in the power spectral density can also be extracted from the waiting-time density and the form-factor of a single spike. The renewal assumption holds not only for nonresonant FN neurons, but also for resonant FN neurons.

The interspike interval probability density contains almost all relevant information about the neuron output even in the resonant case. We conclude that the interspike interval density rather than the power spectral density should be preferred in experiments to characterize the firing patterns and to distinguish between resonant and nonresonant neurons.

We therefore use the ISI density in all further investigations as the main statistical instrument to characterize firing patterns in neurons. In Chapter 5 we develop analytical methods to calculate the ISI density for renewal neuron models with threshold and reset. These methods will be used extensively in Chapters 6 and 7 to quantitatively describe experimental data.

4

Markovian approach to the first passage time problem

The first passage time (FPT) is defined as the time T, when a stochastic process $x(t)$ leaves an *a priori* prescribed domain Δ of its phase space for the first time, assumed that $x(t)$ has been started at $t = 0$ from given initial conditions within Δ. This concept was originally introduced by E. Schrödinger (1915), when he discussed the behavior of Brownian particles in external fields. A large variety of problems, ranging from noise in vacuum tubes, chemical reactions and nucleation (Hänggi et al., 1990) to stochastic resonance (Longtin et al., 1991), behavior of neurons (Tuckwell, 1988) and risk management in finance (Redner, 2001) can be reduced to FPT problems. In the majority of applications the attractor of the system's dynamics lies inside Δ. The escape process is characterized by the noise-induced flux across the absorbing boundary of Δ, or by the probability density $\mathcal{F}(T)$ of the first passage time.

Approaches to find $\mathcal{F}(T)$ are typically based either on the Fokker-Planck equation with an absorbing boundary (Risken, 1989) or on the renewal equation (van Kampen, 1992). Despite the long history of the FPT problem, explicit expressions for the FPT density are only known for a few cases. These include overdamped particles under the influence of white noise in the force free case, under time-independent constant forces and linear forces (Tuckwell, 1988; Tikhonov and Mironov, 1977; Gerstein and Mandelbrot, 1964; Stratonovich, 1967), as well as the case of a constant force under colored noise (Lindner, 2004). Reasonable approximations exist for a few nonlinear forces (Sigeti and Horsthemke, 1989; Liepelt et al., 2005).

Of great importance are Markovian escape processes, for which the mean FPT does not depend on initial conditions almost everywhere in Δ. For such processes the probability to escape per unit time, i.e. the escape rate, is independent of the age of a decaying state, and the FPT is exponentially distributed on times exceeding the local relaxation time in Δ. A large variety of escape processes in physics, chemistry and biology can be described by Markovian models, well known examples are chemical reactions, electrical transport and nucleation processes to name but a few (Hänggi et al., 1990; van Kampen, 1992). Many neuronal systems also demonstrate this kind of behavior. It was shown by Gerstein and

Mandelbrot (1964), that interspike interval histograms obtained experimentally from the output of some neurons can be reproduced by the FPT density of a one-dimensional diffusion process.

The first passage time problem for Markovian models reduces to the calculation of a constant escape rate. The analytical theory of rate processes started with the pioneering work of Kramers (1940) and thereafter was intensively studied. Comprehensive reviews of recent progress in the Kramers problem can by found in Hänggi et al. (1990) and Mel'nikov (1991).

In Section 4.1 we introduce the main equations for the statistical characteristics of the first passage time. Dependence of the mean FPT on initial conditions is investigated in Section 4.2, where we also formulate conditions under which an escape processes can be treated as Markovian. In Section 4.3 the Kramers approach to the rate calculation is reviewed and the equivalence of the mean FPT and the Kramers rate is shown.

4.1 First passage time problem in Markovian models

Consider a random process $x(t)$ which has been started at $t = 0$ from given initial conditions within a domain Δ of its phase space. The first passage time is the time T, when $x(t)$ leaves the domain Δ for the first time. Since $x(t)$ is a stochastic process, the first passage time T is a random variable. In reiterated realizations of $x(t)$ the FPT T assumes different values, which are characterized by the corresponding probability density function $\mathcal{F}(T)$. The formulation of the first passage problem assumes, that different realization of the process $x(t)$ are independent, hence the random variable T is completely characterized by its probability density function $\mathcal{F}(T)$. Equivalently, one can use the survival probability $\Phi(T)$, which is the probability that $x(t)$ did not yet leave Δ at time T:

$$\Phi(T) = 1 - \int_0^T \mathcal{F}(t)dt, \qquad \mathcal{F}(T) = -\frac{d\Phi(T)}{dT}. \tag{4.1}$$

All moments of the first passage time are easily obtained from either of these functions. For shorter notation we denote the n-th FPT moment $\mathcal{T}_n = \langle T^n \rangle$. In terms of the FPT density, the moments read:

$$\mathcal{T}_1 = \int_0^\infty t\mathcal{F}(t)dt, \qquad \mathcal{T}_n = \int_0^\infty t^n \mathcal{F}(t)dt, \tag{4.2}$$

and equivalently, in terms of the survival probability:

$$\mathcal{T}_1 = \int_0^\infty \Phi(t)dt, \qquad \mathcal{T}_n = n\int_0^\infty t^{n-1}\Phi(t)dt. \tag{4.3}$$

The escape process out of Δ is characterized by the escape rate κ, which is defined as the probability to leave Δ per unit time and is in general a time dependent quantity. To understand the connection between $\kappa(T)$ and the survival probability $\Phi(T)$, consider an ensemble of N identical particles injected into Δ at $t = 0$ at the same initial conditions. The number of particles leaving Δ between T and $T + dT$ is determined by the reduction of the survival probability and equals $-Nd\Phi(T) = N\mathcal{F}(T)dT$. On the other hand, this number equals the probability $\kappa(T)dT$ to escape during the time interval $(T, T+dT)$ multiplied by the number of particles within Δ at the time T, which is $N\Phi(T)$. Equating these expressions provides the relation between the escape rate $\kappa(T)$ and the survival probability $\Phi(T)$:

$$\kappa(T) = -\frac{1}{\Phi(T)}\frac{d\Phi(T)}{dT}, \qquad \kappa(T) = \frac{\mathcal{F}(T)}{\Phi(T)}. \tag{4.4}$$

Integration of the above equations yields equivalent relations:

$$\Phi(T) = \exp\left(-\int_0^T \kappa(t)dt\right), \qquad \mathcal{F}(T) = \kappa(T)\exp\left(-\int_0^T \kappa(t)dt\right). \tag{4.5}$$

A simple but nevertheless very important class are escape processes with a constant (time-independent) rate κ. For such processes the probability to escape does not depend on the time a trajectory spent inside Δ, i.e. on the age of an unstable state. We will refer to escape processes with a constant rate as Markovian escape processes, in contrast to non-Markovian escape processes with a rate changing in time[1].

From relations (4.5), assuming a constant κ, it immediately follows:

$$\Phi(T) = e^{-\kappa T}, \qquad \mathcal{F}(T) = \kappa e^{-\kappa T}. \tag{4.6}$$

Thus the first passage time in Markovian models is exponentially distributed and is characterized by a single parameter, the escape rate κ. Conversely, substitution of the exponential distribution Eq. (4.6) into the rate definition Eq. (4.4) implies a constant rate κ, hence the escape process with the exponential FPT distribution is necessarily Markovian. Using Eq. (4.3) we obtain:

$$\mathcal{T}_1 = \frac{1}{\kappa}, \qquad \mathcal{T}_n = \frac{n!}{\kappa^n}. \tag{4.7}$$

So the mean FPT in Markovian models is equal to the inverse escape rate.

The Markovian assumption significantly simplifies the first passage time problem, by reducing it to the calculation of a constant escape rate. However, one has to carefully verify whether the Markovian model is a good approximation for a given escape process. We therefore devote the following section to the discussion of conditions under which an escape processes can be treated as Markovian.

4.2 Dependence of the first passage time on initial conditions

The trajectory $x(t)$ of the first passage time process is only important up to the moment when it leaves Δ. Therefore one can assume that the whole exterior of Δ is absorbing. Since we only

---

[1] Do not confuse the definition of a Markovian escape process with a Markov process. The latter is defined as a stochastic process with the property, that for any set of n successive times holds $P_n(x_n, t_n|x_{n-1}, t_{n-1}; \ldots; x_1, t_1) = P_2(x_n, t_n|x_{n-1}, t_{n-1})$, i.e. that the conditional probability density at t_n given the value x_{n-1} at t_{n-1} is uniquely determined and is not affected by any knowledge of the values at earlier times, see e.g. van Kampen (1992) and Risken (1989).

consider Fokker-Planck processes with continuous trajectories in this work, it is sufficient to require the boundary δ of the domain Δ to be absorbing. Such absorbing boundary condition ensures that trajectories having once crossed δ will never return and recross it. The transition probability density $P_\Delta(x,t|x',0)$ of the first passage time process satisfies the Fokker-Planck equation with the appropriate absorbing boundary condition (Risken, 1989; Hänggi et al., 1990; Redner, 2001):

$$\partial_t P_\Delta(x,t|x',0) = L_x P_\Delta(x,t|x',0), \qquad x \in \Delta, \tag{4.8a}$$

$$P_\Delta(x,t|x',0) = 0, \qquad x \in \delta. \tag{4.8b}$$

Here L_x is the Fokker-Planck operator, and x in general denotes the whole set of variables resulting from the Markovian embedding of the process. Initial conditions x' are assumed to lie within Δ. $P_\Delta(x,t|x',0)$ also satisfies the backward Fokker-Planck equation

$$\partial_t P_\Delta(x,t|x',0) = L^\dagger_{x'} P_\Delta(x,t|x',0), \qquad x' \in \Delta, \tag{4.9a}$$

$$P_\Delta(x,t|x',0) = 0, \qquad x' \in \delta, \tag{4.9b}$$

where $L^\dagger_{x'}$ is the adjoint Fokker-Planck operator acting on the x'-dependence of $P_\Delta(x,t|x',0)$. If x' lies outside Δ, the probability $P_\Delta(x,t|x',0)$ vanishes, hence Eq. (4.9a) should be solved with the absorbing boundary condition Eq. (4.9b).

Evidently, the survival probability is related to $P_\Delta(x,t|x',0)$ by

$$\Phi(t,x') = \int_\Delta P_\Delta(x,t|x',0)dx \tag{4.10}$$

and is a function of time and initial conditions x'. Integration of both sides in Eqs. (4.9a) and (4.9b) with respect to x over domain Δ yields an equation for the survival probability, again with an absorbing boundary condition at δ:

$$\partial_t \Phi(t,x') = L^\dagger_{x'} \Phi(t,x'), \qquad x' \in \Delta, \tag{4.11a}$$

$$\Phi(t,x') = 0, \qquad x' \in \delta. \tag{4.11b}$$

For $x' \in \Delta$ it obviously holds: $\Phi(0,x') = 1$ and $\lim_{t\to\infty} \Phi(t,x') = 0$.

Now we are ready to obtain the equations for the moments of the first passage time $\mathcal{T}_n(x')$, which in general depend on the initial conditions x', see Eq. (4.3). Integrating Eqs. (4.11a) and (4.11b) over time from zero to infinity and using the first of the relations in Eq. (4.3) we obtain for the mean FPT $\mathcal{T}_1(x')$:

$$L^\dagger_{x'} \mathcal{T}_1(x') = -1, \qquad x' \in \Delta, \tag{4.12a}$$

$$\mathcal{T}_1(x') = 0, \qquad x' \in \delta. \tag{4.12b}$$

Analogously, if we multiply both sides of Eqs. (4.11a) and (4.11b) by nt^{n-1} and then integrate over time, using Eq. (4.3) we obtain a recursive system of equations for the moments of the first passage time:

$$L^\dagger_{x'} \mathcal{T}_n(x') = -n\mathcal{T}_{n-1}(x'), \qquad x' \in \Delta, \tag{4.13a}$$

$$\mathcal{T}_n(x') = 0, \qquad x' \in \delta. \tag{4.13b}$$

Solution of the partial differential equation (4.12a) with the boundary condition (4.12b) is not trivial for a general multidimensional system. However, let us consider the situation, when the mean FPT does not depend on initial conditions x' almost everywhere in Δ[2]. Under this assumptions we assign to the constant mean first passage time $\mathcal{T}_1 = \kappa^{-1}$. Using independence of $\mathcal{T}_1$ of x' and Eq. (4.13a) one can prove by induction, that all higher FPT moments also do not depend on initial conditions and obey $\mathcal{T}_n = n!\kappa^{-n}$ (Talkner, 1987). These expressions for the FPT moments coincide with expressions (4.7) for the FPT moments of a Markovian escape process. We immediately conclude, that the first passage time is exponentially distributed on times exceeding the local relaxation time, see Eq. (4.6). The FPT density is therefore parameterized by a single number κ, which is the constant escape rate.

If the mean first passage time does not depend on initial conditions, the escape process is Markovian and is completely characterized by the escape rate κ. In the following section we discuss two examples of the FPT processes with the intention to investigate the dependence of the mean first passage time $\mathcal{T}_1(x')$ on initial conditions and to ascertain, under which assumptions the mean FPT is independent of x'. We confine ourselves only to situations, when Δ is a local domain of attraction. If the domain Δ is not attractive the mean FPT evidently depends on initial conditions.

4.2.1 Smoluchowski dynamics: spatial diffusion

Consider the overdamped one-dimensional motion of a Brownian particle with unit mass in the harmonic potential $U(x) = \omega_0^2 x^2/2$. The coordinate x of the particle obeys a Langevin equation (Risken, 1989; Hänggi et al., 1990):

$$\dot{x} = -\frac{1}{\gamma}U'(x) + \frac{\sqrt{2D}}{\gamma}\xi(t), \tag{4.14}$$

where γ is a constant damping rate and the prime denotes the derivative with respect to x. A fluctuating force $\xi(t)$ represents the effect of a heat bath with the inverse temperature $\beta \equiv (k_B\theta)^{-1}$, where k_B is the Boltzmann constant and θ is the temperature. In the simplest case $\xi(t)$ is Gaussian white noise ($\langle\xi(t)\rangle = 0$, $\langle\xi(t)\xi(t+t')\rangle = \delta(t')$), which obeys the fluctuation-dissipation theorem $D = \gamma/\beta$. We put the absorbing boundary at $x = x_b > 0$, so that the domain Δ is a semi-infinite interval $(-\infty, x_b)$.

The adjoint Fokker-Planck operator for this one dimensional Smoluchowski dynamics reads

$$L^\dagger_{x'} = -\frac{1}{\gamma}U'(x')\frac{\partial}{\partial x'} + \frac{D}{\gamma^2}\frac{\partial^2}{\partial x'^2}. \tag{4.15}$$

In this case Eq. (4.12a) is the ordinary differential equation for $\mathcal{T}_1(x')$, which has to be solved with an absorbing boundary at x_b and a reflecting boundary at $x \to -\infty$. The solution is

---

[2] The mean FPT is zero for $x' \in \delta$, see Eq. (4.12b), and assumes a constant value $\mathcal{T}_1$ for x' being far from the boundary δ. For x' chosen inside the region adjacent to the boundary, the mean FPT increases from 0 to $\mathcal{T}_1$ and thus depends on x'.

found in the quadratures (Pontryagin et al., 1933):

$$\mathcal{T}_1(x') = \gamma\beta \int_{x'}^{x_b} dy e^{\beta U(y)} \int_{-\infty}^{y} dz e^{-\beta U(z)}. \tag{4.16}$$

It is sufficient to consider the dependence of $\mathcal{T}(x')$ on initial conditions only for $0 \leqslant x' \leqslant x_b$. Indeed, the main contribution of the term $e^{\beta U(y)}$ to the outer integral in Eq. (4.16) comes from two regions: $y \sim x_b$ and $y < -x_b$. The inner integral vanishes for $y < -x_b$, hence only the contribution from $y \sim x_b$ is significant and $\mathcal{T}_1(x' < 0) \approx \mathcal{T}_1(x' = 0)$. Qualitatively, it means that for $x' < 0$ the particle relaxes very quickly to the potential minimum and then behaves as if it has been started at $x' = 0$. $\mathcal{T}_1(x_b) = 0$ and saturates to a constant value if the distance $x_b - x'$ becomes large. Let us estimate x', where $\mathcal{T}_1(x')$ saturates and ascertain how this value depends on the system parameters.

Evaluation of the inner integral in Eq. (4.16) for positive y yields

$$\int_{-\infty}^{y} dz \exp(\beta U(z)) = \sqrt{\frac{\pi}{2\beta\omega_0^2}} \left(1 + \operatorname{erf}\left(\sqrt{\frac{\beta\omega_0^2}{2}} y\right)\right). \tag{4.17}$$

The outer integral can then be evaluated in terms of the generalized hypergeometric and complex error functions. To get a qualitative understanding of the dependence of the mean FPT on initial conditions, it is worth to evaluate integrals in Eq. (4.16) approximately for the case of weak noise and high activation energy. The noise intensity is determined by the thermal energy β^{-1}, and the activation energy is the potential energy at x_b and equals $U_b = U(x_b) = \omega_0^2 x_b^2/2$. The condition for weak noise and high activation energy $\beta U_b \gg 1$ reads:

$$\beta U_b = \beta \frac{\omega_0^2 x_b^2}{2} \gg 1. \tag{4.18}$$

Since the main contribution to the integral Eq. (4.16) comes from the region $y \sim x_b$ and in view of Eq. (4.18), we can replace the inner integral (Eq. (4.17)) by a constant value $\sqrt{2\pi/(\beta\omega_0^2)}$. To evaluate the outer integral in Eq. (4.16) we approximate the potential near x_b by a linear function $U(x) \approx U(x_b) - \omega_0^2 x_b (x_b - x)$. Substitution of these approximate expressions into Eq. (4.16) and evaluation of the integral leads to the mean FPT in the form:

$$\mathcal{T}_1(x') = \mathcal{T}_1 f(x'), \tag{4.19}$$

where $\mathcal{T}_1$ is a constant prefactor

$$\mathcal{T}_1 = \frac{\gamma}{\omega_0^2} \sqrt{\frac{\pi}{\beta U_b}} e^{\beta U_b}, \tag{4.20}$$

and $f(x')$ expresses the dependence of the mean FPT on initial conditions:

$$f(x') = 1 - \exp\left(-2\beta U_b \left(1 - \frac{x'}{x_b}\right)\right). \tag{4.21}$$

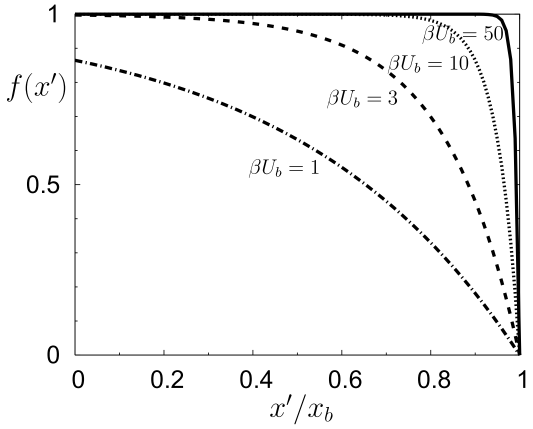

Figure 4.1: Function $f(x')$ expressing the dependence of the mean first passage time $\mathcal{T}_1(x') = \mathcal{T}_1 f(x')$ for the Smoluchowski dynamics on the initial condition x', for different values of the ratio βU_b of the activation and thermal energies. The mean FPT does not depend on x' if $\beta U_b \gg 1$ holds and $(x_b - x') > x_b(2\beta U_b)^{-1}$.

We plot the function $f(x')$ in Fig. (4.1) for different values of the ratio βU_b of the activation and thermal energies. The accuracy of approximations, made in the evaluation of the integrals, reduces with decrease of βU_b and is still satisfactory for $\beta U_b = 1$. As follows from Eq. (4.21), the dependence of the mean FPT on the initial conditions saturates for $(x_b - x') > x_b(2\beta U_b)^{-1}$. The width of the region where $\mathcal{T}_1(x')$ depends on the initial conditions is of the order $x_b(2\beta U_b)^{-1}$. Thus for a very low noise intensity, $\beta U_b \gg 1$, the mean FPT is almost constant for nearly all initial conditions inside Δ except for those close to x_b, whereas for a high noise intensity, $\beta U_b \sim 1$, the dependence of $\mathcal{T}_1(x')$ on x' extends to the minimum of the potential.

Consider a particle injected into the domain Δ at x', as shown in Fig. 4.2(a). If the noise strength exceeds the energy required for the particle to escape, the particle escapes immediately prior to the formation of a local quasiequilibrium within Δ. However, if the noise strength is lower, a local quasiequilibrium distribution first establishes inside Δ (Fig. 4.2(b)). The escape occurs then from this quasiequilibrium state with a constant rate κ and the mean first passage time is independent of the initial condition x' (Fig. 4.2(c)). If the local relaxation time is much smaller than the typical escape time, then the mean FPT does not depend on the initial conditions.

The example of the one-dimensional Smoluchowski dynamics demonstrates, that the ratio of the activation and thermal energies is essential for the dependence of the mean FPT on the initial conditions in the overdamped regime. If $\beta U_b \gg 1$ then $\mathcal{T}_1(x')$ does not depend on x' almost everywhere in Δ. Initial conditions at $x' \ll 0$ with arbitrary high energy will not accelerate the escape process, since the energy dissipation rate is high in the overdamped regime. The case is different in systems with low energy dissipation rates, as illustrated in the next example, the underdamped motion in a harmonic potential.

4.2.2 Underdamped dynamics: energy diffusion

Consider a Brownian particle with unit mass moving in a harmonic potential, and assume that the constant damping rate γ is small. The Langevin equation for the coordinate x of

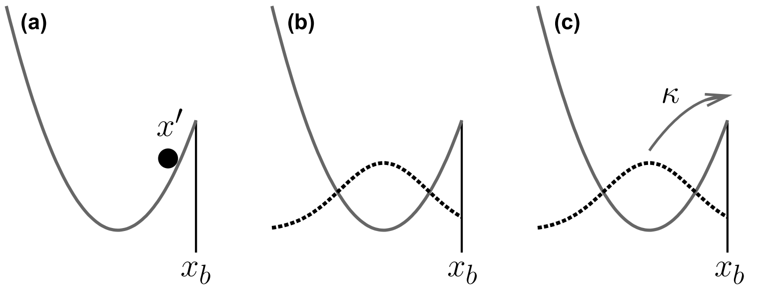

Figure 4.2: Sketch of escape from a potential well in the Kramers problem. (a) Particles are injected in the well. (b) Quasistationary distribution is established inside the well. (c) Escape occurs with a constant rate κ.

the particle reads:

$$\ddot{x} + \gamma\dot{x} + U'(x) = \sqrt{2D}\xi(t), \tag{4.22}$$

with $\xi(t)$ again being a white Gaussian noise of unit intensity. This equation describes the two-dimensional Markovian dynamics for x and its velocity $v = \dot{x}$. The corresponding Fokker-Planck equation is referred to as the Kramers-Klein equation (Kramers, 1940; Risken, 1989), and the adjoint Fokker-Planck operator reads

$$L^\dagger_{x',v'} = v'\frac{\partial}{\partial x'} - \left(\gamma v' + U'(x')\right)\frac{\partial}{\partial v'} + D\frac{\partial^2}{\partial v'^2}. \tag{4.23}$$

In this case, the equation (4.12a) for the mean first passage time is a partial differential equation, and its solution $\mathcal{T}_1(x', v')$ is a function of initial coordinate and velocity.

Here we consider a simple case, when the domain Δ is a half plane $x < x_b$. In this case the absorbing boundary condition should be imposed on the half infinite line $P_\Delta(x_b, v, t|x', v', 0) = 0$ for $v < 0$. It follows from Eqs. (4.1) and (4.10) that the FPT density is given by the probability current at $x = x_b$ in positive x-direction:

$$\mathcal{F}(T) = \int_0^\infty v P_\Delta(x_b, v, t|x', v', 0)dv. \tag{4.24}$$

The solution of Eqs. (4.8a) and (4.12a) with $L^\dagger$ given by Eq. (4.23) and absorbing boundaries is not trivial, and is only known for the case of a single boundary and a constant force $U'(x) = \text{const}$. Analytical expressions for the Laplace transforms of $P_\Delta(x, v, t|x', v', 0)$ and $\mathcal{F}(T)$, as well as the mean first passage time and the asymptotic behavior of the FPT distribution for large T were obtained by Marshall and Watson (1985, 1987) for a constant force. Even the case of vanishing force $U'(x) = 0$ is not trivial (Hagan et al., 1989a,b).

Since no analytical solution for the mean first passage time of an underdamped Brownian particle in a harmonic potential is available, let us consider a specific limit situation. Namely, let the damping rate γ be low, so that the particle performs fast oscillations within the well and the energy variation during one oscillation cycle is small. The energy E remains almost constant over many oscillation cycles, whereas the effect of the random force is essentially to shift the motion between different energy surfaces. The Brownian motion in the limit of a very low damping rate is effectively described by diffusion in the energy space. The particle immediately escapes as soon as it acquires the energy U_b.

H.A. Kramers was the first who realized, that in the limit of low damping the escape is governed by the energy diffusion rather than by the spatial diffusion. In his celebrated paper

(Kramers, 1940) he also derived the diffusion equation for the dynamics of the energy of the Brownian particle for the first time. The approach consists in the transformation of the Fokker-Planck equation to the action I and angle ϕ variables, and further averaging over the period of the angle variable. This is the standard procedure known as adiabatic elimination of the fast variable (Zwanzig, 1959; Risken, 1989), which can be applied if the energy dissipation during one oscillation cycle is smaller than the thermal energy (i.e. $\gamma\beta I_b < 1$, where I_b is the action corresponding to the energy U_b). In the case of a harmonic potential the action variable I is related to energy by $I = (2\pi/\omega_0)E$ and the adjoint Fokker-Planck operator acting on the energy variable E reads (Kramers, 1940):

$$L_E^\dagger = -\gamma E \frac{\partial}{\partial E} + \gamma E \beta^{-1} \frac{\partial^2}{\partial E^2}. \tag{4.25}$$

This operator is a nonlinear due to the explicite dependence of the diffusion coefficient on the energy E. Since we are interested in the escape process, when the energy E approaches the threshold value U_b, we can simplify $L_E^\dagger$ by the substitution of U_b instead of E in the drift and diffusion coefficients in Eq. (4.25), which leads to

$$L_E^\dagger = -\gamma U_b \frac{\partial}{\partial E} + \gamma U_b \beta^{-1} \frac{\partial^2}{\partial E^2}. \tag{4.26}$$

The two-dimensional first passage time problem for the coordinate x of the Brownian particle is reduced to the one-dimensional first passage time problem for its energy E. Solution of the latter is analogous to the case of the Smoluchowski dynamics considered above. Integration of the ordinary differential equation (4.12a) with $L_E^\dagger$ given by Eq. (4.26) yields the mean FPT dependent on the initial value of the energy U_0. Eqs. (4.12a), (4.26) should be solved together with an absorbing boundary condition at $E = U_b$ and a reflecting boundary condition at $E = 0$. This provides the mean FPT in the form:

$$\mathcal{T}_1(U_0) = \mathcal{T}_1 f(U_0), \tag{4.27}$$

where $\mathcal{T}_1$ is a constant prefactor:

$$\mathcal{T}_1 = \frac{1}{\gamma\beta U_b} e^{\beta U_b}, \tag{4.28}$$

and $f(U_0)$ expresses the dependence of the mean FPT on the initial energy:

$$f(U_0) = 1 - \exp\left(-\beta U_b \left(1 - \frac{U_0}{U_b}\right)\right). \tag{4.29}$$

Here we assumed that $\beta U_b \gg 1$ and neglected the term $\exp(-\beta U_b)$ as compared with unity. The dependence of the mean FPT on the initial energy for an underdamped motion, Eq. (4.29), is similar to the dependence of the mean FPT on the initial position for the Smoluchowski dynamics, see Eq. (4.21) and Fig. 4.1. Function Eq. (4.29) saturates $f(U_0) \approx 1$, if $\beta U_b(1 - U_0/U_b) \gg 1$, which is equivalent to $\beta U_b \gg 1$ and $U_0 \ll (U_b - \beta^{-1})$.

In the case of an underdamped motion ($\gamma\beta I_b < 1$), the mean FPT does not depend on the initial energy value U_0, if the ratio of the activation and thermal energies is high ($\beta U_b \gg 1$)

and the energy of injected particles is low, i.e. smaller than the difference between the activation and thermal energies ($U_0 \ll (U_b - \beta^{-1})$). The first condition is the same as for the overdamped dynamics. The second condition means, that if the initial energy is close to the activation energy, the random force can push the particle to the absorbing boundary prior to relaxation. Only for initial conditions in the vicinity of the potential minimum, formation of a local quasiequilibrium inside the well precedes an eventual escape and the particles escape with a constant rate κ, as sketched in Fig. 4.2.

To summarize, an escape process from the domain Δ can be treated as Markovian in good approximation, if the mean FPT does not depend on initial conditions and the formation of a local quasiequilibrium precedes the escape. For an overdamped dynamics these conditions are fulfilled if the activation energy considerably exceeds the fluctuations energy ($\beta U_b \gg 1$). In the case of an underdamped dynamics only particles injected with low initial energies can thermalize prior to escape, hence the range of Markovian initial states is additionally restricted by the condition $U_0 \ll (U_b - \beta^{-1})$.

4.3 Kramers approach

Assume that the conditions discussed in the previous section are fulfilled, and that the escape from the domain Δ can be adequately described by a Markovian rate process. The first passage time problem reduces then to the calculation of the escape rate.

The rich history[3] of the rate theory begins with the works of Van't Hoff (1884) and Arrhenius (1889), who studied the reaction-rate data as a function of the inverse temperature $\beta = (k_b\theta)^{-1}$. The dependence of the reaction rate κ on the temperature was found to have an activation-like form, known as the Van't Hoff-Arrhenius law:

$$\kappa = \nu \exp(-\beta U_b). \tag{4.30}$$

Here U_b denotes the activation energy, and ν is a prefactor. To explain this activation-like dependence, Arrhenius (1889) introduced the "hypothetical body", an activated reactant complex with energy U_b, and proposed the existence of thermal equilibrium between normal and active reactant molecules. The dependence of the prefactor ν on temperature and damping rate remained to be understood.

Quantitative progress in the rate theory came with advances in the theory of fluctuations. The first quantitative description of an activated rate process was given by Farkas (1927) in the study of homogeneous nucleation in supersaturated vapors. Kinetics of nucleation processes was further developed by Becker and Döring (1935) and Kuhrt (1951). Eyring (1935) considered a nonlinear decomposing molecule consisting of n atoms, and calculated the probability of the activated state using the ordinary statistical mechanics.

The major contribution was made by Kramers (1940), whose ideas laid the foundation of the modern rate theory. Kramers (1940) explained the escape mechanism as a noise-assisted reaction for the first time. Starting from the Fokker-Planck equation for the Brownian motion in a nonlinear potential, Kramers succeeded to calculate the escape rate as the ratio of a

---

[3] For exhaustive account of the history of rate theory see Hänggi et al. (1990).

quasistationary flux through the potential barrier and the population within the well. He separately treated the cases of weak, moderate and strong friction and obtained analytical expressions for the escape rate in these three regimes.

Since Kramers' landmark paper a lot of new insights and developments were acquired in rate theory. These include the generalization of Kramers theory to the multidimensional transition state theory in full phase space of all degrees of freedom (Pollak, 1986, 1990), the turnover between weak and strong friction, and stationary nonequilibrium rate theory (Hänggi et al., 1990). The rate theory found many applications in diverse fields of science. Recent experiments in nonlinear optics (Roy et al., 1985; James et al., 1988), condensed matter physics (Fulton and Dunkleberger, 1974; Turlot et al., 1989) and biology (Acar et al., 2005) can be accurately interpreted in terms of Kramers' rate theory.

4.3.1 Evaluation of escape rate

Kramers' escape rate can be calculated by means of several methods. The most common are the flux-over-population method, the methods of reactive flux, of lowest eigenvalue and of the mean first passage time (Hänggi et al., 1990). Here we consider an example of Brownian motion in a harmonic potential with an absorbing boundary at x_b. The potential barrier has a cusp form in this case (see Fig. 4.2) and the methods making explicit use of the parabolic approximation of the potential barrier cannot therefore be applied. To calculate the rate κ we use the flux-over-population method in the Smoluchowski and energy-diffusion limits and the mean FPT method in the moderate damping regime. The escape problem in a cusp shaped potential is of great practical importance for applications such as electron transfer reactions (Kuznecov and Ulstrup, 1999).

I. Escape in equilibrium system. We start our discussion with the simple transition state theory (TST), which is based on two assumptions: (i) the equilibrium state prevails throughout the entire system, and (ii) trajectories that have crossed the transition state once will never return and recross it. The first assumption states that all absorbing boundaries are removed and an equilibrium distribution is established between regions within and outside Δ. The second assumption is plausible if the system is treated as Hamiltonian with all degrees of freedom in a full phase space of the escaping particle and heat bath (multidimensional TST). The transition state is then a saddle point in the full phase space, and the classical system is very unlikely to return to the narrow bottleneck around the saddle point. If however the system is approximated in terms of only few degrees of freedom (simple TST), so that the transition state is a low-dimensional surface in a reduced phase space, then the probability of correlated recrossings of the transition state is high and the escape rate will be overestimated. Here we only consider the simple TST, which is often used as an upper bound estimate for the escape rate. For a review of the multidimensional TST we refer the reader to Hänggi et al. (1990).

In an equilibrium system, the rate of crossing the boundary δ is given by a stationary probability efflux across δ. In our example of a harmonic oscillator Eq. (4.22) with a boundary at x_b, the escape rate in the TST approximation, κ_{TST}, reads

$$\kappa_{\text{TST}} = \int_0^\infty vP(x_b, v)dv = \frac{\omega_0}{2\pi}\, e^{-\beta U_b}, \tag{4.31}$$

where $P(x, v)$ is the stationary probability density of the entire system. For a nonlinear potential $U(x)$, the Gaussian approximation for the stationary probability density within Δ is usually used, i.e. the potential is approximated by a parabolic well with the frequency $\omega_0^2 = U''(x)|_{x=0}$. In this approximation the escape rate is also expressed by Eq. (4.31), where U_b is the activation energy, i.e. the difference of $U(x)$ at the barrier and at the minimum of the potential: $U_b = U(x_b) - U(0)$.

The potential barrier enters the TST rate Eq. (4.31) only in form of the activation energy U_b through the exponential Arrhenius factor. The prefactor $\omega_0/2\pi$ describes the dynamics in the vicinity of the local attractor within Δ. Thus the TST rate disregards the form of the potential near the barrier. We have already mentioned that, if the noise intensity is low or moderate ($\beta U_b \gg 1$), κ_{TST} overestimates the true escape rate due to probable correlated recrossings of the transition state. For a vanishing noise intensity ($\beta U_b \to \infty$) trajectories approach the transition state extremely rarely, and particles thermalize prior to eventual return to the transition state. Therefore, for vanishing noise intensities, recrossings of the transition state are uncorrelated and κ_{TST} gives an accurate estimate for the escape rate. In the regime of strong noise ($\beta U_b \sim 1$), escape occurs from a nonequilibrium state and the first assumption (i) of the TST is violated. In this case the mean escape rate defined as the inverse mean FPT can exceed the TST estimate.

The result Eq. (4.31) was generalized by Rice (1945) to the case of arbitrary Gaussian differentiable processes. He obtained the mean frequency of upcrossings of a given level x_b by a stationary process $x(t)$, see Eq. (5.15). In the case of white noise the Rice frequency Eq. (5.15) coincides with the TST rate Eq. (4.31).

II. Escape in nonequilibrium system. The escape problem has an essentially nonequilibrium character: since particles are immediately absorbed at the boundary δ, the particle density outside Δ is zero, and thus considerably differs from the equilibrium distribution. In the following paragraphs we illustrate the mean FPT and the flux-over-population approaches, which assume a quasiequilibrium distribution within the domain Δ and the vanishing particle density outside Δ.

Mean first passage time. The complete formal solution to the mean FPT problem was given by Matkowsky and Schuss (1977) in form of the asymptotic expansion in small parameter D, being the noise intensity. The approach is based on the approximate solution of the equation (4.12a) with absorbing boundary condition Eq. (4.12b) in the limit $D \to 0$. For the special case of one-dimensional system with a boundary placed at x_b, the resulting expression for the escape rate κ_{MFPT}, which equals the inverse mean first passage time $\mathcal{T}_1$, reads in leading order of D:

$$\kappa_{\mathrm{MFPT}} = \frac{1}{\mathcal{T}_1} = \frac{\int_0^\infty dv \exp\left(-\beta\left[\frac{v^2}{2} + U(x_b)\right]\right)}{\int_{-\infty}^{x_b} dx \int_{-\infty}^{\infty} dv \left(-\beta\left[\frac{v^2}{2} + U(x)\right]\right)}. \tag{4.32}$$

Examination of expression Eq. (4.32) reveals that this result implies the formation of a stationary Maxwell-Boltzmann distribution within the domain Δ. The integral in the numerator of Eq. (4.32) is a stationary flux across x_b, and the denominator gives the population within the domain Δ. Note that, in the limit of vanishing noise, the equilibrium distribution of the entire system is concentrated in close vicinities of local attractors, hence within domain Δ it coincides with the local quasiequilibrium distribution except for normalization. The latter is provided by the denominator in Eq. (4.32). Therefore, in the limit of vanishing noise intensity, the rate κ_{MFPT} approaches the TST rate κ_{TST}.

Evaluating the integrals in Eq. (4.32) for the case of a harmonic potential yields for the escape rate

$$\kappa_{\mathrm{MFPT}} \;=\; \frac{\omega_0}{\pi\left[1+\operatorname{erf}\left(\sqrt{\beta U_b}\right)\right]}\; e^{-\beta U_b}. \tag{4.33}$$

This expression is valid for low noise intensities and turns into Eq. (4.31) for $\beta U_b \gg 1$.

Flux-over-population method. In strongly underdamped and strongly overdamped regimes the flux-over-population method can be used for the rate calculation in a cusp-shaped potential. The probability efflux J across the boundary δ is given by the product of the population N within Δ and the probability to escape per unit time, which is the escape rate κ. One assumes a stationary regime in a system subjected to the following nonequilibrium constraint: the particles are absorbed at the boundary δ and then reinjected into the domain Δ resulting in a stationary probability current. The escape rate κ is calculated as the stationary flux J divided by the population N, as the name of the method suggests:

$$\kappa \;=\; J/N. \tag{4.34}$$

Energy diffusion limit. Let us first concentrate on the underdamped regime. The escape process is governed by energy diffusion if the damping rate is sufficiently low ($\gamma\beta I_b < 1$). For the Langevin dynamics in Eq. (4.22), evolution of the corresponding probability density $P(E,t)$ in the energy space obeys the Fokker-Planck equation (compare with Eq. (4.25)):

$$\frac{\partial}{\partial t}P(E,t) \;=\; \gamma\frac{\partial}{\partial E}E\left[1+\beta^{-1}\frac{\partial}{\partial E}\right]P(E,t) \;=\; -\frac{\partial}{\partial E}J(E,t), \tag{4.35}$$

where $J(E,t)$ is the probability flux. In the stationary regime the time derivative $\partial_t P(E,t)$ vanishes. Integration of Eq. (4.35) under this condition provides for the arbitrary prescribed stationary flux J and the stationary energy distribution $P(E)$:

$$J \;=\; -\gamma E\beta^{-1}\left(\beta P(E)+\frac{\partial}{\partial E}P(E)\right). \tag{4.36}$$

This equation can be rewritten as

$$J \;=\; -\gamma E\beta^{-1}\, e^{-\beta E}\,\frac{\partial}{\partial E}\left(P(E)\, e^{\beta E}\right). \tag{4.37}$$

Integration of Eq. (4.37) over energies from E to U_b and using the absorbing boundary condition $P(U_b)=0$ yields for the stationary probability distribution:

$$P(E) = \frac{\beta J}{\gamma}\, e^{-\beta E}\int_E^{U_b}\frac{1}{E'}\, e^{\beta E'}\, dE'. \tag{4.38}$$

$P(E)$ has a singularity at $E=0$ due to the probability source concentrated at the potential minimum. However, for $\beta U_b \gg 1$ this singularity does not contribute to the population within the domain Δ. Indeed, for $\beta U_b \gg 1$ the main contribution to the integral in Eq. (4.38) comes from the region near the barrier. Therefore we can approximate[4] the factor in front of the exponential by U_b^{-1}. Evaluation of the integral and neglecting the terms ~ 1 as compared to $\exp(\beta U_b)$, leads to

$$P(E) = \frac{J}{\gamma U_b}\, e^{\beta U_b}\, e^{-\beta E}. \tag{4.39}$$

Finally, to obtain the population N within the domain Δ, the stationary probability distribution Eq. (4.39) should be integrated from 0 to U_b over energy: $N = \int_0^{U_b} P(E)dE$. Performing this integration and due to Eq. (4.34) we obtain the escape rate κ_{ED} in the energy diffusion limit:

$$\kappa_{\mathrm{ED}} = \gamma\beta U_b\, e^{-\beta U_b}. \tag{4.40}$$

This expression is valid if the activation energy significantly exceeds the thermal energy ($\beta U_b \gg 1$) and if the damping rate is low ($\gamma\beta I_b < 1$). Note that the rate κ_{ED} is equal to the inverse mean FPT $\mathcal{T}_1$ in Eq. (4.28), which was obtained by solving Eqs. (4.12a), (4.26) in the energy space, avoiding the calculation of the stationary distribution.

Smoluchowski limit. The evaluation of the escape rate in the overdamped limit ($\gamma \gg \omega_0$) is analogous to the energy diffusion limit. The probability density $P(x,t)$ for the one-dimensional overdamped dynamics given by the Langevin equation (4.14) obeys the Smoluchowski equation:

$$\frac{\partial}{\partial t}P(x,t) \;=\; \frac{1}{\gamma}\frac{\partial}{\partial x}\left[U'(x) + \frac{D}{\gamma}\frac{\partial}{\partial x}\right]P(x,t) \;=\; -\frac{\partial}{\partial x}J(x,t), \tag{4.41}$$

with $J(x,t)$ being the probability flux in the coordinate space. Assuming a stationary distribution, integration of Eq. (4.41) yields for the stationary flux J:

$$J \;=\; -\frac{1}{\gamma\beta}\, e^{-\beta U(x)}\, \frac{\partial}{\partial x}\left(P(x,t)\, e^{\beta U(x)}\right). \tag{4.42}$$

Particles arriving at x_b are immediately absorbed, hence $P(x_b,t) = 0$. Integration of Eq. (4.42) from x to x_b therefore leads to the stationary probability distribution $P(x)$ in the form:

$$P(x) = J\gamma\beta\, e^{-\beta U(x)} \int_x^{x_b} e^{\beta U(x')}\, dx'. \tag{4.43}$$

To evaluate the integral in Eq. (4.43) we again make use of the condition $\beta U_b \gg 1$ and note that the main contribution to the integral comes from the region near the barrier. Approximating[5] the potential near the barrier by a linear function $U(x) \approx U(x_b) - \omega_0^2 x_b(x - x_b)$, we obtain

$$P(x) = \frac{J\gamma}{\omega_0^2 x_b}\, e^{\beta U_b}\, e^{-\beta U(x)}. \tag{4.44}$$

---

[4] The same approximation was made in Eq. (4.26).

[5] The same approximation was made by evaluation of the outer integral in Eq. (4.16).

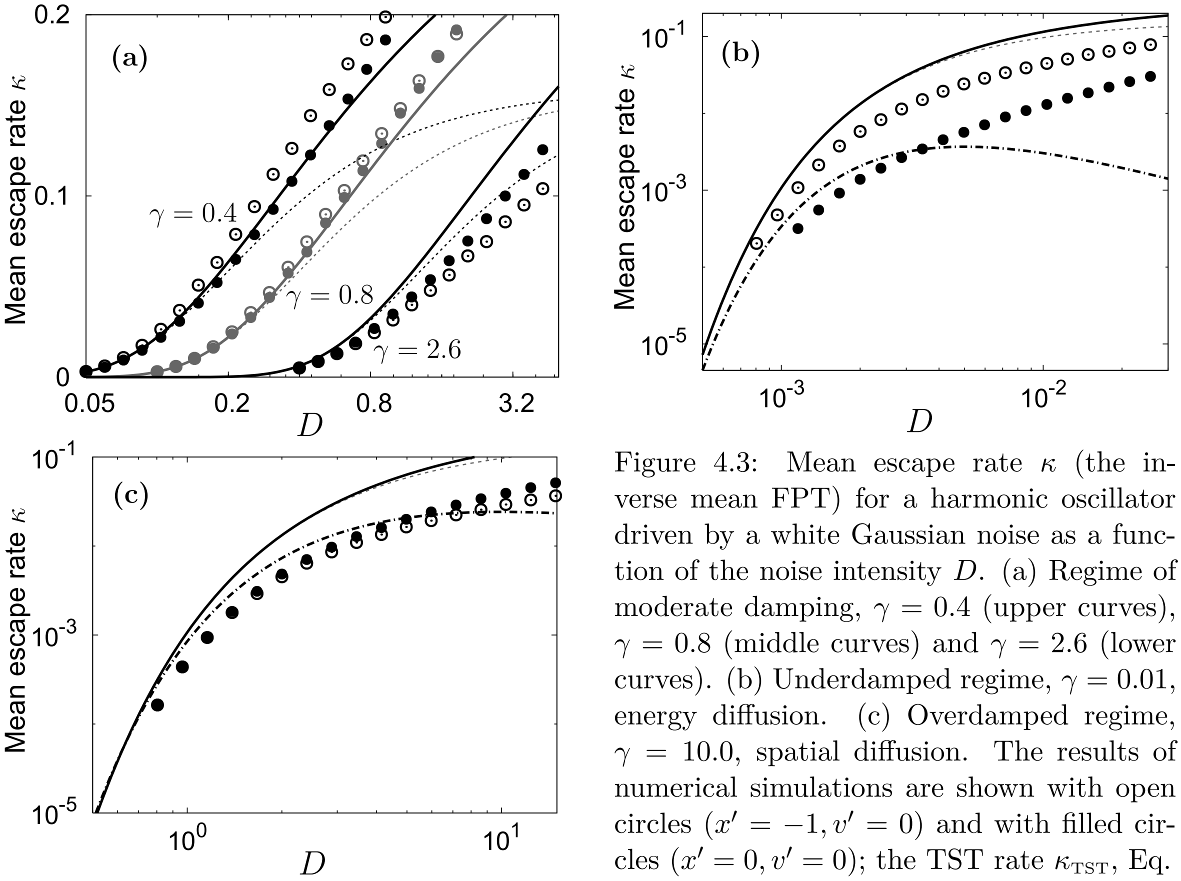

Figure 4.3: Mean escape rate κ (the inverse mean FPT) for a harmonic oscillator driven by a white Gaussian noise as a function of the noise intensity D. (a) Regime of moderate damping, $\gamma = 0.4$ (upper curves), $\gamma = 0.8$ (middle curves) and $\gamma = 2.6$ (lower curves). (b) Underdamped regime, $\gamma = 0.01$, energy diffusion. (c) Overdamped regime, $\gamma = 10.0$, spatial diffusion. The results of numerical simulations are shown with open circles ($x' = -1, v' = 0$) and with filled circles ($x' = 0, v' = 0$); the TST rate κ_{TST}, Eq. (4.31) with a dashed line, the mean FPT result κ_{MFPT}, Eq. (4.33) with a solid line; the energy-diffusion limited rate κ_{ED}, Eq. (4.40) and the Smoluchowski rate κ_{SM}, Eq. (4.45) are shown with dash-dot lines in (b) and (c), respectively. Other parameters are $\omega_0 = 1$ and $x_b = 1$. Note the logarithmic scale in (a) and the double logarithmic scale in (b) and (c).

Further integration of the stationary distribution Eq. (4.44) over the domain Δ provides the population $N = \int_{-\infty}^{x_b} P(x)dx$ within Δ and due to Eq. (4.34) the escape rate κ_{SM} in the Smoluchowski limit reads:

$$\kappa_{\mathrm{SM}} = \frac{\omega_0^2}{\gamma}\sqrt{\frac{\beta U_b}{\pi}}\, e^{-\beta U_b}. \tag{4.45}$$

This expression for the escape rate can be applied if the noise intensity is low ($\beta U_b \gg 1$) and the damping rate is high ($\gamma \gg \omega_0$). The rate κ_{SM} equals the inverse mean FPT given by Eq. (4.20), which was obtained without evaluating the stationary probability distribution.

In conclusion let us illustrate the applicability of different expressions for the escape rate using the example of a one-dimensional Brownian motion in a harmonic potential. We fix the frequency $\omega_0 = 1$ and the barrier position $x_b = 1$, and vary the damping rate γ and the noise intensity D. For these specific parameter values the validity condition for the rate description

$\beta U_b \gg 1$ reduces to $D \ll \gamma/2$. In numerical estimations of the escape rate we used two sets of initial conditions: (i) at the potential minimum ($x' = 0, v' = 0$) with zero initial energy $U_0 = 0$, and (ii) at ($x' = -1, v' = 0$) with initial energy U_0 equal to the activation energy U_b. Obviously, the mean FPT depends on initial conditions in the underdamped regime and for high noise intensities. Therefore, in simulations we determine the mean escape rate κ as the inverse mean FPT for given initial conditions.

Numerical results for the mean escape rate κ are shown in Fig. 4.3 with open circles ($x' = -1, v' = 0$) and with filled circles ($x' = 0, v' = 0$) as a function of the noise intensity D for different damping rates γ. In the case of moderate and strong friction (Figs. 4.3(a) and 4.3(c)) the mean escape rate does not depend on initial conditions for small D, and only for thermal energies comparable with the activation energy ($D > \gamma/2$) the escape rates for initial values (i) and (ii) differ. In the underdamped regime (Fig. 4.3(b)) the mean escape rates differ over the entire range of D. Indeed, for the initial values (ii) it holds $U_0 = U_b$ and, therefore, the condition for the independence of the mean FPT of the initial energy $U_0 \ll (U_b - \beta^{-1})$ is not fulfilled.

The TST estimate for the escape rate κ_{TST}, Eq. (4.31) is depicted with dashed lines in Fig. 4.3. The behavior of κ_{TST} is similar for low, moderate and strong friction: it is rather accurate for small noise intensities and overestimates the escape rate for moderate noise. For very strong noise ($\beta U_b \ll 1$) the TST rate saturates at $\omega_0/2\pi$, see Eq. (4.31), the time interval between two successive recrossings of x_b in the equilibrium system is in average equal to $T \sim 2\pi/\omega_0$. For low and moderate damping rates γ and strong noise, the escape occurs on the time scale of the half period of motion in the well $\sim \pi/\omega_0$, being smaller than T. Hence κ_{TST} underestimates the escape rate at high noise intensities in the moderate and low damping regimes, see Figs. 4.3(a) and 4.3(b). In the case of overdamped motion the characteristic time scale of the dynamics in the well is $\sim \gamma/\omega_0^2$, which exceeds T for sufficiently large γ. Therefore κ_{TST} overestimates the escape rate at high noise intensities in the overdamped regime, see Fig. 4.3(c).

The escape rate κ_{MFPT}, Eq. (4.33), obtained from solution of the mean FPT problem in the limit $D \to 0$, is depicted with solid lines in Fig. 4.3. At low noise intensities κ_{MFPT} provides accurate results for the escape rate, but becomes less precise for $D > \gamma/2$. For very strong noise ($\beta U_b \ll 1$) the rate κ_{MFPT} saturates at ω_0/π, see Eq. (4.33). By arguments analogous to those presented in the previous paragraph, for high noise intensities κ_{MFPT} remains rather accurate in the regime of moderate damping (Fig. 4.3(a)) and overestimates the escape rate in the overdamped regime (Fig. 4.3(c)). In the underdamped regime (Fig. 4.3(b)), where dependence on the initial conditions is crucial, both κ_{MFPT} and κ_{TST} perform well only for low noise intensities. Finally, for a vanishing noise intensity κ_{MFPT} tends to the TST rate κ_{TST}.

The energy diffusion limited rate κ_{ED}, Eq. (4.40) and the Smoluchowski rate κ_{SM}, Eq. (4.45) are shown with dash-dot lines in Figs. 4.3(b) and 4.3(c), respectively. The accuracy of these rate estimates is comparable with those of κ_{MFPT} in the limit of low noise intensity. For larger noise intensities ($\beta U_b \ll 1$) both κ_{ED} and κ_{SM} strongly underestimate the true escape rate. Indeed, as follows from Eqs. (4.40) and (4.45), the escape rates κ_{ED} and κ_{SM} unrealistically decrease with increasing noise intensity for $\beta U_b < 1$ in the energy diffusion limit and for

$\beta U_b < 1/2$ in the Smoluchowski limit.

To summarize, the rate description of an escape process is suitable only for low noise intensities $\beta U_b \gg 1$. The mean FPT approach retains its accuracy for larger noise intensities in the moderate damping regime. In the strongly underdamped regime, dependence on initial conditions is crucial, the reduced rate description is imprecise, and all rate estimations perform poorly.

4.3.2 Equivalence of mean first passage time and Kramers rate

In the previous section we derived Eqs. (4.40) and (4.45) for escape rate by means of the flux-over-population method, based on the evaluation of the stationary probability distribution in a nonequilibrium system. The resulting rates κ_{ED} and κ_{SM} are equal to the corresponding inverse mean FPT Eqs. (4.28) and (4.20), found from solution of the adjoint Fokker-Planck equation with absorbing boundary condition. This agreement is no coincidence: the inverse mean FPT is identical to the associated Kramers flux-over-population rate for an arbitrary Fokker-Planck process.

Indeed, consider the escape process from domain Δ with the boundary δ for an arbitrary multidimensional Fokker-Planck process. Assume that a stationary regime is established in a system subjected to a nonequilibrium constraint: particles are started at x' within Δ and immediately absorbed once they reach the boundary δ, then particles are reinjected at x' resulting in a stationary probability flux J. The stationary Fokker-Planck equation with a probability source of strength q at x' and probability sinks at δ reads

$$-\,q\,\delta(x-x') = L_x P(x,x') = -\frac{\partial}{\partial x} J(x,x'), \qquad x \in \Delta, \tag{4.46a}$$

$$P(x,x') = 0, \qquad x \in \delta. \tag{4.46b}$$

Here x denotes the whole set of variables in which the stochastic process is Markovian, $P(x,x')$ is the multidimensional stationary probability density, $J(x,x')$ is the probability flux density, and $\delta(x-x')$ is a multidimensional delta-function.

Integration of Eq. (4.46a) over domain Δ and using the Gauss theorem, leads to the expression for the strength q of the source:

$$q = \int_\delta J(x,x')ds, \tag{4.47}$$

where ds denotes the differential surface element of the boundary δ.

Further, multiplying Eq. (4.46a) by the mean FPT $\mathcal{T}_1(x)$ and integrating over Δ, we obtain

$$-\,q\,\mathcal{T}_1(x') = \int_\Delta \mathcal{T}_1(x) L_x P(x,x')dx. \tag{4.48}$$

If we change to the adjoint Fokker-Planck operator on the right hand side of Eq. (4.48), due to Eqs. (4.12a) and (4.47) we arrive at

$$\mathcal{T}_1(x') \;=\; \frac{\int_\Delta\, P(x,x')\,dx}{\int_\delta\, J(x,x')\,ds}. \tag{4.49}$$

Hence, the mean first passage time is expressed as the ratio of the population within Δ and the total outgoing flux across the boundary δ, and is formally equivalent to the inverse Kramers escape rate. Note, that Eq. (4.49) is a valid expression irrespective of whether Δ is a domain of attraction nor whether the noise intensity is small. However, only under these assumptions $\mathcal{T}_1(x')$ is independent of the initial conditions x', and the rate description of the escape process is applicable.

The Equivalence of the mean FPT and Kramers escape rate for an arbitrary time-homogeneous process (not necessary a Fokker-Planck process) was proven by Reimann et al. (1999).

Summary

Escape processes out of a prescribed domain Δ are ubiquitous with many applications in modern physics, chemistry and biology. Calculation of the first passage time to the boundary δ of the domain Δ is in general a nontrivial problem, and exact expressions for the FPT density are known only for few cases.

The problem is considerably simplified in Markovian models, where the mean FPT does not depend on initial conditions. The escape rate in Markovian models is independent of the age of the decaying state and the first passage time is exponentially distributed for times beyond the local relaxation time within Δ. The escape process follows a two stage scheme: first a local quasiequilibrium distribution is formed within Δ, then escape proceeds from this quasiequilibrium state with a constant rate. A Markovian escape process is parameterized by a single number, the constant rate.

The escape process can be treated as Markovian in good approximation, if Δ is a local domain of attraction and the fluctuation strength is low as compared with the activation energy. For underdamped dynamics, in addition, the energy of injected particles should be sufficiently low. In this case, the mean FPT is equivalent to Kramers rate and can be evaluated without explicit solution of the adjoint equation, for example, using the flux-over-population method.

Though many experimental situations can be accurately interpreted in terms of a rate process with a time-independent rate, for many realistic applications (e.g. underdamped resonant neurons) the dependence of the first passage time on initial conditions is crucial. In such non-Markovian models the rates are time-dependent, the FPT densities have complex structures and a Markovian rate description is not suitable. Chapter 5 is devoted to the analytical treatment of non-Markovian escape processes with complex multimodal FPT densities.

5

First passage time densities in non-Markovian models

In Chapter 4 we discussed a Markovian escape of a stochastic process $x(t)$ from a domain Δ of its phase space. This kind of description is suitable for overdamped systems at low noise intensities, when the local relaxation time t_{rel} is much smaller than the typical escape time. Initially a local quasiequilibrium is established within Δ. The escape occurs then from this quasiequilibrium state with a constant rate κ, inversely proportional to the mean FPT. The problem is independent of the detailed initial state and the time the trajectory has spent inside Δ. For times T larger than t_{rel} the FPT probability density decays exponentially: $\mathcal{F}(T) \sim \exp(-\kappa T)$. Well known examples are chemical systems and nucleation processes, where the rates determine the mean velocity of chemical reactions or of forming overcritical nuclei (Hänggi et al., 1990; Nicolis and Prigogine, 1989). Another example are the leaky integrate-and-fire and similar neuron models, for which the corresponding trajectories approach the stable rest state quickly after the reset (Tuckwell, 1988; Lindner et al., 2004).

If the time scale separation between relaxation and escape does not hold, the escape can occur prior to formation of the local quasiequilibrium and the rates are time dependent. The first passage time then depends sensitively on initial conditions and the FPT densities have a complex shape different from an exponential decay. This situation is encountered in the presence of metastable states, where the mean FPT dramatically depends on the initial conditions and effects like the noise enhanced stability emerge (Fiasconaro et al., 2003, 2005). Another example is pertinent to short time scales $T < t_{rel}$, which attracts a growing interest because of recent experiments studying chemical reactions on time scales down to femtoseconds (Diau et al., 1998). In theoretical studies of an underdamped potential system staying initially at the bottom of the well, the flux over the boundary was found to grow in a stepwise manner before formation of the local quasiequilibrium (Soskin et al., 2001). Another interesting example are resonant neurons, which exhibit subthreshold oscillations with relaxation time exceeding the mean interspike interval. In Chapter 3 we showed, that

---

This chapter is adopted from Verechtchaguina et al. (2006a,b).

interspike interval densities obtained from the output of a resonant neuron have a multimodal structure and contain the entire information about the neuron dynamics in the case, that the renewal assumption holds. The Markovian approaches to the FPT problem discussed in Chapter 4 fail to reproduce the complex structure of the FPT densities, which is characteristic for non-Markovian models with nonequilibrium initial conditions.

The FPT density can be obtained from the solution of the adjoint Fokker-Planck equation with absorbing boundary in many dimensions, where auxiliary degrees of freedom, e.g. velocity degrees of freedom, result from the Markovian embedding of a non-Markovian process (Hänggi et al., 1990). However, even the calculation of the mean FPT for a non-Markovian process $x(t)$ is a rather complicated task, since the corresponding boundary problem cannot be treated in a straightforward way, but must be handled with care to prevent a backflow of probability through the hidden channels (Doering et al., 1987; Hänggi et al., 1988).

Another method, which can be used to obtain the FPT density on time scales preceeding the local relaxation time, is the method of optimal fluctuation (Graham and Tél, 1986; Dykman et al., 1992; Soskin, 1999, 2006). In the low-noise limit the time dependent flux $J(T)$ through the absorbing boundary has a characteristic activation-like dependence on the noise intensity D: $J(T) \sim P\exp(-S_a/D)$. The dependence of the prefactor P on time and noise intensity is assumed to be much weaker than that of the activation factor and is neglected. The activation energy S_a can be shown to be the minimum of a certain functional $S_a = S_{min}(T)$ (Soskin, 1999). The path minimizing $S_{min}(T)$ is referred to as the most probable escape path, giving the name to this approach. The method of optimal fluctuation provides a time dependent solution to the FPT problem with logarithmic accuracy in the case of weak noise, when the activation-like dependence of the flux J is a good approximation. However, the generalization of this method to nonpotential systems and the calculation of the prefactor P remains an open problem.

An alternative approach to the FPT problem is based on the theory of level-crossings (Rice, 1945), which lays the foundation for our subsequent work. Suppose that the absorbing boundary is replaced with a transparent one, then a random process $x(t)$ can recross x_b many times. The FPT density for $x(t)$ is related to the waiting-time density for a point process formed by the times, when $x(t)$ crosses the level x_b. The joint densities of multiple level crossings can be obtained in the case of differentiable trajectories. The general theory of level crossings was originally developed by Rice (1945). He derived an expression for the probability density of the recurrence time for a stationary random process to a given level in the form of series of multiple integrals over the joint densities of level crossings. This series is referred to as the Wiener-Rice series in Siegert (1951), where it was derived from the generalized renewal equation. Stratonovich (1967) discussed the Wiener-Rice series in connection with the peak duration of random functions and derived a closed analytical approximation for this series in the case of nonapproaching level crossings. Another analytical approximation was suggested in Gammaitoni et al. (1991). Is is based on the less stringent assumption that the sequence of level crossings is stationary and provides an approximate expression for the Laplace transform of the recurrence time density. The exact expression for the first passage time probability density Eq. (5.6) is analogous to the Wiener-Rice series and was proven by Fomin (1980). We proceed to give a much more elementary derivation of Eq. (5.6), which serves as the main instrument for our further investigations. We discuss several analytical approximations for Eq. (5.6), which proof to be very effective in a broad range of non-Markovian FPT problems and, at the same time, are simple enough to be used in applications.

This chapter is structured as follows. In Section 5.1 we present the general exact expressions for the FPT density in form of the Wiener-Rice series. Several analytical approximations for this series, based either on truncations or on the decoupling of correlations, are discussed in Section 5.2. We examine the quality of these approximations by applying them to a harmonic oscillator with the threshold and reset driven by a white Gaussian noise. Section 5.3 illustrates the applicability of these approximations to high-dimensional FPT problems, using the Ornstein-Uhlenbeck and harmonic noise driving as examples. Finally, a semi-analytical approach to the FPT density for a nonlinear non-Markovian system is suggested in Section 5.4. This approach combines analytical approximations with a numerical solution of the Fokker-Plank equation and is applied to the resonant FitzHugh-Nagumo model, in order to calculate the interspike interval density.

5.1 Counting level crossings

We start with the derivation of the general expression (5.6) for the first passage time density of a differentiable random process $x(t)$.

First consider the probability $n_1(x_b, t|x_0, v_0)dt$ that a continuous differentiable process $x(t)$ crosses the level x_b in the time interval between t and $t+dt$ with positive velocity $v(t) = \dot{x}(t) > 0$ under initial conditions $x(0) = x_0, \dot{x}(0) = v_0$. Generally the whole set of variables resulting from the Markovian embedding of $x(t)$ should be given at $t = 0$. For simplicity we consider the two-dimensional dynamics. The generalization to higher dimensional systems is obvious and will be discussed in Section 5.3. Crossing the level with positive velocity will be referred to as an *upcrossing* throughout the following text.

If $x(t)$ crosses the level x_b within time interval $(t, t + dt)$ with velocity $v > 0$, then the value of the coordinate at time t should lie within the interval $x_b - vdt < x(t) < x_b$, see Fig. 5.1. The probability that $x(t)$ is in this interval equals $\int\limits_{x_b - vdt}^{x_b} P(x, v, t|x_0, v_0, 0)dx = |v|P(x_b, v, t|x_0, v_0, 0)dt$. Since the velocity value at the instant of crossing is positive but otherwise arbitrary, one obtains the probability of an upcrossing by integration over all positive values of v:

$$n_1(x_b, t|x_0, v_0, 0) = \int\limits_0^{\infty} vP(x_b, v, t|x_0, v_0, 0)dv. \tag{5.1}$$

The density $n_1(x_b, t|x_0, v_0, 0)$ is the probability of an upcrossing per unit time. It is a rate of upcrossings rather than a probability density. The function $n_1(x_b, t|x_0, v_0, 0)$ is therefore not normalized. Eq. (5.1) can be simply generalized to give expressions for the joint densities of multiple upcrossings. The probability $n_p(x_b, t_p; \ldots; x_b, t_1|x_0, v_0, 0)dt_p \ldots dt_1$, that the process $x(t)$ crosses the level x_b in each of the p time intervals $(t_1, t_1+dt_1), \ldots, (t_p, t_p+dt_p)$ (Fig. 5.2) is given by:

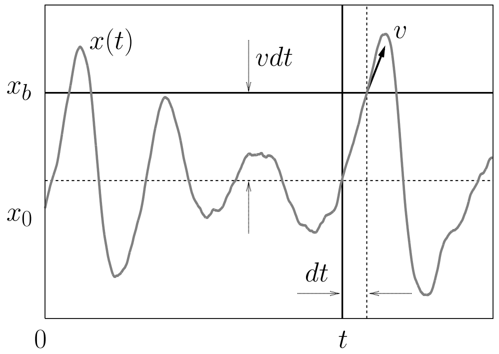

Figure 5.1: Random process $x(t)$ crosses the level x_b between t and $t + dt$ with positive velocity v. The value of x at time t is in interval $x_b - vdt < x(t) < x_b$.

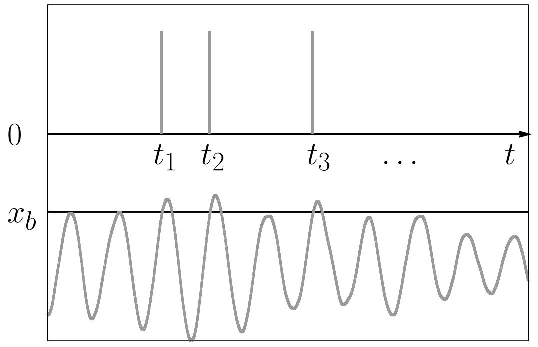

Figure 5.2: Times, when a random process $x(t)$ performs upcrossings of x_b, form a point process $t_1, t_2, t_3 \ldots$.

$$n_p(x_b, t_p; \ldots; x_b, t_1 | x_0, v_0, 0) = \int\limits_0^\infty dv_p \ldots \int\limits_0^\infty dv_1 v_p \ldots v_1 P(x_b, v_p, t_p; \ldots; x_b, v_1, t_1 | x_0, v_0, 0). \quad (5.2)$$

For clarity, in the following we omit x_b and the initial conditions in expressions for the joint densities of upcrossings. The transition probability densities are connected to the joint probability densities of x and v according to Bayes' theorem:

$$P(x_p, v_p, t_p; \ldots; x_b, v_1, t_1 | x_0, v_0, 0) = \frac{P_{2p+2}(x_p, v_p, t_p; \ldots; x_b, v_1, t_{;} x_0, v_0, 0)}{P_2(x_0, v_0, 0)}. \quad (5.3)$$

Our aim is to calculate the first passage time probability density $\mathcal{F}(T)$, that is the fraction of all trajectories starting from the initial point x_0 with initial velocity v_0 which perform the *first* upcrossing of the level at time T. All such trajectories are accounted for in the density $n_1(T)$ (see the upper panel in Fig. 5.3). However, $n_1(T)$ also accounts for trajectories for which the upcrossing at the time T was not the first one, i.e. which had a previous upcrossing at an earlier time $t_1 < T$ (panel 2 in Fig. 5.3). Such trajectories should not contribute to $\mathcal{F}(T)$, and therefore we should subtract their fraction from $n_1(T)$. Taking into account that t_1 can be arbitrary between 0 and T, we obtain:

$$n_1(T) - \int\limits_0^T n_2(T, t_1) dt_1. \quad (5.4)$$

This excludes all trajectories crossing x_b exactly twice until T. However, Eq. (5.4) does not fully solve the problem, since trajectories crossing x_b three times, i.e at time T and at

	$+n_1(T)$	$-\int\limits_0^T n_2(T,t_1)dt_1$	$+\frac{1}{2!}\int\limits_0^T\int\limits_0^T n_3(T,t_2,t_1)dt_2dt_1$	$-\frac{1}{3!}\int\limits_0^T\int\limits_0^T\int\limits_0^T n_4(T,t_3,t_2,t_1)dt_3dt_2dt_1$
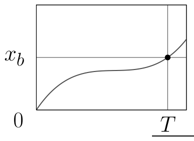	+1			
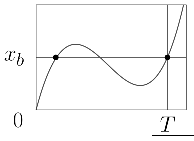	+1	-1		
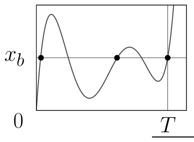	+1	-2	+1	
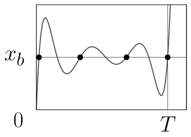	+1	-3	+3	-1

...

Figure 5.3: Counting level crossings. The N-th row corresponds to trajectories with exactly N upcrossings. The p-th column corresponds to the p-th term of the sum Eq. (5.6). The numbers show how many times a trajectory with exactly N upcrossings is accounted for in the p-th term. Sum of all numbers in every row is exactly zero.

two earlier moments $t_i < T, i = 1,2$ (row 3 in Fig. 5.3), are not accounted for correctly. Each such trajectory is counted once in $n_1(T)$. The second term in Eq. (5.4) accounts for the pairs of upcrossings at T and at some $t_i < T$. Each trajectory with two additional upcrossings at $t_i < T, i = 1,2$ is therefore subtracted twice in $\int_0^T n_2(T,t_1)dt_1$. Such trajectories should not contribute to $\mathcal{F}(T)$: in Eq. (5.4) we subtracted too much and have to add the amount of trajectories with three upcrossings at times $0 < t_i < T, i = 1,2$ and T again:

$$n_1(T) - \int\limits_0^T n_2(T,t_1)dt_1 + \frac{1}{2!}\int\limits_0^T\int\limits_0^T n_3(T,t_2,t_1)dt_1dt_2. \tag{5.5}$$

The factor 1/2! in the last term accounts for the number of permutations of variables t_i.

Generally, if a trajectory crosses the level at time T and at N earlier times $t_i < T, i = 1,\ldots,N$, then in $\frac{1}{p!}\int\ldots\int n_{p+1}(T,t_p,\ldots,t_1)dt_1\ldots dt_p$ it is accounted for exactly C_N^p times (C_N^p stands for the number of combinations). Note, that $\sum\limits_{p=0}^{N}(-1)^p C_N^p = (1-1)^N = 0$. Thus in the alternating sum of the type Eqs. (5.4) and (5.5) containing $N+1$ terms, all trajectories crossing x_b at time T and having $i = 1,2,\ldots,N$ additional upcrossings are excluded, however those with a larger number of upcrossings are not accounted for correctly. Extending the sum to infinity we exclude all superfluous trajectories, and only trajectories with the first upcrossing at time T remain. The expression for the first passage time probability density reads:

$$\mathcal{F}(T) = \sum_{p=0}^{\infty} \frac{(-1)^p}{p!} \int_0^T \dots \int_0^T n_{p+1}(T, t_p, \dots, t_1) dt_p \dots dt_1. \tag{5.6}$$

If we express the joint densities of upcrossings using the joint probability densities of x and v given by Eqs. (5.2) and (5.3), we obtain:

$$\mathcal{F}(T) = \frac{1}{P_2(x_0, v_0, 0)} \sum_{p=0}^{\infty} \frac{(-1)^p}{p!} \int_0^T \dots \int_0^T dt_p \dots dt_1 \int_0^\infty \dots \int_0^\infty dv dv_1 \dots dv_p$$
$$v v_1 \dots v_p P_{2p+4}(x_b, v, T; x_b, v_p, t_p; \dots; x_b, v_1, t_1; x_0, v_0, 0).$$

Eq. (5.6) connects $\mathcal{F}(T)$, i.e. the solution of the FPT problem with absorbing boundary at x_b, with all joint densities of upcrossings for the freely evolving process. To obtain $n_p(t_p, \dots, t_1)$ we consider trajectories, which are not absorbed at x_b, but can return after an upcrossing and then cross x_b again and again. The correct combination of all these densities of multiple level crossings results in the probability density for the first upcrossing.

The times, when a random process $x(t)$ performs upcrossings of the level x_b, form a point process, as sketched in Fig. 5.2. The distribution functions of this point process,

$$n_1(t_1), \qquad n_2(t_2, t_1), \qquad n_3(t_3, t_2, t_1), \qquad \dots, \tag{5.7}$$

are the joint densities of upcrossings and can be obtained using Eq. (5.2). Since $x(t)$ has a finite velocity, the interval between two upcrossings cannot be arbitrary small and therefore $n_p(t_p, \dots, t_1)$ vanishes if two of its arguments coincide. Such a point process is called a *system of nonapproaching random points* (Stratonovich, 1967). Results from the theory of point processes reviewed in Section 2.3 can be applied to obtain the FPT density $\mathcal{F}(T)$. In this context $\mathcal{F}(T)$ is the waiting-time density for the corresponding point process, and Eq. (5.6) follows immediately from Eq. (2.37).

In Section 2.3 it was shown, that a point process can be completely characterized by its cumulant functions (see Eqs. (2.29) and (2.30)):

$$\begin{aligned} g_1(t_1) &= n_1(t_1), \\ g_2(t_2, t_1) &= n_2(t_2, t_1) - n_1(t_1) n_1(t_2), \\ g_3(t_3, t_2, t_1) &= n_3(t_3, t_2, t_1) - 3\{n_1(t_1) n_2(t_3, t_2)\}_s + 2 n_1(t_1) n_1(t_2) n_1(t_3), \dots . \end{aligned} \tag{5.8}$$

and that the waiting-time density $\mathcal{F}(T)$ can be expressed in terms of these cumulant functions (see Eqs. (2.34),(2.36)) as

$$\mathcal{F}(T) = S'(T) e^{-S(T)} \tag{5.9}$$

with

$$S(T) = -\sum_{p=1}^{\infty} \frac{(-1)^p}{p!} \int_0^T \dots \int_0^T g_p(t_p, \dots, t_1) dt_p \dots dt_1. \tag{5.10}$$

The equations (5.6) and (5.9), (5.10) together with Eq. (5.2) express the first passage time density for a non-Markovian differentiable random process $x(t)$. The function $\Phi(T) = \exp[-S(T)]$ is the survival probability (see Eq. (4.1)) and $\kappa(T) = S'(T)$ is the time-dependent escape rate (see Eqs. (4.4), (4.5)).

These are the exact results for the FPT probability density of any continuous differentiable random process. We proceed to show, that Eqs. (5.6) and (5.9), (5.10) can be the starting point for several approximations. As it is often in the case of infinite series, useful approximations are based either on truncation of the series after several leading terms evaluated exactly, or on approximation of higher order terms using the lower order terms, which might lead to a closed analytical form. The truncation approximations for Eq. (5.6) are not normalized, hold only on short time scales, and diverge at longer times (due to the miscount of trajectories with several upcrossings. The approximations of the second type are based on a sub-summation in Eq. (5.10) for $S(T)$. They are normalized and can be used in the whole time domain. Note, that only the approximations guaranteeing positive rates $S'(T)$ are reasonable. Thus, the set of possible approximations for the series Eq. (5.10) is rather restricted.

5.2 Analytical approximations for the first passage time density

In this section we discuss several approximations to the Wiener-Rice series for the FPT density, Eqs. (5.6) and (5.9), (5.10). The applicability of approximations is illustrated using a harmonic oscillator with the threshold and reset as an example.

5.2.1 Noise driven harmonic oscillator

To examine the quality of the approximations, we apply them to a simple non-Markovian dynamics. The model we have in mind is the resonate-and-fire model of a neuron introduced in Section 2.1.3. For simplicity we neglect the absolute refractory time. Under this assumption the model is equivalent to a harmonic oscillator with the threshold and reset. By time scale and variable transformations we change to dimensionless parameters and variables. The dynamics of the voltage variable $x(t)$ is then given by:

$$\begin{aligned} \dot{x} &= v, \\ \dot{v} &= -\gamma v - \omega_0^2 x + \sqrt{2D}\xi(t). \end{aligned} \tag{5.11}$$

Here $\gamma > 0$ is the friction coefficient and $\xi(t)$ is a white Gaussian noise of unit intensity. We fix the frequency $\omega_0 = 1$, choose initial conditions for x and its velocity v to be $x_0 = -1, v_0 = 0$ and set the threshold at $x_b = 1$.

The system possesses the only stable fixed point $x = 0, v = 0$ with eigenvalues $-\gamma/2 \pm \sqrt{\gamma^2/4 - \omega_0^2}$. In the underdamped regime, $\gamma < 2\omega_0$, the eigenvalues are complex, i.e. the fixed point is a focus and $x(t)$ shows subthreshold oscillations. In the overdamped regime, $\gamma > 2\omega_0$, the fixed point is a node with real eigenvalues.

In the absence of threshold and reset all joint probability densities of x and v are Gaussian due to the linearity of Eq. (5.11) and have the form (Risken, 1989):

$$P_n(\vec{Q}) = \frac{1}{(2\pi)^{n/2}\sqrt{\det \hat{C}_n}} \exp\left(-\frac{\vec{Q}\hat{C}_n^{-1}\vec{Q}}{2}\right). \tag{5.12}$$

Here $\vec{Q} = (q_1(t_1), \ldots, q_n(t_n))$ is an n-dimensional vector, whose i-th component is the value of coordinate $x(t_i)$ or of velocity $v(t_i)$ at the moment t_i. $\hat{C}_n$ is the symmetric $n \times n$ correlation matrix, whose elements c_{ij} are the correlation functions between the corresponding components of the vector $\vec{Q}$: $c_{ij} = c_{ji} = \langle q_i(t_i) q_j(t_j)\rangle$.

The correlation functions for Eq. (5.11) are easily obtained using the Fourier transformation and the Wiener-Khinchin theorem (Risken, 1989). In the underdamped regime

$$r_{xx}(t) = \langle x(t')x(t'+t)\rangle = \frac{D}{\gamma\omega_0^2} e^{-\frac{\gamma}{2}|t|}\left(\frac{\gamma}{2\Omega}\sin(\Omega|t|) + \cos(\Omega|t|)\right), \tag{5.13}$$

with $\Omega = \sqrt{|\omega_0^2 - \gamma^2/4|}$. In the overdamped case the expression for $r_{xx}(t)$ is the same, except the trigonometric functions are replaced by their hyperbolic counterparts. Further, $r_{xv}(t) = r'_{xx}(t)$ and $r_{vv}(t) = -r''_{xx}(t)$.

The rate of upcrossings $n_1(T)$ is obtained from Eqs. (5.1), (5.12) and (5.13) in a closed analytical form:

$$n_1(T) = \frac{\sigma_x\sigma_v}{2\pi\mu_{22}\sqrt{\det \hat{C}_4}} \exp\left[\frac{\sigma_x^2 v_0^2 + \sigma_v^2 x_0^2}{2\sigma_x\sigma_v}\right] \times \\ \exp\left[-\frac{1}{2}\sum_{i,j\neq 2} \mu_{ij} q_i q_j\right]\left[1 - \sqrt{\pi}\alpha e^{\alpha^2}\operatorname{erfc}(\alpha)\right]. \tag{5.14}$$

Here $\mu_{ij} = \mu_{ji}$ are the elements of the inverse correlation matrix $(\hat{C}_4)^{-1}$ and q_i are the components of the vector $\vec{Q} = (x(T), v(T), x_0(0), v_0(0))$, the variances of x and v are $\sigma_x^2 = r_{xx}(0) = D/\gamma\omega_0^2$ and $\sigma_v^2 = r_{vv}(0) = D/\gamma$, and $\operatorname{erfc}(x)$ is the complementary error function. We also introduced $\alpha = (\sum_{i\neq 2}\mu_{2i}q_i)/\sqrt{2\mu_{22}}$.

For the joint densities of multiple upcrossings $n_p(t_p, \ldots, t_1)$ no closed expression can be obtained. Therefore, we evaluate the integral over v_1 in Eq. (5.2) analytically and then perform a numerical integration of the resulting expression over $v_2, \ldots, v_p$ to obtain $n_p(t_p, \ldots, t_1)$. The integrals over time in the expression for $\mathcal{F}(T)$ are evaluated numerically as well.

In conclusion, let us discuss the time scales, which characterize the system dynamics. The first characteristic time scale corresponds to the mean frequency of upcrossings for a stationary process $n_0 = \lim_{t\to\infty} n_1(t)$, also known as the *Rice frequency* (Rice, 1945). It is equivalent to the TST estimate for the escape rate, Eq. (4.31). The Rice frequency can be found from Eq. (5.1) with $P(x_b, v, t|x_0, v_0, 0)$ replaced by the stationary probability density $P_{st}(x_b, v)$. The general expression for n_0 reads (Cramér and Leadbetter, 1968)

$$n_0 = \frac{1}{2\pi}\left(-\frac{r''_{xx}(0)}{r_{xx}(0)}\right)^{1/2} \exp\left(-\frac{x_b^2}{2r_{xx}(0)}\right). \tag{5.15}$$

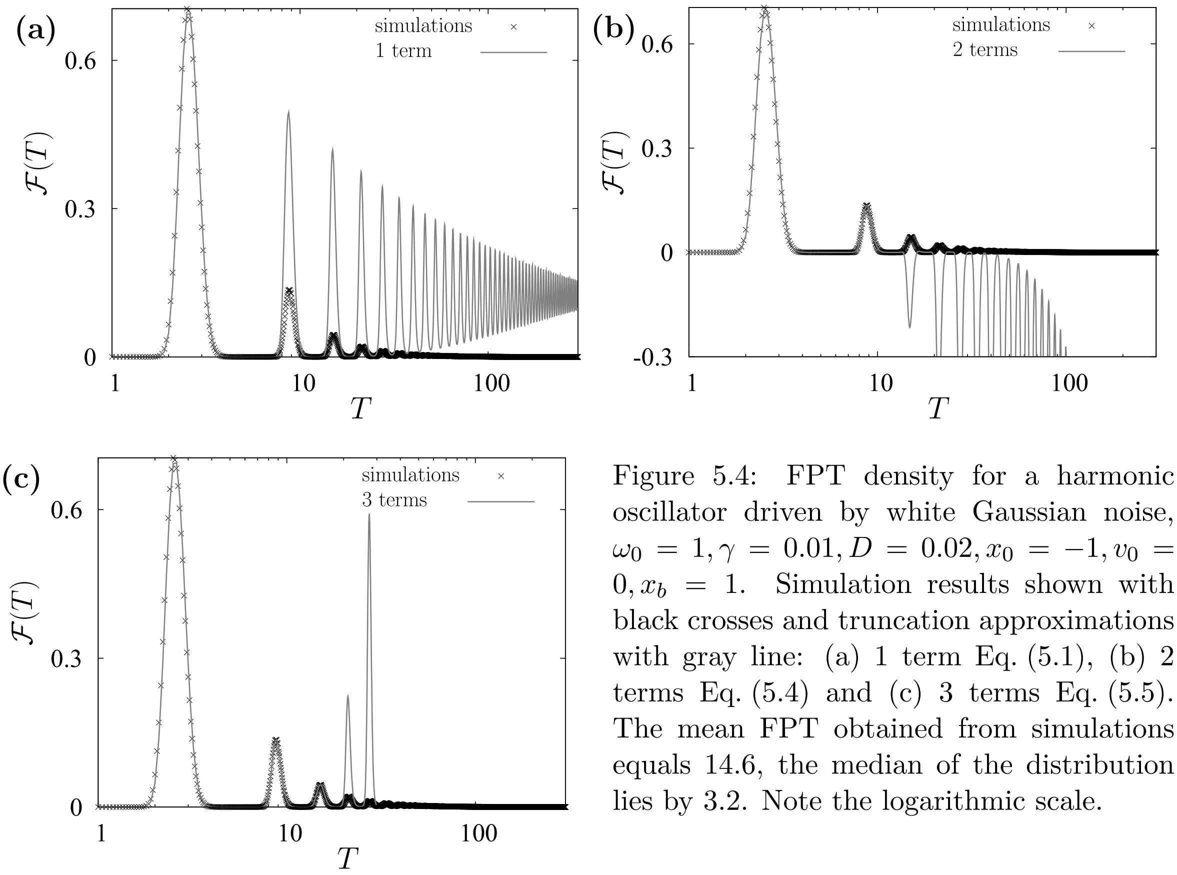

Figure 5.4: FPT density for a harmonic oscillator driven by white Gaussian noise, $\omega_0 = 1, \gamma = 0.01, D = 0.02, x_0 = -1, v_0 = 0, x_b = 1$. Simulation results shown with black crosses and truncation approximations with gray line: (a) 1 term Eq. (5.1), (b) 2 terms Eq. (5.4) and (c) 3 terms Eq. (5.5). The mean FPT obtained from simulations equals 14.6, the median of the distribution lies by 3.2. Note the logarithmic scale.

In the case of a harmonic oscillator driven by white noise $n_0 = (\omega_0/2\pi)\exp\left(-\gamma x_b^2 \omega_0^2/2D\right)$. In the stationary regime the mean interval T_R between two successive upcrossings is given by the inverse Rice frequency $T_R = 1/n_0$.

Another characteristic time scale is given by the local relaxation time t_{rel} and describes the decay of correlations in the system. The correlation functions for a harmonic oscillator decay exponentially with a characteristic time scale $t_{rel} = 2/\gamma$. Finally, in the underdamped regime there is an additional time scale, the period of subthreshold oscillations $T_p = 2\pi/\sqrt{\omega_0^2 - \gamma^2/4}$.

5.2.2 Truncation approximations

Here we discuss approximations for the FPT density, obtained by a simple truncation of the series in Eq. (5.6). Since $x(t)$ has a finite velocity, it crosses x_b only a finite number of times during the finite time interval T. Therefore, for small times T, the higher order terms in the series Eq. (5.6) are negligible, and the first few terms yield a good approximation for $\mathcal{F}(T)$.

The first approximation is given by the first term $n_1(T)$, the second approximation by two terms, Eq. (5.4), and the third by three terms, Eq. (5.5). The higher order approximations entail a numerical estimation of high-dimensional integrals, which at some stage leads to a computational effort larger than that required for a direct simulation. Therefore we restrict

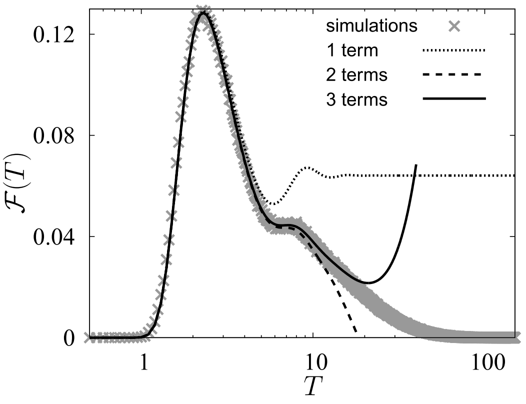

Figure 5.5: FPT density for a harmonic oscillator driven by white Gaussian noise, $\omega_0 = 1, \gamma = 0.8, D = 0.44, x_0 = -1, v_0 = 0, x_b = 1$. Simulation results are plotted with gray crosses; 1 term truncation with a dot line, 2 terms truncation with a dashed line, and 3 terms truncation with a solid line. The mean FPT obtained from simulations equals 13.1, the median of the distribution lies by 9.1. Note the logarithmic scale.

ourselves to the 1-, 2- and 3- terms approximations.

First, consider the case of small friction and intermediate noise intensity, for example choose $\gamma = 0.01$, $D = 0.02$. The first passage time density $\mathcal{F}(T)$ obtained from simulations for those parameter values is depicted with black crosses in Fig. 5.4. The correlation functions of the process oscillate with period T_p and decay slowly within the relaxation time t_{rel}. A typical trajectory is smooth and shows almost regular oscillations with fluctuating phase and amplitude. The probability to reach x_b is high in the maxima of the subthreshold oscillations, and the initial phase of these oscillations is fixed by sharp initial conditions. Thus on shorter time scales $\mathcal{F}(T)$ shows multiple peaks[1] following with the frequency of damped oscillations Ω. For larger times $T \gg t_{rel}$ a quasiequilibrium distribution establishes below the threshold and the FPT density decays exponentially. The number of visible peaks depends on the ratio of t_{rel} and the period of oscillations T_p and is given by the number of periods elapsed before the quasiequilibrium is formed. For parameter values as in Fig. 5.4 $t_{rel} = 200$, which corresponds to about 30 periods $T_p = 6.28$.

The result of the 1 term approximation is shown in Fig. 5.4(a) by the gray line. The first peak of the FPT density is reproduced almost exactly. All further peaks are overestimated, because all trajectories performing multiple upcrossings of x_b are included. For long times the process becomes stationary and the first approximation tends to a constant value, the Rice frequency $n_0 = 1/T_R$. For the chosen parameter values $T_R = 8.06$.

The second approximation (gray line in Fig. 5.4(b)) reproduces almost exactly the first two peaks in the FPT density and then it becomes negative, because in Eq. (5.4) trajectories performing two and more superfluous upcrossings are subtracted too many times. Moreover the second approximation tends to minus infinity for $T \to \infty$. The third approximation well reproduces the three initial peaks in $\mathcal{F}(T)$, and then diverges tending to plus infinity.

Note that the mean first passage time obtained numerically equals 14.6 for these parameter values, and the median of the distribution lies at 3.2. Thus the first three approximations reproduce the larger part of the FPT probability density.

The behavior of $\mathcal{F}(T)$ for the harmonic oscillator with higher damping $\gamma = 0.8$, stronger noise intensity $D = 0.44$, and other parameters as in Fig. 5.4 is presented in Fig. 5.5. For

---

[1] How the structure of the FPT density depends on initial conditions is discussed in detail in Section 2.4.

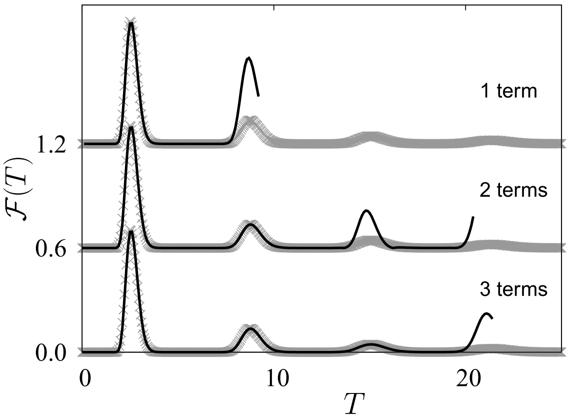

Figure 5.6: The same as in Fig. 5.4, however truncations are correctly normalized by Eq. (5.16). Simulation results are shown with gray crosses; truncations with solid lines. The curves for normalized 1, 2, and 3 terms truncations are vertically shifted by 0.6 for clarity.

these parameter values the relaxation time $t_{rel} = 2.5$ is smaller than the period $T_p = 6.86$. Therefore, the FPT density is practically monomodal with a single maximum and a small shoulder separating it from the exponential tail. The numerically obtained $\mathcal{F}(T)$ is shown with gray crosses, the 1 term truncation with a dot line, the 2 terms truncation with a dashed line, and the 3 terms truncation with a solid line. The truncation approximations again reproduce the larger part of the distribution: the mean FPT equals 13.1 and the median lies at 9.1.

The truncation approximations reproduce the FPT density for short times but are not normalized and diverge for larger times. One can force normalization in truncations, for example as follows

$$|\mathcal{F}_{trunc}(T)|\,\Theta\left(1 - \int_0^T |\mathcal{F}_{trunc}(t)|\,dt\right). \tag{5.16}$$

Here $\mathcal{F}_{trunc}(T)$ is a truncated series for the FPT density, which is given by Eqs. (5.1), (5.4), or (5.5) for 1,2, or 3 terms truncations, respectively. $\Theta(t)$ is the Heaviside step function: the expression Eq. (5.16) vanishes as soon as the integral over the absolute value of $\mathcal{F}_{trunc}(T)$ exceeds unity.

In Fig. 5.6 we show the FPT density for the same parameter values as in Fig. 5.4. Simulation results are shown with crosses, and approximations obtained from Eq. (5.16) with 1,2, and 3 terms by solid lines. The probability distributed over the long exponential tail in the real FPT density, is concentrated in the positive artefact posed on intermediate times in the normalized truncations. Therefore the mean FPT obtained from such approximations is always strongly underestimated.

The more terms are included in the truncation approximation, the longer the time span that is accurately reproduced. However, one has to confine oneself to a few terms, since the calculation of higher order terms implies the computation of multiple integrals and is not more effective than direct simulations. Therefore the truncation approximations provide good results, when the largest fraction of the FPT probability is concentrated in the first few peaks, i.e. when the barrier value is low or the noise is strong.

5.2.3 Padé approximants

The truncation approximations discussed in the previous section are a special case of a more general class of approximations for convergent series, known as Padé approximants. The Padé approximants are a particular type of rational fraction approximations for the value of a function (Baker, 1975). The idea is to match the Taylor series expansion as far as possible.

Consider a function $\phi(x)$ with the series expansion

$$\phi(x) = \sum_{k=0}^{\infty} A_k x^k. \tag{5.17}$$

We denote the L, M Padé approximant to $\phi(x)$ by

$$P[L/M] = P_L(x)/Q_M(x), \tag{5.18}$$

where $P_L(x)$ is a polynomial of a degree at most L and $Q_M(x)$ is a polynomial of degree at most M. The coefficients of $P_L(x)$ and $Q_M(x)$ are determined by the equation

$$\phi(x) - P_L(x)/Q_M(x) = O(x^{L+M+1}). \tag{5.19}$$

Since we can multiply the numerator and denominator by any constant and leave $P[L/M]$ unchanged, we impose the normalization condition $Q_M(0) = 1$.

If we denote the coefficients of P_L and Q_M as

$$\begin{aligned} P_L(x) &= p_0 + p_1 x + \cdots + p_L x^L, \\ Q_M(x) &= 1 + q_1 x + \cdots + q_M x^M, \end{aligned} \tag{5.20}$$

then multiply Eq. (5.19) by $Q_M(x)$ and equate the coefficients by the same powers of x , we obtain a linear system of equations for the coefficients of polynomials:

$$\begin{aligned} p_0 &= A_0, \\ p_1 &= A_1 + A_0 q_1, \\ p_2 &= A_2 + A_1 q_1 + A_0 q_2, \\ &\dots \\ 0 &= A_{L+M} + A_{L+M-1} q_1 + \cdots + A_L q_M, \end{aligned} \tag{5.21}$$

where $p_j \equiv 0$ if $j > L$, $q_j \equiv 0$ if $j > M$, and $A_n \equiv 0$ if $n < 0$. It can be easily shown, that the Padé approximant to any formal power series $\phi(x)$ is unique, if it exists (Baker, 1975).

In applications one often expects on general physical grounds, that the power series representing the quantity of interest converges, what enables the construction of Padé approximants. To determine the $L+M+1$ coefficients $p_0, \dots, p_L, q_1, \dots, q_M$ of the Padé approximant $P[L/M]$, the first $L + M + 1$ terms of the power series should be known.

Let us now obtain the Padé approximants for the FPT density $\mathcal{F}(T)$ represented by the series in Eq. (5.6). Consider the function $\phi(x, T)$ of variable x defined by the power series expansion

$$\phi(x,T) = \sum_{k=0}^{\infty} \left\{ \frac{(-1)^k}{k!} \int_0^T \dots \int_0^T n_{k+1}(T, t_k, \dots, t_1) dt_k \dots dt_1 \right\} x^k. \tag{5.22}$$

Here we consider T to be a parameter. Note that $\mathcal{F}(T) = \phi(1,T)$, hence the series in Eq. (5.22) converges at $x = 1$ for all values of T. We determine the Padé approximants for $\phi(x,T)$ and use their values at $x = 1$ as approximations for $\mathcal{F}(T)$. For simplicity we refer to this approximations as Padé approximants for the FPT density $\mathcal{F}(T)$ and denote them in the same way $P[L/M]$ as the corresponding Padé approximants for $\phi(x,T)$.

The first three coefficients in the power series Eq. (5.22),

$$A_0(T) = n_1(T), \qquad A_1(T) = -\int\limits_0^T n_2(T,t_1)dt_1, \tag{5.23}$$

$$A_2(T) = \frac{1}{2}\int\limits_0^T \int\limits_0^T n_3(T,t_2,t_1)dt_2dt_1,$$

can be calculated for the harmonic oscillator (see Eqs. (5.2),(5.14)). The calculation of higher order terms implies the computation of multiple integrals, which is not more effective than simulations. Therefore, we restrict ourselves to Padé approximants $P[L/M]$ with $L+M \leqslant 2$. As can be seen from Eqs. (5.21), $P[L/0]$ is equivalent to the $(L+1)$-st truncation, which were discussed in detail in the previous section. Therefore only $P[0/1], P[1/1]$ and $P[0/2]$ will be discussed here.

Solving the system of Eq. (5.21) we obtain for the Padé approximants:

$$\begin{aligned} P[0/1] &= A_0^2/(A_0 - A_1), \\ P[1/1] &= A_0 + A_1^2/(A_1 - A_2), \\ P[0/2] &= A_0^3/(A_0^2 + A_1^2 - A_1A_0 - A_2A_0). \end{aligned} \tag{5.24}$$

The disadvantage of these approximations is the lack of normalization. $P[1/1]$ does not even guarantee a positive probability density. Nevertheless, the FPT density on short time scales is reproduced rather well. In the previous section we argued, that for small times T the higher order terms in the series Eq. (5.6) are negligibly small and hence $\mathcal{F}(T)$ coincides with the truncations. For T such that all terms except for A_0 vanish, the Padé approximants Eq. (5.24) approach A_0, which reproduces almost exactly $\mathcal{F}(T)$ at these times. Thus all Padé approximants are accurate in estimating the first peak. From an analogous argument, $P[1/1]$ is almost exact also in the second peak.

Figs. 5.7 (a)-(c) illustrate the quality of Padé approximants on short time scales. Simulation results for a harmonic oscillator driven by a white Gaussian noise are depicted in gray. The approximants $P[1/1]$ and $P[0/2]$ are depicted in red in panels (a) and (b), respectively, for parameters $\gamma = 0.08$ and $D = 0.01$. $P[1/1]$ is almost exact in the first two peaks, $P[0/2]$ reproduces well more than 10 initial peaks. In panel (c) the approximants $P[0/1]$, $P[1/1]$, and $P[0/2]$ are shown in green, blue and red, respectively, for parameters $\gamma = 0.8, D = 0.44$. The higher the order of an approximant, the larger is the fraction of the FPT density it reproduces well.

However, all Padé approximants are inaccurate on long time scales. The behavior for large T is determined by the long time asymptotic of the coefficients A_i. In this limit A_0 saturates to a constant value $\lim_{T\to\infty} A_0(T) = n_0$, which is the Rice stationary frequency of upcrossings, see Eq. (5.15). The multiple densities of level crossings $n_k(t_k, \ldots, t_1)$ factorize into products of

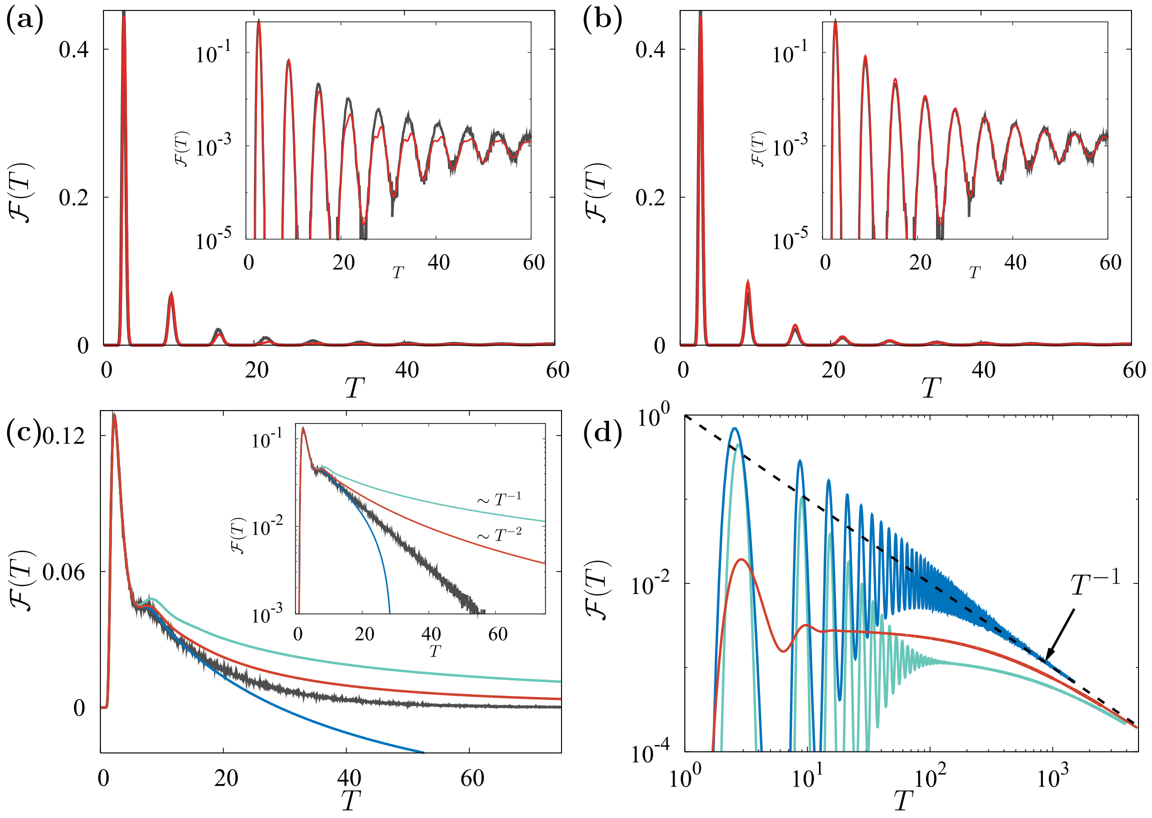

Figure 5.7: Padé approximants to the FPT density for a harmonic oscillator driven by white Gaussian noise. The parameters are $\omega_0 = 1$, $x_0 = -1, v_0 = 0, x_b = 1$, and other parameters are specified below for every panel. (a)-(c) Comparison of simulation results (gray) and Padé approximants (red). The insets show the same curves on a logarithmic scale in $\mathcal{F}(T)$. (a) $P[1/1]$ for $\gamma = 0.08$, $D = 0.01$. (b) $P[0/2]$ for $\gamma = 0.08$, $D = 0.01$. (c) $P[0/1]$ is shown in green, $P[1/1]$ in blue, and $P[0/2]$ in red for $\gamma = 0.8$, $D = 0.44$. (d) $P[0/1]$ asymptotically approaches T^{-1} independent of the system parameters. $P[0/1]$ is depicted in green for $\gamma = 0.08$, $D = 0.01$, in blue for $\gamma = 0.01$, $D = 0.02$, and in red for $\gamma = 0.8$, $D = 0.1$. Dashed black line represents the asymptotical function T^{-1}.

one point densities $n_1(t_k) \dots n_1(t_1)$, if the argument differences $|t_i - t_j|$ exceed the correlation time of upcrossings. Using Eqs. (5.23) and the asymptotic behavior for $n_1(t)$ one obtains: $A_1(T) \to -n_0^2 T$ and $A_2(T) \to n_0^3 T^2/2$ as $T \to \infty$. In general, $A_k(T) \to (-1)^k n_0^{k+1} T^k / k!$ for all finite k. Inserting these asymptotics into Eqs. (5.24) yields the asymptotical behavior of Padé approximants at $T \to \infty$:

$$P[0/1] \to \frac{1}{T}, \qquad P[1/1] \to -n_0 + \frac{4}{T}, \qquad P[0/2] \to \frac{2}{n_0 T^2}. \tag{5.25}$$

Interestingly, the asymptotic of $P[0/1]$ does not depend on system parameters: for all parameter values $P[0/1]$ approaches T^{-1} at large T. An example is given in Fig. 5.7(d), where approximants $P[0/1]$ are depicted for three different parameter sets and all of them approach the same curve T^{-1} at large values of T. This is of course not true for $\mathcal{F}(T)$, which decays exponentially in tail and the rate of this decay depends on the friction γ and the noise intensity D. At large T, the asymptotics of $P[1/1]$ and $P[0/2]$ depend on the Rice frequency n_0 and thus on the system parameters. However, they differ from the asymptotic for the FPT density $\mathcal{F}(T)$. The inset in Fig. 5.7(c) illustrates the long time asymptotic of Padé approximants for parameters $\gamma = 0.8$ and $D = 0.44$.

In general, in the linear system Eq. (5.21) the scaling of coefficients A_k with n_0 and T implies the scaling for the coefficients of polynomials: $p_k \to (\pm) n_0^{k+1} T^k$ and $q_k \to (\pm) n_0^k T^k$ at $T \to \infty$. Therefore, asymptotically $P[L/M] \to (\pm) n_0^{L-M+1} T^{L-M}$, in accordance with Eqs. (5.25). Thus, in the limit $T \to \infty$ Padé approximants $P[L/M]$ diverge to plus or minus infinity if $L > M$, saturate at $\pm n_0$ if $L = M$, and converge to zero if $L < M$. Although, in the last case, the Padé approximants have a correct asymptotical value $\lim_{T\to\infty} P[L/M] = 0$, they approach it polynomial for large T. However, the FPT density $\mathcal{F}(T)$ decays exponentially in tail. In summary, the Padé approximants either decay too slow in tail or have a wrong asymptotical value for large T. They should be preferably used on short time scales only.

5.2.4 Decoupling approximations

Decoupling approximations for Eq. (5.6) or Eq. (5.10) are based on approximation of the higher order terms by the lower order terms. This may lead to a closed analytical form, including infinitely many approximate terms.

The simplest way to obtain such an approximation is to neglect all correlations between upcrossings. This means to neglect all terms in Eq. (5.10) except for the first one and leads to

$$S(T) = \int\limits_0^T n_1(t)dt. \tag{5.26}$$

Equivalently, neglecting all correlations corresponds to the factorization of $n_{p+1}(T, t_p, \ldots, t_1)$ into a product of one-point densities $n_1(T) n_1(t_p) \ldots n_1(t_1)$ in Eq. (5.6). Then the series, Eq. (5.6) sums up to $\mathcal{F}(T) \approx n_1(T) \exp\left(-\int_0^T n_1(t)dt\right)$, which is equivalent to Eqs. (5.9) and (5.26). This approximation will be referred to as the *Hertz approximation* since the form of $\mathcal{F}(T)$ resembles the Hertz distribution (Hertz, 1909). It is a first order approximation in the sense, that the first term of the series is calculated exactly, and all other terms are then approximated by the first term.

The second order approximation should use the first and the second terms evaluated exactly and approximate all higher terms by these two. The general form of $\mathcal{F}(T)$ in terms of the cumulant functions Eq. (5.9) ensures the correct normalization, irrespective of the way how $S(T)$ is approximated. However, the simple truncation of the series Eq. (5.10) after the second term does not guarantee a positive escape rate $S'(T)$.

The second order approximation, which guarantees $S'(T) > 0$, was proposed by Stratonovich (1967) in context of the peak duration. The first and the second cumulant functions are evaluated exactly, and the higher order cumulant functions are approximated by the combinations of these two as

$$g_p(t_p, \ldots, t_1) \approx (-1)^{p-1}(p-1)! n_1(t_p) \ldots n_1(t_1) \{R(t_1, t_2) R(t_1, t_3) \ldots R(t_1, t_p)\}_s. \tag{5.27}$$

Here $\{\ldots\}_s$ is the symmetrization operation of the expression in brackets with respect to permutations of its arguments. $R(t_i, t_j)$ is the correlation coefficient of upcrossings defined by

$$R(t_i, t_j) = 1 - \frac{n_2(t_i, t_j)}{n_1(t_i) n_1(t_j)}. \tag{5.28}$$

Note, that $R(t_1, t_1) = 1$ and $R(t_i, t_j) \to 0$ for large values of $|t_i - t_j|$.

The approximation of the cumulant functions in the form Eq. (5.27) can be motivated by the following argument. Consider the definition of the cumulant functions Eq. (2.29) with $r = 1$. Recall that the joint densities of upcrossings vanish for coinciding arguments: $n_p(t_1, \ldots, t_1) = 0$. Then it follows from Eq. (2.29):

$$\ln(1 + n_1(t_1) z_1) = \sum_{p=1}^{\infty} \frac{1}{p!} g_p(t_1, \ldots, t_1) z_1^p.$$

The above expression should hold for arbitrary z_1. Therefore expanding the logarithm into a series and equating the coefficients by the same powers of z_1 on both sides, one obtains the identity

$$g_p(t_1, \ldots, t_1) = (-1)^{p-1}(p-1)! n_1^p(t_1). \tag{5.29}$$

Equation (5.29) is exact for all arguments coinciding, and Eq. (5.27) extends it to the case, when the arguments differ.

Substitution of Eq. (5.27) into Eq. (5.10) delivers then the *Stratonovich approximation* for $\mathcal{F}(T)$ in the form Eq. (5.9), now with $S(T)$ being

$$S(T) = -\int_0^T n_1(t) \frac{\ln\left[1 - \int_0^T R(t, t') n_1(t') dt'\right]}{\int_0^T R(t, t') n_1(t') dt'} dt. \tag{5.30}$$

We have to specify the domains of applicability for these approximations. The Hertz approximation Eq. (5.26) holds if all correlations considerably decay within the typical time interval between successive upcrossings T_R. The decay of correlations is described by the relaxation time t_{rel} of the process. Therefore, the Hertz approximation holds for $t_{rel} \ll T_R$.

The Stratonovich approximation is applicable when the argument of the logarithm in Eq. (5.30) is positive, $1 - \int_0^T [n_1(t') + n_1(t)^{-1} n_2(t', t)] dt' > 0$. Using the fact that $n_2(t', t)/n_1(t)$ tends to $n_1(t')$ for $|t - t'| > t_{rel}$ and tends to zero for $|t - t'| \to 0$ we obtain $t_{rel} < T_R$ as a rough estimate for the region of validity of Eq. (5.30).

Let us turn to particular results for the harmonic oscillator Eq. (5.11) driven by a white noise. In Figs. 5.8 and 5.9 the FPT probability density obtained from simulations is depicted with a gray line, the Hertz approximation Eq. (5.26) with a black dashed line, and the Stratonovich approximation Eq. (5.30) with a black solid line.

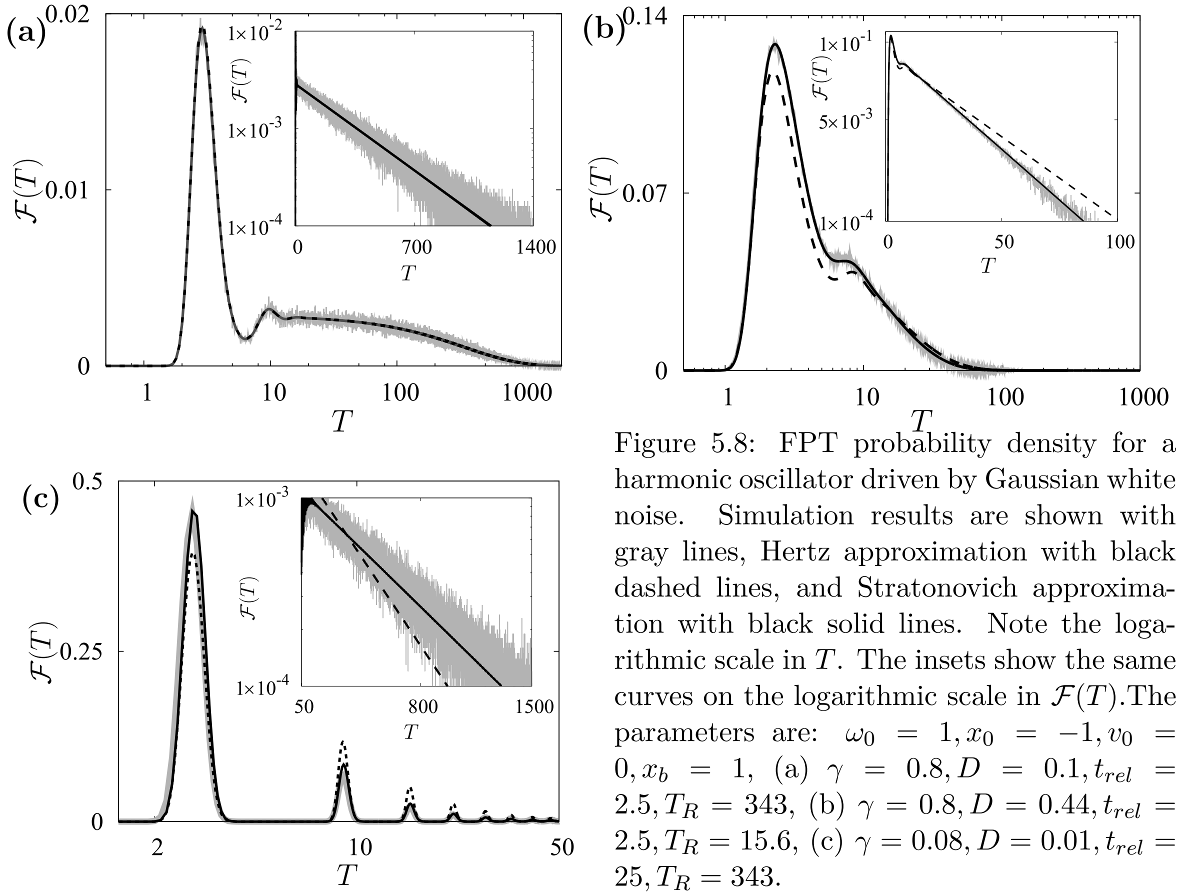

Figure 5.8: FPT probability density for a harmonic oscillator driven by Gaussian white noise. Simulation results are shown with gray lines, Hertz approximation with black dashed lines, and Stratonovich approximation with black solid lines. Note the logarithmic scale in T. The insets show the same curves on the logarithmic scale in $\mathcal{F}(T)$.The parameters are: $\omega_0 = 1, x_0 = -1, v_0 = 0, x_b = 1$, (a) $\gamma = 0.8, D = 0.1, t_{rel} = 2.5, T_R = 343$, (b) $\gamma = 0.8, D = 0.44, t_{rel} = 2.5, T_R = 15.6$, (c) $\gamma = 0.08, D = 0.01, t_{rel} = 25, T_R = 343$.

In Fig. 5.8(a) the parameters are chosen to be $\gamma = 0.8, D = 0.1$, corresponding to moderate friction and moderate noise intensity. For given parameter values $t_{rel} = 2.5$ and $T_R = 343$, so that $t_{rel} \ll T_R$, both Hertz and Stratonovich approximations hold and reproduce well the FPT density in the whole time domain.

In the case of moderate friction and stronger noise the upcrossings become more frequent and T_R decreases. The FPT changes its form to practically monomodal. An example is given in Fig. 5.8(b) with $\gamma = 0.8, D = 0.44$ which correspond to $t_{rel} = 2.5$ and $T_R = 15.6$. The Stratonovich approximation agrees well with simulations, whereas the Hertz approximation fails to reproduce the details of the distribution: It underestimates $\mathcal{F}(T)$ on short times, and shows a slower exponential decay in the tail than observed in simulations (see the inset).

Finally, for small friction and weak noise the upcrossings are rare, but the relaxation time is large. The FPT probability density exhibits multiple decaying peaks. In Fig. 5.8(c) $\gamma = 0.08, D = 0.01$ corresponding to $t_{rel} = 25, T_R = 343$. Again, the Stratonovich approximation performs well, while the Hertz approximation underestimates the first peak, overestimates all further peaks and for large T decays faster than the simulated FPT density.

In the overdamped regime ($\gamma > 2\omega_0$) the condition $t_{rel} < T_R$ is always fulfilled. Nevertheless the validity region of our approximations is limited. With increasing friction the process

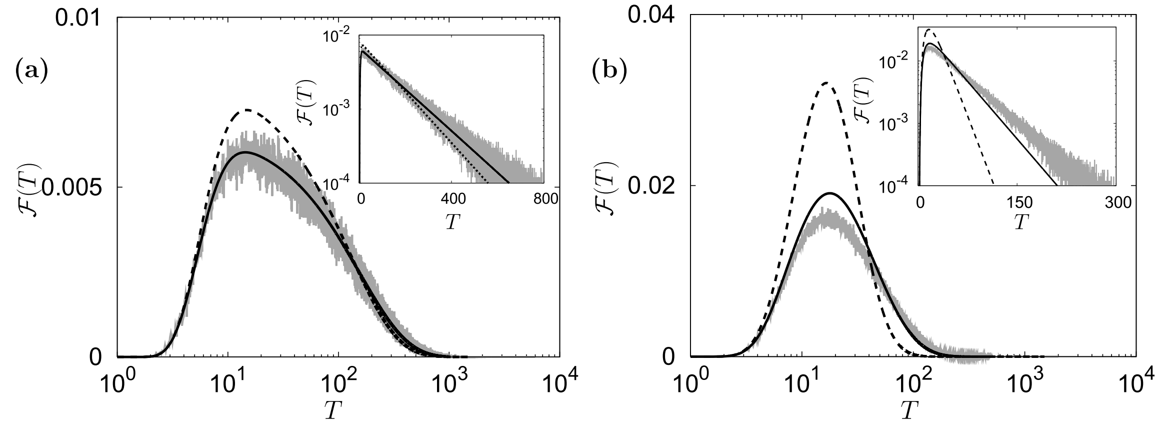

Figure 5.9: Same as in Fig. 5.8 however for the case of stronger friction. The parameters are (a) $\gamma = 3.0, D = 0.5, \omega_0/\gamma = 0.33$, (b) $\gamma = 10.0, D = 5.5, \omega_0/\gamma = 0.1$ and other parameters as in Fig. 5.8.

$x(t)$ approaches a Markovian one (it is Markovian in the overdamped limit $\omega_0/\gamma \ll 1$). For such processes the pattern of upcrossings is not homogeneous, but shows rather well separated clusters of upcrossings (Stratonovich, 1967). Essentially, the property that upcrossings form a system of *nonapproaching* random points is violated in the Markovian limit. The upcrossings within a single cluster are not independent even if their mean density n_0 is low, so that the quality of approximations decreases. This fact is illustrated in Fig. 5.9. In the overdamped regime the correlation functions decay monotonically and the FPT densities are always monomodal. The parameters in Fig. 5.9(a) are $\gamma = 3.0, D = 5.5$, so that $\omega_0/\gamma = 0.33$. The Stratonovich approximation continues to be a good approximation for $\mathcal{F}(T)$, while the Hertz approximation becomes inaccurate. Further increase in friction, for example $\gamma = 10.0, D = 5.5$ as in Fig. 5.9(b) corresponding to $\omega_0/\gamma = 0.1$, brings the system close to the Markovian limit. The Stratonovich approximation becomes inaccurate, and the Hertz approximation fails.

5.2.5 Long time asymptotic

For large T, $\mathcal{F}(T)$ decays exponentially, $\mathcal{F}(T) \propto \exp(-\kappa T)$. The decrement of this decay is obtained from a long time asymptotic: $\kappa = \lim_{T\to\infty} S'(T)$ (compare with equations Eq. (4.5) and (5.9)). Thus, in the Hertz approximation Eq. (5.26) one gets

$$\kappa_{\mathrm{H}} = \lim_{T\to\infty} n_1(t) = n_0. \tag{5.31}$$

The behavior in the Stratonovich approximation Eq. (5.30) is determined by $\lim_{t,t'\to\infty} \int_0^T R(t,t')n_1(t')dt' = n_0\tau_{cor}$, where we have introduced the correlation time

$$\tau_{cor} = \lim_{t\to\infty} \int_0^\infty R(t,t')dt'. \tag{5.32}$$

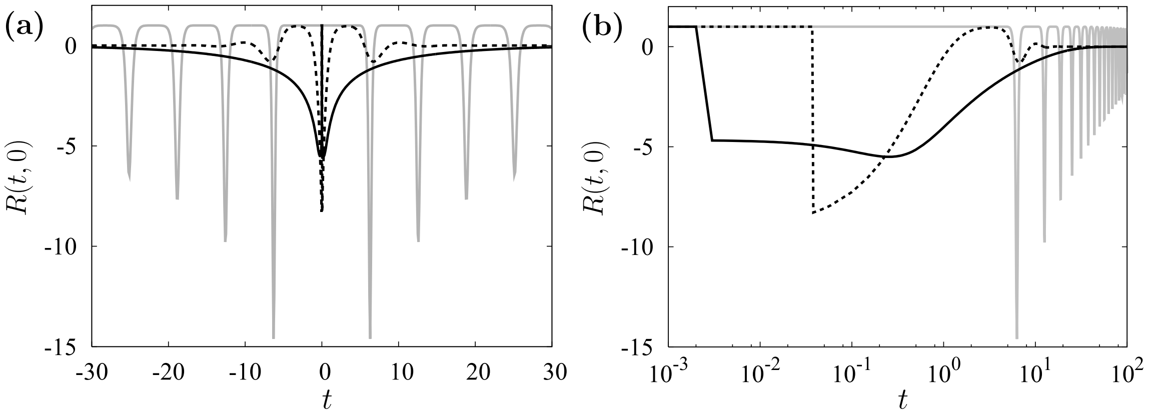

Figure 5.10: Correlation coefficient $R(t,0)$ of the stationary sequence of upcrossings for a harmonic oscillator driven by white Gaussian noise, theoretical curves. (a) The parameters are $\gamma = 0.01, D = 0.02$ (gray line), $\gamma = 0.8, D = 0.1$ (dashed line), $\gamma = 10.0, D = 5.5$ (black solid line). (b) The same curves on the logarithmic t scale. The other parameters are as in Fig. 5.8. $R(t,0)$ approaches zero at large t with and without oscillations in underdamped and in overdamped regimes, respectively. $R(t,0) \approx 1$ on short time scales reveals the nonapproaching character of upcrossings.

Inserting this expression into Eq. (5.30) and expanding the logarithm up to the second term we obtain

$$\kappa_{\mathrm{S}} = n_0 \left(1 + \frac{1}{2} n_0 \tau_{cor}\right) \tag{5.33}$$

providing a correction to κ_{H}. From the definitions Eqs. (5.28) and (5.32) it immediately follows that $\tau_{cor} = 0$ for a Poisson point process with uncorrelated events. Otherwise τ_{cor} is different from zero, and is not necessarily positive due to the oscillating correlation coefficient. In the next paragraphs we discuss the meanings of τ_{cor} and of negative correlation times.

Since we are interested in the long time asymptotic, we consider a stationary process $x(t)$, i.e. we shift the initial conditions to $t \to -\infty$. Then, the sequence of upcrossings for $x(t)$ is a stationary point process, whose distribution functions remain unchanged by an arbitrary shift of all their arguments, see Eq. (2.39). Using Eq. (5.28) one obtains the relation between the distribution function $n_2(t,0)$ of a stationary sequence of upcrossings and the correlation coefficient:

$$n_2(t,0) = n_0^2 \left[1 - R(t,0)\right]. \tag{5.34}$$

If $R(t,0) \approx 1$ for some t, then $n_2(t,0) \approx 0$, i.e. the probability to obtain two upcrossing separated by the time interval t vanishes. This is the case for small values of t, since the upcrossings produced by a differentiable process $x(t)$ are nonapproaching. In Fig. 5.10 the correlation coefficient is plotted for three parameter sets corresponding to strongly underdamped (gray line), slightly underdamped (dashed line), and strongly overdamped (solid black line) situations. The logarithmic scale in Fig. 5.10(b) clearly shows the magnitude of the

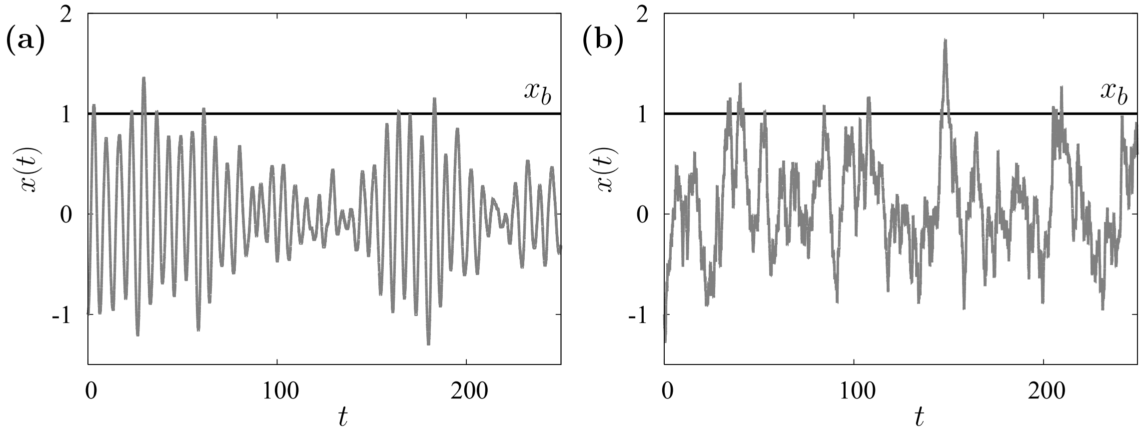

Figure 5.11: Typical patterns of upcrossings generated by a harmonic oscillator driven by white Gaussian noise. The parameters are (a) $\gamma = 0.08, D = 0.01$, underdamped regime, (b) $\gamma = 10.0, D = 5.5$, overdamped regime. The other parameters are as in Fig. 5.8. Black solid line marks the threshold value x_b. The upcrossings are clustered; the interval between upcrossings within a cluster is $\sim T_p$ in the underdamped regime, and is extremely small in the overdamped regime.

minimal interval between two successive upcrossings t_{min}. It approximately equals the period of subthreshold oscillations T_p in the strongly underdamped regime, decreases with increasing friction, and becomes extremely small in the overdamped regime. For $\gamma = 10.0, D = 5.5$ corresponding to $\omega_0/\gamma = 0.1$ the minimal interval between upcrossings $t_{min} \sim 3 \cdot 10^{-3}$ is much smaller than the mean interval between upcrossings $T_R = 15.6$. In the underdamped regime $R(t, 0)$ takes values close to 1 periodically at $t \sim 1.5T_p$, $2.5T_p$ …: the trajectory performs almost regular oscillations in this regime, and the appearance of two upcrossings separated by odd multiples of half the period is highly unlikely.

$R(t, 0)$ tends to zero for $t \to \infty$, when the upcrossings become independent, see Eq. (5.34). $R(t, 0)$ approaches its asymptotic value in an oscillatory manner in the underdamped regime and monotonically in the overdamped regime. Negative values of $R(t, 0)$ indicate the increased probability of two upcrossings separated by time t, see Eq. (5.34). In the overdamped regime $R(t, 0)$ achieves its minimal values on short time scales (for the example in Fig. 5.10 these are 10^{-2} to 10^{0}), indicating the formation of very dense clusters of upcrossings in the overdamped regime. In contrast, $R(t, 0)$ has multiple minima at $t \sim T_p$, $2T_p$ … in the underdamped regime, indicating the clustering of upcrossings on larger time scales, with the typical interval between successive upcrossings within a cluster being $\sim T_p$.

Recall that the functions $n_2(t_2, t_1)$ and $R(t_2, t_1)$ are symmetric under permutation of their arguments. Using this symmetry and stationarity of the sequence of upcrossings, substitution of Eq. (5.34) into Eq. (5.32 yields:

$$\tau_{cor} = \lim_{t\to\infty} 2 \int_0^t \left(1 - \frac{n_2(t', 0)}{n_0^2}\right) dt' = \lim_{t\to\infty} 2 \left(t - \frac{1}{n_0^2} \int_0^t n_2(x, 0) dx\right). \tag{5.35}$$

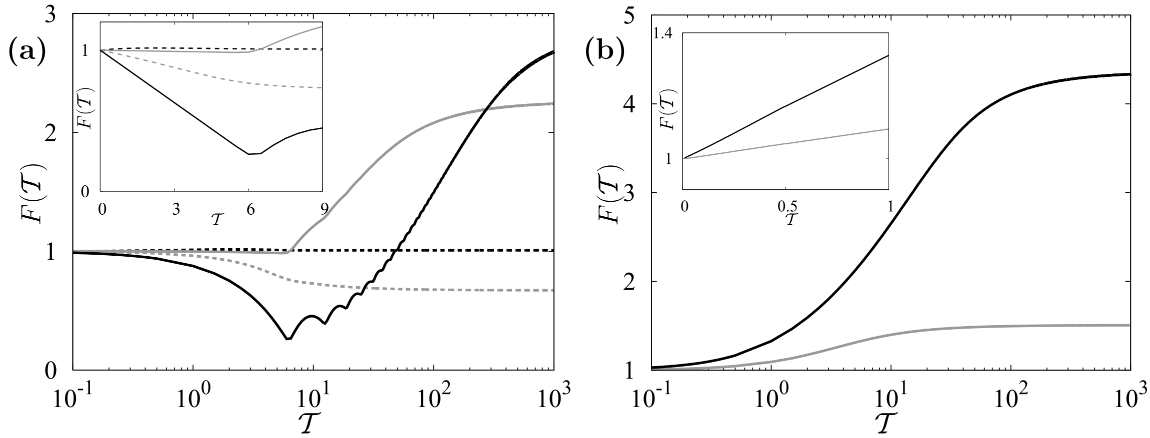

Figure 5.12: Fano factor $F(\mathcal{T})$ for the sequence of upcrossings for a harmonic oscillator driven by white Gaussian noise, theoretical curves. (a) Underdamped regime, $\gamma = 0.01, D = 0.02$ (black solid line), $\gamma = 0.08, D = 0.01$ (gray solid line), $\gamma = 0.8, D = 0.1$ (black dashed line), and $\gamma = 0.8, D = 0.44$ (gray dashed line). (b) Overdamped regime, $\gamma = 3.0, D = 0.5$ (gray line) and $\gamma = 10.0, D = 5.5$ (black line). The other parameters are as in Fig. 5.8. The insets show the same curves on the short time scale.

The correlation time τ_{cor} is determined in terms of the first two distribution functions $n_2(t_2, t_1)$ and $n_1(t)$.

Now we can derive the relation between τ_{cor} and the Fano Factor $F(\mathcal{T})$ of the stationary sequence of upcrossings, since the latter is connected by Eqs. (2.44) and (2.45) to the first two distribution functions. Substituting Eq. (2.44) into Eq. (2.45) and using stationarity of the process, we obtain for the Fano factor

$$F(\mathcal{T}) = 1 + \frac{1}{n_0 \mathcal{T}} \left(2 \int_0^{\mathcal{T}} dt \int_0^t dx \, n_2(x,0) - n_0^2 \mathcal{T}^2 \right)$$

$$= 1 - \frac{n_0}{\mathcal{T}} \int_0^{\mathcal{T}} 2 \left(t - \frac{1}{n_0^2} \int_0^t n_2(x,0) dx \right) dt. \quad (5.36)$$

Hence, in view of Eq. (5.35) the asymptotic value of the Fano factor $F_\infty = \lim_{\mathcal{T}\to\infty} F(\mathcal{T})$ is related to the correlation time by

$$F_\infty = 1 - n_0 \tau_{cor}. \quad (5.37)$$

The correlation time τ_{cor} characterizes the pattern of upcrossings: τ_{cor} is negative if $F_\infty > 1$, and τ_{cor} is positive if $F_\infty < 1$.

If the sequence of upcrossings is overdispersed ($F_\infty > 1$), then τ_{cor} is negative. The overdispersion results from the existence of two time scales in the point process. In the underdamped regime these are the period of oscillations T_p and the inverse Rice frequency $1/n_0 = T_R$. The upcrossings form clusters; the interval between upcrossings within a cluster is

γ	D	t_{rel}	n_0	τ_{cor}	F_∞	C^2_{var}
			underdamped			
0.01	0.02	200.0	0.124	-14.1	2.72	1.42
0.08	0.01	25.0	0.003	-432.0	2.26	2.17
0.8	0.1	2.5	0.003	-2.4	1.007	1.007
0.8	0.44	2.5	0.64	5.1	0.67	0.66
			overdamped			
3.0	0.5	0.66	0.008	-64.1	1.51	1.48
10.0	5.5	0.2	0.064	-52.4	4.36	4.31

Table 5.1: Time scales and variability coefficients for a sequence of upcrossings generated by a harmonic oscillator driven by a white Gaussian noise. The other parameters are as in Fig. 5.8.

$\sim T_p$ (or a multiple of T_p) and the interval between successive clusters is $\sim T_R$, see Fig. 5.11(a). Clustering of upcrossings on the time scale of T_p is pronounced in the Fano factor curves, presented in Fig. 5.12(a) for sequences of upcrossings generated by an underdamped harmonic oscillator for four different parameter sets. On short time scales (inset in Fig. 5.12(a)), $F(\mathcal{T})$ linearly decreases up to $T_p \approx 6$: the probability to find more than one upcrossing in an interval shorter than T_p vanishes. On long times scales, the Fano factor saturates at different values, which can be smaller or larger than 1 depending on the parameter values. Qualitatively, if the mean number of upcrossings within a cluster is large (large t_{rel}) and the mean interval between clusters is also large (large T_R), then the existence of two time scales manifests itself in $F_\infty > 1$ and in the negative correlation time $\tau_{cor} < 0$. Table 5.1 summarizes the relevant time scales and variability coefficients for all parameter sets used in Figs. 5.4 to 5.9. Note that $F_\infty > C^2_{\mathrm{var}}$ indicates positive correlations between upcrossings, see Eq. (2.47).

The Fano factor curves for the sequences of upcrossings in the overdamped regime are depicted in Fig. 5.12(b). Linear decrease in $F(\mathcal{T})$ on short time scales is practically absent, since the upcrossings form very dense clusters, and two successive upcrossings can follow within an arbitrary small interval, see Fig. 5.11(b). In the overdamped regime two time scales are also present in the sequence of upcrossings. With increasing γ the number of upcrossings within a cluster increases. In contrast to the underdamped situation, F_∞ increases with increasing γ. In the overdamped regime F_∞ is always larger than 1 due to the strong separation of time scales corresponding to intervals within and in-between clusters.

Let us return to the long time asymptotic of the Hertz and Stratonovich approximations

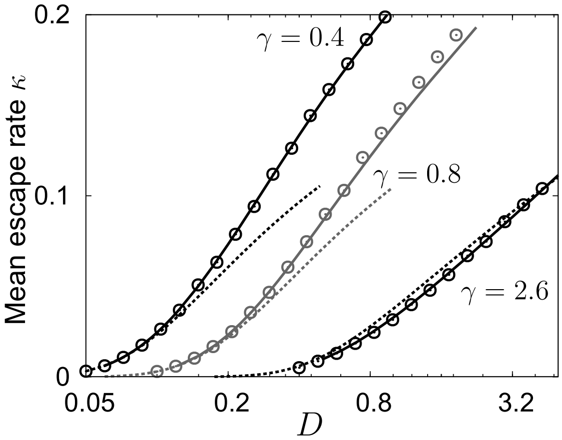

Figure 5.13: Mean escape rates κ (the inverse mean FPT) for a harmonic oscillator driven by white Gaussian noise of moderate intensity D and with moderate damping $\gamma = 0.4$ (upper curves), $\gamma = 0.8$ (middle curves) and $\gamma = 2.6$ (lower curves). The other parameters are as in Fig. 5.8. The rates κ obtained from numerical simulations are plotted with open circles, from the Hertz approximation with dashed lines and from the Stratonovich approximation with solid lines. Compare the curves with those in Fig. 4.3(a).

Eqs. (5.31) and (5.33). If the pattern of upcrossings is close to the Poisson process, then F_∞ is close to 1, and $n_0\tau_{cor}$ vanishes. In this case, the second order correction $n_0\tau_{cor}/2$ provided by Eq. (5.33) to κ_{H} is negligibly small and the Hertz approximation is absolutely sufficient. In particular, this is the case for $\gamma = 0.8, D = 0.1$, when the Hertz approximation is very accurate in the whole time domain. It is very instructive to compare the quality of approximations plotted in Figs. 5.4 to 5.9 with the corresponding values of variability coefficients in Table 5.1. In the Section 5.4 we use of the condition $F_\infty \approx 1$ to test the validity of the Hertz approximation.

5.2.6 Moments of the first passage time

In this subsection we examine how accurate are the analytical approximations in estimating the moments of the first passage time. Truncations and Padé approximants are not normalized and thus are not suitable for the estimation of moments. Therefore we focus on the Hertz and Stratonovich approximations only. In the end of this subsection we briefly discuss the phenomenon of anticoherence resonance emerging in the underdamped regime.

The starting point are expressions for the first and the second FPT moments, which follow from Eqs. (4.3) and (5.9):

$$\mathcal{T}_1 = \langle T \rangle = \int_0^\infty e^{-S(t)} dt, \qquad \mathcal{T}_2 = \langle T^2 \rangle = 2\int_0^\infty t e^{-S(t)} dt. \tag{5.38}$$

Here the function $S(t)$ is expressed by Eqs. (5.26) and (5.30) in the Hertz and Stratonovich approximations, respectively.

Let us first consider the mean first passage time $\mathcal{T}_1$. In Fig. 5.13 the mean escape rate $\kappa = \mathcal{T}_1^{-1}$, defined as the inverse mean FPT, is plotted as a function of noise intensity D. We choose to plot the mean escape rate for a convenient comparison of the results with those obtained using the Kramers approach as discussed in Chapter 4. We emphasize that for a strong noise and nonequilibrium initial conditions the mean FPT sensitively depends on the initial conditions and the Markovian rate description is unsuitable. Thus the mean escape rate is only formally defined as the inverse mean FPT, since averaging of the time-dependent rate Eq. (4.4) over time may lead to a result different from $\mathcal{T}_1^{-1}$.

In Fig. 5.13 the Hertz approximation (dashed lines) reproduces well the values of κ obtained numerically (open circles) up to moderate noise intensities. In the slightly overdamped regime ($\gamma = 2.6$), where the relaxation time is small and upcrossings do not yet form dense clusters, the validity region of the Hertz approximation spreads out even to the domain of strong noise. The excellent quality of the Stratonovich approximation (solid lines) is striking. It produces extremely accurate results for the mean FPT in the regimes of weak, moderate and strong noise. Compare the results in Fig. 5.13 with the Kramers rate estimates in Fig. 4.3. The validity region of the Kramers approach is limited exclusively to the domain of weak noise D and is at least one order of magnitude smaller than the validity region of the Stratonovich approximation.

Let us turn to the second moment $\mathcal{T}_2$. To compare the results with the Markovian rate estimates, instead of plotting $\mathcal{T}_2$ we consider the relative dispersion given by the coefficient of variation $C_{\mathrm{var}} = \sqrt{\mathcal{T}_2 - \mathcal{T}_1^2}/\mathcal{T}_1$ (Eq. (2.41)). Indeed, as follows from Eq. (4.7) $C_{\mathrm{var}} = 1$ for all Markovian escape processes with a constant rate.

In Fig. 5.14 the coefficient of variation of FPT is plotted against the noise intensity D for a harmonic oscillator driven by a white Gaussian noise. The validity regions of the Hertz (dashed line) and Stratonovich (solid line) approximations are again reflected in their accuracy of reproducing C_{var} values obtained numerically (open circles). The approximations become more accurate as the noise intensity decreases. For low noise intensities the Hertz approximation gives good results that are comparable with those of the Stratonovich approximation. The latter remains very accurate in estimation of the second moment in a broad range of noise intensities.

In conclusion we note a very interesting phenomenon appearing in the underdamped regime at low noise intensities. Recall that in the limit $D \to 0$ a point process approaches the Poisson limit, and the coefficient of variation tends to 1. Whereas in the overdamped regime C_{var} reaches the Poisson limit $C_{\mathrm{var}} = 1$ from below, in the underdamped regime C_{var} shows a maximum on very small values of D and reaches 1 from above, see Fig. 5.14(b). The maximum becomes more pronounced with decreasing friction.

The maximum in C_{var} indicates that the highest irregularity and overdispersion ($C_{\mathrm{var}} > 1$) of the first passage time occurs at low noise intensities. This phenomenon is referred to as *anticoherence resonance* (Lacasta et al., 2002) and is in some sense the opposite to the coherence resonance. The latter consists in the enhanced regularity of the output of a noise driven excitable system achieved at a finite noise intensity (Pikovsky and Kurths, 1997) and reflected in C_{var} having a minimum at that noise intensity.

The anticoherence resonance occurs in an excitable dynamical system with a nonmonotonic relaxational behavior driven by very weak noise. The mechanism of anticoherence resonance consist in an interplay of the time scales of excitatory and relaxational behaviors in a system, which depend differently on the noise intensity. Consider the sequence of pulses produced by an underdamped harmonic oscillator with the threshold and reset, Eq. (5.11). The probability to escape is increased at the maxima of subthreshold oscillations. The pulses are clustered with the deterministic time scale within a cluster, which approximately equals

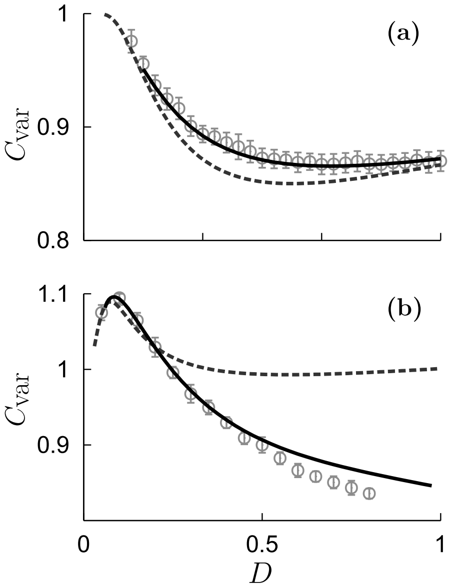

Figure 5.14: Coefficient of variation C_{var} of the first passage time to the threshold x_b for a harmonic oscillator driven by a white Gaussian noise versus noise intensity D. C_{var} obtained from simulations is depicted with open circles, from the Hertz approximation with a dashed line, and from the Stratonovich approximation with a solid line. (a) Overdamped regime $\gamma = 2.6$. (b) Underdamped regime $\gamma = 0.4$. The maximum in C_{var} on low noise intensities is a signature of the anticoherence resonance. The other parameters are as in Fig. 5.8.

$T_p/2$. For very low noise intensities the duration of intervals between successive clusters is governed by a rate process with the Kramers escape mechanism. The time scale of the relaxational behavior does not depend on the noise intensity, whereas the Kramers activation time increases with decreasing noise intensity. For sufficiently weak noise the separation of these times scales leads to the overdispersion of the pulse train ($C_{\mathrm{var}} > 1$). In the overdamped regime the anticoherence resonance does not occur, since the relaxational behavior is monotonic, see Fig. 5.14(a).

5.2.7 Truncation versus decoupling approximations.

In the previous sections we have seen, that the truncation approximations reproduce the FPT density on short time scales. In contrast, the decoupling approximations reproduce the FPT density in the whole time domain and possess the correct normalization. At first glance it may seem that the decoupling approximations perform better than the truncations and should be preferably used in applications. However, it depends on the problem one has to solve and sometimes the truncations turn out to be useful.

One such situation was already mentioned. If the noise intensity is high or the barrier value is low, then the upcrossings occur frequently, and the decoupling approximations cannot be applied. For example, for parameter values as in Fig. 5.4, the relaxation time is $t_{rel} = 200$, and the mean interval between upcrossings $T_R = 8.07$. Thus $t_{rel} > T_R$, and both Hertz and Stratonovich approximations fail. Nevertheless, the largest part of the FPT density is concentrated in the first few peaks in this case, and is well reproduced by the truncation approximations, as shown in Figs. 5.4 and 5.5(b).

One might also be interested in a very accurate approximation for the FPT density on short times. The truncations deliver better results on short times than the decoupling approximations. For example, in Fig. 5.15 the simulation results are compared with the 3

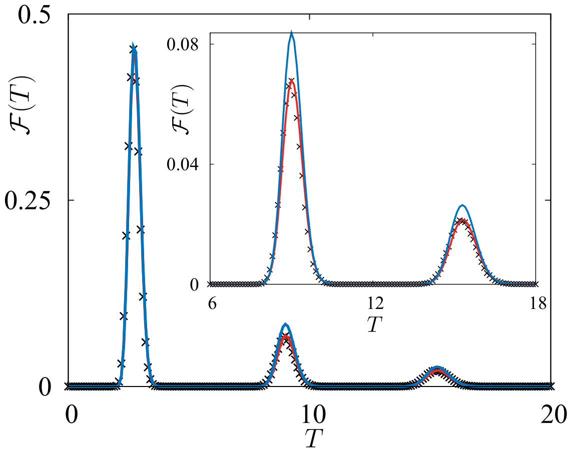

Figure 5.15: FPT density for a harmonic oscillator driven by a white Gaussian noise, $\omega_0 = 1, \gamma = 0.08, D = 0.01, x_0 = -1, v_0 = 0, x_b = 1$. Simulation results are shown with crosses, the 3 terms truncation with red line, and the Stratonovich approximation with blue line. The inset shows the magnification of a part of the curve.

terms truncation and the Stratonovich approximation for the same parameter values as in Fig. 5.8(c). Both approximations very accurately reproduce the first peak in the FPT density. However, the 3 terms truncation is much more accurate in estimating the second and the third peaks (inset in Fig. 5.15).

This can be easily understood. The Stratonovich approximation takes $n_1(t_1)$ and $n_2(t_2, t_1)$ exactly, and approximates all higher order densities through these two. On times, when the first peak occurs, $n_2(t_2, t_1)$ is negligibly small. Then from Eqs. (5.27) and (5.28) we obtain $g_p(t_p, \ldots, t_1) \approx (-1)^{p-1}(p-1)! n_1(t_p) \ldots n_1(t_1)$. Substitution of this expression into Eq. (2.29) yields $n_p(t_p, \ldots, t_1) \approx 0$ for $p > 1$. Thus, on these times the Stratonovich approximation just coincides with the 1 term truncation and reproduces the first peak very accurately. On times, when the second peak in the FPT density occurs, $n_2(t_2, t_1)$ is significantly different from zero. Hence all approximated $n_p(t_p, \ldots, t_1), p > 2$ turn out to be non-vanishing as well, while the real values for these functions are negligibly small on these times. Thus the accuracy of the Stratonovich approximation decreases in the second peak. By analogous argument it becomes clear, that the Hertz approximation is already inaccurate in the estimation of the first peak.

5.3 First passage time densities for harmonic oscillator driven by colored noise

In Section 5.2 we discussed several analytical approximations for the FPT density of a non-Markovian random process $x(t)$. We have shown using the example of a harmonic oscillator driven by a white Gaussian noise, that these approximations are very effective in a broad range of parameters. The general expression Eq. (5.6) and approximations Eqs. (5.9), (5.26) and (5.30) are applicable if the joint probability densities of x and its velocity v in Eq. (5.2) exist. It is necessary that the process $x(t)$ is continuous and differentiable at any time, but there are no further restrictions on the dimension and form of the system. In particular, the approximations provide good results for the FPT density independently of the character of the driving noise.

The case of correlated input signals (colored noise driving) is of a great import in neuroscience. In Section 2.2.2 we have shown, that the random synaptic input can be modeled in the diffusion approximation by an additive colored noise. Also one might consider a harmonic noise as being composed of a signal represented by a peak in the power spectral density and a noise (Neiman and Schimansky-Geier, 1994).

Therefore we consider the resonate-and-fire neuron driven by a colored noise $\eta(t)$:

$$\begin{aligned} \dot{x} &= v; \\ \dot{v} &= -\gamma v - \omega_0^2 x + \eta(t). \end{aligned} \tag{5.39}$$

We do not intend to investigate all aspects of this complex colored noise problem (Hänggi and Jung, 1995). We rather illustrate the applicability of the truncations and the decoupling approximations to the multidimensional first passage time problem using as an example: (i) the Ornstein-Uhlenbeck noise and (ii) the harmonic noise.

The Ornstein-Uhlenbeck noise (Uhlenbeck and Ornstein, 1930; Wang and Uhlenbeck, 1945) is essentially a low pass filtered white noise:

$$\dot{\eta} = -\frac{1}{\tau}\eta + \frac{\sqrt{2D}}{\tau}\xi(t), \tag{5.40}$$

with $\xi(t)$ being the white Gaussian noise of intensity 1. The power spectral density of this process, $S_\eta(\omega) = 2D/(\omega^2 + 1/\tau^2)$, decays monotonically with increasing frequency. The correlation time of the Ornstein-Uhlenbeck noise is τ, the variance D/τ, and the autocorrelation function $r_{\eta\eta}(t) = \langle \eta(t')\eta(t'+t)\rangle = (D/\tau)\exp(-t'/\tau)$. We choose the normalization of the noise intensity in Eq. (5.40) so that in the limit $\tau \to 0$ the process $\eta(t)$ tends to the white noise of intensity $2D$.

The correlation functions for the system Eqs. (5.39) and (5.40), $r_{xx}(t)$,$r_{x\eta}(t)$,$r_{\eta x}(t)$, $r_{xv}(t) = r'_{xx}(t)$,$r_{vv}(t) = -r''_{xx}(t)$, $r_{\eta v}(t) = r'_{\eta x}(t)$, $r_{v\eta}(t) = -r'_{x\eta}(t)$, can be obtained using the Fourier transform as it was done for the white noise case in Section 5.2.1. Then $n_1(T)$ is again obtained analytically and has the form given by Eq. (5.14). Now $\mu_{ij} = \mu_{ji}$ are elements of the inverse correlation matrix $(\hat{C}_5)^{-1}$ and q_i are components of the vector $\vec{Q} = (x(T), v(T), x_0(0), v_0(0), \eta_0(0))$. The factor α is defined in the same way as in Section 5.2.1.

The harmonic noise is a band pass filtered white noise (Schimansky-Geier and Zülicke, 1990; Hesse and Schimansky-Geier, 1991):

$$\begin{aligned} \dot{\eta} &= z; \\ \dot{z} &= -\Gamma z - \Omega_0^2 \eta + \sqrt{2D}\xi(t). \end{aligned} \tag{5.41}$$

The correlation time of the harmonic noise is $2/\Gamma$ and the variance $D/(\Gamma\Omega_0^2)$. If $\Gamma < 2\Omega_0$, the power spectral density of the harmonic noise, $S_\eta(\omega) = 2D/((\Omega_0^2 - \omega^2)^2 + \Gamma^2\omega^2)$, is peaked around the frequency Ω_0. The autocorrelation function is then given by

$$r_{\eta\eta}(t) = \frac{D}{\Gamma\Omega_0^2} e^{-\frac{\Gamma}{2}t} \left(\frac{\Gamma}{2\Upsilon}\sin(\Upsilon t) + \cos(\Upsilon t) \right), \tag{5.42}$$

with $\Upsilon = \sqrt{\Omega_0^2 - \frac{\Gamma^2}{4}}$. Again, all correlation functions for the system Eq. (5.39) and (5.41) can be obtained using the Fourier transform. Equation (5.14) determines analytically $n_1(T)$ with

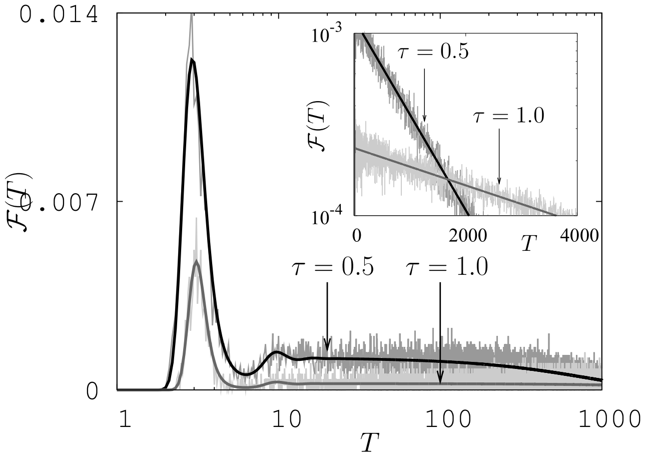

Figure 5.16: Simulation results and the Hertz approximation for the FPT probability density for harmonic oscillator driven by Ornstein-Uhlenbeck noise with correlation times $\tau = 0.5$ (upper curves) and $\tau = 1.0$ (lower curves), with sharp initial conditions for the noise variable and other parameters as in Fig. 5.8(a). Note the logarithmic scale in T. The inset shows the same curves on the logarithmic scale in $\mathcal{F}(T)$.

$\mu_{ij} = \mu_{ji}$ being elements of the inverse correlation matrix $(\hat{C}_6)^{-1}$ and q_i being components of the vector $\vec{Q} = (x(T), v(T), x_0(0), v_0(0), \eta_0(0), z_0(0))$.

For simplicity, we assumed sharp initial conditions for the noise variables, i.e. η is reset after every spike to a fixed value η_0. The alternative assumption, that the neuron variables x, v are reset whenever $x(t)$ reaches the threshold *without* resetting $\eta(t)$, might be more realistic (Lindner, 2004). In this case all probability densities should be averaged with respect to the stationary density of noise variables *upon firing*. In general the calculation of this density is a nontrivial task. However, if the relaxation time of the noise variables is small compared to the refractory time, the stationary distribution of noise variables at $t = 0$ is a good approximation (Brunel and Sergi, 1998). Therefore, we confine ourselves to consideration of two sets of initial conditions for the noise variables: (i) sharp initial conditions: $P(\eta, t = 0) = \delta(\eta - \eta_0)$ for the Ornstein-Uhlenbeck noise and $P(\eta, z, t = 0) = \delta(\eta - \eta_0)\delta(z - z_0)$ for the harmonic noise; and (ii) stationary initial conditions [2] for the harmonic noise: $P_{st}(\eta, z) = (2\pi\sigma_\eta\sigma_z)^{-1} \exp(-\eta^2/2\sigma_\eta^2) \exp(-z^2/2\sigma_z^2)$, with $\sigma_\eta^2 = D/\Gamma\Omega_0^2$ and $\sigma_z^2 = D/\Gamma$.

The following three examples illustrate the quality of the Hertz, Stratonovich and truncation approximations in their validity regions, when applied to multidimensional FPT problems.

I. Hertz approximation. In Fig. 5.16 we plot the simulated FPT probability density and the Hertz approximation for the harmonic oscillator driven by the Ornstein-Uhlenbeck noise with sharp initial conditions. We choose two different values of the noise correlation time: $\tau = 0.5$ and $\tau = 1.0$. The reset value for the noise is $\eta_0 = 0$, and other parameters are as in Fig. 5.8(a). The noise intensity decreases with increasing τ, hence the mean FPT grows. Though $\mathcal{F}(T)$ preserves its structure as a whole, for larger values of τ the height of

---

[2] The averaging over the stationary initial conditions is obtained by the following integration:

$$\int_{-\infty}^{\infty}\int_{-\infty}^{\infty} \frac{P(x_p, v_p, t_p; \dots; x_1, v_1, t_1; x_0, v_0, \eta_0, z_0, 0)}{P_{st}(x_0, v_0, \eta_0, z_0)} P_{st}(\eta_0, z_0) d\eta_0 dz_0.$$

Note, that $P_{st}(x_0, v_0, \eta_0, z_0)$ does not factorize, since the crosscorrelations between x, v and the noise variables are not zero at $t = 0$.

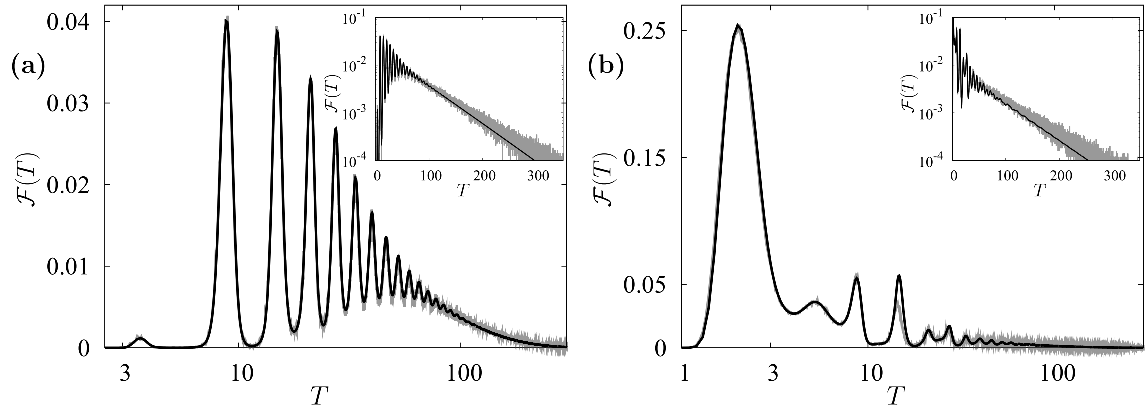

Figure 5.17: Simulation results (gray lines) and the Stratonovich approximation (black lines) for the FPT probability density for harmonic oscillator driven by harmonic noise. The parameters are $\omega_0 = 1, \gamma = 0.08, \Omega_0 = 0.41, \Gamma = 0.05, D = 0.002, x_b = 1, x_0 = -0.5, v_0 = 0$. (a) Sharp initial conditions for the noise $\eta_0 = 0, z_0 = 0$. (b) Stationary initial conditions for the noise. Note the logarithmic scale in T. The insets show the same curves on the logarithmic scale in $\mathcal{F}(T)$.

the main peak decreases and the weight of the exponential tail grows. For chosen values of the noise correlation time the Rice times equal $T_R = 829.2$ and $T_R = 4247.1$, respectively, and both significantly exceed $t_{rel} = 2.5$. This corresponds to the case of moderate friction and weak noise. In this case the Hertz approximation is absolutely sufficient.

II. Stratonovich approximation. In this example we consider the FPT density for the harmonic oscillator driven by harmonic noise of moderate intensity. We choose the following parameter set: $\omega_0 = 1, \gamma = 0.08, \Omega_0 = 0.41, \Gamma = 0.05, D = 0.002, x_b = 1, x_0 = -0.5, v_0 = 0$, such that $T_R = 47.6$ is larger than the relaxation time of the x-variable $t_{rel} = 40.0$ and the Stratonovich approximation is applicable. Panels (a) and (b) in Fig. 5.17 show the FPT density obtained with the sharp ($\eta_0 = 0, z_0 = 0$) and the stationary initial conditions for harmonic noise, respectively. As expected, the Stratonovich approximation reproduces the simulated FPT density with high accuracy in the whole time domain and for both sets of initial conditions for the noise variables.

It is worth to note the interesting structure of the FPT density in Fig. 5.17(a): its second peak is higher than the first one. This effect is due to the sharp initial conditions as discussed in Sections 2.4. The variance of x equals zero at $t = 0$ and then increases up to the stationary value. When the $x(t)$-trajectory approaches the threshold for the first time, the x-variance is not yet sufficiently large to provide a high probability to cross x_b. This probability turns out to be larger when the trajectory approaches the turning point for the second time. This effect disappears if we choose the stationary initial conditions for the colored noise, see Fig. 5.17(b).

III. Truncation approximations. We consider the harmonic oscillator driven by harmonic noise with sharp initial conditions. Let us choose the same parameter set as in the previous example except for a larger noise intensity $D = 0.01$. In this case of strong noise, the

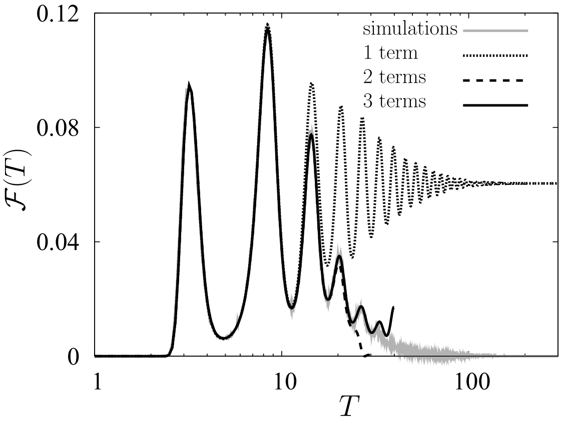

Figure 5.18: Simulation results and truncations for the FPT density for the harmonic oscillator driven by harmonic noise with sharp initial conditions. Parameters are as in Fig. 5.17 (a) except for a larger noise intensity $D = 0.01$. Simulation results are shown with a gray line, 1 term truncation with a black dot line, 2 terms truncation with a black dashed line, and 3 terms truncation with a black solid line. The mean FPT obtained from simulations equals 16.1, the median of distribution lies by 14.0. Note the logarithmic scale in T.

mean interval between upcrossings $T_R = 16.5$ is smaller than the relaxation time $t_{rel} = 40.0$ and the decoupling approximations cannot be applied. However, the largest part of the first passage probability is concentrated in the first few peaks of $\mathcal{F}(T)$ and is well reproduced by the truncation approximations. Fig. 5.18 shows the simulated FPT density (gray line) and 1,2 and 3 terms truncations (dot, dashed and solid black lines, respectively). The numerically estimated mean FPT equals 16.1 and the median of the distribution is 14.0 for the given parameter set. In absolute agreement with results of Section 5.2.2, the 1 term truncation saturates at constant value $n_0 = 1/T_R$ for large T , and the second and the third truncations diverge to minus and plus infinity, respectively, as $T \to \infty$.

5.4 Interspike interval densities in the FitzHugh-Nagumo model

Two previous sections were devoted to the detailed examination of analytical approximations for the FPT density of a differentiable non-Markovian process $x(t)$. Although we applied the theory to the linear case of a harmonic oscillator driven by white or colored Gaussian noise, the linearity of the system is in general not required. The approximations connect the FPT density to the joint densities of upcrossings $n_p(t_p, \ldots, t_1)$, which are expressed through the joint PDFs of $x(t)$ and its velocity $v(t)$, Eq. (5.2). In a generic nonlinear system these joint PDFs are not Gaussian and cannot be obtained analytically. To overcome this difficulty, one can solve the Fokker-Planck equation numerically and then insert the numerically obtained joint PDFs of x and v into Eq. (5.2). We apply this approach to obtain the ISI density in the FitzHugh-Nagumo model in order to demonstrate the applicability of our approximations to nonlinear FPT problems.

We have to emphasize the rather illustrative character of this section for two reasons. First, the numerical solution of the backward Fokker-Planck equation with an absorbing boundary at x_b gives immediately the FPT density, see Eqs. (4.11a) and (4.11b), and is not computationally more expensive than the solution of the forward Fokker-Planck equation without the absorbing boundary. Hence the former method might be more adequate in applications. Second, to obtain $n_p(t_p, \ldots, t_1)$ one has to compute the joint PDFs of x and v at $x = x_b$ for all $t_p, \ldots, t_1$. For $p \geqslant 2$ this requires the numerical solution of the Fokker-

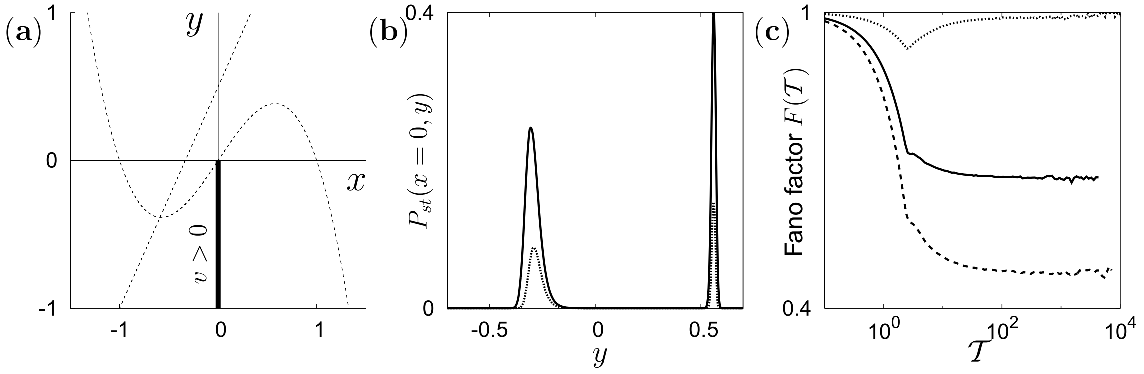

Figure 5.19: (a) Phase space of the FN model. Nullclines are plotted with the dashed lines. The thick line marks the part of the boundary $x = 0$, where the velocity is positive $\dot{x} = v > 0$. (b) Stationary probability distribution $P_{st}(x = 0, y)$ at the boundary $x = 0$ obtained from the numerical solution of the Fokker-Planck equation for the FN model with $D = 0.0002$ (dashed line) and $D = 0.0004$ (solid line) and with other parameters $\epsilon = 0.05, \gamma = 1.5, b = 0.5$. (c) Fano factor $F(\mathcal{T})$ for spike trains obtained from simulations of the FN model with $D = 0.0002$ (dot line), $D = 0.0004$ (solid line) and $D = 0.0006$ (dashed line) and other parameters as in (b).

Planck equation for all possible initial conditions lying on the boundary x_b. This task is impracticable, therefore one has to restrict oneself to the 1 term truncation and the Hertz approximation, which make use of $n_1(t)$ only. However, these approximations have rather narrow validity regions, and the direct Langevin simulation might be more efficient in most cases. The practical value of the approach, combining numerical solution of the Fokker-Planck equation and analytical approximations for the FPT density, is limited to weak noise situations, when the Hertz approximation is accurate and the mean FPT is large and requires long simulation time.

We consider the FitzHugh-Nagumo (FN) model driven by white Gaussian noise:

$$\begin{aligned} \epsilon\dot{x} &= x - x^3 - y, \\ \dot{y} &= \gamma x - y + b + \sqrt{2D}\xi(t). \end{aligned} \tag{5.43}$$

This model generates spike trains similar to those presented in Fig. 3.4. We choose the parameter set $\epsilon = 0.05, \gamma = 1.5, b = 0.5$, for which the FN model possesses one stable focus in the phase space and shows subthreshold oscillations. In Chapter 3 we have shown, that in this resonant regime spikes form clusters and the density of interspike intervals (ISI) has a multimodal structure (see Fig. 3.6). Let us see how such multimodal ISI densities can be obtained semi-analytically using the Hertz approximation and numerically obtained joint PDFs of x and y.

The problem of finding the ISI density is essentially the *recurrence time* problem for the x-variable (Rice, 1945; Stratonovich, 1967). The recurrence time is defined as the time T, when a random process $x(t)$ performs an upcrossing of the level x_b, assumed there was an upcrossing at $t = 0$ and no upcrossings in-between. The moment of the spike occurrence in the FN model can be determined as the time when the x-variable crosses $x_b = 0$ with positive velocity. The ISI density is given by the probability density of the recurrence time.

The problems of the first passage and of recurrence to a given boundary x_b are closely related. The only difference consist in the initial conditions, which coincide with the boundary x_b in the case of the recurrence time problem. The same line of reasoning developed in Sections 5.1 and 5.2 can be applied to obtain analytical approximations for the recurrence time PDF. The latter have the same form as the approximations for the FPT density although with different initial conditions for $n_p(t_p, \ldots, t_1)$. Namely, $n_1(t)$ is given by

$$n_1(t) = \int_0^\infty vP^\star(x_b, v, t|x_b, \{v_0\}, 0)dv, \tag{5.44}$$

where $P^\star(x, v, t|x_b, \{v_0\}, 0)$ is the transition probability density for the FN model in the variables x and $v = \dot{x}$. We formally put $\{v_0\}$ for the velocity initial condition and postpone its specification to the next paragraph. Since in our case $x_b = 0$, from Eq. (5.43) it follows that the velocity at the moment of an upcrossing equals $v = -y$. Changing in Eq. (5.44) to the x- and y-variables we get

$$n_1(t) = \int_{-\infty}^0 yP(x_b, y, t|x_b, \{y_0\}, 0)dy. \tag{5.45}$$

Here $P(x, y, t|x_b, \{y_0\}, 0)$ is the transition probability density in the x, y plane obeying the Fokker-Planck equation (Risken, 1989)

$$\partial_t P(x, y, t) = \left(-\frac{1}{\epsilon}\partial_x(x - x^3 - y) + \partial_y(y - \gamma x - b + D\partial_y)\right) P(x, y, t) \tag{5.46}$$

with initial conditions

$$P(x, y, t = 0) = \delta(x - x_b)P_0(y). \tag{5.47}$$

Notice from Eq. (5.45) that $n_1(t)$ is the probability current in the x-direction across the boundary $x = 0, y < 0$, marked with a thick line in Fig. 5.19(a).

Let us now specify the initial conditions. $P_0(y)$ is the stationary density of y values *upon firing*, which we have already encountered in Section 5.3. For the FN model with $x_b = 0$ this is simply the normalized stationary density on the line $x = 0, y < 0$ (see Fig. 5.19(a)): $P_0(y) = n_0^{-1}\Theta(-y)P_{st}(x = 0, y)$, where $\Theta(y)$ is the Heaviside step function and the normalization constant $n_0 = \int_{-\infty}^0 P_{st}(x = 0, y)dy$ is the mean firing rate as follows from Eq. (5.45).

We numerically solved the Fokker-Planck equation (5.46) using the method of finite differences (Thomas, 1995) to obtain the stationary solution $P_{st}(x, y)$. Numerically found $P_{st}(x = 0, y)$ is shown in Fig. 5.19(b) for $D = 0.0002$ and $D = 0.0004$ and exhibits two peaks. The peak on negative y values corresponds to $P_0(y)$ except for normalization. The peak on positive y is extremely narrow, thus the probability flow in the negative x-direction is confined to a very narrow region in phase space. Note that the integral over $P_{st}(x = 0, y)$ increases with the noise intensity due to increase of the mean firing rate.

We can formally split the recurrence time into the relaxation from x_b to the fixed point and further activation to x_b. The activation process is dominated by the noise and escape

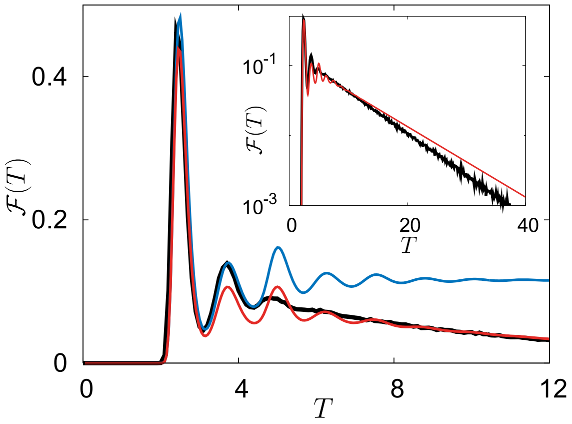

Figure 5.20: Semi-analytical approximations for the ISI density in the FN model with parameters $\epsilon = 0.05, \gamma = 1.5, b = 0.5, D = 0.0004$. ISI density obtained from the Langevin simulations is depicted with a black line, the Hertz approximation with a red line, and the 1 term truncation $n_1(T)$ with a blue line. The inset shows the curves on the logarithmic scale in $\mathcal{F}(T)$.

from the vicinity of the fixed point occurs along random trajectories, in accordance with a finite variance of $P_0(y)$. In contrast, due to the small parameter ϵ, the relaxation occurs almost along a deterministic trajectory, only slightly perturbed by noise, once the trajectory approaches the right branch of the cubic nullcline. This is manifested in the narrowness of the peak in $P_{st}(x=0,y)$ on $y>0$. Therefore the initial value of y on the line $x=x_b$ does not significantly influence the recurrence time. Without lost of accuracy we can replace the initial conditions Eq. (5.47) with the sharp initial conditions

$$P(x,y,t=0) = \delta(x-x_b)\delta(y-y_0), \tag{5.48}$$

where we choose $y_0 = -0.3$, approximately corresponding to the maximum of $P_0(y)$.

We numerically solve the Fokker-Planck equation (5.46) with initial conditions (5.48) using the finite differences method, and then insert the numerically calculated joint PDF of x and y into Eq. (5.45) to obtain $n_1(t)$. The ISI density $\mathcal{F}(T)$ in the Hertz approximation is found by numerical evaluation of $\mathcal{F}(T) = n_1(T)\exp(-\int_0^T n_1(t)dt)$.

Before discussing results for the Hertz approximation, recall that it is effective only if all correlations decay during the time interval between two successive upcrossings. In Section 5.2.5 we derived the condition for the applicability of the Hertz approximation in the form $F_\infty \approx 1$, where F_∞ is the asymptotic value of the Fano factor for the sequence of upcrossings, i.e. for the spike train in the FN model. To assess whether this condition is fulfilled for different noise intensities, we plot the Fano factor curves for the spikes trains obtained by Langevin simulations of the FN model with $D = 0.0002, 0.0004$ and 0.0006 in Fig. 5.19(c). For low noise intensities ($D = 0.0002$) F_∞ is quite close to 1, and deviates stronger from 1 with increasing D. This dependence of F_∞ on the noise intensity follows from the relation Eq. (5.37). The correlation time τ_{cor} does not depend on noise, whereas the mean firing rate n_0 increases with D involving decrease of F_∞. We expect the Hertz approximation to be very accurate for $D = 0.0002$. The quality of the approximation is reduced for higher noise intensities.

The semi-analytical approximations for the ISI density in the FN model with $D = 0.0004$ are presented in Fig. 5.20. The ISI density obtained from Langevin simulations is plotted with a black line, the Hertz approximation with a red line, and the 1 term truncation $n_1(T)$ with a blue line. The accuracy of the Hertz approximation is fairly good in the whole time domain, though $F_\infty = 0.66$ for these parameter values. We also computed the Hertz approximation for the FN model with other noise intensities. For $D = 0.0002$ the Hertz approximation is very accurate in the whole time domain, and for $D = 0.0006$ its quality is still satisfactory (data not shown).

In accord with the results of Section 5.2.2, $n_1(T)$ in Fig. 5.20 reproduces the initial part of the ISI density and then saturates to the mean firing rate n_0. In contrast to the harmonic oscillator, $n_1(T)$ is very accurate in the estimation of the two initial peaks and fails only in the third peak of the ISI density. This is explained by the existence of an additional time scale in the FN model, the refractory time τ_{ref}, which is absent in the harmonic oscillator. τ_{ref} is essentially the relaxation time from x_b to the fixed point and determines the minimal interspike interval. Therefore $\int_0^T n_2(T,t)dt$ vanishes for times $T < 2\tau_{ref}$ and $n_1(t)$ is very accurate up to $2\tau_{ref}$. For parameter values as in Fig. 5.20 $\tau_{ref} \sim 2$. Since the peaks in the ISI density follow with the period of subthreshold oscillations $T_p \sim 1.1$, the two initial peaks are reproduced by $n_1(t)$.

Summary

In a multitude of physical systems the escape from a metastable state is characterized by a time-dependent escape rate and a non-exponential first passage time distribution. In this chapter we discussed the first passage time problem for systems with subthreshold oscillations and non-negligible relaxation time after a reset. The FPT densities in such non-Markovian models can be obtained by means of the theory of level-crossings. The joint densities of multiple upcrossings for a random process $x(t)$ can be obtained in the case of differentiable trajectories. The FPT density is expressed in terms of an infinite series of multiple integrals over all joint densities of upcrossings, or equivalently, in terms of the cumulant functions.

We consider two types of approximations for this infinite series. The truncations and Padé approximants include the first few terms of the series calculated exactly. They reproduce well the FPT density on short and intermediate time scales and can be used, when the largest part of the FPT probability is concentrated in the first few peaks, i.e. when the threshold value is low or the noise is strong.

The decoupling approximations can be derived for the case of weakly correlated upcrossings. The higher order cumulant functions are approximately expressed through the lower order cumulant functions and the infinitely many terms sum up to the closed expression for $\mathcal{F}(T)$. The Hertz approximation (which neglects all correlations between upcrossings) is sufficient for the case of moderate friction and moderate noise intensity. The Stratonovich approximation (which approximates the higher order cumulant functions through the first and the second order cumulant functions) performs even better and does not loose its accuracy for high noise intensities or in the slightly overdamped regime.

The applicability of these approximations is illustrated by a noise driven harmonic oscillator, with a threshold at x_b and reset to sharp initial conditions, i.e. the resonate-and-fire model of a neuron. The regions of validity for the approximations cover all different types of the subthreshold dynamics. The approximations reproduce all qualitatively different structures of the FPT densities: from monomodal through bimodal to multimodal densities with several decaying peaks. The approximations hold for systems of arbitrary dimension as is illustrated by application of the approximations to a harmonic oscillator driven by the Ornstein-Uhlenbeck or by harmonic noise.

The analytical approximations are also applicable to the nonlinear FPT and recurrence time problems. The difficulty consist in obtaining the joint PDFs for the random variables involved. The semi-analytical approach, which combines the numerical solution of the Fokker-Planck equation and the Hertz approximation, might be useful in the case of weak noise, when Langevin simulations would require long simulation time.

6

Firing statistics in stochastic resonate-and-fire neurons

In Chapter 3 we have shown, that the interspike interval density is one of the most important functions characterizing random firing patterns in neurons. It provides a very sensitive instrument for assessment of the type of subthreshold dynamics. Its first moment is the inverse mean firing rate, its second moment defines the coefficient of variation for a spike train, and the Fourier transform of the ISI density is connected to the power spectrum of the spike train. Using the analytical methods developed in Chapter 5 allows to calculate the ISI densities for some renewal neuron models, including the resonate-and-fire model. With the help of these methods, several questions concerning the dynamics of a single cell can be answered. Among them there are two of great importance:

— What is the impact of intrinsic channel noise on the neuron dynamics?

— How do subthreshold properties influence the firing patterns in neurons?

Though these questions have been addressed in many experimental and theoretical studies, the joint effect of the channel noise and subthreshold resonance on the spike generation is still not completely understood. The aim of this chapter is to show, that the interplay of these two phenomena in a cell may lead to new dynamical behaviors with possible implications for increasing the reliability and selective communication in networks.

Intrinsic noise of ion channels is constantly present in neurons (White et al., 2000). It was shown to be an essential ingredient for a variety of phenomena in the nervous system. For example, channel noise may be critical in determining the reliability and precision of spike timing (Schneidman et al., 1998). It may expand the repertoire of dynamical behaviors of some neurons (Dorval and White, 2005; Ozer and Ekmekci, 2005; Ginzburg and Pustovoit, 2003; Lowen et al., 1999; White et al., 1998). Nowadays, the idea that channel noise may play a constructive role in information processing became widely accepted (Traynelis and

---

This chapter is adopted from Verechtchaguina et al. (2007).

Jaramillo, 1998). In particular, the well known phenomenon of stochastic resonance was ascribed to a collective property of ion channel assemblies. (Moss et al., 2004; Adair, 2003; Schmid et al., 2001; Jung and Shuai, 2001; Goychuk and Hänggi, 2000; Collins et al., 1995a).

The relations between sub- and suprathreshold responses in neurons have also been extensively studied. The influence of subthreshold resonance on the neuronal firing rate (Svirskis and Rinzel, 2003; Brunel et al., 2003; Richardson et al., 2003; Schreiber et al., 2004), firing rate modulation and spike timing precision (Desmaisons et al., 1999; Haas and White, 2002) has been explored. In particular, the spike clustering was associated with the subthreshold oscillations of the membrane potential (Chen and Shepherd, 1997; Izhikevich et al., 2003). Desmaisons et al. (1999) and Amir et al. (2002) observed, that the number of spikes within a cluster becomes larger as the constant input current I_0 increases. The ISI within a cluster was found to be almost independent of the value of I_0, whereas the intervals between neighboring clusters decrease with increasing I_0.

Motivated by these experimental observations, we systematically analyze the relation between the subthreshold resonance and the statistics of spontaneous firing in the resonate-and-fire model in response to a constant input current. We find, that the qualitative features observed experimentally in firing patterns of resonant neurons are reflected in the interspike interval densities, and demonstrate how these features arise from the interplay between intrinsic oscillations and channel noise. Recent experimental findings (Braun et al., 1994; Huber and Braun, 2006; Izhikevich et al., 2003; Villacorta and Panetsos, 2005) reveal, that noise in combination with intrinsic oscillations can provide new encoding properties to neurons, suggesting possible implications of our results for neuron communication.

The first two sections of this chapter are devoted to the derivation of the resonate-and-fire model with an additive noise term accounting for the stochastic nature of ion channels. This version of the RaF model will be used in Section 6.3 and throughout Chapter 7 to model spontaneous activity in resonant and nonresonant neurons. In Section 6.1 we give a detailed derivation of the Langevin dynamics for a population of Markovian ion channels. The resulting fluctuating conductance enters the resonate-and-fire model as a multiplicative noise term, which can be reduced to an additive noise term after simplifications based on time scale separation, as is shown in Section 6.2. In Section 6.3 we study the influence of intrinsic noise and subthreshold oscillations on the firing statistics in the resonate-and-fire model with physiologically relevant parameters.

6.1 Langevin description of stochastic ion channels

Even in the absence of an input signal, the membrane potential fluctuates around the holding potential due to the stochastic opening and closing of ion channels (for a review see White et al., 2000). Stochastic ion channels are typically represented as Markovian transitions between open and closed states with rates depending on the membrane potential (Sakmann and Neher, 1995). Three methods have been used for modeling a population of stochastic ion channels. In the first method, the states of individual ion channels are tracked and updated according to appropriate probability functions (Sakmann and Neher, 1995). The second method takes advantage of the presumed independence and Markovian property of individual channels and only tracks the instantaneous number of channels in each state (Lowen et al., 1999). The third method is based on the Gaussian approximation of the channel noise terms, which is accurate if the number of channels is sufficiently large. Destexhe et al. (2001) modeled synaptic conductances in the Hodgkin-Huxley equations by the Ornstein-Uhlenbeck process. In Fox and Lu (1994) the Langevin description of the Hodgkin-Huxley conductances is derived from the master equation for the gating variables. The Gaussian approximation method is especially attractive, because it allows an analytical treatment of the stochastic neuronal dynamics.

Following Fox and Lu (1994), we present here the derivation of the Langevin dynamics for a population of N ion channels, entering the RaF model as leak conductance $g(t) = 1/R(t)$. In the simplest description, every channel resides in one of only two possible states, open or closed, with transition rates $\alpha(V)$ and $\beta(V)$ between them, which are generally voltage dependent:

$$\text{Open} \underset{\beta}{\overset{\alpha}{\rightleftarrows}} \text{Closed.}$$

Since the linear RaF model is only valid for small deviations from the holding potential, the voltage dependence of α and β can be disregarded.

Let p denote the probability for a single channel to be in the open state. The rate equation for p has the form

$$\dot{p} = \beta(1-p) - \alpha p, \tag{6.1}$$

and its stationary solution p_0 determines the steady-state fraction of open ion channels:

$$p_0 = \frac{\beta}{\alpha+\beta}. \tag{6.2}$$

The probability $P(n,t)$ that n channels in the population are open at time t satisfies the master equation for a one-step process[1] (van Kampen, 1992):

$$\dot{P}(n,t) = \beta(N-n+1)P(n-1,t) + \alpha(n+1)P(n+1,t) - (\alpha n + \beta(N-n))P(n,t), \tag{6.3}$$

whose stationary solution $P(n)$ is a binomial distribution

$$P(n) = \frac{1}{\sqrt{2\pi N p_0(1-p_0)}} \exp\left(-\frac{(n-Np_0)^2}{2Np_0(1-p_0)}\right), \tag{6.4}$$

with p_0 given by Eq. (6.2).

For sufficiently large N, the standard procedure (van Kampen, 1992; Fox, 1978) leads to the Fokker-Planck approximation of the Markov process determined by the master equation (6.3). Introducing the instantaneous fraction of open channels $y = n/N$, we obtain the Fokker-Plank equation for the corresponding probability density $P(y,t) = P(n,t)/N$ in the form:

$$\frac{\partial}{\partial t}P(y,t) = -\frac{\partial}{\partial y}\left[\beta(1-y) - \alpha y\right]P(y,t) + \frac{\partial^2}{\partial y^2}\left[\frac{\alpha y + \beta(1-y)}{2N}\right]P(y,t). \tag{6.5}$$

---

[1] To account for reflecting boundary conditions, Eq. (6.3) has to be replaced with $\dot{P}(0,t) = \alpha P(1,t) - \beta N P(0,t)$ and with $\dot{P}(N,t) = \beta P(N-1,t) - \alpha N P(N,t)$ for $n = 0$ and $n = N$, respectively.

We further simplify this Fokker-Planck equation (6.5) by replacing y in the diffusion term by its steady-state value p_0 given by Eq. (6.2). Indeed, fluctuations of y are of the order $1/\sqrt{N}$ and the diffusion term itself is proportional to $1/N$. Hence the y-dependence of the diffusion term is negligibly small for large N. Substitution of p_0 instead of y leads to the Fokker-Planck equation with a constant diffusion coefficient:

$$\frac{\partial}{\partial t}P(y,t) = -\frac{\partial}{\partial y}\left[\beta(1-y) - \alpha y\right]P(y,t) + \frac{\partial^2}{\partial y^2}\left[\frac{\alpha\beta}{N(\alpha+\beta)}\right]P(y,t). \tag{6.6}$$

The stationary solution of Eq. (6.6) is a Gaussian distribution with mean p_0 and variance $p_0(1-p_0)$.

Now the Langevin description for the instantaneous fraction of open ion channels $y(t)$ can be formulated. The Langevin equation, equivalent to the Fokker-Planck equation (6.6), reads (van Kampen, 1992):

$$\dot{y} = \beta(1-y) - \alpha y + \sqrt{\frac{2\alpha\beta}{N(\alpha+\beta)}}\xi(t), \tag{6.7}$$

where $\xi(t)$ is Gaussian white noise of unit intensity. The membrane conductance $g(t) = \varepsilon y N$ is proportional to the instantaneous number of open channels and to the single-channel conductance ε. From Eq. (6.7) it therefore follows the Langevin equation for the fluctuating conductance:

$$\dot{g}(t) = -\frac{g(t) - g_0}{\tau} + \sqrt{2D}\xi(t). \tag{6.8}$$

Here, the new parameters are: the steady-state membrane conductance $g_0 = \varepsilon p_0 N$, the activation time constant $\tau = 1/(\alpha+\beta)$, and the noise intensity $D = \varepsilon^2 N p_0(1-p_0)/\tau$. The conductance $g(t)$ determined by Eq. (6.8) is the Ornstein-Uhlenbeck noise, whose correlation time is τ, mean g_0 and variance $D\tau$. Hence the relative dispersion of conductance fluctuations $\sqrt{D\tau}/g_0 = \sqrt{(1-p_0)/p_0 N}$ decreases with the number of ion channels as $1/\sqrt{N}$.

Summarizing the above arguments, the effect of a population of N ion channels which open and close independently and with constant rates can be reduced to the Langevin dynamics for the corresponding conductance as described by Eq. (6.8). Parameters entering this description are the single-channel conductance ε, the number of ion channels N, the activation time constant τ, and the steady-state opening probability p_0.

We note that conductance fluctuations have been studied experimentally in neurons of neocortex (Jacobson et al., 2005), hippocampus (Diba et al., 2004), entorhinal cortex (White et al., 1998) and in cerebellar Purkinje cells (Kay et al., 1998). In neurons of the entorhinal cortex White et al. (1998) established, that the persistent Na$^+$ channels are responsible for as much as 80% of the variance of recorded currents and were able to estimate the parameters ε, τ, N and p_0 for this type of channels. In particular, the frequency content of the Na$^+$ current was found to be broadband with the cut off frequency $\geqslant$1 kHz, which implies that the activation time constant of the persistent Na$^+$ channels is $\tau \leqslant$0.16 ms. The relative dispersion of the conductance fluctuations estimated from the data of White et al. (1998) ranges from 0.05 to 0.13.

6.2 Stochastic resonate-and-fire model

In Section 2.1.3 we introduced the deterministic resonate-and-fire model of a neuron, represented by the electric circuit in Fig. 2.4(b). In the underdamped regime the RaF model shows oscillatory relaxational behavior and a maximum in the impedance function at finite frequency, consistent with the subthreshold properties of resonant neurons. In contrast, the relaxational behavior is monotonic and the impedance function is maximal at zero frequency in the overdamped RaF model, as is the case for nonresonant neurons.

In the deterministic RaF model the dynamics of the membrane potential $V(t)$ and the current $I_L(t)$ through the inductive branch are given by (see Eq. (2.6)):

$$\begin{aligned} C\frac{dV}{dt} &= -\frac{1}{R}V - I_L + I_0, \\ L\frac{dI_L}{dt} &= -I_L R_L + V - V_0. \end{aligned} \tag{6.9}$$

The fluctuations arising from stochastic acting of ion channels are described by the Langevin equation (6.8) for the conductance $g(t) = 1/R(t)$, derived in the previous section. The fluctuating conductance $g(t)$ enters the RaF model Eq. (6.9) as a multiplicative noise term. Therefore several simplifications are necessary to make the stochastic RaF model mathematically more tractable.

First, we introduce a new variable $U(t) = V(t) - V_r$ describing the deviation of the voltage $V(t)$ from the resting potential $V_r = V_0/(1+R_L/R)$. We only consider constant input currents I_0 and replace the two first order differential equations (6.9) by a second order differential equation:

$$C\frac{d^2U}{dt^2} + \left(g(t) + \frac{R_L C}{L}\right)\frac{dU}{dt} + \frac{1}{L}\left(1 + R_L g(t)\right)U = \frac{R_L I_0}{L} - (U + V_r)\frac{dg(t)}{dt}. \tag{6.10}$$

The time scale of conductance fluctuations ($\tau \leqslant 0.16\,\text{ms}$) is small compared to the characteristic time scale of the subthreshold voltage dynamics (10 to 100 ms). Using this time scale separation, we replace $g(t)$ in Eq. (6.10) by its mean value $g_0 = 1/R$ and $U(t)$ in front of the noise term by its stationary value $U_s = I_0 R_L/(1 + R_L/R)$. The last term in Eq. (6.10) thus reads: $(U_s + V_r)\sqrt{2D}\xi(t)$. After these transformations, the stochastic RaF model, Eqs. (6.10) and (6.8) reduces to the equation for a harmonic oscillator driven by white Gaussian noise:

$$C\frac{d^2U}{dt^2} + \gamma\frac{dU}{dt} + \omega^2 U = f_0 + \sqrt{2Q}\xi(t). \tag{6.11}$$

Here the frequency ω, the friction coefficient γ, the external constant force f_0 and the noise intensity Q are related to the parameters of the RLC circuit by

$$\begin{aligned} \gamma &= \frac{1}{R} + \frac{R_L C}{L}, & \omega^2 &= \frac{1}{L}\left(1 + \frac{R_L}{R}\right), \\ f_0 &= \frac{R_L}{L}I_0, & Q &= D\left(\frac{I_0 R_L + V_0}{1 + R_L/R}\right)^2. \end{aligned} \tag{6.12}$$

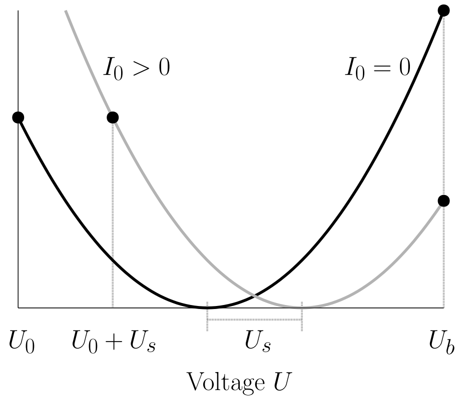

Figure 6.1: Schematic sketch of the effective harmonic potential revealing the effect of the constant input current $I_0 \propto U_s$. Whereas the reset voltage U_0 shifts together with U_s, the location of the barrier value U_b remains unaffected by changing I_0.

In the underdamped regime ($\gamma < 2\omega$), the stochastic RaF model Eq. (6.11) shows noisy subthreshold oscillations with the period $T_p = 2\pi/\sqrt{\omega^2 - \gamma^2/4}$ and the relaxation time $t_{rel} = 2/\gamma$. In the overdamped regime ($\gamma > 2\omega$) the RaF model Eq. (6.11) exhibits a nonresonant subthreshold dynamics with monotonically decaying correlation functions.

To account for excitability of the neuron dynamics, the RaF model has to be supplemented with a spike generation mechanism, which in the simple description can be reduced to the fixed threshold and reset value for the voltage variable. Since we intend to study the changes in the firing statistics caused by the injection of a constant current, we have to specify how the threshold and reset values depend on the holding potential. To the best of our knowledge, no experimental data on this has been published. Therefore we opt for the intuitive scheme sketched in Fig. 6.1. Equation (6.11) describes the diffusion of the voltage $U(t)$ in a harmonic potential, whose minimum is at $U = 0$ if $I_0 = 0$. The threshold is set at value $U_b > 0$ and reset at $U_0 < 0$. The injection of an input current I_0 shifts the stationary voltage drop to $U_s = I_0 R_L/(1 + R_L/R)$. Thereby the reset value shifts to $U_0 + U_s$ together with the holding potential, while the threshold value remains unchanged. All other parameters are assumed to be unaffected by the shift of the stationary voltage. In this scheme the injection of a positive current $I_0 > 0$ effectively lowers the threshold and involves increase in the firing rate, in consistency with observations made in stellate and pyramidal cells (Erchova et al., 2004; Desmaisons et al., 1999).

We derived the RaF model Eq. (6.11), where the additive noise term accounts for the stochasticity of ion channels. In the case of a constant input current, the ISI density in the RaF model, with threshold and reset conditions formulated above, is given by the first passage time density for a harmonic oscillator. Several approximate analytical solutions for the latter were derived in Chapter 5. In the next section we use the Stratonovich approximation to calculate the ISI densities in the resonate-and-fire model with parameters similar to those in stellate and pyramidal cells. The Stratonovich approximation is the most accurate approximation for these parameters, corresponding to the regime of moderate friction and moderate noise intensity.

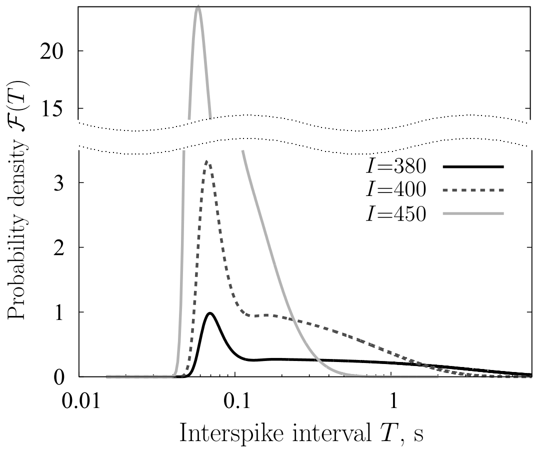

Figure 6.2: ISI density in the RaF model with conductance noise for three different values of the input current I_0 (in pA) in Stratonovich approximation. Parameters are chosen as for a typical stellate cell: $1/g_0 = R$=56.7 MΩ, R_L=46.1 MΩ, C=3.1·10^{-4}μF, L=1.26 MH, $V_r = -61.5$ mV, D=10^{-5}Hz·MΩ^{-2}, $U_0 = -7$mV, U_b=12mV.

6.3 Firing statistics in resonate-and-fire neurons

In this section we perform explicit calculations of the ISI densities for typical stellate and pyramidal cells modeled by the stochastic RaF model. We use parameter sets obtained by Erchova et al. (2004) by fitting the impedance function of the RaF model to those measured in stellate (resonant) and pyramidal (nonresonant) cells in the entorhinal cortex in rat. These parameter sets only relate to the deterministic subthreshold voltage dynamics and disregard nonlinearities, such as the change of parameters with the shift of the holding potential. In Erchova et al. (2004) no measurements related to the intensity of intrinsic noise were performed. In our theoretical calculations, the noise intensity will be therefore tuned to match realistic values of the mean firing rate, similar to those in Erchova et al. (2004), and of the relative dispersion of conductance fluctuations, similar to those in White et al. (1998). Finally, the threshold and reset values for the voltage variable are fixed at $U_0 = -7$ mV and $U_b = 12$ mV; and the spike duration, i.e. the time between the onset of a spike and the reset to U_0, is assumed to be τ_r=15 ms. The choice of these values is based on our observations of the records provided by I. Erchova.

In Figs. 6.2 and Fig. 6.4 we use the mean values of R, R_L, L and C obtained experimentally for populations of stellate and pyramidal cells, respectively. In Fig. 6.3 we chose a particular parameter set from the range of values measured in the stellate cells. These parameter sets correspond to the slightly underdamped and slightly overdamped situations for a harmonic oscillator, both in the range of validity for the Stratonovich approximation (Verechtchaguina et al., 2006a,b). All ISI densities are shifted by τ_r to larger values to account for a finite spike duration.

The ISI densities for a typical stellate cell are presented in Fig. 6.2. They exhibit a well pronounced peak on short times separated by a minimum from the rest of the distribution. The occurrence of this peak is explained by the increased probability to reach the threshold in the maxima of the subthreshold oscillation, whose initial phase is fixed by the reset value. In terms of spike clusters, the peak corresponds to the ISI within a cluster, that is the

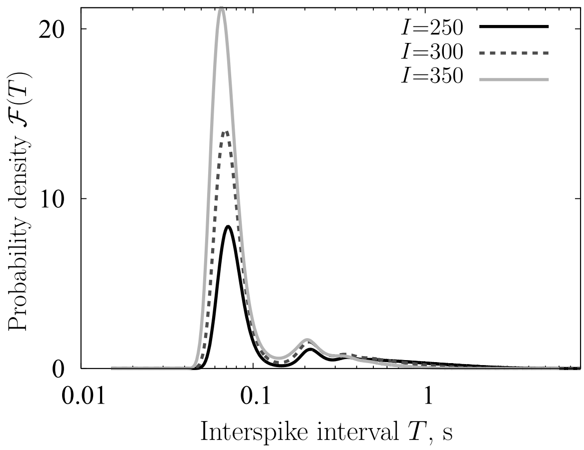

Figure 6.3: ISI density in the RaF model with conductance noise for three different values of the input current I_0 (in pA) in Stratonovich approximation. The parameters are chosen to model a stellate cell: $1/g_0 = R$=500 MΩ, R_L=25 MΩ, C=2.1 $\cdot 10^{-4}\mu$F, L=2.5 MH, $V_r = -61.5$ mV, D=5 $\cdot$ 10^{-6}Hz·MΩ^{-2}, U_0=−7mV, U_b = 12mV.

most probable interspike interval and equals approximately $0.5T_p + \tau_r \sim 70$ ms. On time scales larger than the relaxation time t_{rel} the phase of the subthreshold oscillation becomes stationary, and the ISI density therefore decays exponentially. This exponential tail of the distribution reflects the intervals between neighboring spike clusters.

The bimodal structure of the ISI densities reflects the existence of two time scales in the neuron output. These are the ISI within a spike cluster determined by the subthreshold relaxational behavior, and the time interval between neighboring clusters governed by a noise-activated rate process. Whereas the former is independent of the threshold position, the latter becomes smaller for lower thresholds. The different dependence of these time scales on the threshold value explains the changes in the ISI density caused by injection of a constant current I_0. With increasing I_0, the threshold becomes lower and the mean ISI decreases mostly due to the reduction of intervals between clusters: the exponential decay becomes faster. The time scale within a cluster, i.e. the most probable ISI, remains almost unaffected: there is no shift of the main peak as I_0 changes. The weight of the main peak grows with increasing I_0, reflecting the increase in the mean number of spikes within a cluster. All results are in good agreement with experimental observations (Desmaisons et al., 1999; Amir et al., 2002).

The number of peaks visible in the ISI density depends on the ratio between T_p and the relaxation time t_{rel}. For parameter values as in Fig. 6.2 T_p = 126 ms and t_{rel} = 21 ms, and therefore only one peak is really pronounced. In Fig. 6.3 we show results for another stellate cell, with parameters chosen so that the period of the subthreshold oscillation equals T_p = 144 ms and the relaxation time t_{rel} = 102 ms is considerably larger than t_{rel} for the cell in Fig. 6.2. The ISI densities in Fig. 6.3 show two distinct peaks followed by an exponential tail. All other properties of these ISI densities are analogous to those described in the previous paragraph.

In contrast to resonant neurons, we plot in Fig. 6.4 the ISI densities for a typical non-resonant pyramidal cell, with parameters corresponding to the overdamped situation. All interspike interval densities obtained for this cell have a monomodal structure with a single

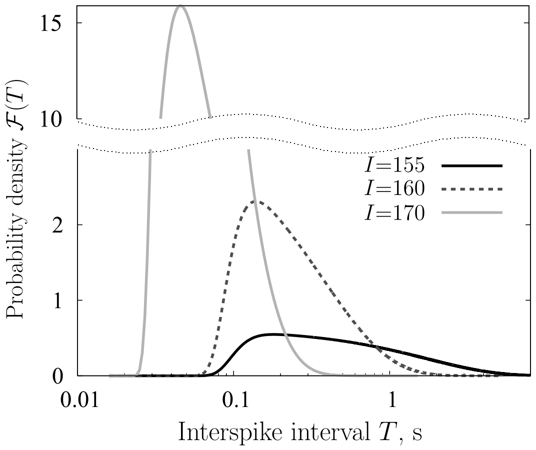

Figure 6.4: ISI density in the RaF model with conductance noise for three different values of the input current I_0 (in pA) in Stratonovich approximation. The parameters are as for a typical pyramidal cell: $1/g_0 = R = 69.9$ MΩ, R_L=34661 MΩ, C=$3.1 \cdot 10^{-4}\mu$F, L=173 MH, $V_r = -70.4$mV, D=10^{-5}Hz·MΩ^{-2}, $U_0 = -7$mV, $U_b = 12$mV.

maximum followed by an exponential decay. As the value of I_0 increases, the mean interspike interval decreases due to both: the faster exponential decay and the shift of the maximum of the ISI density to smaller values. The most probable interspike interval equals approximately 180 ms, 140 ms and 45 ms for I_0 = 155 pA, 160 pA and 170 pA, respectively. There exists only one time scale in the spike trains, which is noise-activated and depends on the threshold value. No spike clustering is observed in the overdamped RaF model, again in consistency with experimental observations made in pyramidal cells.

The generation of clustered spike patterns by resonant neurons may have an implication for the collective dynamics in networks of neurons. Spike clusters are responsible for increasing reliability (Lisman, 1997) and the selective communication between neurons (Izhikevich et al., 2003). Spike clusters, considered as units of neural information, are characterized by the following three parameters: the intra-cluster spike frequency, the duration of a spike cluster and the occurrence frequency of clusters. As we have shown, the first parameter depends only on the intrinsic properties of a neuron, whereas the two latter depend on the value of the input current. The different dependence of the spike cluster parameters on the input parameters might offer new coding capacities.

Summary

In this chapter we have studied the joint effects of channel noise and subthreshold properties on the spike patterns in resonant and nonresonant neurons. Both types of neurons are modeled by the stochastic resonate-and-fire model with physiologically relevant parameters and an additive noise term modeling the intrinsic channel noise. The differences in spike patterns of resonant and nonresonant neurons are reflected in their interspike interval densities. The latter are analytically calculated for the RaF model using the Stratonovich approximation, derived in Chapter 5.

Resonant neurons generate clustered spike patterns due to the influence of intrinsic noise and the subthreshold resonance, whereas spike patterns in nonresonant neurons appear to be rather homogenous. This fact is reflected in the corresponding ISI densities, which have mono- and multimodal structures in nonresonant and in resonant neurons, respectively.

There are two time scales in the dynamics of resonant neurons: the deterministic period of subthreshold oscillations and the excitation time related to the activation by intrinsic noise. These time scales depend differently on the value of the injected input current I_0, which explains the changes observed in the ISI densities. The interspike interval within a cluster is unaffected by changes of the input current, whereas the mean interval between clusters decreases with increasing I_0. Therefore the most probable ISI in resonant neurons remains almost unchanged as I_0 varies and the mean interspike interval decreases only due to faster exponential decay in the ISI density. In contrast, there exists only one time scale in the dynamics of nonresonant neurons, which is the excitation time by noise. Correspondingly, both the mean and the most probable ISI shift to smaller values with increasing input current I_0.

In the next Chapter 7 we analyze experimental data obtained in stellate (resonant) and pyramidal (nonresonant) cells in the entorhinal cortex and rat, in order to show that the mechanisms, shaping the spike patterns in real neurons, are similar to those discussed in this chapter.

7

Patterns of spontaneous firing in neurons of the entorhinal cortex

In Chapters 3 and 6 simple neuron models were used to demonstrate how the subthreshold frequency preference of resonant neurons shapes their spike patterns. The appearance of complex spike patterns in resonant neurons can be attributed to the non-Markovian escape mechanism of the voltage variable over its excitation threshold. Non-Markovian first passage time problem have been discussed in great detail in Chapter 5, where we derived several analytical approximations for the interspike interval distribution for a simple threshold model. However, the impact of the subthreshold frequency preference on the spike patterns in real neurons still remains to be elucidate. This chapter is devoted to the analysis of experimental data recorded in stellate (resonant) and pyramidal (nonresonant) cells in the entorhinal cortex in rat. Our intention is to understand the impact of the subthreshold resonance properties on the spike patterns in these cells.

The relation between subthreshold resonance and the dynamics of voltage dependent membrane currents is well investigated: The specific combination of voltage dependent ion channels and their dynamics determine the subthreshold properties (for a review see Hutcheon and Yarom, 2000). However, the effect of subthreshold resonance on the spike generation is less understood. It has been established, that the presence of intrinsically oscillating excitatory neurons can stabilize global network oscillations (reviewed in Kopell and Ermentrout, 2002). Also, the influence of subthreshold resonance on the neuronal firing rate (Svirskis and Rinzel, 2003; Brunel et al., 2003; Richardson et al., 2003; Erchova et al., 2004; Schreiber et al., 2004), the firing rate modulation and the precision of spike timing (Desmaisons et al., 1999; Haas and White, 2002) has been explored. A number of studies in olfactory bulb and brainstem indicate, that oscillations of the subthreshold membrane potential are associated with clustered spike patterns (Chen and Shepherd, 1997; Desmaisons et al., 1999; Pedroarena et al., 1999; Wu et al., 2001; Izhikevich et al., 2003).

Based on these observations, we systematically analyze the relation between subthreshold

---

This chapter is adopted from Engel et al. (2007).

resonance and interspike interval statistics in neurons of the entorhinal cortex. We investigate to what extent spike patterns are shaped by the subthreshold resonance properties. As information is most likely not only carried by the firing rate, but also coded in the sequence of spikes, an understanding of the relation between subthreshold resonance and the spike patterns is vital for the understanding of the neural code. The differential firing properties of resonant and nonresonant neurons might provide a mechanism of context dependent routing of information flow (Gloveli et al., 1997; Izhikevich et al., 2003). In particular, in the entorhinal cortex two distinct anatomical pathways (perforant and temporoammonic) project into the hippocampus. The corresponding neurons have already been shown to differ in their resonance properties (Erchova et al., 2004).

In this chapter we focus on the spontaneous (driven by intrinsic noise) neuronal activity. We use a combination of experimental, analytical and numerical methods to identify the resonance related differences in the ISI statistics. We find significantly different spike patterns for resonant and nonresonant cells in the entorhinal cortex, attributable to the subthreshold frequency preference. Resonant cells exhibit multimodal ISI distributions, whereas nonresonant cells exhibit unimodal distributions. We show that the experimentally observed ISI statistics can be reproduced by a threshold model that takes the frequency dependent subthreshold dynamics into account. Independent of the resonance properties, the correlations between ISIs on time scales of 200–400 ms are present close to the threshold in both types of cells. The ISI correlations can only be reproduced by a modified model with a nonrenewal threshold, such that the spike generation also depends on the spike history. The analysis of the interspike interval and the spike-count variability indicates, that the variability of spike trains strongly depends on resonance properties.

7.1 Resonant and nonresonant cells in the entorhinal cortex

To demonstrate the impact of subthreshold resonance on the spike train statistics, we investigated two types of neurons in the entorhinal cortex – stellate and pyramidal. Layer II stellate cells typically exhibit a clear subthreshold resonance around the theta range of frequencies (5 to 15 Hz); layer III pyramidal cells show a small subthreshold resonance at low frequencies (2 and 4 Hz) or no resonance at all. Experimental recordings were obtained from 19 neurons (7 stellate, 12 pyramidal) in the upper layers of medial entorhinal cortex of adult rats. The measured cell parameters (resting potential, input resistance and membrane time constant) were similar to those previously reported for this kind of cells (Erchova et al., 2004). All details concerning the experimental methods and theoretical data analysis are presented in Appendix A.

The sub- and suprathreshold properties of resonant stellate and nonresonant pyramidal cells are summarized in Fig. 7.1. The top panel illustrates the frequency-dependent membrane impedance function $|Z|(f)$ for typical cells. The impedance function was obtained from the responses to ZAP currents (see Appendix A and Section 2.1.2); the corresponding voltage responses are depicted in the inset. For stellate cells the impedance profile $|Z|(f)$ (Fig. 7.1A) exhibits a clear maximum at frequencies 5–15 Hz, whereas the impedance of pyramidal cells monotonically decays with increasing frequency (Fig. 7.1B). In a number of pyramidal cells

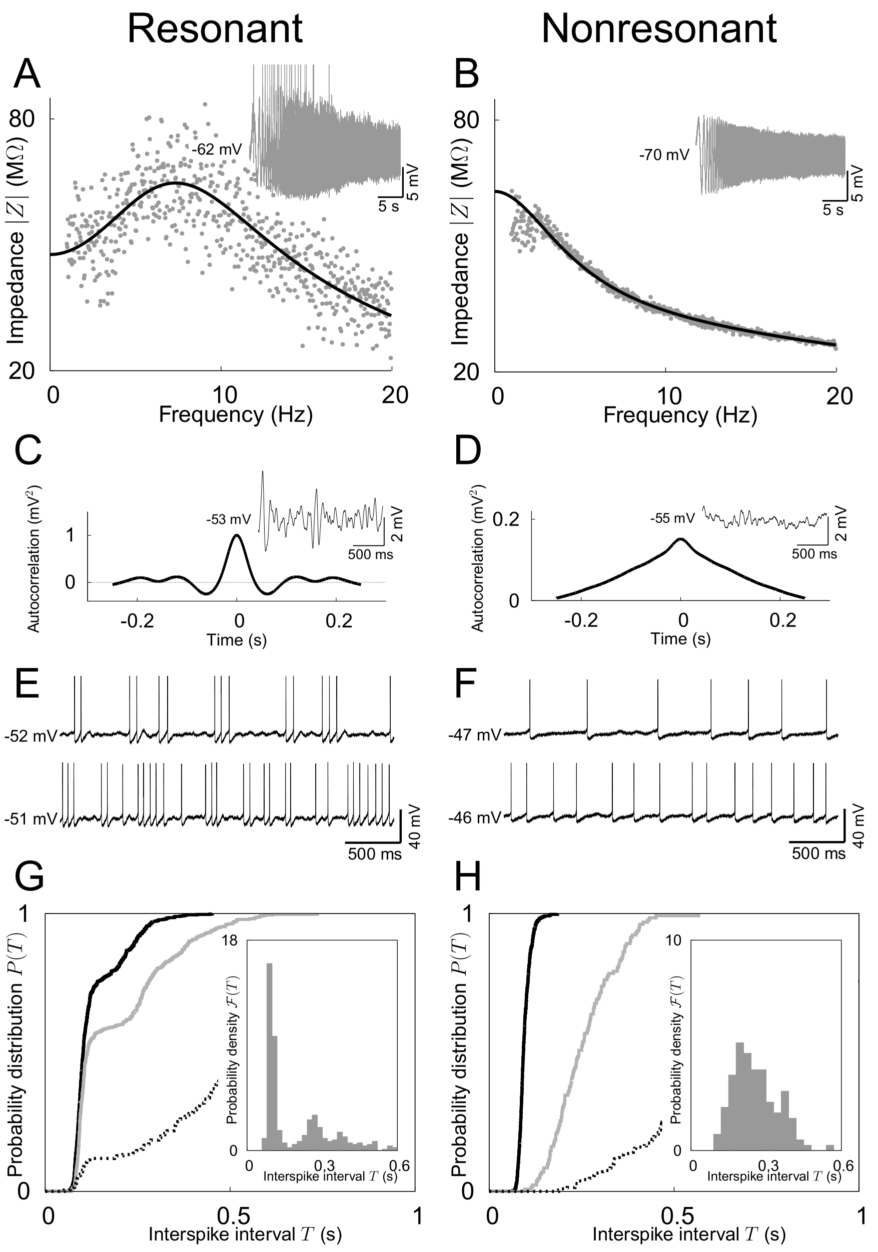

Figure 7.1: Electrophysiological response properties of stellate and pyramidal cells in medial entorhinal cortex. **A,B**: Impedance amplitude profile (main) and voltage response to a ZAP current with an amplitude of 100 pA (inset) for a stellate (A) and a pyramidal (B) cell at the resting potential −62 mV and −70 mV, respectively. The stellate cell has a clear maximum at 7 Hz. The impedance of the pyramidal cell decays monotonically with frequency. **C,D**: The voltage autocorrelation function (main) for a constant current stimulation characterizes regular membrane potential oscillations (examples in the inset) in stellate cells (C, 250 pA) and non-rhythmic fluctuations in pyramidal cells (D, 300 pA). **E,F**: Voltage responses to injection of a depolarizing current: 400 and 650 pA for the stellate cell (E), 700 and 900 pA for the pyramidal cell (F). In contrast to the pyramidal cell, the stellate cell shows clustering of action potentials. **G,H**: Interspike interval statistics: cumulative ISI distributions $P(T)$ (main) and ISI probability density $\mathcal{F}(T)$ (inset) for a stellate (G) and a pyramidal (H) cell. Cumulative distribution functions are shown for three levels of depolarization (corresponding to the firing rate of 1.5, 5.1, and 7.5 Hz for the stellate cell, and 1.3, 3.9, and 10.4 Hz for the pyramidal cell). The probability density $\mathcal{F}(T)$ is only shown for one level of membrane potential corresponding to the middle $P(T)$. In stellate cells the ISI probability density has a multimodal structure; $P(T)$ has a prominent step and at least three inflection points. For all the levels of firing rate the sharp rise in $P(T)$ occurs at the same T corresponding to the ISI within a cluster. The ISI probability density for the pyramidal cell is monomodal; $P(T)$ has a single inflection point.

a weak resonance maximum was observed at low frequencies 2–4 Hz with the amplitude not exceeding 20 % of the input resistance, as previously described in Erchova et al. (2004).

In response to a constant depolarizing current, resonant cells showed regular oscillations of the membrane potential at frequencies close to the resonance frequency. The autocorrelation functions of the subthreshold voltage response in stellate and pyramidal cells are depicted in Figs. 7.1C and 7.1D, respectively. The oscillating decay of the autocorrelation function in stellate cells (Fig. 7.1C) indicates rhythmic subthreshold oscillations, whereas the monotonic decay of the autocorrelation in pyramidal cells (Fig. 7.1D) indicates the nonoscillatory character of subthreshold voltage fluctuations. Examples of the underlying voltage trajectories are shown as insets.

Analysis of the spontaneous spiking activity at different holding potentials (under constant current stimulation) revealed qualitative differences in spike patterns between resonant and nonresonant cells. Stellate cells showed a clustering of action potentials (Fig. 7.1E), the firing frequency within a cluster was similar to the frequencies of subthreshold oscillations and subthreshold resonance. The spike patterns in pyramidal cells appeared to be more homogeneous (Fig. 7.1F). Differences in the spike patterns of stellate and pyramidal cells are reflected in the statistics of the interspike intervals (ISI). The cumulative ISI distributions $P(T)$ and the ISI densities $\mathcal{F}(T)$ are shown in Figs. 7.1G and 7.1H. In stellate cells, the spike clustering becomes apparent in a multimodal structure of the ISI density. The main peak in the ISI density and a prominent step in the ISI distribution occur at a time T corresponding to the ISI within a cluster (intra-cluster interval). The exponential tail of the ISI distribution corresponds to the ISI between successive clusters (inter-cluster interval). In contrast, the ISI density in pyramidal cells exhibits a monomodal structure and the cumulative ISI distribution lacks a prominent step.

Noticeable are the changes in the ISI statistics caused by changes in the firing rate. Higher levels of depolarization involve a higher average firing rate. In stellate cells the peak positions in the ISI density are almost unaffected by changes in the firing rate, i.e. the intra-cluster intervals are almost independent of the average firing rate. The weight (and the height) of the main peak in the ISI density grows with the firing rate: the average number of spikes within a single cluster becomes larger. The decay in the tail of the ISI density is faster for higher firing rates, reflecting a decrease in the average inter-cluster interval with increasing firing rate. In pyramidal cells, the increase in the average firing rate involves a faster decay in the tail of the ISI density as well as a shift of its maximum to shorter ISI values.

We conclude, that the spike patterns obtained in pyramidal cells are characterized by a single time scale related to the mean ISI, which decreases with increasing firing rate. The spike patterns obtained in stellate cells contain two distinct time scales corresponding to intra- and inter-cluster intervals. The former decreases with increasing firing rate. The latter is independent of the firing rate and is close to the period of subthreshold oscillations. This suggests, that the additional time scale, present in the output of resonant neurons, is related to their subthreshold resonance properties.

To confirm this assumption we proceed to show, that the simple renewal resonate-and-fire model (see Chapter 6) quantitatively captures the ISI statistics observed experimentally in stellate and pyramidal cells. The mechanism responsible for shaping the spike patterns can be understood from the simple resonate-and-fire model, and it is reasonable to assume, that the spike patterns in more complex models can be explained using the mechanism described here.

7.2 Estimation of subthreshold parameters for the RaF model

The resonate-and-fire (RaF) model can reproduce both types of subthreshold voltage dynamics – resonant and nonresonant (Mauro et al., 1970; Izhikevich, 2001; Richardson et al., 2003; Erchova et al., 2004; Verechtchaguina et al., 2006b). In the subthreshold regime the RaF model is related to more complex conductance-based models through linearization of the latter at specific levels of the holding potential (Mauro et al., 1970; Villacorta and Panetsos, 2005). The spike generation mechanism in the RaF model is reduced to threshold and reset conditions (see Section 2.1.3). In this section we concentrate on the subthreshold voltage dynamics only, and postpone the specification of threshold and reset conditions to Sections 7.3 and 7.5.

The subthreshold voltage dynamics in the RaF model is governed by the equation (see Eq. (6.11)):

$$C\frac{d^2V(t)}{dt^2} + \gamma\frac{dV(t)}{dt} + \delta V(t) = \delta(R_0 I(t) + V_r) + \frac{dI(t)}{dt} + \sqrt{2D}\xi(t). \tag{7.1}$$

Here the membrane potential $V(t)$ is the dynamic variable, $I(t)$ represents the time-dependent input current, and $\xi(t)$ is a white Gaussian noise of unit intensity. Since the synaptic transmission was blocked in the recorded cells, the noise term $\xi(t)$ models a cell-intrinsic noise, which presumably is dominated by the channel noise (White et al., 2000). The stochastic RaF model in the form Eq. (7.1) was derived in Section 6.2.

Fixed parameters of the model characterize the membrane capacity C, the resting membrane potential V_r, the membrane input resistance R_0, and the noise intensity D. Further fixed parameters are γ and δ, which together define the type of subthreshold voltage dynamics. Thus γ/C is the effective damping coefficient, and $\sqrt{\delta/C}$ is the effective eigenfrequency of the system. In the underdamped regime ($\gamma < 2\sqrt{\delta C}$) the RaF model exhibits subthreshold oscillations, whereas in the overdamped regime ($\gamma > 2\sqrt{\delta C}$) subthreshold dynamics is nonoscillatory (see Section 2.1.3).

The frequency-dependent impedance function $|Z|(f)$ of the RaF model is obtained analytically from the deterministic version of Eq. (7.1) (with $D = 0$). In experiments the impedance function was estimated from the voltage response averaged over at least five individual realizations, therefore we can neglect the contribution of noise to the impedance function. The impedance function of the deterministic RaF model reads:

$$|Z_{\text{theory}}|(f) = \sqrt{\frac{4\pi^2 f^2 + R_0^2\delta^2}{[\delta - 4\pi^2 C f^2]^2 + 4\pi^2\gamma^2 f^2}}. \tag{7.2}$$

In the underdamped regime the impedance function Eq. (7.2) has a maximum at the frequency

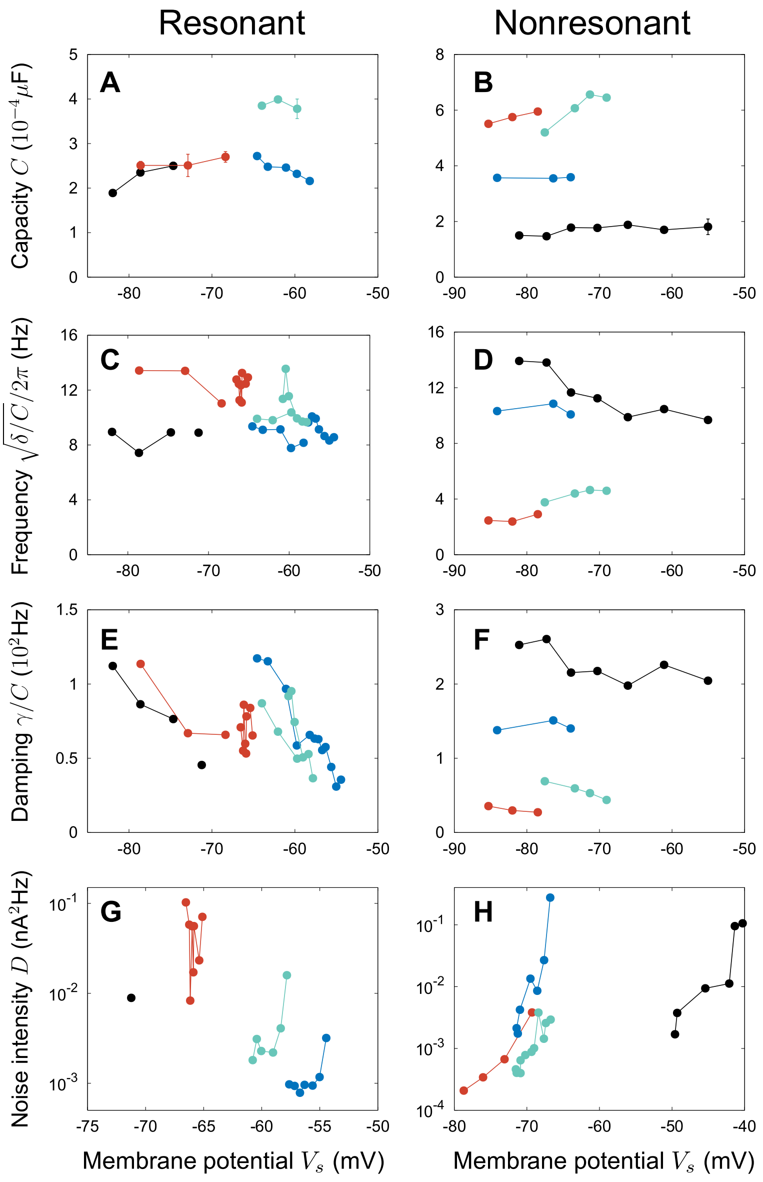

Figure 7.2: Voltage-dependent changes in the subthreshold model parameters obtained from fits to experimental responses. The vertical columns represent the four subthreshold parameters (C, $\sqrt{\delta/C}/2\pi$, γ/C, D) for four stellate and four pyramidal cells (left and right columns, respectively). Different colors correspond to different cells; cells presented in Fig. 7.1 are marked in black. **A,B**: phenomenological capacity C of the cell (from impedance fit); **C,D**: effective eigenfrequency (from impedance fit and autocorrelation); **E,F**: effective damping coefficient (from impedance fit and autocorrelation); **G,H**: noise intensity D (from autocorrelation). The noise intensity in stellate and pyramidal cells, as well as the effective damping coefficient in stellate cells strongly depend on the level of depolarization.

f_{res}:

$$f_{\text{res}} = \frac{1}{2\pi}\sqrt{\frac{\delta}{C}}\sqrt{\sqrt{(1 + C\delta R_0^2)^2 - \gamma^2 R_0^2} - C\delta R_0^2}. \tag{7.3}$$

Note that for small γ, the resonance frequency f_{res} is similar to the effective eigenfrequency $\sqrt{\delta/C}/2\pi$.

To characterize the spontaneous firing activity in neurons we studied their response to a constant current stimulation $I(t) = I_0$. Injection of a constant current I_0 shifts the stationary voltage drop to $V_r + I_0R_0$. Here we are only interested in deviations from this holding potential in the presence of intrinsic noise. We therefore introduce a new variable $x(t) =$

$V(t) - V_r - I_0 R_0$, which directly describes the deviation from the stationary holding potential and has zero mean:

$$C\frac{d^2x(t)}{dt^2} + \gamma\frac{dx(t)}{dt} + \delta x(t) = \sqrt{2D}\xi(t). \tag{7.4}$$

The RaF model Eq. (7.4) describes the subthreshold voltage dynamics around a fixed holding potential. The parameters of the model may, however, change with the level of depolarization. Therefore the experimental data for each value of the input current I_0 have to be analyzed separately, providing separate parameter sets for different levels of depolarization. Still, for a given holding potential the linear model Eq. (7.1) was shown to well represent the voltage response to small amplitude stimuli (Schreiber et al., 2004; Erchova et al., 2004).

Estimates for almost all subthreshold parameters can be obtained from impedance measurements. The values of the parameters C, δ, γ and R_0 were obtained from least square fits of the theoretical impedance function $|Z_{\text{theory}}|(f)$, Eq. (7.2), to the measured membrane impedance. An example is shown in Figs. 7.1A and 7.1B, where the measured impedance is depicted by gray dots, and the fit with $|Z_{\text{theory}}|(f)$ is depicted by a solid black line. The noise intensity has to be estimated separately using the autocorrelation analysis of spontaneous subthreshold activity. The voltage autocorrelation function $r_x(t) = \langle x(t+t')x(t')\rangle$ for the RaF model Eq. (7.4) in the underdamped regime reads (see Eq. (5.13)):

$$r_x(t) = \frac{D}{\gamma\delta}e^{-\frac{\gamma}{2C}|t|}\left[\frac{\gamma}{2\Omega C}\sin(\Omega|t|) + \cos(\Omega t)\right], \tag{7.5}$$

where $\Omega = \sqrt{\delta C - \gamma^2/4}/C$. The autocorrelation function oscillates with the period $T_p = 2\pi/\Omega$ and decays with the relaxation time $t_{rel} = 2C/\gamma$. In the overdamped regime ($\gamma > 2\sqrt{\delta C}$), the voltage autocorrelation function is given by Eq. (7.5), where the trigonometric functions are replaced by their hyperbolic counterparts. In this case the autocorrelation function decays monotonically with time. In both, the under- and overdamped regimes, the value of the autocorrelation function at $t = 0$ (i.e. the voltage variance) gives assess to the noise intensity: $D = r(0)\gamma\delta$.

We estimated the subthreshold model parameters for each recorded level of membrane depolarization separately (for details see Appendix A). Fig. 7.2 presents the voltage-dependent changes of the model parameters for four stellate (left column) and four pyramidal (right column) cells.

For both, resonant and nonresonant cells, the intrinsic noise intensity D strongly increased with the membrane depolarization (note the logarithmic D-scale in Figs. 7.2G and 7.2H). This observation goes along with the assumption, that the channel noise increases towards the threshold. The channel open probability tends to increase, but remains on average below 50 % (see White et al., 2000). In stellate cells the damping γ/C decreased with depolarization, while the eigenfrequency $\sqrt{\delta/C}$ remained almost unchanged. This agrees with experimental observations, that the resonance strength and the coherence of subthreshold oscillations increase with depolarization without significant changes in the resonance frequency. In pyramidal cells, a similar trend of the damping could be observed though less pronounced. Pyramidal cells remain in a nonresonant regime, because the absolute values of the damping were large compared to the corresponding eigenfrequencies. The membrane capacity C did not significantly change with depolarization in both cell types.

7.3 The renewal RaF model and ISI distributions

The five parameters of the linear model (C,δ, γ, D, R_0) describe the cell at the subthreshold level. The simplest way to account for the spike generation mechanism is to supply the model Eq. (7.4) with fixed values for the threshold x_b and the reset x_0. Whenever $x(t)$ reaches x_b a spike is generated, $x(t)$ is then reset to x_0 after the period τ_r referred to as the reset time. The voltage derivate $dx(t)/dt$ is reset to zero. Note, that for the existence of spike-induced subthreshold oscillations it is important, that the reset value x_b is different from the steady-state voltage $x = 0$, in our case $x_b < 0$. This spiking mechanism leads to a renewal spike train with all ISIs being independent. We refer to the RaF model with this type of threshold as the *renewal* RaF model. The ISI distribution in the renewal RaF model is given by the first passage time (FPT) distribution for the stochastic variable $x(t)$.

To verify whether the renewal RaF model can reproduce the ISI statistics, we fit the ISI distributions theoretically predicted by the RaF model to the measured ISI distributions. The ISI distribution in the renewal RaF model can be obtained analytically using the Stratonovich approximation, which is discussed in great detail in Section 5.2.4, see Eqs. (5.9) and (5.30). The parameter values of the RaF model estimated in stellate and pyramidal cells belong to a regime of moderate damping and moderate noise intensity, so that the Stratonovich approximation is applicable and accurate. The Stratonovich approximation was used to scan the relevant parameter range and to find the sets of parameter, for which the measured and theoretically predicted ISI distributions agree.

We used the Kolmogorov-Smirnov (KS) test for comparison between the measured and theoretically predicted ISI distribution functions. The test statistics $\mathcal{D}$ in the KS test is the largest difference between measured and predicted distribution functions (see Appendix A for details). We used the technique of simulated annealing to find the parameter set minimizing $\mathcal{D}$. The corresponding theoretical ISI distribution $P_S(T)$ was considered as the best fit. If the minimal $\mathcal{D}$-value exceeds the critical value $\mathcal{D}_K$ for a given sample size (see Appendix A), then the hypothesis, that the best fit $P_S(T)$ is the distribution underlying the measured ISIs, has to be rejected. Otherwise we can regard the measured ISIs as consistent with the hypothesis, that they come from the distribution $P_S(T)$. In other words, we draw a tube with radius $\mathcal{D}_K$ around the measured ISI distribution. If the best fit $P_S(T)$ completely lays inside the tube, it can be regarded as the distribution underlying the measured ISIs. All details concerning the fit procedures, estimation of the spike parameters (x_0, x_b and τ_r) and scanned parameter ranges are specified in Appendix A.

The best fits $P_S(T)$ for the measured ISI distributions at a single level of depolarization in the stellate and pyramidal cells are shown in Figs. 7.3A and 7.3B, respectively. In both cases the experimental data are in quantitative agreement with the predictions of the renewal RaF model, as confirmed by the KS test. Starting form parameter sets adjusted to match the subthreshold cell response, we calculate the ISI statistics as predicted by the renewal RaF model. From the fact that the RaF model reproduces the ISI distributions obtained experimentally and also accounts for the differences in resonant and nonresonant spike patterns, we may conclude that the resonate-and-fire model is sufficient to explain the mechanism shaping the spike patterns in stellate and pyramidal cells.

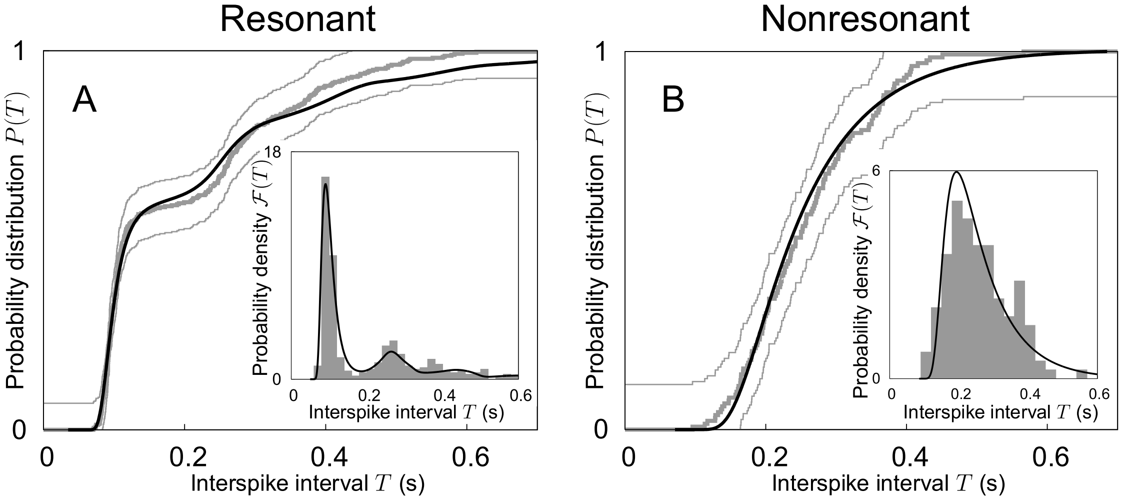

Figure 7.3: ISI distributions predicted by the renewal RaF model. Experimentally obtained ISI distributions are shown with solid gray lines, thin gray lines mark the tube of the Kolmogorov-Smirnov test. **A**: stellate cell from Fig. 7.1. The best Stratonovich approximation is depicted in black. The parameters of the RaF model are $C = 2.5 \cdot 10^{-4} \mu\,\mathrm{F}$, $\sqrt{\delta/C}/2\pi = 5.7\,\mathrm{Hz}$, $\gamma/C = 0.088 \cdot 10^2\,\mathrm{Hz}$, $D = 0.0238\,\mathrm{nA}^2\mathrm{Hz}$, $\tau_r = 31\,\mathrm{ms}$, $x_0 = -7.8\,\mathrm{mV}$, $x_b = 5.8\,\mathrm{mV}$. **B**: pyramidal cell from Fig. 7.1. The best Stratonovich approximation is depicted in black. The parameters of the RaF model are $C = 1.7 \cdot 10^{-4} \mu\,\mathrm{F}$, $\sqrt{\delta/C}/2\pi = 12.9\,\mathrm{Hz}$, $\gamma/C = 3.44 \cdot 10^2\,\mathrm{Hz}$, $D = 0.212\,\mathrm{nA}^2\mathrm{Hz}$, $\tau_r = 71\,\mathrm{ms}$, $x_0 = -11.2\,\mathrm{mV}$, $x_b = 0.8\,\mathrm{mV}$. The insets show the corresponding ISI densities.

In stellate cells this mechanism consists in the interplay between subthreshold oscillations (caused be the subthreshold resonance) and intrinsic noise, as discussed in Chapter 6. Briefly, every spike resets the phase of subthreshold oscillations to an almost constant value and the relaxation time of these oscillations is large compared to the average ISI. As a consequence the instantaneous firing rate (probability to obtain a spike per unit time) is time-dependent. There are preferred spike times set by the subthreshold oscillations and reflected in the spike clustering. The intra-cluster interval corresponds to the main peak in the ISI density. The intra-cluster interval is determined by the time interval between the initiation of a spike and the first maximum of the subsequent subthreshold oscillation induced by this spike. The distance between the first and the second peak in the ISI density corresponds to the period of the subthreshold oscillations. The time scale set by the subthreshold oscillations is deterministic and independent of the firing rate. Noise-driven inter-cluster intervals correspond to the exponential tail of the ISI density. Since the noise intensity grows with the level of depolarization, the average inter-cluster interval decreases and the decay in the tail becomes faster. The number of visible peaks in the ISI density depends on the ratio between the relaxation time of subthreshold oscillations and their period. The more periods of subthreshold oscillations elapse prior to relaxation, the more peaks are pronounced in the ISI density.

In pyramidal cells, the relaxation time of the subthreshold voltage dynamics is small compared to the average ISI. After every spike the voltage variable relaxes quickly to the resting potential, and the instantaneous firing rate is constant for times larger than the reset time plus the voltage relaxation time. There is no additional deterministic time scale in the dynamics and all ISIs are noise-driven. Since the noise intensity increases with the level of depolarization, all ISIs also decrease. This is reflected in the shift of the distribution maximum to shorter ISI values with increasing firing rate.

7.4 Interspike interval correlations

The renewal RaF model is able to reproduce quantitatively the spike patterns observed in resonant and nonresonant neurons. This model is based on the renewal assumption, that all ISIs are independent. To verify whether this assumption is reasonable, we analyze the serial dependence of interspike intervals. We use following measures:

(i) We visualize the relation between successive ISIs using the joint probability density of neighboring interspike intervals $\mathcal{F}(T_1, T_2)$ (also called the density of the ISI return map). Let X_i denote the i-th interspike interval in the measured spike train. $\mathcal{F}(T_1, T_2)dT_1dT_2$ gives the probability to obtain two successive ISIs in the spike train with lengths $X_i \in (T_1, T_1 + dT_1)$ and $X_{i+1} \in (T_2, T_2 + dT_2)$. The joint densities $\mathcal{F}(T_1, T_2)dT_1dT_2$ were estimated by histograms and normalized to unity.

(ii) If the renewal assumption holds and the ISIs are independent, the joint ISI density factorizes: $\mathcal{F}(T_1, T_2) = \mathcal{F}(T_1)\mathcal{F}(T_2)$. To characterize the deviation of the experimentally observed spike trains from a sequence of independent spikes, we construct correlation maps $C(T_1, T_2)$ from the joint ISI probability densities by subtraction of the renewal part:

$$C(T_1, T_2) = \mathcal{F}(T_1, T_2) - \mathcal{F}(T_1)\mathcal{F}(T_2). \tag{7.6}$$

Positive values of C indicate ISI pairs that are observed more frequently than expected in the renewal spike train with the given ISI distribution. Negative values of C indicate pairs that are observed less frequently.

(iii) We calculate the serial correlation coefficients (SCC) ρ_k, as a measure for the serial dependence of correlations in a spike train, see Eq. (2.42):

$$\rho_k = \frac{\langle X_i X_{i+k}\rangle - \langle X_i\rangle\langle X_{i+k}\rangle}{\langle X_i^2\rangle - \langle X_i\rangle^2}. \tag{7.7}$$

Here the averages are taken over all ISIs in the spike train. The index k is usually called a lag and denotes the number of intercepting interspike intervals. For a renewal spike train $\rho_k = 0$ for $k > 0$. To estimate the typical correlation time, we plot the SCC as a function of time, which is obtained by linear scaling of the lag axis with the average firing rate.

The experimental estimates of these three measures are presented in Fig. 7.4. The left column refers to the resonant stellate cell and the right column to the nonresonant pyramidal cell. Figs. 7.4A and Fig. 7.4B show the densities of the ISI return map $\mathcal{F}(T_1, T_2)$. For stellate cells the density of the ISI return map revealed a patchy structure. The main peak occurs

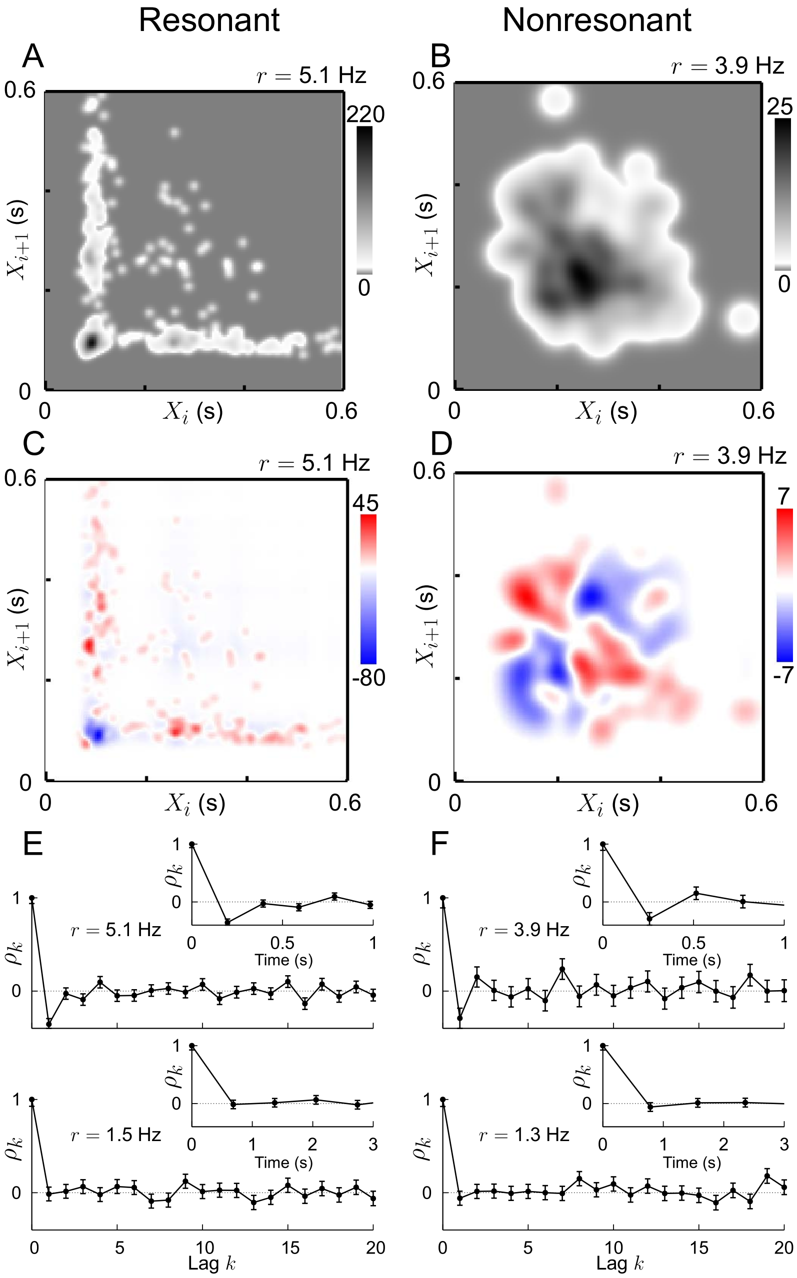

Figure 7.4: Second order statistics of interspike intervals. Left panel: stellate cell, right panel: pyramidal cell (both are the same examples as in Fig. 7.1). **A,B**: The probability density of the return map for stellate and pyramidal cells. The plot for the stellate cell (A) has a characteristic two-arm structure. The main peak and the arms are located at a time, corresponding to the ISI within a cluster. In contrast, the plot for the pyramidal cell (B) exhibits a cloudy structure. **C,D**: Density of correlation maps for stellate and pyramidal cells. Both cell types exhibit negative correlations between the adjacent ISIs. **E,F**: Main panel: Serial correlation coefficients (SCCs) ρ_k for lags k=1…20 for two different levels of depolarization (stellate, panel E, the firing rate is 1.5 Hz and 5.1 Hz; pyramidal, panel F, the firing rate is 1.3 Hz and 3.9 Hz). The insets show SCCs scaled by the average firing rate of the time series to illustrate the average correlation time. The SCCs for both, stellate and pyramidal cells, show similar negative correlations at low lags for the higher mean firing rates. The correlation time is similar and around 300 ms.

at ∼(100 ms;100 ms) corresponding to two successive ISIs within a single cluster. The two arms extend at ISI values, when one ISI is ∼100 ms and the other ISI is of the order of 200–500 ms, which corresponds to a pair of one intra-cluster ISI and one inter-cluster ISI. This result agrees with the multimodal ISI density $\mathcal{F}(T)$ in stellate cells. The return map of the pyramidal cell (Fig. 7.4B) exhibited a single broad maximum localized at ∼(250 ms;250 ms), in agreement with the unimodal ISI density in these cells.

Figs. 7.4C and Fig. 7.4D show the correlation maps $C(T_1, T_2)$ for both cell types. The correlation map quantifies the deviation of the measured ISI sequence from the ISI sequence of a renewal spike train with the same ISI distribution. The correlation maps in both cell types revealed negative values ($C < 0$) along the line $T_1 - T_2 = \text{const}$ and positive values ($C > 0$) along the line $T_1 + T_2 = \text{const}$, which reflects the presence of negative correlations in the spike train. Negative values of C indicate that the pairs of two successive short ISIs and the pairs of two successive long ISIs appeared less frequently in the measured spike train than they would occur in a renewal spike sequence. Positive values of C indicate that the pairs consisting of a short ISI followed by a long ISI and vice versa appeared more frequently than in a renewal sequence.

The negative correlations between successive ISIs are also pronounced in the negative values of the serial correlation coefficients on short lags. Figs. 7.4E and 7.4F show the SCCs as a function of lag k for two different firing rates in stellate and pyramidal cells, respectively. The insets present the same data as a function of time (scaled by the average firing rate). At higher firing rates (3-10 Hz) the first few SCCs were significantly different from zero. From the time dependence of the SCCs (see insets) we can estimate the order of the correlation time τ_c, which ranged from 200 ms to 400 ms. At low firing rates (<2 Hz) all ρ_k for $k > 0$ did not differ significantly from zero, since the serial ISI dependence can only be observable when the mean ISI does not exceed the correlation time scale τ_c. Correspondingly, the number of SCCs significantly different from zero (i.e. the number of consecutive ISIs that were correlated) increased with firing rate for both cell types.

7.5 The nonrenewal RaF model and ISI correlations

The presence of a serial dependence in the ISI sequences cannot be captured by the renewal RaF model, though this model can reproduce the first order ISI statistics. The correlations observed in experimental data can be explained by spike-induced memory effects. To account for these correlations we introduce a minimal modification to the RaF model, which only affects the spike generation mechanism and which leaves the subthreshold dynamics unchanged. This modified version of the RaF model with a stochastic spike generation mechanism will be referred to as the *nonrenewal* RaF model.

The nonrenewal RaF model has the same subthreshold dynamics as the renewal model (see Eq. (7.4)) combined with a modified threshold mechanism. To account for negative correlations between ISIs, the deterministic spike generation is replaced by a stochastic rule. Whenever the membrane potential $x(t)$ crosses the threshold x_b from below (i.e. with a positive velocity), a spike is generated with probability $1 - p_s(t)$. A spike is skipped with the probability $p_s(t)$, and the voltage variable $x(t)$ evolves further without reset according to its

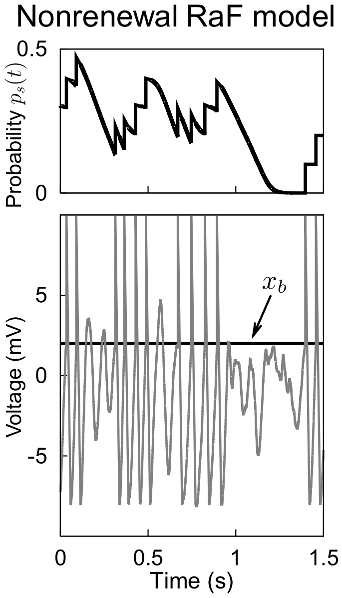

Figure 7.5: Example of a spike train in the nonrenewal RaF model (gray) and corresponding time evolution of the probability $p_s(t)$ to skip a spike (black). Not every threshold crossing triggers a spike. The spike train is nonrenewal with negative correlations.

subthreshold dynamics. The probability to skip a spike is time-dependent:

$$p_s(t) = \min\left[1,\ \sum_i p_0 \frac{1}{2}\left[1 - \tanh\left[\beta(t - t_i - \tau_c)\right]\right]\right]. \tag{7.8}$$

Here t_i denote the spike arrival times, and the summation is taken over all spikes, which occurred before t. If the sum in Eq. (7.8) exceeds unity, than $p_s(t) = 1$ and the generation of spikes is impossible. Every time the threshold x_b is crossed from below $p_s(t)$ is evaluated. With probability $1 - p_s(t)$ a spike is generated and the voltage is reset as in the renewal model. With probability $p_s(t)$ the spike is skipped and $x(t)$ evolves further without reset. In the latter case, only a new threshold crossing from below will trigger a spike eventually.

In the nonrenewal RaF model the probability $p_s(t)$ to skip a spike is a dynamic variable. Triggered by a single spike, the probability $p_s(t)$ is instantaneously increased by p_0 and remains almost constant at this new level for the correlation time τ_c. Afterwards the spike probability decreases to zero during a period $2/\beta$. The occurrence of several spikes within a time window smaller than the correlation time leads to the probability $p_s(t)$ with a complex dynamics, as illustrated in Fig. 7.5. As each individual spike increases p_s, the generation of many spikes in close succession (on the order of the correlation time τ_c) will temporarily inhibit the spike generation. The example shown in Fig. 7.5 demonstrates that the dynamics of $p_s(t)$ effectively limits the number of spikes within a cluster and causes “overshoots”, when the membrane potential is significantly above the threshold but no spike is fired. This probabilistic spike generation mechanism results in a nonrenewal spike train with negative correlations between neighboring ISIs.

To verify whether the nonrenewal RaF model can reproduce the correlations observed experimentally as well as capture the ISI distribution, we fit the ISI statistics as predicted by

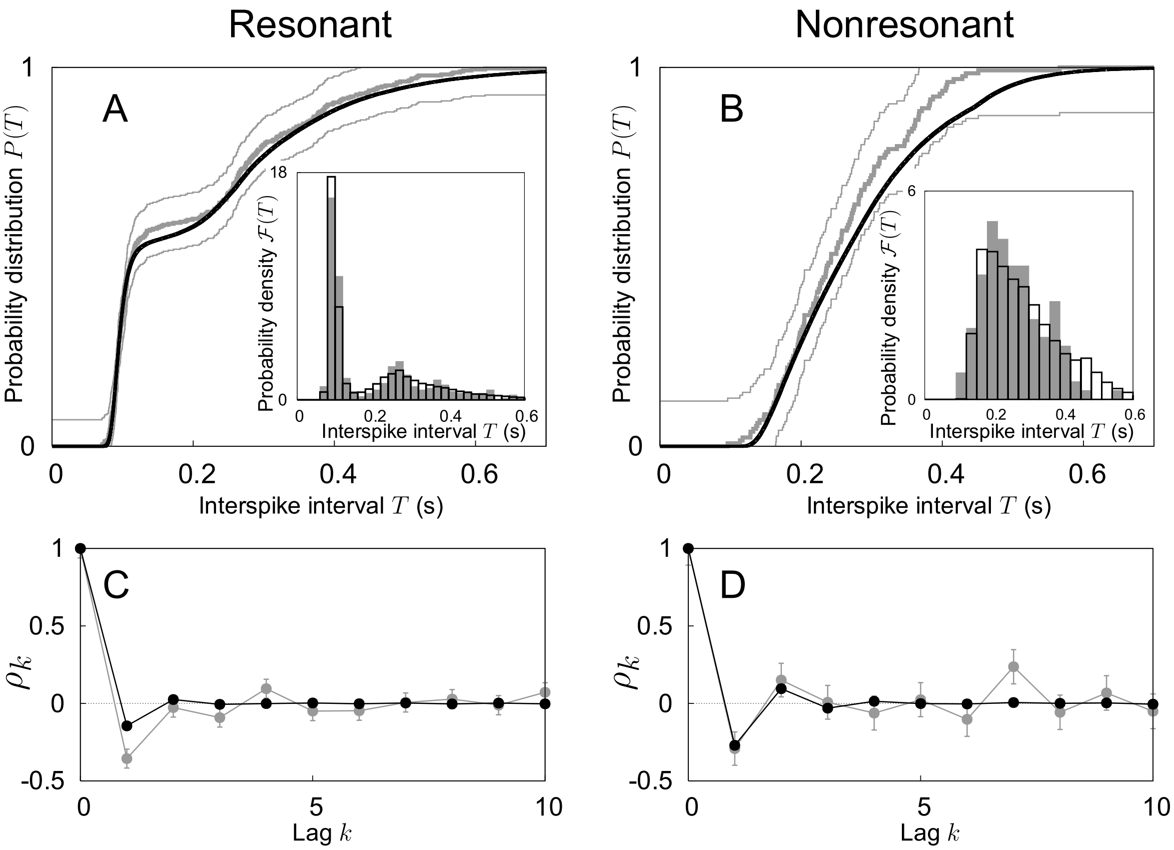

Figure 7.6: ISI distribution and the ISI correlations as predicted by the nonrenewal RaF model are in a quantitative agreement with the experimental data for stellate and pyramidal cells. Left panel: stellate cell, right panel: pyramidal cell (both are the same examples as in Fig. 7.1). The experimental ISI statistics are depicted in gray color, the ISI statistics numerically obtained in the nonrenewal RaF model with black lines. **A, B**: The ISI distributions (main) and the corresponding ISI densities (inset). **C, D** The serial correlation coefficients ρ_k. The values of the fit parameters for the nonrenewal RaF model for the stellate cell (panels A,C) are $C = 2.5 \cdot 10^{-4} \mu\,\mathrm{F}$, $\sqrt{\delta/C}/2\pi = 6.6\,\mathrm{Hz}$, $\gamma/C = 0.27 \cdot 10^2\,\mathrm{Hz}$, $D = 0.017\,\mathrm{nA}^2\mathrm{Hz}$, $\tau_r = 38\,\mathrm{ms}$, $x_0 = -11.7\,\mathrm{mV}$, $x_b = 2.0\,\mathrm{mV}$, $\tau_c = 258\,\mathrm{ms}$, $\beta = 249\,\mathrm{s}^{-1}$, $p_0 = 0.25$. The values of the fit parameters for the nonrenewal RaF model for the pyramidal cell (panels B,D) are $C = 1.7 \cdot 10^{-4} \mu\,\mathrm{F}$, $\sqrt{\delta/C}/2\pi = 13.9\,\mathrm{Hz}$, $\gamma/C = 3.0 \cdot 10^2\,\mathrm{Hz}$, $D = 0.25\,\mathrm{nA}^2\mathrm{Hz}$, $\tau_r = 92\,\mathrm{ms}$, $x_0 = -9.5\,\mathrm{mV}$, $x_b = 0.04\,\mathrm{mV}$, $\tau_c = 355\,\mathrm{ms}$, $\beta = 226\,\mathrm{s}^{-1}$, $p_0 = 0.41$.

the nonrenewal RaF model to experimental data. Since no analytical expression is available for the ISI distribution and SCCs in the nonrenewal RaF model, we estimated these functions for every parameter set on the basis of stochastic simulations (based on at least 2000 spikes). We scanned the parameter space of the nonrenewal RaF model searching for a parameter set minimizing the KS-statistics $\mathcal{D}$ and the discrepancy between measured and theoretically predicted values of ρ_1. All details concerning this fitting procedure are described in Appendix A.

The fitting procedure we used does not guarantee convergence to the optimal solution. Our aim was rather to demonstrate, that the measured ISI distributions and correlations can be simultaneously captured by the nonrenewal RaF model. An example of the ISI statistics predicted by the nonrenewal RaF model is depicted in Fig. 7.6 for the stellate (resonant, left column) and the pyramidal (nonresonant, right column) cell. Figs. 7.6A and 7.6B present the ISI distribution and ISI densities. Agreement between measured and theoretically predicted ISI distributions is confirmed by the KS test. The serial correlation coefficients for these parameter sets are similar to those obtained in experiments: the negative correlations observed at low lag values are captured quantitatively in both cell types (Figs. 7.6C and 7.6D). We attribute quantitative deviations of the SCCs at higher lags to the precision of the experimental correlation estimate, whose quality is limited by the sample size of the experimental data (in our case 130–600 spikes per data set).

We conclude, that the spike patterns observed in resonant and nonresonant neurons are mainly shaped by the subthreshold voltage dynamics. The spike-induced dynamics further modifies the spike patterns, in particular the second order ISI statistics as reflected in the negative correlations found experimentally in both cell types. The nonrenewal RaF model with the stochastic, spike-history dependent threshold mechanism can capture both: the qualitative differences in the ISI distributions and the similar correlations in resonant and nonresonant neurons.

7.6 Spike train variability

Differences in the subthreshold dynamics and correlations are likely to influence the variability of the spiking response. We therefore investigated the variability of ISI sequence in terms of the coefficient of variation C_{var} (see Eq. (2.41)) and the spike-count variability in terms of the Fano factor $F(\mathcal{T})$ (see Eq. (2.45)).

ISI variability. Multiple time scales are present in the dynamics of resonant and nonresonant neurons. These include the refractory time, the period T_p and relaxation time t_{rel} of the subthreshold oscillations, the noise activation time τ_a and the time scale of the spike-induced correlations τ_c. Except for the noise activation time τ_a, these time scales are all deterministic and almost independent of the depolarization level and the average firing rate. In contrast, the noise activation time τ_a decreases with the depolarization level due to increase of the noise intensity (see Figs. 7.2G and 7.2H). Different dependences of the time scales on the depolarization level suggest, that the spike-train variability depends on the average firing rate.

Figs. 7.7A and 7.7B show measured values of the coefficient of variation C_{var} in dependence on the average firing rate r for seven stellate and five pyramidal cells, respectively. In Fig. 7.7C the dependence of C_{var} on the firing rate is summarized by two histograms, which present C_{var} averaged over the populations of stellate (dark gray) and pyramidal (light gray) cells. To obtain the histograms we divide the r-axis into bins of width 1 Hz. For every bin we calculate C_{var} averaged over all data points from Figs. 7.7A and 7.7B, respectively, whose r falls in the

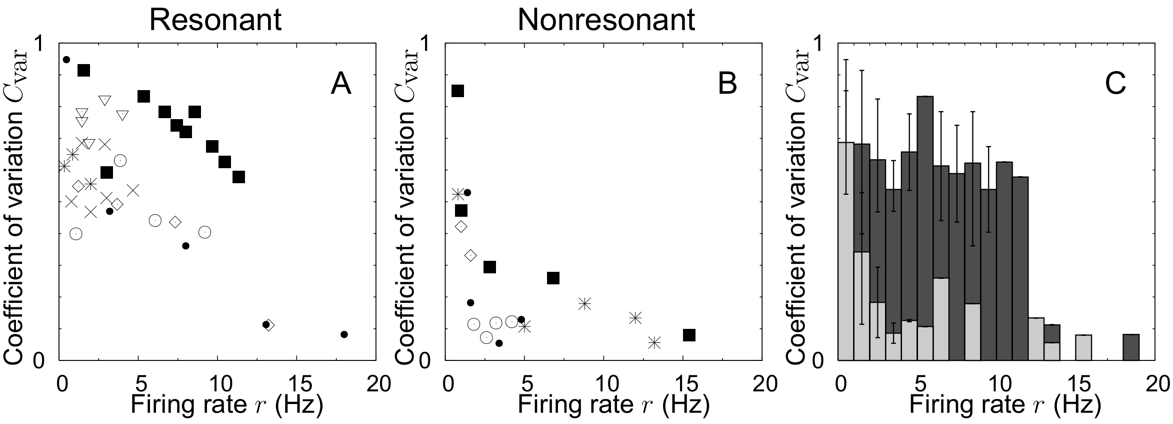

Figure 7.7: The coefficient of variation C_{var} as a function of the average firing rate. **A, B**: the C_{var}-values estimated in seven stellate (panel A) and five pyramidal (panel B) cells are plotted against the average firing rate r. Different symbols correspond to different cells; the cells presented in Fig. 7.1 are marked by squares. **C**: The histograms for values of C_{var} averaged over the population of seven stellate (dark gray) and of five pyramidal (light gray) cells. The bin width of the r-axis is 1 Hz. At low and high firing rates the coefficients of variation C_{var} in stellate and pyramidal cells are comparable. At intermediate firing rates the stellate cells exhibit higher values of C_{var} than the pyramidal cells.

corresponding bin. The experimentally observed changes in the coefficient of variation C_{var} caused by the changes in the firing rate r can be understood from the following argument.

At low levels of depolarization the intensity of intrinsic noise is small (see Figs. 7.2G and 7.2H), and the firing rate r is low. Spikes occur rarely, the mean ISI is determined by the noise activation time τ_a and significantly exceeds all deterministic time scales mentioned above. The ISIs are purely noise-driven in both cell types and the subthreshold resonance does not noticeably influence the spike patterns in resonant neurons. The spike train is therefore close to a Poisson process and the coefficient of variation C_{var} approaches the Poisson limit $C_{\mathrm{var}} \to 1$ at low firing rates in both cell types. As confirmed by Fig. 7.7, the measured values of C_{var} are close to 1 and similar in both cell types for the firing rates $r < 1\,\mathrm{Hz}$.

Intermediate levels of depolarization correspond to a moderate noise intensity as well as moderate firing rates r ($\sim 3-10\,\mathrm{Hz}$). The noise activation time τ_a decreases into the range of the deterministic time scales of neuron dynamics. The differences in the spike-train variability for resonant and nonresonant neurons appear in this regime. In nonresonant neurons the spike times are still noise-driven. The mean ISI, as determined by the noise activation time τ_a, is comparable with the relative refractory time, which is jointly determined by the refractory time itself and the time scale τ_c of negative correlations. The ISI-values are therefore bounded from below and the ISI distribution becomes narrower. This is reflected in the decrease of C_{var} with increasing firing rate r in pyramidal cells, see Figs. 7.7B and 7.7C for $r \sim 3-10\,\mathrm{Hz}$.

In resonant cells the noise activation time τ_a becomes comparable to the relaxation time of subthreshold oscillations t_{rel}. Therefore many spikes are fired from the maxima of spike-induced subthreshold oscillations and form spike clusters. The intra-cluster interval is deterministic and determined by the period of subthreshold oscillations T_p, whereas the noise-driven inter-cluster interval is related to the noise activation time τ_a. The difference in time scales of intra- and inter-cluster intervals leads to inhomogeneous spike patterns and multimodal ISI distributions. This manifests itself in high values of C_{var} in stellate cells at intermediate firing rates, see Figs. 7.7A and 7.7C for $r \sim 3 - 10\,\text{Hz}$. Overall, stellate cells exhibited higher values of the coefficient of variation C_{var} than pyramidal cells at comparable intermediate firing rates (Fig. 7.7C).

Finally, for high depolarization levels the intrinsic noise is strong and the firing rates are high ($r > 10\,\text{Hz}$). The noise activation time τ_a becomes smaller than all deterministic time scales of neuron dynamics. In both cell types the refractory time alone determines the spike times. In resonant cells at firing rates exceeding the resonance frequency, the mean ISI is smaller than the time scale of the intra-cluster interval. Therefore the subthreshold oscillations do not influence the spike patterns at firing rates $r > 10\,\text{Hz}$. In both cell types the spike patterns are very regular, which is reflected in low values of C_{var} measured in stellate and pyramidal cells for $r > 10\,\text{Hz}$ (Fig. 7.7).

Spike-count variability. Changes in the spike train variability are also pronounced in the Fano factor $F(\mathcal{T})$, which is a measure for the spike-count variability, see Eq. (2.45).

The Fano factor $F(\mathcal{T})$ is a function of the time window $\mathcal{T}$. To estimate $F(\mathcal{T})$ for an experimental spike train, we split the spike train in non-overlapping time windows of length $\mathcal{T}$ and counted the number of spikes $N_i(\mathcal{T})$ in each window. The Fano factor was estimated as the ratio between the variance and the mean of $N_i(\mathcal{T})$ in all time windows:

$$F(\mathcal{T}) = \frac{\langle N_i^2(\mathcal{T})\rangle - \langle N_i(\mathcal{T})\rangle^2}{\langle N_i(\mathcal{T})\rangle}. \tag{7.9}$$

$F(\mathcal{T})$ gives the spike-count variability on the time scale of $\mathcal{T}$. For a Poisson process $F(\mathcal{T}) = 1$ holds on all time scales.

Figs. 7.8A and 7.8B show the Fano factor measured in stellate and pyramidal cells, respectively, for three levels of the average firing rate r. For $\mathcal{T}$ smaller than the minimal ISI observed in a spike train, the behavior of $F(\mathcal{T})$ is predefined: it approaches unity for $T \to 0$ and then decays linearly as $F(\mathcal{T}) = 1 - r\mathcal{T}$ (see discussion following Eq. (2.46)). The first deviation of the Fano factor from the linear decrease indicates the size of the minimal ISI. The arrows in Fig. 7.8 point to times $\mathcal{T}$, where $F(\mathcal{T})$ starts to deviate from the linear behavior. In stellate cells at intermediate firing rates, the size of the minimal ISI is determined by the time scale of the intra-cluster interval and is therefore independent of the firing rate. In pyramidal cells the minimal ISI is noise driven and shifts towards smaller values with increasing firing rate.

For a periodic spike train with a constant ISI equal to X, the Fano factor equals (Middleton et al., 2003)

$$F(\mathcal{T}) = \frac{\text{mod}(\mathcal{T}, X)}{\mathcal{T}} \left(1 - \frac{\text{mod}(\mathcal{T}, X)}{X}\right). \tag{7.10}$$

In this case, $F(\mathcal{T})$ is a sequence of inverted parabola with local maxima of $X/(4\mathcal{T})$ at every odd multiple of $X/2$ and $\lim_{\mathcal{T}\to\infty} F(\mathcal{T}) = F_\infty = 0$. Imperfect periodicity and timing jitter in

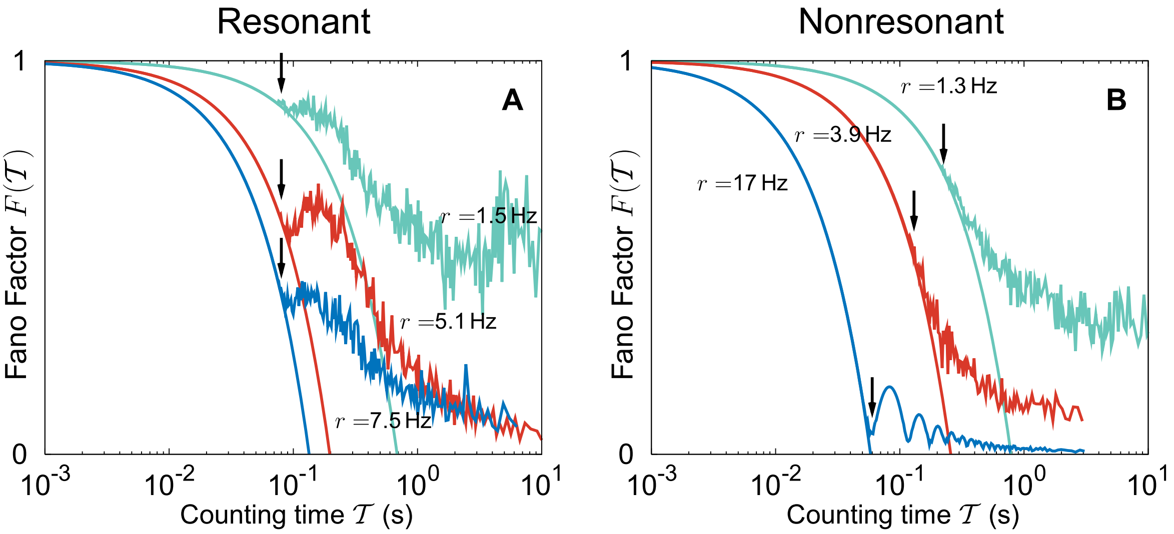

Figure 7.8: Fano factor for experimentally recorded cells. The Fano factor indicates spike clustering in stellate cells and high regularity of spike trains in pyramidal cells. **A**: Fano factor $F(\mathcal{T})$ for a stellate cell (the same example as in Fig. 7.1) for three levels of the average firing rate: $r = 1.5$ Hz (green), $r = 5.1$ Hz (red), and $r = 7.5$ Hz (blue). The oscillatory behavior of $F(\mathcal{T})$ on $\mathcal{T}$ ranging from 70 ms to 200 ms indicates the existence of regular spike patterns (clustering) on this time scale that becomes more pronounced with increasing average firing rate. The solid lines show the linear function $1 - r\mathcal{T}$ with corresponding color. The arrows point to times $\mathcal{T}$, where $F(\mathcal{T})$ starts to deviate from the linear behavior, corresponding to the minimal ISI in a spike train. **B**: Fano factor for a pyramidal cell (the same example as in Fig.7.1) for three levels of the average firing rate: $r = 1.3$ Hz (green), $r = 3.9$ Hz (red), and $r = 17$ Hz (blue). For high firing rates ($r = 17$ Hz) the oscillating $F(\mathcal{T})$ indicates a regular spike pattern on all time scales. The variability of spike trains in pyramidal cells is lower than in stellate cells. Note the logarithmic $\mathcal{T}$-scale.

experimental spike trains result in an asymptotic value F_∞ different from zero. The oscillating behavior of $F(\mathcal{T})$ over a range of $\mathcal{T}$ indicates a high regularity in the spike train on this time scale.

In stellate cells the oscillatory behavior of $F(\mathcal{T})$ was observed for $\mathcal{T}$ ranging from 70 ms to 200 ms, see Fig. 7.8A. Oscillating $F(\mathcal{T})$ indicates the existence of regular spike patterns (clustering) on this time scale that becomes more pronounced with increasing firing rate. In pyramidal cells at low and intermediate firing rates the oscillatory behavior of the Fano factor cannot be observed (see $r = 3.9$ Hz and $r = 1.3$ Hz in Fig. 7.8B). However, for high firing rates the Fano factor curves exhibit an almost perfect sequence of inverted parabola, reflecting the high regularity of the spike train on all time scales $\mathcal{T}$ larger than the minimal ISI (see the Fano factor curve for $r = 17$ Hz in Fig. 7.8B).

7.7 Discussion

In this chapter we investigated how the frequency dependence of the membrane impedance determines the spontaneous (driven by intrinsic noise) firing statistics of individual neurons. Based upon recordings in entorhinal cortex and phenomenological models we show, that the presence of a subthreshold resonance in resonant cells systematically results in firing patterns significantly different from those in nonresonant cells. The subthreshold dynamics alone is not sufficient to account for the observed firing statistics. The spike dynamics leads to correlations between interspike intervals in both resonant and nonresonant cells, which proved necessary to fully explain the observed spike statistics.

7.7.1 The influence of subthreshold resonance on firing properties

The influence of the subthreshold resonance extends from the subthreshold regime to the spiking regime. The most apparent property of the spiking statistics in resonant neurons is the clustering of spikes, reflected in the multimodality of the ISI distribution. The ISI distributions of all nonresonant cells measured were unimodal, in contrast.

The discharge of clustered spikes in neurons with subthreshold membrane potential oscillations were previously observed in olfactory bulb (Chen and Shepherd, 1997; Desmaisons et al., 1999) and brainstem (Pedroarena et al., 1999; Wu et al., 2001). Our results suggest that a frequency selective impedance favoring frequencies above zero is sufficient to cause the spike clustering.

Coding with resonant cells offers advantages that have previously been discussed for bursting cells: the cluster length and the time intervals between clusters may form a code (Kepecs and Lisman, 2003). The reliability of synaptic transmission can be increased due to spike clustering (Lisman, 1997). In addition, spike clustering with stable intra-cluster frequencies may allow for frequency specific routing of information, if the frequency selectivity of individual neurons matches the synaptic frequency preference (Izhikevich et al., 2003). The coding capacity of neurons with multimodal distributions is potentially increased, in the case the peaks of the distribution are distant enough. This fact agrees with our observation that the coefficient of variation is larger for stellate cells than for pyramidal cells at comparable intermediate firing rates.

We show that in resonant stellate cells the size of the minimal ISI is determined by the frequencies of subthreshold resonance and subthreshold oscillations. This minimal ISI (found within a spike cluster) can already be observed at low firing rates and is also maintained at higher firing rates. The increase in the firing rate is mainly accompanied by the reduction of the distance between spike clusters. The stabilization of firing frequencies within spike clusters in stellate cells may be important for frequency selective information routing, as mentioned in the previous paragraph. Note that this may only apply to stellate cells, whose resonance frequency remains almost constant over the broad range of depolarization levels. In nonresonant pyramidal cells the minimal ISI is noise-driven and strongly depends on the mean firing rate.

7.7.2 Implications of ISI correlations

Negative ISI correlations in spontaneous neural activity have been described in many other cell types (as early as Kuffler et al., 1957). More recently, it was shown that negative correlations improve the coding capabilities of neurons with regard to information transfer and signal detection (Chacron et al., 2001). A likely cause for the observed negative correlations on a time scale of 200–400 ms is the spike-induced activation of slowly deactivating currents that prolong the relative refractory period. Such currents are known to mediate adaptation, which also results in ISI correlations of the observed type. Prominent candidates to mediate such correlations are slow potassium currents (Brown and Adams, 1980; Madison and Nicoll, 1984). Interestingly, these currents do contribute to the subthreshold frequency preference (Hutcheon and Yarom, 2000), although their presence does not automatically guarantee a subthreshold resonance. We cannot conclude from our data, to what extent the currents underlying the correlations in the recorded stellate cells are also involved in shaping the subthreshold resonance. The measurements in pyramidal cells, however, show, that the correlations can also be expressed independently of the existence of a subthreshold resonance.

We found ISI correlations on a time scale of 200–400 ms only for intermediate levels of depolarization close to the threshold. Presumably the cause of the correlations, i.e. currents counteracting the initiation of a successive spike, is also present at less depolarized levels of the membrane potential. Due to the lower mean firing rate at these levels, the action of these currents does not significantly affect the ISI statistics. Only for sufficiently high firing rate, a significant number of short ISIs appear during the deactivation time of the slowly deactivating currents, which lead to the pronounced negative ISI correlations. In addition, the ISI correlations effectively limit the number of spikes per cluster in resonant cells.

The ISI correlations cannot be captured by the renewal model. Surprisingly, a simple modification of the threshold model, which makes it nonrenewal and covers correlations, is able to describe ISI distributions in both cell types as well. This indicates, that the frequency-dependent subthreshold dynamics in combination with the simple spike-induced dynamics are well suited to capture the essence of steady state firing.

7.7.3 Discussion of the model

We used three aspects of the model to describe experimental data. (i) The linear resonating model is well suited to cover subthreshold responses. (ii) In combination with a static renewal threshold, the differences between the firing statistics of resonant and nonresonant neurons could be quantitatively captured. Especially the multimodality of ISI distributions in resonant cells versus the monomodality of these distributions in nonresonant cells were reproduced by the model. (iii) The modified model, with a stochastic nonrenewal threshold, proved to capture quantitatively the ISI distributions as well as the negative ISI correlations in resonant and nonresonant cells. The spike probability in the nonrenewal model takes the spike history into account, such that a recent occurrence of spikes lowers the firing probability.

We observed that the intensity of intrinsic noise always increased towards the threshold (Fig.7.2). This effect is most likely due to the stochasticity in the opening and closing of ion channels (for a review on channel noise see White et al., 2000). The influence of noise on spike initiation has been shown to be important (Schneidman et al., 1998), we therefore chose to make the spike probability a dynamical variable. The increased level of noise around the threshold as well as the influence of spike history on spike initiation are therefore incorporated into a single step.

Overall, the nonrenewal model is simple and captures the essential properties of the subthreshold frequency preference and interspike correlations. It may prove useful for network simulations, where subthreshold properties of individual neurons and correlations in their spike trains may be of importance. Other nonrenewal models that capture correlations and adaptive effects have been suggested before. These models modify, either dynamically or stochastically, the absolute threshold value (Chacron et al., 2004) or explicitly model currents that prolong the interspike interval in dependence on the spike history (Benda and Herz, 2003; Izhikevich, 2004). We have no reason to assume, that these nonrenewal models cannot also represent our experimental data.

The results of this chapter provide new insight how intrinsic cell properties acting on the subthreshold level of signal processing affect the spike generation in the entorhinal cortex. Whereas clustering of action potentials clearly is a hallmark of resonant neurons, additional spike-induced dynamics further modifies the firing statistics. Simple threshold models, that combine the subthreshold dynamics with nonrenewal spike initiation, are easy and efficient to use in network simulations and faithfully reflect the intrinsic neuronal frequency selectivity.

8

Concluding remarks

In this thesis various aspects of the non-Markovian first passage time problem have been investigated, using a combination of analytical, numerical and experimental methods. Two main issues have been addressed in this text:

I. the elaboration of analytical methods to treat the non-Markovian first passage time problem,

II. the exploration of mechanisms leading to complex spike patterns in neurons.

I. Non-Markovian first passage time problem

Recent experiments (Diau et al., 1998; Desmaisons et al., 1999; Nowakowski and Kawczyński, 2006) revealed essentially non-Markovian character of the escape dynamics in many physical systems. This explains a growing theoretical interest in the challenging non-Markovian first passage time problem. The distinctive features of the non-Markovian escape dynamics are the time dependent escape rates and the sensitivity to initial conditions. Complex multimodal structures are characteristic for the distribution of the first passage time in the non-Markovian case. Therefore, habitual Kramers approach reveals its inherent limitations when confronted with non-Markovian situations. Several analytical approaches to the non-Markovian first passage time problem have been proposed in the literature. These include the method of optimal fluctuation (Soskin et al., 2001) and approximations based on the generalized renewal equation (Wilemski and Fixman, 1974; Likthman and Marques, 2006).

We hope, this work provides a new insight into the non-Markovian first passage time problem. Our analytical approach is based on the theory of level-crossings first developed by Rice (1945). An exact expression for the first passage time density of a differentiable random process can be derived in form of an infinite series of integrals over the joint densities of level-crossings. We demonstrate, how effective and accurate analytical approximations for this series can be obtained on the basis of either truncations or the correlations decoupling. In the former case, a few initial terms evaluated exactly are used to approximate the series (direct truncations and Padé approximants). In the latter case infinitely many terms evaluated approximately lead to a closed analytical expression for the first passage time density (Hertz and Stratonovich approximations). Our approximations are applicable to processes with differentiable trajectories, but there are no further restrictions on the dimension and form of the dynamical system. We compare the quality of different approximations and ascertain their regions of validity. The approximations complement one another: in regimes of strong noise and low threshold the truncations are more suitable, whereas for a weak noise or high threshold the decoupling approximations are more effective. Overall, the regions of validity for our approximations cover all types of escape dynamics, ranging from almost Markovian to strongly non-Markovian cases.

In the general Markovian case, a single parameter – the constant escape rate – completely describes the statistics of the escape times. In contrast, in the non-Markovian case multiple time scales are involved in the escape problem. These time scales are pertinent to the deterministic subthreshold dynamics and are reflected in the statistics of the escape times, for example in the multipeak first passage time densities. Our analytical approach to the non-Markovian first passage time problem allows a closer inspection of these complex multipeak first passage time densities: the number of pronounced peaks, their position and height are reproduced by the analytical approximations and can be related to the deterministic subthreshold time scales.

The level-crossing approach is rather general. It relates the statistical properties of a freely evolving random process (in the absence of boundaries) to the statistical properties of a point process formed by the times, when this random process crosses a prescribed level. This general approach is applicable whenever the joint level-crossing rates are finite. Besides the differentiable random processes the level-crossing approach can also be applied to discrete random walks with arbitrary waiting-time distributions. The generalization of this approach to processes with nondifferentiable trajectories may be a further challenging problem. Finally, inspired by negative correlations found in the dynamics of resonant and nonresonant neurons, a very appealing problem is to develop the modified level-crossing approach for a nonrenewal escape dynamics, with the level-crossing rates being dependent on the history of escape times.

II. Spike patterns in resonant and nonresonant neurons

The neural code (Rieke et al., 1997; Koch, 1999) is the central problem discussed in the computational neuroscience. Current theories hypothesize that information is encoded by the spike frequency, the spike times and the correlations between spike times. Insight into the neural code could be therefore gained by understanding the spike patterns generated in neurons.

In this work we investigate the joint influence of deterministic and stochastic properties of neuron dynamics on the spiking behavior. In particular, we study the random spike patterns in resonant and nonresonant neurons. The former exhibit subthreshold resonance with maximal response amplitude achieved at a finite resonance frequency. The subthreshold response amplitudes in the latter decay monotonically with the frequency. We show in phenomenological neuron models (FitzHugh-Nagumo model and resonate-and-fire model) as well as in the experimental data obtained from stellate (resonant) and pyramidal (nonresonant) cells in the entorhinal cortex in rat, that the differences in the deterministic subthreshold properties yield qualitatively different spike patterns. Resonant neurons exhibit spike clustering reflected in the multimodal interspike interval (ISI) densities, whereas nonresonant neurons show monomodal ISI densities.

The idea that the subthreshold resonance properties of neurons may shape their spike patterns is intuitive and have been proposed in several studies (Desmaisons et al., 1999; Pedroarena et al., 1999; Izhikevich, 2001). In this work we systematically investigate this connection and demonstrate, that the subthreshold frequency selectivity of resonant neurons is sufficient to explain the spike clustering. We use the resonate-and-fire model with experimentally estimated subthreshold parameters and show, that this simple phenomenological model can quantitatively capture the ISI distributions measured in stellate and pyramidal cells. The ISI density obtained analytically for the resonate-and-fire model in the Stratonovich approximation agrees well with experimental data. The advantage of using an analytical approximation is that it allows to relate the characteristic time scales observed in spike trains (inter- and intra-cluster intervals) to the characteristic time scales of the subthreshold voltage dynamics (period and relaxation time of the subthreshold oscillations). Moreover, the mechanism shaping the spike patterns in resonant neurons can be easily understood from the simple resonate-and-fire model. This mechanism is expected to be the same in more complex models.

The subthreshold properties alone are not sufficient to completely explain the observed spike patterns: Negative spike-induced ISI correlations, which are found in stellate as well as in pyramidal cells, cannot be explained by the subthreshold properties. To also account for negative correlations, we introduce a novel nonrenewal threshold mechanism in the resonate-and-fire model. Modified model can capture both: the differences in spike patterns as well as similar correlations in resonant and nonresonant neurons. The predictions of the model are in quantitative agreement with experimental data.

Spike clustering and negative correlations might be essential for the neural computation. Spike clusters may enhance the reliability of synaptic transmission and allow for frequency specific information routing (Lisman, 1997; Izhikevich et al., 2003). Negative ISI correlations were shown to improve the signal detection and information transfer by neurons (Chacron et al., 2001). Understanding of the interplay between subthreshold resonance properties and spike-induced correlations and their joint influence on the information processing by a neuron are therefore very interesting open problems. The precise mechanism leading to the ISI correlations in stellate and pyramidal cells also remains to be elucidated.

A

Experimental methods

A.1 Experimental data

All details of experimental procedures and data acquisition[1] have been previously described in (Erchova et al., 2004; Schreiber et al., 2004). Briefly, the sharp electrode intracellular recordings were obtained from entorhinal cortex neurons in adult Wistar rats (above 300 g, older than three months). We used medial horizontal slices of the retro-hippocampal region (400 μm, at 35°C). Synaptic transmission was blocked. The following drugs were added to the aCSF (in μM): 306-cyano-7-nitroquinoxaline-2,3-dione (CNQX), 60 DL-2-amino-5-phosphonopentanoic acid (APV), 5 bicucculine and 1 CGP (all from Sigma-Aldrich, Deisenhofen, Germany). All recordings were done in current-clamp mode using sharp micropipettes filled with 2 M potassium acetate containing 1% biocytin (75–100 MΩ). The experiment and acquisition were controlled by custom software written in LabView via a digital-analog converter card (AI-16E-4, National Instruments Inc., TX, USA). Data were sampled at 8 kHz and stored for offline analysis. The cells were identified based on their location and electrophysiological properties, 25% of recorded cells were histologically identified, as described in Erchova et al. (2004). Only cells that had an input resistance of more than 20 MΩ, a resting potential less then -60 mV, and a spike amplitude larger than 50 mV were used for the analysis.

We used hyper- and depolarizing current steps with a duration of 500 ms, 10 s, 20 s and 30 s to characterize cells and to obtain distributions of interspike intervals. The oscillatory stimuli (ZAP) of 30 s duration were applied to characterize the resonance properties of a cell:

$$I(t) = I_0 + I_1 \sin[2\pi f(t)t], \tag{A.1}$$

with $f(t) = f_m t/2T$. Here $I_1 = 50\,\text{pA}$ is the stimulus amplitude, I_0 the constant holding current, $T = 30\,\text{s}$ the stimulus length, and $f_m = 20\,\text{Hz}$ the maximum stimulus frequency.

---

[1] All experiments were performed by Irina Erchova (University of Edinburgh).

A.2 Parameter estimation of the model

Subthreshold parameters

Subthreshold parameters of the resonate-and-fire model Eq. (7.4) were estimated from the experimental data on the basis of both the frequency-dependent impedance $Z(f)$ and the autocorrelation function $r_x(t)$.

The impedance was obtained from the measured voltage response $V(t)$ to the applied ZAP current $I(t)$, Eq. (A.1), as the ratio of the Fast Fourier Transform (FFT) of the measured voltage FFT $[V(t)]$ and the FFT of the applied ZAP current FFT $[I(t)]$:

$$Z(f) = \frac{\mathrm{FFT}\,[V(t)]}{\mathrm{FFT}\,[I(t)]}. \tag{A.2}$$

The amplitude of the impedance vector $|Z|(f)$ was calculated and fitted with the theoretical impedance-frequency function Eq. (7.2), yielding estimates for the parameters C, R_0, γ and δ.

In order to obtain an estimate for the noise variance, the voltage autocorrelation function $r(t)$ was calculated from the voltage traces obtained in response to hyper- and depolarizing current steps with a duration of 10 s and 20 s. Only traces containing less than 5 spikes were used. In resonant cells the autocorrelation showed oscillatory behavior (see Fig. 7.1C). Using Eq. (7.5) and the values of the autocorrelation function $r(t)$ at $t = 0$ and at the first minimum at $t = t_1$, as well as the C-value (based on the impedance estimate), we could obtain the parameter values for stellate cells

$$\begin{aligned} &\text{(a)}\quad \Omega = \frac{\pi}{t_1}; && \text{(b)}\quad \gamma = \frac{2C}{t_1}\ln\left(-\frac{r(0)}{r(t_1)}\right); \\ &\text{(c)}\quad \delta = C\Omega^2 + \gamma^2/4C; && \text{(d)}\quad D \;=\; r(0)\,\gamma\,\delta. \end{aligned} \tag{A.3}$$

The autocorrelation function in nonresonant cells decays monotonically (see Fig. 7.1D). Therefore only the value $r(0)$ was used to estimate the noise intensity from Eq. (A.3d). In stellate cells the estimates for the parameters γ and δ were obtained on the basis of the impedance as well as the autocorrelation function. The values obtained with both methods were in good agreement.

ZAP and constant current recordings were performed for several values of the constant offset current I_0, and provided values of parameters C, γ, δ, R_0 and D for several values of the holding potential.

Spike parameters

To determine the voltage threshold and the reset value (valid for both threshold mechanisms) we analyzed the voltage traces recorded in response to depolarizing current steps with a duration of 10 s and 20 s containing more than 40 spikes. The beginning of a spike was marked by a rise in the voltage derivative. We first estimated the mean and standard deviation (SD)

$\sqrt{\delta/C}/2\pi$ (Hz)	γ/C (10^2Hz)	D (nA^{2}Hz)	τ_r (ms)	x_0 (mV)	x_b (mV)	τ_c (ms)	β (Hz)	p_0
				stellate cell				
5–7.5	0.02–0.4	0.005–0.05	0–51	-12–-7	1–7	100–500	1–1000	0–1
				pyramidal cell				
7–14	1.8–3.5	0.05–0.5	0–97	-12–-7	0.02–6.0	100–500	1–1000	0–1

Table A.1: Parameter ranges of the resonate-and-fire model used for fitting to experimental ISI distributions, based on experimental estimations of these parameters.

of the voltage derivative in absence of spikes. The threshold value V_b was determined as the voltage value, where the voltage derivative exceeded three times its SD. The reset value V_0 was determined as the minimal voltage value within 25 ms following a spike (after the voltage derivative decreased below the mean value plus one SD). The reset time τ_r was given by the time elapsed between the time of threshold crossing (marking the beginning of a spike) and the time, when the voltage minimum following the spike was reached. These parameters were determined for every spike in a record and averaged over all spikes. The reset and threshold values for the RaF model were then directly taken from the data as $x_b = V_b - V_s$ and $x_0 = V_0 - V_s$, where V_s is the holding potential. The holding potential was estimated by the mean voltage (preferentially in time intervals without spikes). If individual spikes had to be included (at larger firing rates), these spikes were cut off at V_b. Note that a larger number of spikes in the estimation interval biases the holding potential towards lower voltages, because of the period of afterhyperpolarization following a spike.

Specification of parameter ranges

Our goal was to match the theoretical and experimental ISI distributions. Therefore, we take the parameter ranges as estimated from experiments and allow the parameters of the RaF model to vary within these limits. An optimized combination of parameters was then determined using technique of simulated annealing.

Specifically, C was taken directly from the experiment and remained fixed as it did not vary strongly with the holding potential ($C = 2.5 \cdot 10^{-4}\,\mu$F for the stellate cell and $C = 1.7 \cdot 10^{-4}\,\mu$F for the pyramidal cell). In contrast, γ, δ and D depended on the holding potential and therefore were optimized within a range dictated by their experimental estimates (see

Fig. 7.2 and Table A.1). Spike parameters x_b and x_0 differed for individual spikes and were therefore allowed to vary within the range of values observed in the corresponding experimental voltage traces. The reset time τ_r was allowed to extend beyond the experimental range, but was limited by the size of the minimal ISI observed in the specific spike train. The experimental value of the voltage threshold V_r is very sensitive to the definition of the threshold. In biological systems, spike threshold may depend on additional dynamical variables, such as the voltage derivative. Therefore, we tested an extended range of thresholds (see Table A.1) to circumvent biases caused by a particular choice of threshold definition described above.

For the nonrenewal threshold mechanism, three additional parameters τ_c, β, and p_s had to be specified, which were not directly estimated in experiments. These were varied freely within the range specified in Table A.1 to account for the experimentally observed negative correlations between neighboring ISIs.

A.3 Spike train statistics

Let us denote a measured spike train by

$$\{t_i\} = \{t_1, t_2, t_3, \dots, t_{N+1}\}, \tag{A.4}$$

where $t_1, t_2, t_3, \dots, t_{N+1}$ are the successive spike arrival times and i denotes the position of a spike in the sequence. The i-th interspike interval (ISI) is defined as $X_i = t_{i+1} - t_i$. ISI histograms were obtained from the spike train and used as an estimate for the probability density $\mathcal{F}(T)$ of interspike intervals. Due to the limited experimental data size (150–600 spikes per spike train) the estimate of $\mathcal{F}(T)$ strongly depends on the bin size and cannot be directly compared with predictions of the model. Instead, we used the cumulative ISI distribution $P(T)$, which gives the probability to obtain $X_i < T$ in a spike train and is related to the ISI density by $P(T) = \int_0^T \mathcal{F}(t)dt$. The cumulative ISI distribution was estimated from a spike train as

$$P_X(T) = \frac{1}{N}\sum_{i=1}^{N} \Theta(T - X_i), \tag{A.5}$$

where $\Theta(T)$ is the Heaviside step function.

To verify whether the distribution $P_{\mathrm{exp}}(T)$ underlying the experimental data $\{X_i\}$ and the theoretically predicted ISI distribution $P_0(T)$ differ, we used the Kolmogorov-Smirnov (KS) test (Ledermann, 1984). We test the null hypothesis

$$H_0: \quad P_{\mathrm{exp}}(T) = P_0(T) \ \text{ for all } \quad T$$

against

$$H_1: \quad P_{\mathrm{exp}}(T) \neq P_0(T) \ \text{ for some } \ T.$$

The test statistics $\mathcal{D}$ in the KS test is the largest difference between the experimentally estimated $P_X(T)$ and the theoretical ISI distributions:

$$\mathcal{D} = \sup_{0<T<\infty} |P_X(T) - P_0(T)|. \tag{A.6}$$

For a given significance level α, the critical value $\mathcal{D}_K$ can be calculated. It depends on α and the sample size N, but does not depend on the particular form of the distribution $P_0(T)$. In all cases we used $\alpha = 5\%$, and the corresponding critical value $\mathcal{D}_K$ is obtained as

$$\mathcal{D}_K = 1.36/\sqrt{N}. \tag{A.7}$$

To test the predictions of the nonrenewal RaF model, we have to compare the experimental sample $\{X_i\}$ and the sample $\{Y_i\}$ of N_1 interspike intervals obtained by stochastic simulations of the nonrenewal RaF model. From the sample $\{Y_i\}$ the empirical distribution function $P_Y(T)$ is estimated as

$$P_Y(T) = \frac{1}{N_1}\sum_{i=1}^{N_1}\Theta(T - Y_i). \tag{A.8}$$

The test statistics is then defined as

$$\mathcal{D} = \sup_{0<T<\infty} |P_X(T) - P_Y(T)|, \tag{A.9}$$

and the critical value $\mathcal{D}_K$ for the significance level $\alpha = 5\%$ equals

$$\mathcal{D}_K = 1.36/\sqrt{NN_1/(N+N_1)}. \tag{A.10}$$

If $\mathcal{D} > \mathcal{D}_K$, then the null hypothesis has to be rejected and the theoretical distribution cannot be assumed to underly the experimental data $\{X_i\}$. If $\mathcal{D} < \mathcal{D}_K$, then with significance level α one may regard the experimental data $\{X_i\}$ as consistent with the hypothesis that they come from the distribution $P_0(T)$.

In Figs. 7.3 and 7.6 we draw a tube $P_X(T) \pm \mathcal{D}_K$ with the radius $\mathcal{D}_K$ around the estimated cumulative ISI distribution $P_X(T)$. The theoretical ISI distribution can be assumed to underly the experimental data, if $P_0(T)$ or $P_Y(T)$ lie inside the tube.

A.4 Fitting procedures

Our aim was to verify whether (i) the renewal and (ii) the nonrenewal RaF models can reproduce the ISI statistics measured in stellate and pyramidal cells. We performed a systematical search in the parameter spaces of these models using the simulated annealing (SA) algorithm. The scanned parameter ranges, based on the experimental estimates, are specified for both models in Table A.1.

An “energy” value E was ascribed to every point in the parameter space of the models as follows. For (i) the renewal model, the theoretically predicted ISI distribution $P_0(T)$ was calculated for a given parameter set (C, δ, γ, D) in the Stratonovich approximation, which corresponds to $\tau_r = 0$. The reset time τ_r results in the shift of the ISI distribution as a whole to the larger T values by this amount, therefore the ISI distribution for a nonzero τ_r reads $P_0(T - \tau_r)$. For every value of τ_r from the range specified in Table A.1 with a step of 1 ms, we determined the KS statistics $\mathcal{D}$ for the measured ISI distribution $P_X(T)$ and the theoretical distribution $P_0(T - \tau_r)$, according to Eq. (A.6). The value of τ_r was selected, which minimized $\mathcal{D}$ for the given set (C, δ, γ, D). The "energy" for this parameter set was determined as the corresponding value of the KS statistics: $E = \mathcal{D}$.

For (ii) the nonrenewal model, we intended to fit both, the cumulative distribution $P_X(T)$ and the first serial correlation coefficient ρ_1. For a given parameter set (C, δ, γ, D, τ_r, x_0, x_b, τ_c, β, p_0) we simulated the nonrenewal RaF model to produce 2000 spikes. From this spike train the theoretical ISI distribution $P_Y(T)$ was estimated by Eq. (A.8) and the first SCC ρ_1^Y by Eq. (7.7). The KS statistics $\mathcal{D}$ was calculated for the measured $P_X(T)$ and theoretical $P_Y(T)$ ISI distributions according to Eq. (A.9). The "energy" E was determined as

$$E = \mathcal{D} + \alpha \frac{|\rho_1 - \rho_1^Y|}{|\rho_1|}. \tag{A.11}$$

Here $0 < \alpha < 1$ is a weighting factor, $\alpha = 0$ means that the ISI distribution is fitted alone irrespective of the SCC value, and $\alpha = 1$ means that the both measures equally contribute to the "energy" function. We repeated all simulations for three values of α (0, 0.25 and 0.5).

The energy functions defined above were minimized using the simulated annealing (SA) algorithm (Press et al., 1999). The SA algorithm takes random walks through the parameter space searching for points with low energy. Let z denote one of the model parameters, and let Δz denote the width of the z-range as specified in Table A.1. If the z-value at the i-th step of the random walk was z_i, then the value z_{i+1} was chosen to be $z_{i+1} = z_i + \zeta$, where ζ is a random variable uniformly distributed in the interval $(-0.2\Delta z, 0.2\Delta z)$. This was done for all model parameters independently, in order to determine the next position of the random walk in the parameter space. The step $i \to i + 1$ was accepted with the probability p determined by the Boltzmann distribution:

$$p = \min\left[1,\ \exp\left(-\frac{E_{i+1} - E_i}{T}\right)\right]. \tag{A.12}$$

Here E_i denotes the "energy" at the i-th point and T is the current "temperature". In other words, a step is always accepted if $E_{i+1} < E_i$, otherwise the step is accepted only with the probability $p < 1$. The "temperature" T was initially set to a high value ($T = 5$ in our case), and a random walk was carried out at this temperature. The number of steps made at a constant "temperature" was 10 for the renewal model and 250 for the nonrenewal model. The "temperature" was then slowly decreased according to a cooling schedule $T \to T/\mu$ with $\mu = 1.01$, until the "temperature" $T = 0.01$ was achieved.

The SA belongs to the class of heuristic algorithms, which do not guarantee to converge to the global minimum. We therefore repeated the annealing procedure several times (up to 5) and chosen the best solution encountered.

Bibliography

M. Abeles. NEUROSCIENCE: Enhanced: Time Is Precious. *Science*, 304(5670):523–524, 2004.

M. Acar, A. Becskei, and A. van Oudenaarden. Enhancement of cellular memory by reducing stochastic transitions. *Nature*, 435(7039):228–232, 2005.

R.K. Adair. Noise and stochastic resonance in voltage-gated ion channels. *PNAS*, 100(21): 12099–12104, 2003.

B. Alberts, D. Bray, and J. Lewis. *Molecular Biology of the Cell.* Garland Science, New York, 2002.

K. Amemori and S. Ishii. Gaussian process approach to spiking neurons for inhomogeneous poisson inputs. *Neural Computation*, 13(12):2763–2797, 2001.

R. Amir, M. Michaelis, and M. Devor. Membrane potential oscillations in dorsal root ganglion neurons: Role in normal electrogenesis and neuropathic pain. *J. Neurosci.*, 19(19):8589–8596, 1999.

R. Amir, M. Michaelis, and M. Devor. Burst discharge in primary sensory neurons: Triggered by subthreshold oscillations, maintained by depolarizing afterpotentials. *J. Neurosci.*, 22 (3):1187–1198, 2002.

S. Arrhenius. Über die Reaktionsgeschwindigkeit bei der Inversion von Rohrzucker in Säuren. *Z. Phys. Chem*, 4:226–248, 1889.

G.A. Jr. Baker. *Essentials of Padé Approximants.* Academic Press, London, 1975.

R. Becker and W. Döring. Kinetische Behandlung der Keimbildung in übersättigten Dämpfen. *Ann. Phys. (5.)*, 24:719–752, 1935.

J. Benda and A.V.M. Herz. A universal model for spike-frequency adaptation. *Neural Computation*, 15:2523–2564, 2003.

S.M. Bezrukov and I. Vodyanoy. Noise-induced enhancement of signal transduction across voltage-dependent ion channels. *Nature*, 378(6555):362–364, 1995.

H.A. Braun, H. Wissing, K. Schäfer, and M.C. Hirsch. Oscillation and noise determine signal transduction in shark multimodal sensory cells. *Nature*, 367:270–273, 1994.

D.A. Brown and P.R. Adams. Muscarinic supression of a novel voltage-sensitive K^+ current in a vertebrate neuron. *Nature*, 183:673–676, 1980.

N. Brunel and S. Sergi. Firing frequency of leaky intergrate-and-fire neurons with synaptic current dynamics. *J. theor. Biol.*, 195:87–95, 1998.

N. Brunel, V. Hakim, and M.J.E. Richardson. Firing-rate resonance in a generalized integrate-and-fire neuron with subthreshold resonance. *Phys. Rev. E*, 67:051916, 2003.

M.J. Chacron, A. Longtin, and L. Maler. Negative interspike interval correlations increase the neuronal capacity for encoding time-dependent stimuli. *J. Neurosci.*, 21(14):5328–5343, 2001.

M.J. Chacron, B. Lindner, and A. Longtin. Noise shaping by interval correlations increases information transfer. *Phys Rev Lett*, 21(92):080601, 2004.

W.R. Chen and G.M. Shepherd. Membrane and synaptic properties of mitral cells in slices of rat olfactory bulb. *Brain Res.*, 745(1-2):189–196, 1997.

D.T.W. Chik, Y. Wang, and Z.D. Wang. Stochastic resonance in a Hodgkin-Huxley neuron in the absence of external noise. *Phys. Rev. E*, 64(2):021913, 2001.

J. J. Collins, C.C. Chow, and T.T. Imhoff. Stochastic resonance without tuning. *Nature*, 376:236–238, 1995a.

J. J. Collins, C.C. Chow, and T.T. Imhoff. Aperiodic stochastic resonance in excitable systems. *Phys. Rev. E*, 52(4):R3321–R3324, 1995b.

J.J. Collins, T.T. Imhoff, and P. Grigg. Noise-enhanced information transmission in rat sa1 cutaneous mechanoreceptors via aperiodic stochastic resonance. *J. Neurophysiol.*, 76: 642–645, 1996.

D.R Cox. *Renewal Theory.* Chapman & Hall, London, 1967.

D.R. Cox and V. Isham. *Point Processes.* Chapman & Hall, London, 1980.

D.R Cox and P.A.W. Lewis. *The Statistical Analysis of Series of Events.* Wiley, New York, 1966.

H. Cramér and M.R. Leadbetter. *Stationary and Related Stochastic Processes.* Wiley, New York, 1968.

P. Dayan and L.F. Abbott. *Theoretical Neuroscience. Computational and Mathematical Modeling of Neural Systems.* MIT Press, Cambridge, Massachusetts, 2001.

D. Desmaisons, J.-D. Vincent, and P.-M. Lledo. Control of action potential timing by intrinsic subthreshold oscillations in olfactory bulb output neurons. *J. Neurosci.*, 19(24):10727–10737, 1999.

A. Destexhe and T.J. Sejnowski. Interactions between membrane conductances underlying thalamocortical slow-wave oscillations. *Physiol. Rev.*, 83(4):1401–1453, 2003.

A. Destexhe, M. Rudolph, J.-M. Fellous, and T.J. Sejnowski. Fluctuating synaptic conductances recreate in vivo-like activity in neocortical neurons. *Neuroscience*, 107(1):13–24, 2001.

E.W.-G. Diau, J.L. Herek, Z.H. Kim, and A.H. Zewail. Femtosecond activation of reactions and the concept of nonergodic molecules. *Science*, 279(5352):847–851, 1998.

K. Diba, H.A. Lester, and C. Koch. Intrinsic noise in cultured hippocampal neurons: Experiment and modeling. *J. Neurosci.*, 24(43):9723–9733, 2004.

C.R. Doering, P.S. Hagan, and C. D. Levermore. Bistability driven by weakly colored gaussian noise: The fokker-planck boundary layer and mean first-passage times. *Phys. Rev. Lett.*, 59(19):2129–2132, 1987.

A.D. Dorval, Jr. and J.A. White. Channel noise is essential for perithreshold oscillations in entorhinal stellate neurons. *J. Neurosci.*, 25(43):10025–10028, 2005.

M.I. Dykman, P.V.E. McClintock, V.N. Smelyanski, N.D. Stein, and N.G. Stocks. Optimal paths and the prehistory problem for large fluctuations in noise-driven systems. *Phys. Rev. Lett.*, 68(18):2718–2721, 1992.

W. Ebeling and R. Feistel. *Chaos und Kosmos: Prinzipien der Evolution.* Spektrum, Berlin, 1994.

T.A. Engel, S. Schreiber, L. Schimansky-Geier, A.V.M. Herz, and I. Erchova. Membrane resonance shapes the pattern of spontaneous firing in the entorhinal cortex. *To be submitted.*, 2007.

I. Erchova, G. Kreck, U. Heinemann, and A.V.M. Herz. Dynamics of rat entorhinal cortex layer II and III cells: characteristics of membrane potential resonance at rest predict oscillation properties near threshold. *J. Physiol*, 560:89–110, 2004.

H. Eyring. The activated complex in chemical reactions. *J. Chem. Phys.*, 3(2):107–115, 1935.

U. Fano. Ionization yield of radiations. ii. the fluctuations of the number of ions. *Phys. Rev.*, 72(1):26–29, 1947.

L. Farkas. The velocity of nucleus formation in supersaturated vapors. *Z. Physik. Chem.*, 125:236–242, 1927.

A. Fiasconaro, D. Valenti, and B. Spagnolo. Role of the initial conditions on the enhancement of the escape time in static and fluctuating potentials. *Physica A*, 325(1-2):136–143, 2003.

A. Fiasconaro, B. Spagnolo, and S. Boccaletti. Signatures of noise-enhanced stability in metastable states. *Phys. Rev. E*, 72(6):061110, 2005.

R. FitzHugh. Impulses and physiological states in theoretical models of nerve membrane. *Biophys. J.*, 1(6):445–466, 1961.

Ya.A. Fomin. *Excursions Theory of Stochastic Processes.* Svyaz, Moscow, 1980.

R.F. Fox. Gaussian stochastic processes in physics. *Phys. Rep.*, 48(3):179–283, 1978.

R.F. Fox and Y.-N. Lu. Emergent collective behavior in large numbers of globally coupled independently stochastic ion channels. *Phys. Rev. E*, 49(4):3421–3431, 1994.

J. Franklin and W Bair. The effect of a refractory period on the power spectrum of neuronal discharge. *SIAM J. APP. MATH.*, 55(4):1074–1093, 1995.

T.A. Fulton and L.N. Dunkleberger. Lifetime of the zero-voltage state in josephson tunnel junctions. *Phys. Rev. B*, 9(11):4760–4768, 1974.

L. Gammaitoni, F. Marchesoni, E. Menichella-Saetta, and S. Santucci. Zero-crossing distributions for smoothed random signals. *Phys. Lett. A*, 158:9–13, 1991.

L. Gammaitoni, P. Hänggi, P. Jung, and F. Marchesoni. Stochastic resonance. *Rev. Mod. Phys.*, 70(1):223–287, 1998.

G.L. Gerstein and B. Mandelbrot. Random walk models for the spike activity of a single neuron. *Biophys. J.*, 4:41–68, 1964.

W. Gerstner and W. Kistler. *Spiking Neuron Models: Single Neurons, Populations, Plasticity.* Cambridge University Press, Cambridge, 2000.

G. Giacomelli, M. Giudici, S. Balle, and J.R. Tredicce. Experimental evidence of coherence resonance in an optical system. *Phys. Rev. Lett.*, 84(15):3298–3301, 2000.

S.L. Ginzburg and M.A. Pustovoit. Bursting dynamics of a model neuron induced by intrinsic channel noise. *Fluct. Noise Lett.*, 3(3):L265–L274, 2003.

T. Gloveli, D. Schmitz, R.M. Empson, and U. Heinemann. Frequency-dependent information flow from the entorhinal cortex to the hippocampus. *J. Neurophysiol.*, 78(6):3444–3449, 1997.

I. Goychuk and P. Hänggi. Stochastic resonance in ion channels characterized by information theory. *Phys. Rev. E*, 61(4):4272–4280, 2000.

R. Graham and T. Tél. Nonequilibrium potential for coexisting attractors. *Phys. Rev. A*, 33 (2):1322–1337, 1986.

H.G. Gu, M.H. Yang, L. Li, Z.Q. Liu, and W. Ren. Experimental observation of the stochastic bursting caused by coherence resonance in a neural pacemaker. *Neuroreport*, 13(13):1657–1660, 2002.

A. Guderian, G. Dechert, K.-P. Zeyer, and F.W. Schneider. Stochastic resonance in chemistry. 1. the belousov-zhabotinsky reaction. *J. Phys. Chem.*, 100(11):4437–4441, 1996.

Y. Gutfreund, Y. Yarom, and I. Segev. Subthreshold oscillations and resonant-frequency in guinea-pig cortical-neurons - physiology and modeling. *J. Physiol. (London)*, 483(3): 621–640, 1995.

J.S. Haas and J.A. White. Frequency selectivity of layer ii stellate cells in the medial entorhinal cortex. *J. Neurophysiol.*, 88(5):2422–2429, 2002.

P.S. Hagan, C.R. Doering, and C.D. Levermore. Mean exit times for particles driven by weakly colored noise. *SIAM J. Appl. Math.*, 49(5):1480–1513, 1989a.

P.S. Hagan, C.R. Doering, and C.D. Levermore. The distribution of exit times for weakly colored noise. *J. Stat. Phys.*, 54(5–6):1321–1352, 1989b.

H. Haken. *Synergetics.* Springer, Berlin, 1983.

P. Hänggi and P. Jung. Colored noise in dynamical systems. *Advances in Chem. Phys.*, 89: 239–326, 1995.

P. Hänggi, P. Jung, and P. Talkner. Comment on "Bistability driven by weakly colored gaussian noise: The fokker-planck boundary layer and mean first-passage times". *Phys. Rev. Lett.*, 60(26):2804, 1988.

P. Hänggi, P. Talkner, and M. Borkovec. Reaction-rate theory: fifty years after kramers. *Rev. Mod. Phys.*, 62:251–341, 1990.

P. Hertz. Über den gegenseitigen durchschnittlichen Abstand von Punkten, die mit bekannter mittlerer Dichte im Raume angeordnet sind. *Math. Ann.*, 67:387–398, 1909.

J.J. Hesse and L. Schimansky-Geier. Inversion in harmonic noise driven bistable oscillators. *Z. Phys. B Condensed Matter*, 84(3):467–470, Oct 1991.

A.L. Hodgkin and A.F. Huxley. Quantitative description of membrane current and its application to conduction and excitation in nerve. *J. Physiol. London*, 117(4):500–544, 1952.

Z.H. Hou and H.W. Xin. Enhancement of internal signal stochastic resonance by noise modulation in the cstr system. *J. Phys. Chem. A*, 103(31):6181–6183, 1999.

M.T. Huber and H.A. Braun. Stimulus-response curves of a neuronal model for noisy subthreshold oscillations and related spike generation. *Phys. Rev. E*, 73(4):041929, 2006.

S.W. Hughes and V. Crunelli. Thalamic mechanisms of eeg alpha rhythms and their pathological implications. *Neuroscientist*, 11(4):357–372, 2005.

B. Hutcheon and Y. Yarom. Resonance, oscillation and the intrinsic frequency preferences of neurons. *Trends Neurosci.*, 23(5):216–222, 2000.

B. Hutcheon, R.M. Miura, and E. Puil. Subthreshold membrane resonance in neocortical neurons. *J. Neurophysiol.*, 76(2):683–697, 1996.

E.M. Izhikevich. Neural excitability, spiking and bursting. *Int. J. Bifurcation Chaos Appl. Sci.*, 10(6):1171–1266, 2000.

E.M. Izhikevich. Resonate-and-fire neurons. *Neural Netw.*, 14:883–894, 2001.

E.M. Izhikevich. Which model to use for cortical spiking neurons? *IEEE Transactions on Neural Networks*, 15:1063–1070, 2004.

E.M. Izhikevich, N.S. Desai, E.C. Walcott, and Hoppensteadt. F.C. Bursts as a unit of neural information: selective communication via resonance. *Trends Neurosci.*, 26:161–167, 2003.

G. G. Izús, R. R. Deza, and H. S. Wio. Exact nonequilibrium potential for the FitzHugh-Nagumo model in the excitable and bistable regimes. *Phys. Rev. E*, 58(1):93–98, 1998.

G.A. Jacobson, K. Diba, A. Yaron-Jakoubovitch, Y. Oz, C. Koch, I. Segev, and Y. Yarom. Subthreshold voltage noise of rat neocortical pyramidal neurones. *J. Physiol.*, 564(1): 145–160, 2005.

M. James, F. Moss, P. Hänggi, and C. Van den Broeck. Switching in the presence of colored noise: The decay of an unstable state. *Phys. Rev. A*, 38(9):4690–4695, 1988.

F. Jaramillo and K. Wiesenfeld. Mechanoelectrical transduction assisted by brownian motion: a role for noise in the auditory system. *Nat. Neurosci.*, 1(5):384–388, 1998.

P. Jung and J.W. Shuai. Optimal sizes of ion channel clusters. *Europhys. Lett.*, 56(1):29–35, 2001.

A.R. Kay, M. Sugimori, and R. Llinas. Kinetic and stochastic properties of a persistent sodium current in mature guinea pig cerebellar purkinje cells. *J. Neurophysiol.*, 80(3): 1167–1179, 1998.

J. Keener and J. Sneyd. *Mathematical Physiology.* Springer, New York, 1998.

A. Kepecs and J. Lisman. Information encoding and computation with spikes and bursts. *Network*, 14:103–18, 2003.

C. Koch. *Biophysics of Computation: Information Processing in Single Neurons.* Oxford University Press, New York, 1999.

N. Kopell and G.B. Ermentrout. *Mechanisms of phase-locking and frequency control in pairs of coupled neural oscillators, Handbook on Dynamical Systems: Toward applications. Ed. B. Fiedler*, volume 2. Elsevier, 2002.

H.A. Kramers. Brownian motion in a field of force and the diffusion model of chemical reactions. *Phys.*, VII(4):284–304, 1940.

S.W. Kuffler, R. FitzHugh, and H.B. Barlow. Maintained activity in the cat's retina in light and darkness. *J. Gen. Physiol.*, 40:862–702, 1957.

F. Kuhrt. Das tropfchenmodell übersattigter realer gase. *Z. Phys.*, 131(2):205–214, 1951.

C. Kurrer and K. Schulten. Effect of noise and perturbations on limit cycle systems. *Physica D*, 50(3):311–320, 1991.

A.M. Kuznecov and J. Ulstrup. *Electron Transfer in Chemistry and Biology : an Introduction to the Theory.* Wiley, Chichester, 1999.

A.M. Lacasta, F. Sagués, and J.M. Sancho. Coherence and anticoherence resonance tuned by noise. *Phys. Rev. E*, 66:045105(R), 2002.

I. Lampl and Y. Yarom. Subthreshold oscillations and resonant behavior: two manifestations of the same mechanism. *Neuroscience*, 78:325–341, 1997.

W. Ledermann. *Handbook of Applicable Mathematics, vol.6, Statistics.* Wiley, Chichester, 1984.

J.E. Levin and J.P. Miller. Broadband neural encoding in the cricket cereal sensory system enhanced by stochastic resonance. *Nature*, 380(6570):165–168, 1996.

S. Liepelt, J.A. Freund, L. Schimansky-Geier, D. Russell, A.B. Neiman, and F. Moss. Information processing in noisy burster models of sensory neurons. *J. Theor. Biology*, 237(1): 30–40, 2005.

A.E. Likthman and C.M. Marques. First-passage problem for the rouse polymer chain: An exact solution. *Europhys. Lett.*, 75(6):971–977, 2006.

B. Lindner. *Coherence and Stochastic Resonance in Nonlinear Dynamical Systems.* Logos Verlag, Berlin, 2002.

B. Lindner. Interspike interval statistics of neurons driven by colored noise. *Phys. Rev. E*, 69:022901, 2004.

B. Lindner and L. Schimansky-Geier. Analytical approach to the stochastic FitzHugh-Nagumo system and coherence resonance. *Phys. Rev. E*, 60(6):7270–7276, 1999.

B. Lindner, L. Schimansky-Geier, and A. Longtin. Maximizing spike train coherence or incoherence in the leaky integrate-and-fire model. *Phys. Rev. E*, 66(3):031916, 2002.

B. Lindner, J. García-Ojalvo, A. Neiman, and L. Schimansky-Geier. Effects of noise in excitable systems. *Phys. Reports*, 392(6):321–424, 2004.

J.E. Lisman. Bursts as a unit of neural information: making unreliable synapses reliable. *Trends Neurosci.*, 20(1):38–43, 1997.

R.R. Llinas, A.A. Grace, and Y. Yarom. In vitro Neurons in Mammalian Cortical Layer 4 Exhibit Intrinsic Oscillatory Activity in the 10- to 50-Hz Frequency Range. *PNAS*, 88(3): 897–901, 1991.

A. Longtin. Stochastic resonance in neuron models. *J. Stat. Phys.*, 70:309–327, 1993.

A. Longtin, A. Bulsara, and F. Moss. Time-interval sequences in bistable systems and the noise-induced transmission of information by sensory neurons. *Phys. Rev. Lett.*, 67:656–659, 1991.

S.B. Lowen, L.S. Liebovitch, and J.A. White. Fractal ion-channel behavior generates fractal firing patterns in neuronal models. *Phys. Rev. E*, 59(5):5970–5980, 1999.

D.V. Madison and R.A. Nicoll. Control of the repetitive discharge of rat CA1 pyramidal neurones in vitro. *J. Physiol.*, 354:319–331, 1984.

Z.F. Mainen and T.J. Sejnowski. Reliability of spike timing in neocortical neurons. *Science*, 268(5216):1503–1506, 1995.

V. A. Makarov, V. I. Nekorkin, and M. G. Velarde. Spiking behavior in a noise-driven system combining oscillatory and excitatory properties. *Phys. Rev. Lett.*, 86(15):3431–3434, 2001.

E. Manjarrez, J.G. Rojas-Piloni, I. Méndez, L. Martínez, D. Vélez, D. Vázquez, and A. Flores. Internal stochastic resonance in the coherence between spinal and cortical neuronal ensembles in the cat. *Neurosci. Lett.*, 326(2):93–96, 2002.

T.W. Marshall and E.J. Watson. A drop of ink falls from my pen. . . it comes to earth, I know not when. *J. Phys. A*, 18(18):3531–3559, 1985.

T.W. Marshall and E.J. Watson. The analytic solutions of some boundary layer problems in the theory of brownian motion. *J. Phys. A*, 20(6):1345–1354, 1987.

B.J. Matkowsky and Z. Schuss. The exit problem for randomly perturbed dynamical systems. *SIAM J. Appl. Math.*, 33(2):365–382, 1977.

A. Mauro, F. Conti, F. Dodge, and R. Schor. Subthreshold behavior and phenomenological impedance of the squid giant axon. *J. Gen. Physiol.*, 55(4):497–523, 1970.

D.A. McCormick and D. Contreras. On the cellular and network bases of epileptic seizures. *Ann. Rev. Physiol.*, 63:815–846, 2001.

V.I. Mel'nikov. The Kramers problem: fifty years of development. *Phys. Reports*, 209:1–71, 1991.

J.W. Middleton, M.J. Chacron, B. Lindner, and A. Longtin. Firing statistics of a neuron model driven by long-range correlated noise. *Phys. Rev. E*, 68(2):021920, 2003.

Ruben Moreno-Bote and Nestor Parga. Role of synaptic filtering on the firing response of simple model neurons. *Phys. Rev. Lett.*, 92(2):028102, 2004.

F. Moss, L.M. Ward, and W.G. Sannita. Stochastic resonance and sensory information processing: a tutorial and review of application. *Clinical Neurophysiol.*, 115(2):267–281, 2004.

A. Neiman and L. Schimansky-Geier. Stochastic resonance in bistable systems driven by harmonic noise. *Phys. Rev. Lett.*, 72(19):2988–2991, May 1994.

G. Nicolis and I. Prigogine. *Exploring Complexity.* W.H. Freeman and company, New York, 1989.

B. Nowakowski and A.L. Kawczyński. Multipeak distributions of first passage times in bistable dynamics in a model of a thermochemical system. *ChemPhysChem*, pages 502–507, 2006.

M. Ozer and N.H. Ekmekci. Effect of channel noise on the time-course of recovery from inactivation of sodium channels. *Phys. Lett. A*, 338(2):150–154, 2005.

C.M. Pedroarena, I.E. Pose, J. Yamuy, M.H. Chase, and F.R. Morales. Oscillatory membrane potential activity in the soma of a primary afferent neuron. *J. Neurophysiol.*, 82:1465–1476, 1999.

A.S. Pikovsky and J. Kurths. Coherence resonance in a noise-driven excitable system. *Phys. Rev. Lett.*, 78:775–778, 1997.

E. Pollak. Theory of activated rate processes: A new derivation of Kramers' expression. *J. Chem. Phys.*, 85(2):865–867, 1986.

E. Pollak. Variational transition state theory for activated rate processes. *J. Chem. Phys.*, 93(2):1116–1124, 1990.

L.A. Pontryagin, A. Andronov, and A. Vitt. On the statistical treatment of dynamical systems. *Zh. Eksp. Teor. Fiz.*, 3:165–180 (translated by J.B. Barbour and reproduced in *Noise in Nonlinear Dynamics*, 1989, edited by F. Moss and P.V.E. McClintock (Cambridge University Press, Cambridge) Vol.1 p. 329), 1933.

W.H. Press, S.A. Teukolsky, W.T. Vetterling, and B.P. Flannery. *Numerical Recipes in C.* Cambrige University Press, Cambrige, 1999.

E. Puil, H. Meiri, and Y. Yarom. Resonant behavior and frequency preferences of thalamic neurons. *J. Neurophysiol.*, 71(2):575–582, 1994.

A. Reboreda, E. Sanchez, M. Romero, and J.A. Lamas. Intrinsic spontaneous activity and subthreshold oscillations in neurones of the rat dorsal column nuclei in culture. *J. Physiol.*, 551(1):191–205, 2003.

S. Redner. *A Guide to First-Passage Processes.* Cambridge University Press, Cambridge UK, 2001.

P. Reimann, G. J. Schmid, and P. Hänggi. Universal equivalence of mean first-passage time and Kramers rate. *Phys. Rev. E*, 60(1):R1–R4, 1999.

S.O. Rice. Mathematical analysis of random noise. *Bell Syst. Tech. J*, 24:45–156, 1945.

M.J.E. Richardson. Effects of synaptic conductance on the voltage distribution and firing rate of spiking neurons. *Phys. Rev. E*, 69(5):051918, 2004.

M.J.E. Richardson, N. Brunel, and V. Hakim. From subthreshold to firing-rate resonance. *J. Neurophysiol.*, 89(5):2538–2554, 2003.

F. Rieke, D. Warland, R. de Ruyter van Steveninck, and W. Bialek. *Spikes: Exploring the Neural Code.* MIT Press, Cambridge, Mass., 1997.

H. Risken. *The Fokker-Planck Equation.* Springer, Berlin, 1989.

R.M. Rose and J.L. Hindmarsh. The assembly of ionic currents in a thalamic neuron .1. the 3-dimensional model. *Proc. R. Soc. Lond. B*, 237(1288):267–288, 1989.

R. Roy, A. W. Yu, and S. Zhu. Quantum fluctuations, pump noise, and the growth of laser radiation. *Phys. Rev. Lett.*, 55(25):2794–2797, 1985.

B. Sakmann and E. Neher. *Single-Channel Recording.* Plenum Press, New York, 1995.

L. Schimansky-Geier and Ch. Zülicke. Harmonic noise: Effect on bistable systems. *Z. Phys. B Condensed Matter*, 79(3):451–460, Oct 1990.

G. Schmid, I. Goychuk, and P. Hänggi. Stochastic resonance as a collective property of ion channel assemblies. *Europhys. Lett.*, 56(1):22–28, 2001.

E. Schneidman, B. Freedman, and I. Segev. Ion channel stochasticity may be critical in determining the reliability and precision of spike timing. *Neural Comput.*, 10(7):1679–1703, 1998.

S. Schreiber, I. Erchova, U. Heinemann, and A.V. M. Herz. Subthreshold resonance explains the frequency-dependent integration of periodic as well as random stimuli in the entorhinal cortex. *J. Neurophysiol.*, 92(1):408–415, 2004.

E. Schrödinger. Zur Theorie der Fall- unf Steigversuche an Teilchen mit Brownscher Bewegung. *Physik. Z.*, 16:289–295, 1915.

T. Shmiel, R. Drori, O. Shmiel, Y. Ben-Shaul, Z. Nadasdy, M. Shemesh, M. Teicher, and M. Abeles. Neurons of the cerebral cortex exhibit precise interspike timing in correspondence to behavior. *PNAS*, 102(51):18655–18657, 2005.

A.J.F Siegert. On the first passage time probability problem. *Phys. Rev*, 81(4):617–623, 1951.

D. Sigeti and W. Horsthemke. Pseudo-regular oscillations induced by external noise. *J. Stat. Phys.*, 54:1217–1222, 1989.

W. Singer. Neuronal synchrony: A versatile code for the definition of relations? *Neuron*, 24 (1):49–65, 1999.

S. M. Soskin. Large Fluctuations in Multiattractor Systems and the Generalized Kramers Problem. *J. Stat. Phys.*, 97(3):609–676, 1999.

S. M. Soskin. Most probable transition path in an overdamped system for a finite transition time. *Phys. Lett. A*, 353(4):281–290, 2006.

S. M. Soskin, V. I. Sheka, T. L. Linnik, and R. Mannella. Short time scales in the Kramers problem: A stepwise growth of the escape flux. *Phys. Rev. Lett.*, 86(9):1665–1669, 2001.

M. Steriade. Corticothalamic resonance, states of vigilance and mentation. *Neuroscience*, 101(2):243–276, 2000.

M. Steriade, R.C. Dossi, D. Pare, and G. Oakson. Fast oscillations (20-40 Hz) in thalamocortical systems and their potentiation by mesopontine cholinergic nuclei in the cat. *PNAS*, 88(10):4396–4400, 1991.

R.L. Stratonovich. *Topics in the Theory of Random Noise.* Gordon and Breach, New York, 1967.

G. Svirskis and J. Rinzel. Influence of temporal correlation of synaptic input on the rate and variability of firing in neurons. *Biophys. J.*, 79(2):629–637, 2000.

G. Svirskis and J. Rinzel. Influence of subthreshold nonlinearities on signal-to-noise ratio and timing precision for small signals in neurons: minimal model analysis. *Network*, 14(1): 137–150, 2003.

P. Talkner. Mean 1st passage time and the lifetime of a metastable state. *Z. Phys. B.*, 68 (2–3):201–207, 1987.

J.W. Thomas. *Numerical Partial Differential Equations: Finite Difference Methods.* Springer, New-York, 1995.

V.I. Tikhonov and M.A. Mironov. *Markovian Processes.* Sov. Radio, Moscow, 1977.

S.F. Traynelis and F. Jaramillo. Getting the most out of noise in the central nervous system. *Trends Neurosci.*, 21(4):137–145, 1998.

H.C. Tuckwell. *Introduction to Theoretical Neurobiology.* Cambridge University Press, Cambridge UK, 1988.

E. Turlot, D. Esteve, C. Urbina, J.M. Martinis, M.H. Devoret, S. Linkwitz, and H. Grabert. Escape oscillations of a josephson junction switching out of the zero-voltage state. *Phys. Rev. Lett.*, 62(15):1788–1791, 1989.

G. E. Uhlenbeck and L. S. Ornstein. On the theory of the Brownian motion. *Phys. Rev.*, 36 (5):823–841, Sep 1930.

E. Ullner, A. Zaikin, J. García-Ojalvo, R.B. Báscones, and J. Kurths. Vibrational resonance and vibrational propagation in excitable systems. *Phys. Lett. A*, 312(5-6):348–354, 2003.

E. Vaadia, I. Haalman, M. Abeles, H. Bergman, Y. Prut, H. Slovin, and A. Aertsen. Dynamics of neuronal interactions in monkey cortex in relation to behavioural events. *Nature*, 373 (6514):515–518, 1995.

N.G. van Kampen. *Stochastic Processes in Physics and Chemistry.* North-Holland, Amsterdam, 1992.

J.H. Van't Hoff. *Etudes de dynamique chimique, p. 114. Deutsch: Studien zur chemischen Dynamik. 1898.* F. Muller and Co., Amsterdam, 1884.

T. Verechtchaguina, L. Schimansky-Geier, and I.M. Sokolov. Spectra and waiting-time densities in firing resonant and nonresonant neurons. *Phys. Rev. E*, 70:031916, 2004.

T. Verechtchaguina, I.M. Sokolov, and L. Schimansky-Geier. First passage time densities in non-markovian models with subthreshold oscillations. *Europhys. Lett.*, 73(5):691–697, 2006a.

T. Verechtchaguina, I.M. Sokolov, and L. Schimansky-Geier. First passage time densities in resonate-and-fire models. *Phys. Rev. E*, 73:031108, 2006b.

T. Verechtchaguina, I.M. Sokolov, and L. Schimansky-Geier. Interspike interval densities of resonate-and-fire neurons. *Biosystems*, 89:63–68, 2007.

C. Viboud, O.N. Bjornstad, D.L. Smith, L. Simonsen, M.A. Miller, and B.T. Grenfell. Synchrony, waves, and spatial hierarchies in the spread of influenza. *Science*, 312(5772):447–451, 2006.

J.A. Villacorta and F. Panetsos. Information coding by ensembles of resonant neurons. *Biological Cybernetics*, 92(5):339–347, 2005.

E.I. Volkov, E. Ullner, A.A. Zaikin, and J. Kurths. Oscillatory amplification of stochastic resonance in excitable systems. *Phys. Rev. E*, 68(2):026214, 2003.

M.M. Waldrop. *Complexity: the Emerging Science at the Edge of Order ans Chaos.* Simon & Schuster Paperbacks, New York, 1992.

M. C. Wang and G. E. Uhlenbeck. On the theory of the Brownian motion II. *Rev. Mod. Phys.*, 17(2-3):323–342, Apr 1945.

J.A. White, R. Klink, A. Alonso, and A.R. Kay. Noise from voltage-gated ion channels may influence neuronal dynamics in the entorhinal cortex. *J. Neurophysiol.*, 80(1):262–269, 1998.

J.A. White, J.T. Rubinstein, and A.R. Kay. Channel noise in neurons. *Trends Neurosci.*, 23 (3):131–137, Mar 2000.

G. Wilemski and M. Fixman. Diffusion-controlled intrachain reactions of polymers. I theory. *J. Chem. Phys.*, 60(3):866–877, 1974.

N. Wu, C.-F. Hsiao, and S.H. Chandler. Membrane resonance and subthreshold membrane oscillations in mesencephalic v neurons: Participants in burst generation. *J. Neurosci.*, 21 (11):3729–3739, 2001.

R.W. Zwanzig. Contribution to the theory of Brownian motion. *Phys. Fluids*, 2(1):12–19, 1959.

List of symbols and abbreviations

Symbol	Description	Dimension	Definition
$\delta(x)$	Dirac δ-function	$[x]^{-1}$	
$\Theta(x)$	Heaviside step function	1	
$\xi(t)$	white Gaussian noise of unit intensity	$\mathrm{s}^{-1/2}$	
r	spike-count rate	s^{-1}	2.12
$n_p(t_p, \ldots, t_1)$	distribution function of a point process	s^{-p}	2.27
$g_p(t_p, \ldots, t_1)$	cumulant function of a point process	s^{-p}	2.28
$L_T[v(t)]$	generating functional	1	2.31
$\mathcal{F}(T)$	waiting-time density, first passage time density, interspike interval density	s^{-1}	2.34
$\Phi(T)$	survival probability	1	2.34
C_{var}	coefficient of variation	1	2.41
ρ_k	serial correlation coefficients	1	2.42
$F(\mathcal{T})$	Fano factor	1	2.45
$\kappa(T)$	time-dependent escape rate	s^{-1}	4.4

Abbreviation	Description	Abbreviation	Description
ISI	interspike interval	IF	integrate-and-fire
FPT	first passage time	RaF	resonate-and-fire
PDF	probability density function	FN	FitzHugh-Nagumo
SCC	serial correlation coefficient		

LIST OF PUBLICATIONS

T.A. Engel, S. Schreiber, L. Schimansky-Geier, A.V.M. Herz, and I. Erchova.
Membrane potential resonances shape spontaneous firing patterns in the entorhinal cortex. *To be submitted.*

T. Verechtchaguina, I. M. Sokolov, and L. Schimansky-Geier.
Interspike interval densities of resonate and fire neurons. *Biosystems*, **89**, 63–68 (2007).

T. Verechtchaguina, I. M. Sokolov, and L. Schimansky-Geier.
First passage time densities in resonate-and-fire models. *Physical Review E*, **73**, 031108 (2006).

T. Verechtchaguina, I. M. Sokolov and L. Schimansky-Geier.
First passage time densities in non-Markovian models with subthreshold oscillations. *Europhysics Letters*, **73** (5), pp. 691–697 (2006).

T. Verechtchaguina, L. Schimansky-Geier, and I. M. Sokolov.
Spectra and waiting-time densities in firing resonant and nonresonant neurons. *Physical Review E*, **70**, 031916 (2004).

T. Verechtchaguina.
Resonance effects in ensembles of FitzHugh-Nagumo oscillators. *Diploma thesis*, Moscow State University (2003).

DANKSAGUNG

Ich danke Prof. Schimansky-Geier und Prof. Sokolov für den gemeinsam zurückgelegten Weg, der stets anspruchsvoll aber niemals zu schwierig war. Es erfüllt mich mit Stolz, Ihre Schülerin zu sein und in den Genuss Ihrer wissenschaftlichen Förderung gekommen zu sein. Beiden gilt mein aufrichtiger Dank.

Prof. Herz möchte ich für seine Begeisterung für die Neurowissenschaft danken, welche mich besonders beeindruckt und geprägt hat. Seine Aufgeschlossenheit gegenüber neuen Ideen hat mich stets motiviert und ermutigt meine Ideen zu verfolgen.

Sehr gerne würde ich Prof. Heinrich für die Möglichkeit der Mitarbeit im Graduiertenkolleg danken. Das von Ihm ins Leben gerufene Graduiertenkolleg *Dynamik und Evolution zellulärer und makromolekularer Prozesse* gibt vielen jungen Wissenschaftlern die Möglichkeit, weltweit miteinander in Kontakt zu kommen und Ihre Ideen auszutauschen. Das damit verbundene Stipendium stellte die Grundlage für meine Promotion in Deutschland dar.

Dr. Irina Erchova hat mir ermöglicht, einen Einblick in die experimentellen Grundlagen der Neurowissenschaft zu erhalten. Die Ergebnisse unserer theoretischen Arbeit wurden erst durch Ihre Experimente mit Leben erfüllt. Die vielen Stunden in Skype und ihre Gastfreundschaft in Edinburgh habe ich sehr genossen. Dr. Susanne Schreiber möchte ich sehr für ihren kritischen Blick auf die Grundlagen unserer gemeinsamen Arbeit danken, der stets neue Ideen hervorgebracht hat.

Vitaly Belik, Robert Engel, Dr. Lars Meinhold, Dr. Tobias Prager und Dr. Susanne Schreiber danke ich für die undankbare Aufgabe des Korrekturlesens dieser Arbeit. Ihre zahlreichen Kommentare haben zum Gelingen meiner Arbeit mit beigetragen.

Ich bedanke mich bei den Arbeitsgruppen TSP und TSD, und im Besonderen bei Dr. Bartek Dybiec, Robert Engel, Dr. Dirk Henning, Dr. Axel Hutt, Dr. Tobias Prager, Tilo Schwalger und Dr. Ramon Xulvi-Brunet für die zahlreichen und interessanten Diskussionen.

Mein besonderer Dank gilt meiner Familie und meinen Freunden in Russland und in Berlin. Ohne Ihre Unterstützung wäre diese Arbeit nicht möglich gewesen. Sie haben die schwierigen Zeiten so viel erträglicher und die schönen Zeiten so viel angenehmer gestaltet.

Last but not least I thank my neurons, who by their constant subthreshold oscillations and their noise-enhanced synchrony created all these ideas about themselves.

Selbständigkeitserklärung

Hiermit erkläre ich, die vorliegende Arbeit selbständig ohne fremde Hilfe verfaßt und nur die angegebene Literatur und Hilfsmittel verwendet zu haben.

Tatiana Engel

Berlin
20 Dezember 2006